Vesicles are spherical macromolecular self-assembly structures formed by one or several closed bilayers in an aqueous medium. Their structural and functional versatility has led to numerous research and some industrial-scale applications, particularly in the fields of drug delivery and cosmetics. The main challenge in transferring the increasing number of suggested vesicle formulations from the academic bench to the market is the lack of gentle and controlled vesicle production processes.

This work explored new design and process strategies to generate functionalized vesicles for applications in the food industry in particular.
The assembly of food grade polymersomes from a new type of biocompatible and biodegradable amphiphilic diblock copolymer is reported. They showed controlled release properties under duodenal conditions. Furthermore, the gentle and scalable process of dynamically enhanced vesicle extrusion was introduced by constructing a ROtating Membrane ExtrudeR (ROMER). The device generates a defined shear flow at the outlet of a nanopore membrane to tear off the leading endcaps of extruded vesicles. The ability of the ROMER device to specifically adjust vesicle size and lamellarity was studied as a function of shear rate, pore shape, and bilayer elasticity. Finally, the functionalization of vesicles with superparamagnetic nanoparticles was evaluated with regard to creating versatile magnetic absorbents for bioseparation applications.

The experimental section of this work provides a useful set of simple and reliable methods for the routine characterization of vesicle suspensions during their development and production. Included are dynamic light scattering techniques to measure vesicle size and polydispersity, an optimized protocol of the TNBS assay to estimate vesicle lamellarity, the Stewart assay for total phospholipid determination, and the calcein leakage assay to characterize the encapsulation efficiency and release behavior of vesicles towards hydrophilic molecules.

Flow Processing to Structure and Functionalize Vesicles for Food Applications

Helen Engel

Helen Engel

Flow Processing to Structure and Functionalize Vesicles for Food Applications

Zürich 2014

Dissertation ETH number 22016

Flow Processing to Structure and Functionalize Vesicles for Food Applications

A thesis submitted to attain the degree of

DOCTOR OF SCIENCES of ETH ZURICH

(Dr. sc. ETH Zurich)

presented by

Helen Engel

Dipl. Lm.-Ing. ETH Zurich

born on 16 May 1981

citizen of Bülach, ZH, Switzerland

accepted on the recommendation of

Prof. Dr. Erich J. Windhab, Examiner

Prof. Dr. Peter Walde, Co-Examiner
Dr. Martin E. Leser, Co-Examiner

2014

Flow Processing to Structure and Functionalize Vesicles for Food Applications

To my parents and my siblings Cécile, Luca, and Robertino

Acknowledgements

It is a pleasure to thank all those who made this thesis possible and supported me along the way. Many people have shared their time and enthusiasm with me to give invaluable scientific advice, help with experimental procedures, data analysis, and technical installations, and to simply give me a great time. I am very grateful to all these people.

Mein Dank gilt in erster Linie meinem Doktorvater Prof. Dr.-Ing. Erich J. Windhab für die Möglichkeit zur Promotion im Labor für Lebensmittelverfahrenstechnik (LMVT) an der ETH Zürich. Seine Begeisterung, positive Energie und inspirierenden Visionen, die er immerzu in seinem Umfeld einbringt, haben mich stets beeindruckt und motiviert. Besonders dankbar bin ich ihm für sein grosses Vertrauen in meine Arbeit und für seine fachlichen, organisatorischen und manchmal auch philosophischen Wegweisungen. Seine Hilfe zur Fokussierung auf meine wissenschaftliche Arbeit bei zwischenzeitlich abweichenden Projektpriorisierungen haben dieser Arbeit den nötigen Rückhalt gegeben. Ich danke ihm auch für die vielen bereichernden Zusammenarbeiten mit nationalen und internationalen Industrie- und Forschungspartnern, die er mir ermöglicht hat. Nicht zuletzt bedanke ich mich für seine Offenheit sowie das positive und kreative Zusammenwirken seiner Gruppe, das er auf seine ganz persönliche und grosszügige Art zu fördern weiss.

Ein besonderer Dank gebührt auch Prof. Dr. Peter Walde vom Institut für Polymere, ETH Zürich. Die Übernahme des Korreferats war nur der krönende Abschluss der wertvollen Zusammenarbeit mit Peter, die ich während meiner ganzen Doktoratszeit geniessen durfte. Sein Expertenwissen und seine grosse Erfahrung auf dem Gebiet der Vesikel haben massgeblich zum Gelingen dieser Arbeit beigetragen. Ich danke ihm für die zahlreichen Diskussionen, die praktischen Inputs und die sorgfältigen und kritischen Auseinandersetzungen mit meinen Daten. Besonders dankbar bin ich über die gemeinsamen Publikationen, die diese Zusammenarbeit ermöglicht hat.
Not only the door to Peter's office, but also the one to his lab was always open for me and my students. He allowed us in a very generous way to perform many experiments using his facilities, where, in addition, we received great support from his PhD students. I would like to extend my gratitude to Dr. Sara Fornera, Dr. Andrea Grotzky, Dr. Zengwei Guo, and Dr. Katja Junker for always welcoming me in the lab G520 and for teaching me the laboratory skills I used in my experimental work.

Dr. Martin E. Leser (Nestlé Research Center, Lausanne, Switzerland) danke ich herzlich für sein Interesse an meiner Arbeit und seine freundliche Bereitschaft, das Korreferat zu übernehmen. Mit dem Blickwinkel aus der Praxis hat er als externer Gutachter eine besonders wertvolle Brücke meiner Forschungsarbeit zur Industrie geschlagen. Zudem hat

Contents

Notation

Latin Letters

Symbol	Unit	Meaning
$A_{(\lambda)}$	-	absorbance (at wavelength λ)
A	m^2	area
a_0	Å^2	mean headgroup or surface area per amphiphile
B	-	baseline value of autocorrelation function
C	m^{-1}	mean curvature
C_0	m^{-1}	spontaneous curvature
c	g or mol L^{-1}	mass or molar concentration
D	$\text{m}^2\,\text{s}^{-1}$	diffusion coefficient
D	-	Taylor deformation parameter
D_h	nm	hydrodynamic diameter
d	m	diameter
d	nm	lamellar repeat distance
d_B	nm	thickness of bilayer membrane
d_C	nm	hydrophobic core thickness of bilayer/membrane
E	%	relative external surface area of vesicle
E_b	$k_\text{B}T$ [J]	bending or curvature elastic energy of membrane
F	-	form factor
$G(\Gamma)$	-	distribution function of decay rates
h	m	height of plate-plate shear gap
h	m	thickness of lubrication layer
I	a. u.	intensity of light or neutrons
L_C	m	cylinder length of spherocylindrical vesicle
L_P	m	length of a pore channel
l_crit	Å	critical hydrophobic chain length per amphiphile
K	m^4	permeability of a pore channel
K_A	mN m^{-1}	area expansion or stretching elastic modulus
k	s^{-1}	rate constant for vesicle membrane permeation

Symbol (cont.)	Unit (cont.)	Meaning (cont.)
k_{B}	J K^{-1}	Boltzmann constant $(1.381 \times 10^{-23}$ JK$^{-1})$
$\bar{M}_n$	g mol^{-1}	number-average molecular weight of polymers
M_w	g mol^{-1}	weight-average molecular weight
N	-	number of stacked, coherent scattering bilayers
N_{diff}	-	number of single, diffuse scattering bilayers
n	rpm [s^{-1}]	number of revolutions
n	-	power-law index
n	m^{-1}	number density of vesicles in a pore channel
n_i	-	number of vesicles or pores in the size interval i
P	m s^{-1}	permeability coefficient of vesicle membrane
PDI	-	polydispersity index
p	-	critical packing parameter
Q	m^3 s^{-1}	volume flow rate
$Q_0(x)$	-	cumulative size distribution, number-weighted
$Q_3(x)$	-	cumulative size distribution, volume-weighted
$q_r(\lg x)$	-	logarithmic size density distribution
q	nm^{-1}	magnitude of scattering vector
r	m	radius
R_h	nm	hydrodynamic radius
R_G	nm	radius of gyration
R_0	m	radius of equivalent sphere of undeformed vesicle
R_{P}	m	radius of a pore channel
R_{V}	m	radius of a vesicle
R	mol/mol%	Percentage of molecules released from vesicle
R_{B}	-	molar ratio of detergent to lipid in bilayer
$R_{\mathrm{B}}^{\mathrm{sat}}$	-	R_{B} in detergent-saturated bilayer
$R_{\mathrm{B}}^{\mathrm{sol}}$	-	R_{B} at complete bilayer solubilization
R^2	-	coefficient of determination (goodness of a fit)
S	-	solubility or partition coefficient
S	-	structure factor
T	K	absolute temperature
T	°C	temperature
T_{g}	°C	glass transition temperature of polymers
T_{m}	°C	main phase transition temp. of membrane lipids
t	s	time
V	m^3	volume
V_{int}	μL	internal aqueous volume of a vesicle in μL water/μmole amphiphile
v	Å^3	hydrophobic chain volume per amphiphile

Symbol (cont.)	Unit (cont.)	Meaning (cont.)
v	-	reduced volume of vesicle
v	m s^{-1}	local velocity of fluid or vesicle
w_A	-	weight ratio of block A in multiblock copolymer
x	m	vesicle or pore size defined by equivalent diameter
x_0	m	nominal pore diameter of a commercial membrane
$x_{10,r}$	m	lower limiting diameter at which $Q_r(x)$ is 10%
$x_{50,r}$	m	median diameter at which $Q_r(x)$ is 50%
$x_{90,r}$	m	upper limiting diameter at which $Q_r(x)$ is 90%
x_i	m	diameter at the upper limit of the size interval i
$\bar{x}_i$	m	mean diameter in the size interval i

Greek Letters

Symbol	Unit	Meaning
α	-	fractional area expansion of bilayer/membrane
β	-	optical constant of experimental DLS setup
Γ	s^{-1}	decay rate of autocorrelation function
$\bar{\Gamma}$	s^{-1}	average decay rate of autocorrelation function
γ	-	shear deformation (strain)
$\dot{\gamma}$	s^{-1}	shear rate
Δ	-	relative excess area of vesicle
ΔP	Pa	pressure difference
$\Delta Q_3(x)$	%	relative size frequency, volume-weighted
Δx_i	m	width of the size interval i
$\dot{\varepsilon}$	s^{-1}	elongation rate
η	Pa s	dynamic viscosity under simple shear flow
η_E	Pa s	dynamic viscosity under uniaxial elongation flow
η_{ext}	Pa s	dynamic viscosity of vesicle's external fluid
η_S	mN m^{-1} s	shear viscosity of bilayer/membrane (in-plane)
θ	rad	scattering angle
κ_c	10^{-19} J	bending or curvature elastic modulus of membrane
κ_G	10^{-19} J	Gaussian curvature modulus of bilayer/membrane
κ_m	s^{-m}	mth cumulant of the distribution $G(\Gamma)$
λ	-	viscosity ratio η_{int}/η_{ext}

Symbol (cont.)	Unit (cont.)	Meaning (cont.)
λ	nm	wavelength of radiation source
λ_{em}	nm	emission wavelength detected from sample
λ_{ex}	nm	excitation wavelength of radiation source
λ_{max}	nm	wavelength at which absorbance is maximal
μ	mN m^{-1}	shear elastic modulus of membrane (in-plane)
μ	nm	location parameter of lognormal size distribution
μ_m	s^{-m}	mth moment about the mean of distribution $G(\Gamma)$
ρ	kg m^{-3}	density
σ	-	with parameter of lognormal size distribution
σ	mN m^{-1}	bilayer or membrane tension
σ_0	mN m^{-1}	effective membrane tension of undeformed vesicle
σ_l	mN m^{-1}	lysis tension of vesicle membrane
τ_{S}	mN m^{-1}	shear stress in bilayer/membrane plane
τ	s	delay time
ϕ	v/v%	volume fraction of dispersed nanoparticles
ω	s^{-1}	angular velocity

Indices

Symbol	Meaning
0	initial value; nominal value; value of undeformed vesicle
B	bilayer
b	bending
c	curvature
E	elongation
ext	external fluid of vesicle suspension
int	internal fluid of vesicle suspension
r	size distribution index (r = 0: number-weighted; r = 3: volume-weighted)
S	shear
x, y, z	across-, up- and down- pore channel/shear gap directions

Dimensionless Numbers

Symbol	Meaning
Ca_K	stretching capillary number for vesicle deformation
$Ca_{K,\mathrm{crit}}$	critical stretching capillary number for vesicle breakup
Ca_κ	bending capillary number for vesicle deformation
$Ca_{\kappa,\mathrm{crit}}$	critical bending capillary number for vesicle breakup
Re_{gap}	Reynolds number for fluid flow behavior in plate-plate shear gap
Re_{V}	Reynolds number for vesicle flow behavior in simple shear flow

Abbreviations

Abbrevation	Meaning
AAS	atomic absorption spectroscopy
ac	alternating current
b	*block*
BCP	block copolymer
Cer	ceramic
Chol	cholesterol
cryo-TEM	cryogenic transmission electron microscopy
DLPC	1,2-dilinoleoyl-*sn*-glycero-3-phosphocholine
DLS	dynamic light scattering
DTNB	5,5'-dithiobis-2-nitrobenzoic acid
D_2O	deuterium oxide; heavy water
E80	phosphatidylcholine isolate from egg yolk from Lipoid GmbH
FA	fatty acid
Fe_3O_4	iron oxide, magnetite
GUV	giant unilamellar vesicle
H_1	hexagonal phase
H_2	inverse hexagonal phase
ITO	indium tin oxide
L_α	liquid-disordered or fluid-like lamellar phase
$L_{\beta'}$	solid-ordered or gel-like lamellar phase with tilted alkyl chains
L_0	liquid-ordered lamellar phase
LA-LA	lauric acid bilayer
LM	light microscopy
LUV	large unilamellar vesicle
$LUVETs_{100}$	vesicles prepared by the repetitive extrusion technique using 100 nm pore membranes for final extrusions

Abbrevation (cont.)	Meaning (cont.)
MLV	multilamellar vesicle
MNF	magnetic nanofluid
MNP	magnetic nanoparticle
NP	nanoparticle
OA-OA	oleic acid bilayer
OLV	oligolamellar vesicle
PAA	poly(acrylic acid)
PBD	polybutadiene
PBO	poly(butylene oxide)
PC	phosphatidylcholine
PC200	polycarbonate membrane with 200 nm nominal pore diameter
PCL	poly(caprolactone)
PDMS	poly(dimethylsiloxane)
PE	phosphatidylethanolamine
PEE	poly(ethyl ethylene)
PEO	poly(ethylene oxide)
PET	poly(ethylene therephthalate)
PMCL	poly(γ-methyl-ε-caprolactone)
PMOXA	poly(methyloxazoline)
POPC	1-palmitoyl-2-oleoyl-*sn*-glycero-3-phosphocholine
POPE	1-palmitoyl-2-oleoyl-*sn*-glycero-3-phosphoethanolamine
PPO	poly(propylene oxide)
PS	polystyrene
Pt	platinum
ROMER	rotating membrane extruder
rpm	revolutions per minute
SANS	small angle neutron scattering
SC	sodium cholate
SEC	size exclusion chromatography
SEM	scanning electron microscopy
SUV	small unilamellar vesicle
S100	phosphatidylcholine isolate from soybean from Lipoid GmbH
TNBS	2,4,6-trinotrobenzene sulfonate
TNP	trinitrophenyl
Triton	Triton X-100
VETs$_{200}$	vesicles prepared by the repetitive extrusion technique using 200 nm pore membranes for final extrusions

Summary

Vesicles are spherical compartment structures in an aqueous medium. They consist of an aqueous core and one or more self-assembled, closed bilayers of amphiphilic molecules. The amphiphiles may be biomembrane phospholipids, synthetic surfactants, or amphiphilic block copolymers. The structural and functional versatility of vesicles has led to numerous successful and even some commercial applications in various fields, such as biomembrane research, biomedicine, diagnostics, cosmetics, and food technology. This wide applicability and the strong interest in vesicles can be understood on the basis of their most outstanding properties which include (i) a high biocompatibility, (ii) the adjustability in composition and size, ranging from 20 nm to several tens of micrometers, (iii) the ease of surface modification, and (iv) the ability of encapsulating both hydrophilic and hydrophobic molecules into the aqueous core and the membrane interior, respectively.

Whereas vesicles have been developed to the point where they serve as stimuli-responsive drug delivery vehicles in biomedical applications, their application in food systems is currently lagging behind the technologies established in the biomedical field. Furthermore, the increasing variety of vesicle formulations suggested in either field of biomedicine, cosmetics, or foods needs to be augmented by gentle and controlled production processes.

The present work explored the design and controlled formation of functionalized vesicle structures, in particular but not exclusively for food applications with nutritional, large-scale processing, and technological perspectives. This included the assembly of edible polymersomes from a new type of food grade, amphiphilic block copolymer for controlled delivery-release applications under gastrointestinal conditions. The gentle and scalable process of dynamically enhanced vesicle extrusion was introduced and investigated for its ability to specifically adjust vesicle size and lamellarity. Finally, vesicles were combined with superparamagnetic iron oxide nanoparticles (NPs) with the aim of creating versatile magnetic adsorbents for bioseparation applications.

Multilamellar vesicle (MLV) precursors were prepared by the thin film hydration method. They were homogenized by repetitive extrusion through polycarbonate membranes with 800 nm, 400 nm, and 100 nm pore diameters to obtain VETs$_{800}$, VETs$_{400}$, and LUVETs$_{100}$, i.e. (large unilamellar) vesicles prepared by the extrusion technique, respectively. Giant unilamellar vesicles (GUVs) were formed using

the electroformation method. The mean size and polydispersity of LUVET suspensions, NP dispersions, and their composites were analyzed by dynamic light scattering (DLS). The degree of vesicle lamellarity was estimated using an optimized version of the TNBS assay for external vesicle surface area determination. These routine measurements were complemented with cryo transmission electron microscopy (cryo-TEM) and small angle neutron scattering (SANS) experiments. The Stewart assay was used to determine total phospholipid concentrations, while vesicle release properties were studied by the calcein leakage assay.

The biocompatible and biodegradable PEO-b-PMCL diblock copolymer was investigated for its ability to form food grade polymersomes with high storage stability and controlled release properties under gastrointestinal conditions.
The membrane bound vesicle structure was demonstrated by the successful preparation of LUVETs$_{100}$ from PEO$_{23}$-b-PMCL$_{63}$ with the hydrophilic, fluorescent dye calcein encapsulated in the aqueous core at high self-quenching concentration. The stability of the obtained polymer vesicles in terms of load retention was, however, not significantly higher than that of conventional, thin-walled lipid vesicles. This was revealed by the small difference between the passive permeability coefficients of calcein from LUVETs$_{100}$ prepared from PEO$_{23}$-b-PMCL$_{63}$ and 1-palmitoyl-2-oleoyl-sn-glycero-3-phosphocholine (POPC), respectively. In terms of barrier properties towards hydrophilic molecular cargo, the increased membrane thickness of the PEO$_{23}$-b-PMCL$_{63}$ bilayer was compensated by its less hydrophobic nature and its less ordered, entangled structure compared to the densely packed POPC membrane. The presence of external bile salts at duodenal concentration triggered an immediate and complete release of calcein from the POPC LUVETs$_{100}$. In contrast, calcein release from the PEO$_{23}$-b-PMCL$_{63}$ LUVETs$_{100}$ under the same gastrointestinal stress conditions followed a first-order release kinetic and was only complete after an incubation time of 30 min. This controlled destabilization behavior renders the food grade PEO-b-PMCL vesicles promising carriers for the delivery of nutrients and neutraceuticals to their site of absorption at increased bioavailability. To this end, the synthesis protocol of aqueous PEO-b-PMCL LUV suspensions needs, however, to be optimized in terms of coexisting mixed morphologies, vesicle yield, and encapsulation efficiency.
The self-assembly of certain PEO-b-PMCL polymers into predominantly lamellar vesicle structures was also directly observed under the light microscope by the formation of GUVs from PEO$_{23}$-b-PMCL$_{50}$ using an adapted electroformation protocol. The higher voltage required for the PEO-b-PMCL membrane to grow and its higher resistance to lateral fusion compared to POPC bilayers reflected the enhanced mechanical stability of polymersome membranes.

The gentle, continuous, and scalable process of dynamically enhanced vesicle extrusion was introduced within the scope of this work by designing and setting up the ROtating Membrane ExtrudeR (ROMER). The device couples the conventional

(static) extrusion process with a defined shear flow induced directly at the outlet of a nanopore membrane. Varying shear rates were expected to allow for a controlled shearing-off of leading vesicle endcaps emerging from the nanopore membrane. Thereby, vesicle size and lamellarity were meant to be controlled by a single, dynamically enhanced extrusion cycle. This was investigated in systematic parameter studies using regularized MLV, i.e. pre-extruded VET_{800}, suspensions from pharmaceutical grade phosphatidylcholines (PCs) and nanopore membranes with 200 nm pore diameters and different pore shapes.

Dynamically enhanced VET_{800} extrusion resulted in a small decrease in mean vesicle size and lamellartiy with increasing shear rates, if the shear forces acted at the outlet of a nanopore membrane with cylindrical pore channels. However, the collected vesicle suspensions were still characterized by the presence of heterogeneous, uni-, oligo- and multilamellar vesicles, irrespectively of the applied shear rate. The ROMER shear flow had no influence on the structure of vesicles emerging from conical pore exits. This showed that nanometer-sized lipid vesicles are only broken up by the action of the ROMER shear forces in the limit where they emerge from the confinement of cylindrical pore channels in a deformed, i.e. pre-stretched, state. However, since large MLV precursors are extensively broken down by a pressure-induced rupture mechanism at the pore entrance, this precondition for the effective shearing-off of pre-stretched vesicle endcaps at the pore exit is hardly given. Therefore, dynamically enhanced extrusion of MLV pre-suspensions did not allow the controlled generation of homogeneous, unilamellar to n-multilamellar vesicles by adjusting the shear rate at the membrane outlet. Nevertheless, the ROMER setup gave valuable insight into the mechanism of vesicle extrusion as discussed in this work.

Water-based magnetic nanofluids containing fatty acid bilayer stabilized, superparamagnetic iron oxide NPs were considered to load magnetic nanoparticles (MNPs) into the lumen of pharmaceutical grade phospholipid vesicles for bioseparation applications. The resulting magnetoliposomes could serve as cost-effective and versatile magnetic adsorbents offering the wide variety of liposomal surface functionalization, while showing no remanent magnetization.

Magnetoliposomes were prepared following the standard passive encapsulation protocol. This included MLV formation in the magnetic nanofluid, repetitive extrusion, and removal of nonentrapped MNPs by size exclusion chromatography (SEC). It turned out that fatty acid double layer coated iron oxide NPs were prone to agglomeration and to interactions with phospholipid bilayers. As a consequence, extrusion of the composite suspension was not practicable through pore sizes < 400 nm. Furthermore, the separation of $VETs_{400}$ from nonentrapped particle agglomerates by SEC was not successful. Finally, the particle agglomerates did not partition into the liposome lumen but were mainly localized in the external medium, often accumulated at the outer surface of the phospholipid vesicles. The poor stability of fatty

acid bilayer coated iron oxide NPs was attributed to the reversible adsorption of the dispersant layer and to the dynamic nature of fatty acid bilayers. Alternative strategies to sterically stabilize iron oxide NPs for subsequent liposome functionalization have been suggested.

In summary, this work provides a versatile platform of simple and reliable methodologies for the development, optimization, and in-process control of new vesicle formulations and processing technologies.

Zusammenfassung

Vesikel sind sphärische Kompartiment-Strukturen in wässrigen Medien. Sie bestehen aus einem wässrigen Kern und einem oder mehreren selbstorganisierten, geschlossenen Bilayern aus amphiphilen Molekülen. Bei den amphiphilen Molekülen kann es sich um biologische Phospholipide, synthetische Surfactants oder amphiphile Block Copolymere handeln. Die strukturelle und funktionelle Vielseitigkeit von Vesikeln hat zu vielen erfolgreichen, z. T. sogar kommerziellen Anwendungen in verschiedenen Gebieten geführt. Dazu gehören die Grundlagenforschung von Biomembranen, die Biomedizin, Diagnostik, und Kosmetik sowie die Lebensmitteltechnologie. Die breite Anwendbarkeit und das grosse Interesse an Vesikeln ist auf deren ausserordentliche Eigenschaften zurückzuführen. Die wichtigsten sind (i) eine hohe Biokompatibilität, (ii) die Einstellbarkeit der Zusammensetzung und Grösse, welche sich von 20 nm bis zum dreistelligen Mikrometer-Bereich erstreckt, (iii) die Leichtigkeit für Oberflächenmodifikation, und (iv) die Fähigkeit, sowohl hydrophile als auch hydrophobe Moleküle im wässrigen Kern oder im Membraninneren zu enkapsulieren.
Während Vesikel in biomedizinischen Anwendungen bis hin zu stimulus-reagierenden Vehikeln für die Abgabe von Arzneimitteln entwickelt wurden, hinkt ihre Anwendungsvielfalt in Lebensmittelsystemen den etablierten Technologien des biomedizinischen Bereichs hinterher. Des weiteren muss die zunehmende Vielfalt von vorgeschlagenen Vesikel-Rezepturen, nicht nur im Bereich der Biomedizin, sondern auch in Kosmetik- und Lebensmittelanwendungen, durch schonende und kontrollierte Produktionsprozesse erweitert werden.

Die vorliegende Arbeit erkundet das Design und die kontrollierte Bildung von funktionalisierten Vesikelstrukturen, vor allem aber nicht nur für Lebensmittelanwendungen mit Perspektiven in der Ernährung, der Herstellung im Industriellen Massstab und technologischer Anwendungen. Dies beinhaltete das Zusammenfügen von essbaren Polymersomen aus einem neuen, lebensmitteltauglichen, amphiphilen Block Copolymer für kontrollierte Freisetzungsanwendungen unter gastrointestinalen Bedingungen. Der schonende und skalierbare Prozess der dynamisch erweiterten Vesikelextrusion wurde eingeführt und bezüglich seiner Fähigkeit, Vesikelgrösse und -lamellarität spezifisch einzustellen, untersucht. Schliesslich wurden Vesikel mit superparamagnetischen Eisenoxid Nanopartikeln (NP) kombiniert, um vielseitige, magnetische Absorbenzien für Bioseparationsanwendungen zu kreieren.

Multilamellare vesikel (MLV) wurden mit der Film Hydratationsmethode herge-stellt. Diese wurden durch wiederholte Extrusion durch Polycabonatmembranen mit 800 nm, 400 nm, und 100 nm Porendurchmessern homogenisiert, um VETs$_{800}$, VETs$_{400}$, und LUVETs$_{100}$ ((large unilamellar) vesicles prepared by the extrusion technique) zu erhalten. Gigantische unilamellare Vesikel (GUV) wurden mit Hil-fe der Elektroformationsmethode hergestellt. Die Durchschnittsgrösse und Polydi-spersität von LUVET-Suspensionen, NP-Dispersionen und deren Komposite wur-den mittels dynamischer Lichtstreuung (DLS) analysiert. Der Grad der Vesikel-Lamellarität wurde unter Verwendung einer optimierten Version des TNBS assays für die Bestimmung der externen Vesikeloberfläche abgeschätzt. Diese Routinemes-sungen wurden mit cryo-TEM and SANS Experimenten ergänzt. Der Stewart assay wurde zur Bestimmung der Phospholipidkonzentration verwendet, während die Frei-setzungseigenschaften von Vesikeln mittels Calcein assay untersucht wurden.

Das biokompatible und biologisch abbaubare PEO-*b*-PMCL Block Copolymer wur-de im Hinblick auf seine Fähigkeit untersucht, lebensmitteltaugliche Polymersomen mit hoher Lagerstabilität und kontrollierten Freisetzungseigenschaften unter gastro-intestinalen Bedingungen zu bilden.

Die erfolgreiche Herstellung von LUVETs$_{100}$ aus PEO$_{23}$-*b*-PMCL$_{63}$ konnte durch die Enkapsulierung des hydrophilen, fluoreszierenden Farbstoffs Calcein im wäss-rigen Kern in hoher, selbst-quenchender Konzentration nachgewiesen werden. Die Freisetzungskinetik von Calcein aus diesen Polymervesikeln im Vergleich zu den konventionellen, dünnwandigen Lipidvesikeln wird jedoch nicht signifikant verzö-gert. Dies wurde ersichtlich aus dem geringen Unterschied zwischen den passiven Permeabilitätskoeffizienzen von Calcein aus PEO$_{23}$-*b*-PMCL$_{63}$ und 1-palmitoyl-2-oleoyl-*sn*-glycero-3-phosphocholine (POPC) LUVETs$_{100}$. Bezüglich Barriereeigen-schaften gegenüber hydrophilen Molekülen wurde die erhöhte Membrandicke des PEO$_{23}$-*b*-PMCL$_{63}$-Bilayers durch seine geringere Hydrophobizität und seine weniger geordnete, verkeilte Struktur im Vergleich zu der dicht gepackten POPC Membran kompensiert.

Die Gegenwart von externen Gallensalzen in Duodenumkonzentration löste bei den POPC LUVETs$_{100}$ eine unmittelbare und komplette Freisetzung von Calcein aus. Im Gegensatz dazu folgte die Calcein-Freisetzung aus den PEO$_{23}$-*b*-PMCL$_{63}$ LUVETs$_{100}$ unter denselben gastrointestinalen Stressbedingungen einer Kinetik erster Ordnung und war erst nach 30 min Inkubationszeit abgeschlossen. Diese kontrollierte Destabi-lisierung macht die lebensmitteltauglichen PEO-*b*-PMCL Vesikel besonders attrak-tiv als Transporter für die Auslieferung von Nährstoffen zu ihrem Absorptionsort mit erhöhter Bioverfügbarkeit. Hierfür muss aber das Syntheseprotokoll von wässrigen PEO-*b*-PMCL LUV-Suspensionen hinsichtlich coexistierenden gemischten Morpho-logien, Vesikelausbeute und Enkapsulierungseffizienz optimiert werden.

Die Selbstorganisation von bestimmten PEO-*b*-PMCL Molekülen in mehrheitlich lamellare Vesikelstrukturen konnte auch direkt während der Bildung von GUVs aus

PEO_{23}-b-$PMCL_{50}$ unter Verwendung eines angepassten Elektroformationsprotokolls unter dem Lichtmikroskop beobachtet werden. Die höhere Spannung, die von der PEO-b-PMCL Membran benötigt wurde um zu wachsen, und der höhere Wiederstand gegenüber lateraler Fusion im Vergleich zu POPC Bilayern spiegelte die erhöhte mechanische Stabilität von Polymermembranen wider.

Der schonende, kontinuierliche und skalierbare Prozess der dynamisch erweiterten Vesikel-Extrusion wurde im Rahmen dieser Arbeit eingeführt. Hierfür wurde ein ROtating MEmbrane Extruder (ROMER) entwickelt und erfolgreich aufgebaut. Das Gerät verbindet den konventionellen (statischen) Extrusionsprozess mit einer definierten Scherströmung, die direkt am Austritt einer Nanoporenmembran erzeugt wird. Es wurde angenommen, dass die eingestellte Scherrate das Abscheren von aus der Nanoporenmembran austretenden Vesikelabschnitten kontrolliert, so dass die Vesikelgrösse und -lamellarität nach einem einzigen dynamisch erweiterten Extrusionszyklus spezifisch angepasst werden kann. Dies wurde im Rahmen einer systematischen Parameterstudie untersucht. Dabei wurden normalisierte MLV, d. h. vorextrudierte VET_{800}-Suspensionen aus pharmazietauglichen Phosphatidylcholinen (PC) und Nanoporenmembranen mit 200 nm Porendurchmesser sowie unterschiedlichen Porenformen verwendet.

Die dynamisch erweiterte Extrusion von VET_{800} resultierte lediglich in einer geringen Abnahme der mittleren Vesikelgrösse und -lamellarität mit zunehmenden Scherraten, wenn die Scherkräfte am Ausgang von Nanoporenmembraen mit zylindrischen Porenkanälen wirkten. Unabhängig von der angewandten Scherrate waren die so produzierten Vesikelsuspensionen durch die Präsenz von heterogenen, uni-, oligo- und multilamellaren Vesikeln charakterisiert. Die ROMER Scherströmung hatte keinen Einfluss auf die Struktur der Vesikel, die aus konischen Porenausgängen hinaustraten. Dies zeigte, dass nanometer-grosse Lipidvesikel nur durch die Einwirkung von ROMER Scherkräften aufbrechen, wenn sie in einem deformierten, gestreckten Zustand aus der Einschränkung von zylindrischen Porenkanälen austreten. Weil grosse MLV-Vorläufer allerdings bereits am Poreneingang durch einen druckinduzierten Reissmechanismus stark aufgebrochen werden, wird diese Voraussetzung für die effektive Abscherung von gestreckten Vesikelabschnitten am Porenausgang kaum noch erfüllt. Deshalb war es nicht möglich, mittels dynamisch erweiterter Extrusion von MLV-Vorsuspensionen homogene, unilamellare bis n-multilamellare Vesikel durch Variation der Scherrate am Membranaustritt gezielt zu generieren. Nichtsdestotrotz hat der ROMER-Setup einen wertvollen Einblick in den Mechanismus der Vesikelextrusion ermöglicht.

Wasserbasierte, magnetische Nanofluide, die fettsäurebilayer-stabilisierte, superparamagnetische Eisenoxid-NPs beinhalten, wurden evaluiert, um magnetische Nanopartikel (MNP) in das Lumen von pharmazietauglichen Posphlipidvesikeln für Bioseparationsanwendungen zu laden. Die resultierenden Magnetoliposomen könnten als kostengünstige und vielseitige magnetische Absorbenzien dienen, die eine

grosse Vielfalt von liposomalen Oberfächenfunktionalisierungen offerieren und keine magnetische Remanenz zeigen.

Magnetoliposomen wurden mittels Standardprotokoll der passiven Enkapsulierung hergestellt. Dies beinhaltet die Bildung von MLVs im magnetischen Nanofluid, mehrfache Extrusion und die Entfernung von uneingschlossenen MNPs durch Gelfiltration (SEC). Es hat sich herausgestellt, dass fettsäurebilayer-beschichtete Eisenoxid-NPs stark zu Agglomeration und zur Interaktion mit Phospholipid-Bilayern neigen. Deshalb war die Extrusion der Kompositsuspension durch Porengrössen $< 400\,\text{nm}$ nicht praktikabel und die Trennung von VETs_{400} von uneingeschlossenen Partikelagglomeraten mittels SEC nicht erfolgreich. Schliesslich lagerten sich die Partikelagglomerate nicht in das Lumen der Liposomen ein, sondern befanden sich hauptsächlich im äusseren Medium, oft an der Oberfläche von den Phospholipidvesikeln akkumuliert. Die geringe Stabilität der fettsäurebilayer-beschichteten Eisenoxid-NPs wurde der reversiblen Adsorption der Dispersionsschicht und den dynamischen Eigenschaften von Fettsäurebilayern zugeschrieben. Alternative Strategien zur sterischen Stabilisierung von Eisenoxid-NPs für die darauffolgende Funktionalisierung von Liposomen wurden vorgeschlagen.

Abschliessend bleibt festzuhalten, dass die vorliegende Arbeit eine nützliche Sammlung von einfachen und zuverlässigen Methoden zur Entwicklung, Optimierung und Qualitätskontrolle von neuen Vesikelrezepturen und Verarbeitungstechnologien beinhaltet.

1 Introduction

Vesicle structure and properties: Vesicles are nanometer- to micrometer-sized spherical compartments formed in vitro in an aqueous medium. They consist of an aqueous core and one or more closed shells, also called lamellae or membranes, composed of amphiphilic molecules. The amphiphiles may comprise a single species or a mixture of bilayer-forming low molar mass compounds (phospholipids or synthetic surfactants) or amphiphilic block copolymers. The common feature of vesicle-forming amphiphiles is their ability to self-assemble into highly ordered flexible membranes that self-close in excess water with the hydrophilic parts of the amphiphiles facing towards the inner and outer aqueous medium and the hydrophobic parts forming the membrane interior [1, 2]. If the membrane is constituted from lipids present in biological membranes, vesicles are also called *lipid vesicles* or more commonly *liposomes.* Accordingly, vesicles prepared from polymers are referred to as *polymersomes.*
Owing to the variability of amphiphile structures, vesicle membrane compositions, medium conditions, and methods available for vesicle preparation, the physicochemical properties of the resulting aggregate structures can be adjusted to numerous possible applications [3–8]. Vesicle properties include, for example, their mean size and lamellarity [9, 10], as well as the thickness, permeability, bending elasticity (rigidity), and lysis tension (mechanical strength) of the vesicle membrane [11–19].

Functional versatility and applications of vesicles: A high biocompatibility, the structural specificity and the possibility of tailoring vesicle properties via the process-structure-property functions indicated in Figure 1.1 (top plane) render vesicles one of the most researched biomimetic and nanocarrier systems in fundamental and applied science. First described in 1964 [20], today, vesicles are often used as templates to build highly engineered multifunctional compartment structures that serve for example as stimuli-responsive drug delivery vehicles [21–24], nanoreactors [25–27], biosensors [28, 29], image contrast agents [30, 31], or cell-like systems [32–34]. It is again the well-defined structure of vesicles that allows to create this functional versatility by assembling the functional components (Fig. 1.1, mid plane) into and/or onto the vesicles (Fig. 1.1, top plane), while preserving the structure and properties of each component in the resulting composite (Fig. 1.1, bottom plane) [6, 35]. The structure of plain vesicles allows, for example, the passive encapsulation of both

1

Structure

vesicles

functional nanomaterials

functional vesicle-based composite

Property

Process

Chapter 3

Chapter 4

Chapter 5
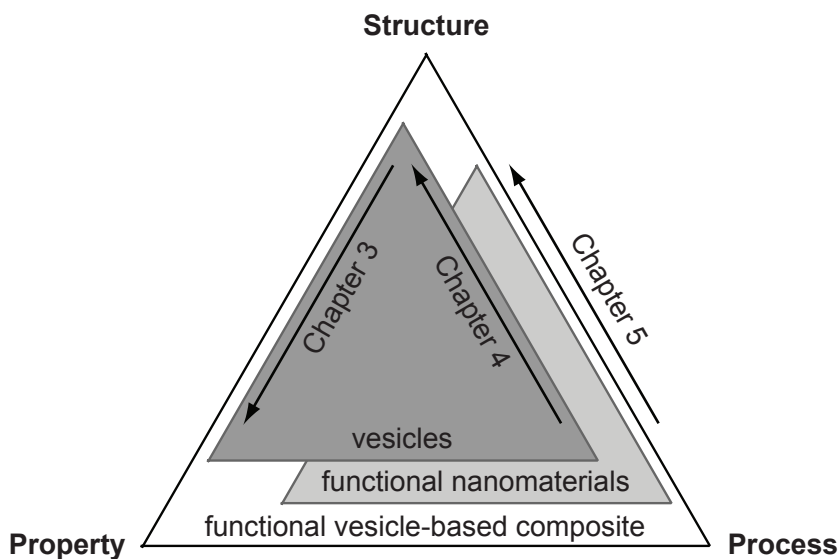
Figure 1.1: Contents of this thesis. Process-structure-property functions of vesicles (top plane), functional nanomaterials (mid plane) and their versatile composites (bottom plane). Vesicles can be combined with a wide range of functional nanomaterials, e. g. hydrophilic and hydrophobic bioactive cargo, surface-functional components, macromolecules, and nanoparticles, to create multifunctional compartment structures for numerous applications. This requires close control over the process-structure-property functions of each component and of the resulting composite material. In the present work, this task has been broken down to the indicated individual relationships with the overall aim of developing new processing technologies for the controlled formation of functionalized and application-tailored vesicle systems.

hydrophilic and hydrophobic molecular cargo into the aqueous lumen and the hydrophobic membrane core, respectively. This is the basic and most unique functionality of vesicles that has been used ever since the early, traditional liposome formulations up to the new-generation carrier systems developed today. Furthermore, vesicles can readily be surface modified, e. g. with protective polymers, targeting ligands, or diagnostic labels [35]. Enzymes [36], cellular macromolecules [32], and nanoparticles [24, 37] are other examples of functional nanomaterials that are integrated into vesicles along the synthesis path of the multifunctional compartments listed above. It has to be noted that close control over the process-structure-property functions of each component and of the composite material is required to harness the full potential of multifunctional vesicles (Fig. 1.1).

Vesicles in an industrial context: The enormous scientific interest in functionalized vesicle systems is closely related to the high demand of the pharmaceutical, cosmetic and food industries for stable, stimuli-responsive capsules with controlled

release properties. To act as such, the capsules should protect the encapsulated cargo from degradation through all steps of preparation, storage, and administration, while releasing the cargo at a target destination by an internal or external trigger (stimulus) [23]. Decreased degradation and a high degree of localization of released cargo promotes the efficacy of the encapsulated agent at the target destination and allows to lower its overall concentration in the initial product. In the case of pharmaceuticals, encapsulation of cytotoxic drugs and the decrease in administered dose also reduces the risk of adverse side effects which is especially promising in cancer treatment [38, 39].

Vesicles are highly attractive for the design of such 'smart' delivery-release vehicles due to the unique properties outlined above, including their biocompatibility, adjustability in physicochemichal properties, and functional versatility. In the biomedical field, targeting and triggered cargo release from functionalized vesicles has been demonstrated in a multitude of experimental drug delivery applications [22–24]. A considerable number of therapeutic liposome formulations has also been approved for clinical use, however, most of them lack selective targeting properties [21, 35, 40]. The use of vesicles in cosmetic and food applications has been explored to a more limited extent and is, so far, almost exclusively based on traditional liposomes with no targeting and triggered release properties [6, 41, 42]. Following the design strategies developed for the assembly of 'smart' vesicle-based drug delivery vehicles, there is obviously great potential and interest of the food industry to use vesicles as 'smart' carriers of nutritional and health supplements for targeted delivery of the supplements to the site of absorption [6, 43, 44].

While multifunctional vesicles are being shown to perform well in an increasing number of experimental applications, the transfer from academic bench to industrial application is still a challenge [21]. In particular, the large variety of suggested vesicle applications needs to be augmented by simple, gentle, and controlled production processes [35, 45]. With this perspective, one of the main **objectives of this work** is to provide new, scalable processing technologies to the pharmaceutical, cosmetic and food industries for the controlled formation of functionalized and application-tailored vesicle systems. In terms of vesicle properties and functions, special emphasis is placed on food applications. In the pursuit of this aim, individual relationships within the process-structure-property functions of (functionalized) vesicles are evaluated as indicated in Figure 1.1 and as mentioned in the following outline of the present thesis.

Chapter 2 gives general background information on the structure and properties of self-assembled vesicles. The principles of their conventional preparation methods, of the new process introduced in this work, as well as of the main characterization methods used are presented. The latter include, in particular, a simple chemical assay for external vesicle surface area determination that has been optimized in the frame of this work and published in *Analytical Biochemistry* 442, 262-271 (2013).

Chapter 3 focuses on the structure-property function of standard phospholipid vesicles and polymersomes prepared from a new type of food grade block copolymer, namely poly(ethylene oxide)-*block*-poly(γ-methyl-ε-caprolactone) (PEO-*b*-PMCL). Large unilamellar vesicles are used to study the release properties of encapsulated molecular cargo under undisturbed and gastrointestinal stress conditions, while the formation of giant unilamellar vesicles gives information about the mechanical properties of the vesicle membranes.

Chapter 4 studies the process-structure relationship of lipid vesicles generated by dynamically enhanced vesicle extrusion using the so-called ROtating Membrane ExtrudeR (ROMER) prototype. The structure of the collected vesicles in terms of mean size, polydispersity, and relative external surface area, i.e. lamellarity, is described as a function of the applied shear rate, pore shape, and bilayer elasticity. A discussion of vesicle deformation and breakup criteria in the ROMER device is included.

Chapter 5 reports on the design of functionalized liposomes for magnetic bioseparation applications following a reverse engineering approach. That is, combining the well-known properties/advantages of superparamagnetic nanoparticles (NPs) and lipid vesicles in a vesicle-based, NP-entrapping composite system with the aim of preserving the structure and property of each component.

Chapter 6 closes this thesis with a summary of the main achievements in the general conclusions. It also gives an outlook on the potential of the investigated systems as well as a collection of ideas for further research.

The three result chapters 3 to 5 contain their own introductions and materials & methods sections so that they can also be read and understood individually.

2 Background

2.1 Self-assembly of amphiphilic molecules

Amphiphilic molecules (amphiphiles), such as surfactants, lipids, copolymers, and proteins, are composed of hydrophilic and hydrobhobic parts. Due to this dual character they are able to spontaneously self-assemble into a variety of highly organized aggregate structures in aqueous solution. Thereby, the actual morphology assumed by an aggregate depends on the molecular constitution and concentration of the amphiphile as well as on the bulk solution conditions, as outlined below.

The main driving forces in the self-assembly of amphiphilic molecules originate from (i) the hydrophobic attraction of the hydrophobic chains based on their tendency to minimize contact with water (hydrophobic effect) and from (ii) the hydrophilic repulsion of the headgroups imposed by their opposite requirement to be in contact with water. The latter repulsive forces between the hydrophilic headgroups include contributions from steric, hydration, and, in the case of charged headgroups, electrostatic forces [2, 46].

Preferred self-assembly structures based on the critical packing parameter: To a first approximation, the preferred self-assembly structure formed can be predicted by simple geometric considerations of the molecular shape and packing behavior of the amphiphilic building blocks. This can be done according to Israelachvili's simple concept of the **critical packing parameter p** that describes the molecular shape of an amphiphile within an equilibrium aggregate structure as [2]:

$$p = v/a_0 l_{\mathrm{crit}} \tag{2.1}$$

Here, v is the volume and l_{crit} the critical length of the hydrophobic chain(s) in the fluid state, while a_0 is the optimal headgroup area at which the opposing interaction forces of hydrophobic attraction and headgroup repulsion are balanced. It has to be noted that the optimal headgroup area a_0 is not a simple geometrical value, but an equilibrium parameter that depends on the solution conditions, such as temperature, pH, and electrolyte concentration. As a consequence, the aggregate structure formed by certain amphiphiles can readily transform from one to another simply by changing the solution conditions [2, 47, 49].
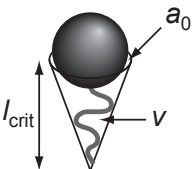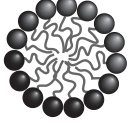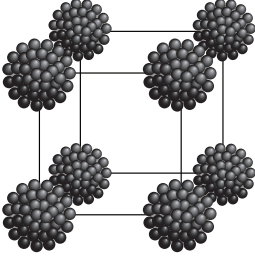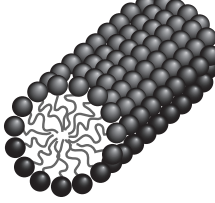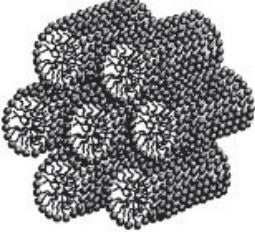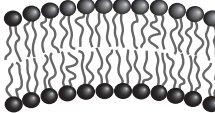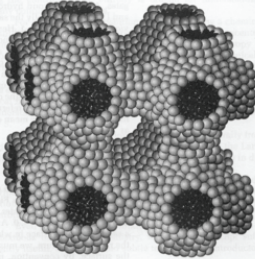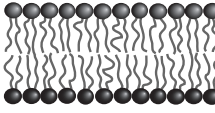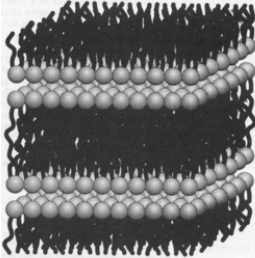
Critical packing parameter p	Molecular packing shape	Aggregate structure in isotropic solution	Lyotropic liquid-crystalline phase
$p = \dfrac{v}{a_0 l_{crit}} \leq 1/3$	a_0 l_{crit} v cone	spherical micelle	micellar cubic (M_1)
$1/3 < p \leq 1/2$	truncated cone	cylindrical micelle	hexagonal (H_1)
$1/2 < p < 1$	tapered cylinder	flexible bilayer ($\rightarrow$ vesicle)	bicontinuous cubic (C_1)
$p \approx 1$	cylinder	planar bilayer	lamellar (L)

Figure 2.1: Israelachvili's concept of the critical packing parameter. Schematic representation of the molecular shapes of amphiphilic molecules and their preferred self-assembly structures in dilute and concentrated aqueous solution according to Israelachvili's critical packing parameter model. Amphiphilic molecules are represented by a sphere (hydrophilic headgroup) and one or two connecting lines (hydrophobic chain(s) in the fluid state). Adapted from Israelachvili [2], Holmberg *et al.* [47], and Evans *et al.* [48].

Dilute amphiphile–water systems: Figure 2.1 illustrates some of the well-known self-assembly structures that are formed above the critical aggregation concentration (CAC) of an amphiphile in aqueous solution according to its molecular packing shape. Cone shaped molecules with a large headgroup area ($p \leq 1/3$) will preferentially assemble into spherical micelles. Less pronounced cone shapes ($1/3 < p \leq 1/2$) indicate the formation of nonspherical, cylindrical, or rod-like micelles. Amphiphiles exhibiting only a small mismatch between the hydrophilic and the hydrophobic moieties ($1/2 < p < 1$) self-assemble into flexible bilayers, while cylindrical molecules ($p \approx 1$) form planar, extended bilayers. Finally, amphiphilic molecules with $p > 1$ will associate into a range of inverted structures incorporating aqueous cores, such as inverse cylindrical micelles ($p \approx 2$) and inverse spherical micelles ($p \approx 3$) (not shown in Fig. 2.1) [2]. In dilute systems, these normal structures are singularly dispersed in the aqueous medium generating **isotropic disperions**.

Concentrated amphiphile–water systems: At higher amphiphile concentrations, the aggregate structures also interact between each other and further self-assemble into more ordered, three-dimensional networks. The resulting concentrated amphiphile–water systems are known as **lyotropic liquid-crystalline phases** or mesophases [2, 47, 49]. The terms *liquid-crystalline* and *mesophase* refer to the physical behavior of these highly viscous phases that is intermediate to liquid and solid, while *lyotropic* relates to their concentration-dependent phase behavior.
The rightmost column in Figure 2.1 depicts the preferred liquid-crystalline phases formed with increasing critical packing parameter from $p \leq 1/3$ to 1. In analogy to the gradation of isotropic normal structures, they range from micellar cubic phases (M_1) to columnar hexagonal phases (H_1) to various interconnected, bicontinuous cubic phases (C_1), such as Im3m (geometry shown in Fig. 2.1), Pn3m, or Ia3d, and to lamellar phases (L). At $p > 1$ the aggregate structures proceed again through the corresponding inverted phases designated as inverse cubic phases (C_2), inverse hexagonal phases (H_2) and, finally, inverse micellar cubic phases (M_2) [2].
It has to be noted that, due to the ordering effect in liquid crystals, the optimum headgroup area of a given amphiphile is decreased with increasing amphiphile concentration. As a consequence, the isotropic aggregate structures are usually driven to higher p values upon transition into lyotropic phases. Hence, at higher amphiphile concentrations, spherical micelles tend to transform into ordered hexagonal phases, cylindrical micelles into interconnected cubic phases, and flexible bilayers stack to form lamellar phases (Fig. 2.1).
Lamellar phases are the precursors of self-assembled vesicle structures as described in the following Section 2.2. They are built up of connected bilayer sheets (lamellae) alternating with water layers. The amphiphiles constituting the bilayers are arranged such that the hydrophilic headgroups face toward the aqueous surroundings on either side of the bilayer surface, while the hydrophobic chains form the bilayer interior.

Phase behavior of amphiphilic molecules: The phase behavior of amphipiles in aqueous solution is generally summarized in so-called phase diagrams which describe the range of equilibrium structures formed under specified conditions, most commonly amphiphile concentration and temperature [47, 50]. Varying amphiphile concentrations, i.e. solvent contents, describe the *lyotropic* phase behavior of a given amphiphile, while changing temperatures reveal its *thermotropic* phase behavior. In the case of amphiphilic block copolymers, the sequence of phases can also be studied as a function of amphiphile molecular weight or hydrophobic to hydrophilic block weight ratio (see later Fig. 2.5) [51, 52].

The phase behavior of a number of important biomembrane lipids, including phosphatidylcholines (PCs) which are most commonly used for vesicle preparation, and some lipid mixtures have been determined and reviewed [53, 54]. The lyotropic phase diagrams of the main amphiphiles used in this work are presented in Section 2.4 and Figure 2.5.

2.2 Vesicle structure

Vesicles enter the scheme of self-assembly structures as they evolve from bilayer forming amphiphiles with $1/2 < p < 1$ in excess water (Fig. 2.1). Upon hydration, vesicle forming amphiphiles first self-assemble into a lamellar phase before they transform to unbound flexible bilayer sheets and, finally, to closed spherical bilayers, i.e. vesicles [55–58]. The self-closing of flexible bilayer sheets in dilute aqueous solution is driven by the elimination of the energetically unfavorable contact of the hydrophobic edges with water.

According to this self-assembly process of vesicle formation, the **basic vesicle structure** can be described as a spherical shell consisting of one or more bilayer membranes and encapsulating a small volume of the aqueous solution in which the vesicle is formed. From a structural perspective, vesicles are most commonly classified by their size and number of bilayers (lamellae) as schematically shown in Figure 2.2. Unilamellar vesicles consist of a single bilayer. Based on their mean diameter d, they are subdivided into small unilamellar vesicles (SUVs; $d \lesssim 50\,\text{nm}$), large unilamellar vesicles (LUVs; $50\,\text{nm} \lesssim d \lesssim 1\,\text{µm}$), and giant unilamellar vesicles (GUVs; $d \gtrsim 1\,\text{µm}$). Oligolamellar vesicles (OLVs) are comprised of a few and multilamellar vesicles (MLVs) of several concentric bilayer shells. Finally, multivesicular vesicles (MVVs) are large or giant vesicles encapsulating smaller, nonconcentrically arranged vesicles inside [3, 59].

Considering the molecular packing geometry, **vesicle forming amphiphiles** are characterized by relatively large critical packing parameters ($1/2 < p < 1$), i.e. tapered cylindrical to cylindrical molecular shapes (Fig. 2.1). This requires rather
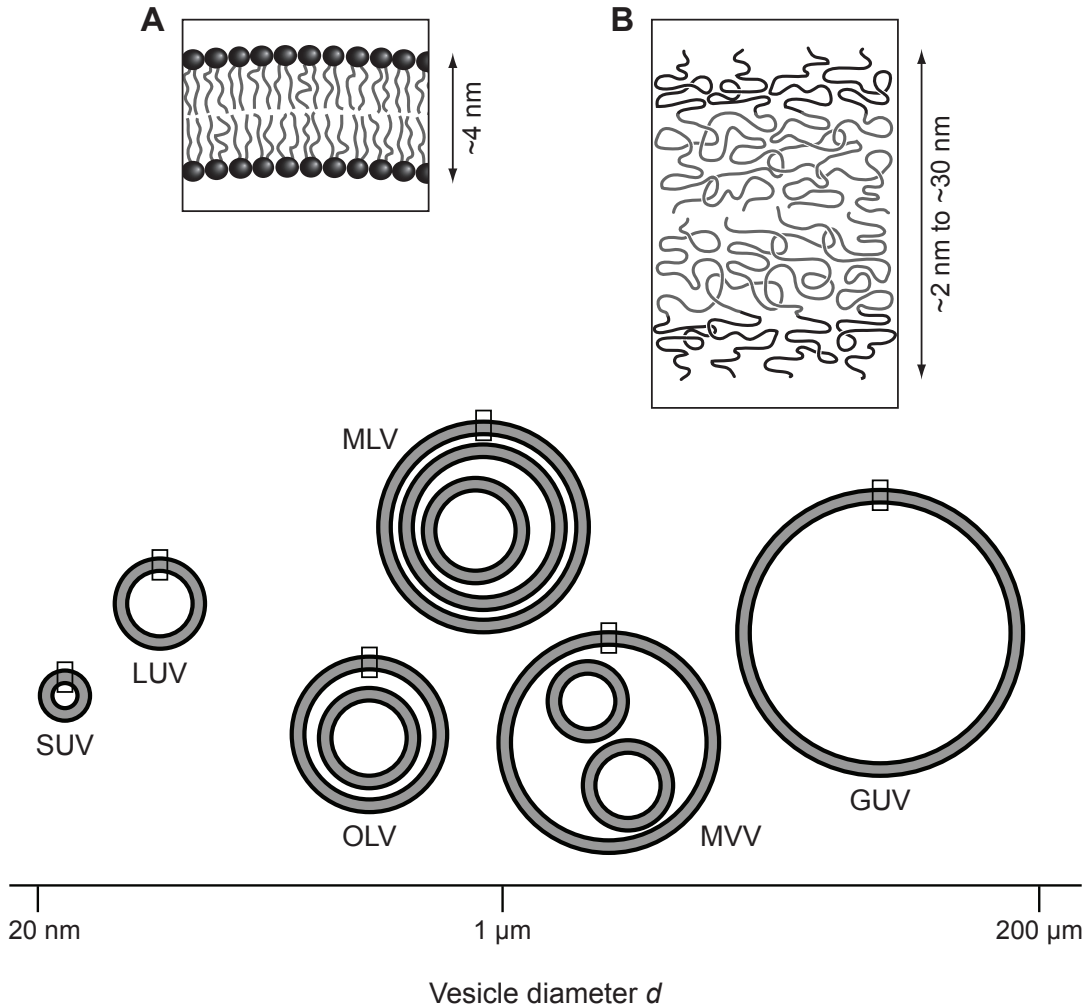
Figure 2.2: Structure of bilayered lipid and polymer vesicles. Schematic illustration of the vesicle membrane structure in the fluid state (enlargements at the top) and overall vesicle structures (bottom) of (A) lipid vesicles (liposomes) formed from a biologically derived phospholipid and (B) polymer vesicles (polymersomes) prepared from an amphiphilic diblock copolymer. Included are the common structural vesicle classes of small unilamellar vesicles (SUVs; $d \lesssim 50\,\text{nm}$), large unilamellar vesicles (LUVs; $50\,\text{nm} \lesssim d \lesssim 1\,\text{µm}$), giant unilamellar vesicles (GUVs; $d \gtrsim 1\,\text{µm}$), oligolamellar vesicles (OLVs), multilamellar vesicles (MLVs), and multivesicular vesicles (MVVs). The drawings are not to scale. Adapted from Jesorka and Orwar [59], Battaglia and Ryan [60], and Discher and Ahmed [16].

small headgroups and bulky hydrophobic moieties as presented for example by double-chain amphiphiles, such as phospholipids. Phospholipids are the basic constituents of all biological membranes and are the traditional and most intensively investigated vesicle building blocks. Vesicles prepared from such naturally occurring lipids, including synthetic biomembrane lipids and natural lipid extracts, are generally called *lipid vesicles* or more commonly **liposomes** [3, 61, 62].
Additionally, a large variety of other amphiphilic molecules has been designed and/or identified for vesicle formation. They include for example synthetic surfactants (yielding *synthetic surfactant vesicles*, including *niosomes* in the case of nonionic surfactants) [8, 63] and amphiphilic block copolymers (constituting so-called *polymer vesicles* or **polymersomes**) [7, 12, 64, 65].

In this work, vesicles were prepared from standard phospholipids or linear amphiphilic diblock copolymers consisting of a hydrophilic and a hydrophobic polymer chain (see Sec. 2.4 for more details). Both types of amphiphiles basically self-assemble into the same **structure of bilayered vesicle membranes** with the hydrophilic parts facing the internal and external aqueous medium and the hydrophobic parts forming the membrane interior as illustrated in Figure 2.2. However, the considerably higher molecular weights of vesicle forming copolymers generally result in thicker (2–30 nm) and often highly entangled polymer membranes (Fig. 2.2B) as opposed to the thin-walled and ordered lipid membranes with a typical bilayer thickness d_B of around 4 nm (Fig. 2.2A) [16, 60, 66–68]. These distinct bilayer architectures provide the polymer and lipid membranes with further differences in their physicochemical properties as summarized in Section 2.4 and discussed in Chapter 3 [12, 16–18].

2.3 Vesicle and vesicle membrane properties

The following sections describe the basic properties of vesicles and their membranes as summarized in [18, 69, 70]. More detailed information of the introduced concepts and the underlying theories can be found in the references given in the text. The theories have originally been developed to describe the behavior of lipid vesicles, but they basically apply to any other type of self-assembled vesicle system, including polymer vesicles as presented in the reviews by Förster and coworkers [71, 72].

2.3.1 Thermodynamic state of vesicle membranes

Lipid bilayers: Based on the thermotropic phase behavior of biomembrane lipids, the bilayers of lipid vesicles exist in different lipid phase states as a function of temperature [53]. The main temperature dependent phase transition taking place
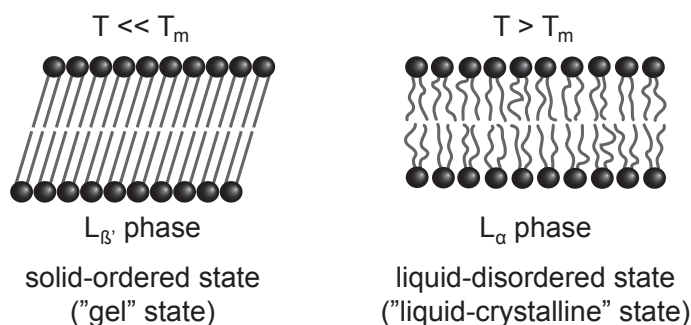
Figure 2.3: Main phase states of lipid bilayers. Schematic representation of the lipid arrangement in a planar bilayer below and above the main phase transition temperature T_m. Adapted from Walde and Ichikawa [36].

in lipid bilayers is referred to as the lamellar gel-to-lamellar liquid-crystalline phase transition or simply melting transition. It is induced at the **main phase transition temperature** (or lamellar chain melting temperature) $\boldsymbol{T_m}$ of the lipid or lipid mixture constituting the bilayer as illustrated in Figure 2.3.

At temperatures at least 5–10 °C below T_m, lipid bilayers are in the so-called *gel*, *crystalline-analogue*, or **solid-ordered state**. The lipid arrangement in the bilayer corresponds to that typically found in the stacked bilayers of the lamellar equilibrium phase $L_{\beta'}$. It is characterized by rigid, extended, and tilted hydrophobic chains allowing for an ordered and dense packing of the lipid molecules in the bilayers. Therefore, solid-ordered bilayers are highly viscous with the mobility of the amphiphiles within the bilayer being rather restricted, similar to a two-dimensional crystal.

Above T_m, lipid bilayers are in the ***liquid-disordered* state**, also referred to as *liquid-crystalline*, *liquid-analogue*, or simply *fluid* state, as is the case for biological membranes under physiological conditions. Here, the hydrophobic chains exist in a flexible and disordered conformation, while the hydrophilic headgroup hydration is increased, i. e. the optimal headgroup and overal bilayer areas are increased, just as in the bilayers of the liquid-crystalline L_α phase. This leads to the fluid-like behavior of liquid-disordered bilayers in which the amphiphiles exhibit fast lateral and rotational diffusions, like in a two-dimensional fluid [3, 36, 53].

Most of the dynamic processes observed in lipid vesicle systems, including their formation by the swelling of a lamellar phase, shape fluctuations, and shape transformations, are restricted to the fluid state of the lipid vesicle membranes [5, 58, 73, 74]. From a practical point of view, this implies that all mechanical treatments of lipid vesicles during their preparation have to be carried out in their fluid state, i. e. at a temperature at least 5 °C above T_m of the lipid or lipid mixture used [3]. Table 2.1 lists the T_m values for the main phosphatidylcholines (PC) used in this work as determined from dilute aqueous PC dispersions, i. e. MLV systems. It has to be

noted that the T_m values of biomembrane lipids depend to some extent on the experimental conditions, such as water content, membrane curvature, and the degree of protonation in the case of charged headgroups. For a comprehensive list of T_m values, see the reviews on lipid vesicles by Walde and references therein [3, 36].

Polymer membranes: In the case of vesicle forming amphiphilic block copolymers, fluid and mechanically treatable polymer membranes are obtained at temperatures above the **glass transition temperatures $T_\mathbf{g}$** of the constituting polymer chains, particularly of the hydrophobic polymer forming the thick membrane interior. T_g induces the transition of a given polymer from the glassy state to the amorphous state which are characterized by rigid, rod-like and flexible, coil-like chain conformations, respectively.
According to this, vesicle forming, all low T_g, and flexible diblock copolymers (also called coil–coil diblock copolymers) are able to form fluid polymer bilayers (Fig. 2.2) by spontaneous self-assembly in aqueous solution and at moderate temperatures [71, 75–77]. Examples of such coil–coil copolymers and their T_g values, including the widely studied polymers PEO-*b*-PEE and PEO-*b*-PBD, as well as the PEO-*b*-PMCL polymer used in this work, are given in Table 2.1. Other hydrophobic polymers that are commonly used in vesicle forming copolymers and have sufficiently low T_g for aqueous self-assembly are listed in reference [77]. It has to be noted that, at high molecular weights of flexible coil–coil copolymers, the hydration kinetics usually have to be enhanced, e.g. by heating, sonication, or exposure to an ac electric field, to aid in the dissolution and self-assembly of such highly hydrophobic copolymers [57, 67, 78].
In the case of high T_g, rigid (rod-rod) or rigid-flexible (rod–coil) copolymers whose hydrophobic blocks are in the glassy state at room temperature, elevated temperatures or an apolar organic solvent are needed to fluidize the hydrophobic membrane core and allow for vesicle formation [75, 77, 79].

2.3.2 Bending elastic energy and parameters controlling vesicle shape

The average size and shape assumed by self-assembled fluid vesicles is determined by the minimum of the bending elastic energy of its closed membrane which originates from the bilayer curvature C [69, 70, 73]. The following paragraphs briefly introduce the concepts of minimal bending energy and equilibrium vesicle shapes that are based on a number of basic vesicle bilayer properties (see for example [73]).

Spontaneous bilayer curvature: Bilayer membranes adopt a **spontaneous curvature C_0** under asymmetric conditions between the two monolayers which cause the membrane to curve in a preferred direction. Such membrane asymmetry can be induced either by different solution conditions on both sides of the membrane or by different compositions of the two monolayers. The latter composition asymmetry can arise from a different number or geometry of the amphiphilic molecules constituting each monolayer. As for the geometry difference, an asymmetric insertion of e. g. cone shaped molecules with a high intrinsic spontaneous curvature into a planar bilayer composed of cylindrical molecules with basically zero spontaneous curvature results in bending of the mixed bilayer (compare Fig. 2.1). The effects of geometry difference and number difference add up to an effective area difference between the two monolayers which gives rise to the effective spontaneous curvature of the bilayer [18, 69, 80–82].

Equilibrium vesicle shapes of minimum bending energy: Single-component, symmetric bilayers prefer to be planar, i.e. $C_0 \approx 0$. However, in dilute aqueous solution, it becomes energetically and entropically more favorable for them to curve into closed bilayers (vesicles), thereby eliminating the energetically unfavorable edges [2]. The energy that is required to curve a membrane patch into a vesicle, is called **bending elastic energy E_b**, curvature elastic energy, or free energy of bending/curvature. Its minimum is responsible for a large variety of experimentally observable, stationary vesicle shapes, such as spheres, prolates, oblates, and stomatocytes [73, 80].

Three models have been developed to estimate the bending energy of vesicle bilayers and to predict the resulting shapes of minimum bending energy [70, 73]: The original spontaneous-curvature model introduced by Helfrich [83, 84], the area-difference-elasticity model [80, 85], and the bilayer-couple model [84, 86]. They allowed the construction of shape phase diagrams describing the minimal energy shapes as a function of (i) the spontaneous curvature of the vesicle membrane (spontaneous-curvature model) or the area difference between the two monolayers (representing the spontaneous curvature in the area-difference-elasticity and bilayer-couple models) and (ii) of the **reduced vesicle volume v**. The latter shape influencing parameter is defined as the ratio between the vesicle volume V and the volume of a sphere having the same surface area as the vesicle and an equivalent radius R_0 [73]:

$$v = \frac{V}{(4/3)\pi R_0^3} \tag{2.2}$$

For $v = 1$, the most stable vesicle shape of minimum bending energy is a sphere. For $v < 1$, the vesicles are deflated and dispose of excess membrane area allowing for the numerous shape transformations away from a sphere as revealed by the shape phase diagrams of the different elastic models [73, 80, 84]. An example of stationary

vesicle shapes for $v < 1$ as predicted by the spontaneous-curvature model can be found in Chapter 4.3.1.

Geometrical parameters describing the vesicle shape: The reduced volume v (Eq. 2.2) is, in general, a convenient geometrical parameter to characterize the (non-) sphericity of vesicles and to quantify their excess area available for shape fluctuations and shape changes. As such, it also enters the more recent theories of nonequilibrium vesicle dynamics, including the small deformation theories for vesicles in external flow fields as discussed in Chapter 4. See some important works and recent reviews on the subject in [74, 87–93].
Some authors prefer to characterize the non-sphericity, i. e. excess area, of vesicles by the **relative excess area** $\boldsymbol{\Delta}$:

$$\Delta = \frac{A - 4\pi R_0^2}{R_0^2} \tag{2.3}$$

where A is the vesicle surface area and R_0 is the radius of a sphere having the same volume. Δ is related to the reduced volume v via $\Delta = 4\pi(v^{-2/3} - 1)$. Spherical vesicles do not have excess area, i. e. $\Delta = 0$ ($v = 1$). As a consequence, they cannot be deformed in the limit of the small deformation regime. For $\Delta > 0$ ($v < 1$), the equilibrium shapes are non-spherical and the vesicles exhibit shape fluctuations at rest and nontrivial dynamics in external flow fields [91, 93].

2.3.3 Basic vesicle properties at equilibrium

Following the background information given in the previous sections, it is worthwhile to summarize the basic vesicle properties under equilibrium conditions at this stage. Vesicles in the fluid state have soft matter characteristics with their amphiphilic building blocks being in constant thermal motion within the bilayer [2]. Hence, fluid vesicles are not static entities but typically highly **dynamic systems** that exhibit thermal shape fluctuations around their mean shape, usually a quasi-sphere [80].
In most cases, vesicles are **not at thermodynamic equilibrium**, i. e. they are not thermodynamically stable structures, due to the bending energy that is confined in the vesicles as they are formed in excess water [70, 94]. Depending on the preparation method used, this necessary bending energy is supplied for example in the form of shear (gentle agitation, vortexing, or magnetic stirring), ultrasound (sonication), pressure (extrusion through narrow pares or high pressure homogenization), or an ac electric field (electroformation) (see Section 2.5). It has to be noted that the bilayer curvature is negligible for giant vesicles, but becomes increasingly important

for vesicles smaller than 100 nm which, therefore, require higher energy inputs during preparation [69].

Once formed, vesicles represent a metastable, **kinetically trapped state** where the enclosed volume and the membrane area of the vesicle can be considered fix at constant temperature and under constant osmotic conditions. This is especially true for polymer vesicles as they consist of entangled, little dynamic, high molar mass amphiphiles [60, 65].

The **area constraint** can be rationalized in terms of the extremely low monomer solubility of most vesicle forming amphiphiles in water, including double-chain phospholipids and high molecular weight block copolymers [3]. This results in low exchange rates of the constituting amphiphilic molecules between the vesicle bilayer and the external bulk phase (or the internal medium) as measured by the *inter-bilayer diffusion* of the amphiphiles (of the order of several hours for PCs) [95, 96]. Furthermore, the exchange rates of amphiphiles between the two monolayers of the vesicle bilayer based on their *transbilayer diffusion* (flip-flop) are known to be extremely low for single-component bilayers (of the order of several days or longer for PCs) [95, 97, 98]. Therefore, for time scales smaller than the typically long inter-bilayer and transbilayer amphiphile diffusion times of a given vesicle system, the number of molecules in the vesicle membrane and, hence, the vesicle membrane area remain absolutely constant. Due to the cohesive forces between the amphiphiles in this condensed state, vesicle membranes exhibit **very limited elastic compressibility**, i.e. great resistance to changes in membrane area (see Sec. 2.3.5).

The **constant volume** of vesicles under constant osmotic conditions is based on the **semi-permeability** of vesicle membranes. They exhibit high permeabilities towards water in the presence of an osmotic pressure gradient between the internal and external media so that the vesicle volume quickly adjusts itself until the osmotic pressures are balanced (of the order of a few minutes for GUVs) [13, 99]. At the same time, amphiphilic vesicle membranes provide a high permeability barrier towards polar solute molecules in the presence of a solute concentration gradient across the membrane which is a key property of vesicles in the multitude of encapsulation applications [17, 40, 100].

2.3.4 Permeability of vesicle membranes

The passive permeability of vesicle membranes towards a specific molecule is characterized by the **permeability coefficient P** which corresponds to the permeation rate of the molecule across the vesicle membrane. For this transmembrane movement, the molecule must partition into and diffuse across the amphiphilic membrane. In the case of hydrophilic solutes, the molecular diffusion along its concentration gradient across the membrane can be described by Fick's first law, where the diffusion rate is inversely proportional to the membrane thickness [17, 101, 102]. Based

on these permeation processes, P depends on many factors which are discussed in the frame of the passive calcein permeability study from lipid and polymer vesicles presented in Section 3.3.2.

Some important factors influencing vesicle membrane permeability include the thickness and relative hydrophobicity of the hydrophobic membrane core [17, 103], the fluidity and order of the bilayer membrane [103–107], the bilayer compressibility and amphiphile packing density [108–110], the electrostatic properties of the bilayer barrier influenced by the internal and external buffer compositions [109, 111], and the size and charge of the solute which, in the latter case, is dependent on the solution pH [17, 112]. As for the fluidity dependent permeability of lipid bilayers according to their lipid phase state, the permeation rates are enhanced for liquid-disordered bilayers above $T = T_m$ and highest around the transition temperature T_m [104].

A more detailed introduction into lipid bilayer permeability, including a discussion of the influencing factors and mechanisms of bilayer permeation is given by [100, 102, 110]. Experimental values of the permeability coefficients P of lipid bilayers to water, neutral solutes such as glucose, glycerol, and urea, as well as small ions can be found in [13, 100, 108, 113, 114]. The permeabilites of lipid and/or polymer membranes towards different charged solutes have been reported in [17, 19, 109, 115, 116].

For a given vesicle membrane formulation, its permeability is often assessed in terms of water permeability which has been extensively measured for both lipid and polymer membranes, e. g. by monitoring the osmotic swelling and shrinking of GUVs [12, 13, 99, 108] or LUVs [78]. Typical P values for the water permeabilities across lipid and polymer membranes in the fluid state are given in Table 2.1 and will be commented in Section 2.4. The passive permeability of vesicle membranes towards polar solutes can be analyzed from a set of simple permeation assays, such as enzymatic assays [17, 117] and fluorescence quenching assays [19, 116, 118]. The latter approach using calcein as fluorescent dye was adopted in this work (see Sec. 3.2.3).

2.3.5 Deformation of bilayer membranes

The unique physical properties of bilayer membranes not only govern the equilibrium shapes and shape fluctuations of vesicles at rest [73, 80], but also their deformation behavior under stress induced e. g. by pressure [11, 14, 119], external flow fields [74, 87–93], or electric fields [120, 121]. This section summarizes the deformation modes of bilayer membranes and their material parameters characterizing the membrane elasticity and membrane viscosity. The context to vesicle bilayers is also given.

Mechanically, a bilayer membrane may be considered as a two-dimensional sheet consisting of two monolayers. Depending on the stresses imposed on the bilayer by different external forces, it can undergo various independent modes of deformation (strain), including area expansion or compression (Fig. 2.4A), bending (Fig. 2.4B),
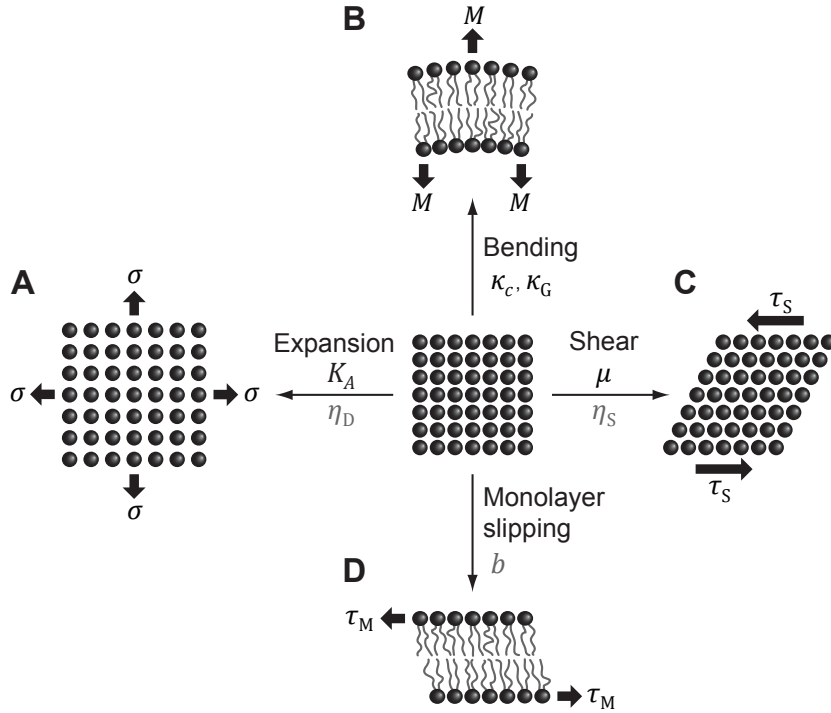
Figure 2.4: Deformation modes of bilayer membranes. Schematic representation of the independent modes of bilayer deformation and the underlying force-moments acting on the bilayer membrane. (A) area expansion (or dilation) resulting from in-plane tensile stresses σ, (B) bending induced by bending moments M, (C) shear deformation induced by in-plane shear stresses τ_S, (D) monolayer slipping induced by intermonolayer shear stresses τ_M. The indicated parameters characterize the elastic (black symbols) and viscous (gray symbols) responses of the bilayer to these deformations as described in the text. Adapted from Dimova *et al.* [18] and Evans and Needham [122].

shear (Fig. 2.4C), and monolayer slipping (Fig. 2.4D). Thereby, the *amplitude* of deformation depends on the elastic properties of the bilayer which are characterized by the set of elastic moduli described below. In the linear limit where deformations are reversible, an elastic modulus is defined as the proportionality constant between the stress acting on the membrane and the resulting deformation (Hook's law; see for example Eq. 2.4) [18, 122]. The rheological properties of bilayer membranes influence the *rates* of deformation and are characterized by the membrane viscosities, e. g. for dilation (expansion) and shear [18, 123, 124]. A full description of the constitutive equations for viscoelastic membranes can be found in [122].

(A) Area expansion (dilation) or area compression (condensation): Area expansion of a bilayer is described by the fractional increase in bilayer area $\alpha = \Delta A/A_0$. It induces a uniform **membrane tension σ** in the plane of the bilayer as illustrated

in Figure 2.4A. The proportionality between the in-plane tensile stress σ and the areal strain α is given by:

$$\sigma = K_A \alpha \tag{2.4}$$

where $\boldsymbol{K_A}$ is the **area expansion elastic modulus**, also called stretching stretching modulus. K_A has the dimension of a tension and characterizes the expansibility/compressibility of the bilayer, i. e. the resistance the bilayer offers to isotropic area expansion/compression. There is a critical fractional area expansion α_{crit} where the bilayer ruptures following $\sigma_{\mathrm{crit}} = K_A \alpha_{\mathrm{crit}}$. The corresponding critical membrane tension σ_{crit}, generally referred to as rupture tension, describes the tensile strength or simply the mechanical strength of bilayer membranes [11, 122].

Vesicles at rest, i. e. undeformed vesicles, exhibit a so-called effective membrane tension, abbreviated as σ_0 in this work, which is zero for spherical vesicles ($\Delta = 0$). For quasispherical vesicles with excess area ($\Delta > 0$), σ_0 is non-zero but smaller than the membrane tension of deformed vesicles, σ [88, 125]. The critical membrane tension (rupture tension) that induces failure of the vesicle membrane and, hence, lysis of the vesicle is referred to as **lysis tension $\boldsymbol{\sigma_l}$** [11–13, 122]. The value of σ_l is a measure of vesicle toughness.

It has to be noted that the area expansion of quasispherical vesicle membranes at lysis (α_l; often referred to as α_{crit} in the vesicle literature) is composed of the area expansion that simply leads to the flattening of excess area (α_Δ; governed by κ_c, see below) and the area expansion that induces the critical membrane tension (α_{crit}; governed by K_A): $\alpha_l = \alpha_\Delta + \alpha_{\mathrm{crit}}$ [14, 18, 123]. Micropipette aspiration experiments of giant vesicles allow probing the complete range of membrane tension as a function of α and extracting the elastic moduli κ_c and K_A, as well as the lysis tension σ_l [12–14, 18, 122, 123]. Table 2.1 lists some typical values of these mechanical parameters for the bilayer membranes of lipid and polymer vesicles in the fluid state. They will be commented in the following Section 2.4.

Finally, it is important to note that the membrane tension σ is often referred to as *surface tension* in the vesicle literature. This is because the thin bilayer membrane (compared to the vesicle diameter) can be idealized as a two-dimensional, homogeneous *surface* to study the classical modes of bilayer deformation, including area expansion, bending, and shear [122]. In the limit of small vesicle deformation theories, bilayer membranes in the fluid state are generally considered as two-dimensional, *incompressible* surfaces [87, 89–93].

(B) Bending: Bending moments M imposed on a bilayer induce bending of the bilayer at constant area which is quantified by the change in bilayer curvature ΔC (Fig. 2.4B). Here, the linear response of the bilayer between the bending moments M and the curvature change ΔC is described by two elastic moduli, namely the curvature or **bending elastic modulus $\boldsymbol{\kappa_c}$** and the Gaussian curvature modulus κ_{G}. They have the dimension of an energy as does the bending elastic energy

of the curved bilayer introduced in Section 2.3.2. The two elastic moduli κ_c and κ_G characterize the bending elasticity of the bilayer, i.e. its resistance to bending. In other words, they represent the resistance of the bilayer towards a deformation away from its preferred, spontaneous curvature C_0. Due to the extreme thinness of bilayer membranes, their resistance to bending is generally small (Tab. 2.1) [14, 55, 73, 91, 94, 122, 126].

In closed bilayers (vesicles), the low bilayer bending rigidity, together with its limited compressibiliy, primarily sets the equilibrium shape of vesicles at rest as described in Section 2.3.2. Moreover, there is no contribution by the Gaussian curvature to the deformation of vesicles as long as the vesicle topology does not change, e.g. no creation of two vesicles out of one nor a transition from a closed to a perforated vesicle membrane [55, 73, 91, 127]. Therefore, continuous vesicle deformation involving bending of the vesicle bilayer is controlled by the bending elastic modulus κ_c only. It characterizes the bending rigidity/elasticity of the vesicle membrane and is often related to vesicle stiffness/softness. Due to its low value for fluid bilayers, κ_c governs the thermal shape fluctuations of quasispherical vesicles in the fluid state from which it can be extracted using fluctuation spectroscopy [127], micropipette aspiration [14, 18], or scattering methods [128, 129]. A comprehensive review on measuring techniques and literature data for the bending rigidity of GUVs has recently been published by Dimova [130]. More values for κ_c of lipid bilayers are listed in [131].

(C) Surface shear: A shear stress acting tangent to the bilayer edge (τ_S) induces a shear deformation in the plane of the bilayer membrane at constant area (γ), i.e. relative displacement of amphiphilic molecules in the monolayer planes (Fig. 2.4C). The proportionality constant between this in-plane (surface) shear stress τ_S and shear strain γ is defined as the shear elastic modulus μ, giving $\tau_S = \mu\gamma$. It characterizes the static resistance of the bilayer membrane to in-plane shear deformation which is negligible for fluid bilayers ($\mu = 0$). Thus, shear elasticity is peculiar to bilayers in the crystalline-analogue state [18, 122].

However, both fluid and crystalline-analogue bilayers oppose to shear deformations dynamically due to inner friction between the displacing molecules (viscous dissipation). The friction between the amphiphiles in the plane of the monolayers is characterized by the so-called shear surface viscosity η_S (again, the term *surface* refers to the thin bilayer membrane as a whole and not to the surface of the bilayer). η_S is defined as the proportionality constant between the in-plane shear stress τ_S and the resulting shear rate $\dot{\gamma}$: $\tau_S = \eta_S\dot{\gamma}$ [75, 122, 123]. Equivalently, a dilatational surface viscosity η_D can be defined to describe the viscous response of bilayer membranes to area dilation (expansion) and condensation (compression) (Fig. 2.4C) [18, 122].

(D) Monolayer slipping (intermonolayer shear): Finally, a shear stress acting normal to the edge of one of the monolayers (τ_M) creates a shear strain across the bilayer membrane resulting in the relative displacement of the monolayers, i. e. monolayer slipping (Fig. 2.4D). Again, their is generally no elastic response of bilayer membranes to intermonolayer shear deformations, but the viscous molecular friction between the displacing monolayers can be characterized by the so-called intermonolayer friction coefficient *b*. The value of *b* increases with the degree of interdigitation between the hydrophobic chains [123, 124]. Monolayer slipping is not observed in closed bilayer membranes (vesicles).

Summary: The closed bilayer membranes of vesicles in the fluid state are characterized by a fluid-like behavior, limited compressibility (K_A, σ_l), low bending rigidity (κ_c), and a negligible resistance to shearing ($\mu = 0$). These unique mechanical properties are responsible for the large variety of equilibrium shapes vesicles can adopt at rest and for the even more complex non-equilibrium dynamics of vesicles in external flow. The continuous deformation of vesicles under application of external forces usually involves the two independent deformation modes of bilayer bending and area expansion. Thereby, the vesicle bilayer eventually ruptures in response to area expansion, while its bending energy primarily sets the vesicle shape at rest.
The deformation and breakup behavior of fluid-phase vesicles in external shear flow is discussed in Chapter 4. Section 2.6 describes the breakup of vesicles by pressure extrusion and their flow behavior in narrow pore channels.

2.4 Vesicle membrane constituents and resulting membrane properties

The physicochemical properties of vesicle membranes, including those summarized in Table 2.1, largely depend on the composition of the membrane and the resulting bilayer architecture. This allows controlling the membrane properties by selecting the molecular structure and mixture of the vesicle building blocks as described in the following for lipid and polymer vesicles. Basically, all amphiphiles that are able to self-assemble into lyotropic lamellar fluid phases in aqueous solution are suitable for the preparation of vesicles. Furthermore, a large variety of amphiphilic guest molecules can be incorporated in the vesicle host bilayer to further adjust the membrane properties or to introduce functionality to the vesicle template.

Table 2.1: Physicochemical properties of selected lipid and polymer vesicle bilayers in the fluid state as measured by the main phase transition temperature T_m (lipid bilayers only), the glass transition temperature T_g (polymer bilayers only), the permeability coefficient P towards water, the area expansion elastic modulus K_A, the lysis tension σ_l, and the bending elastic modulus κ_c.

Bilayer constituent	T_m or $T_g^{(d)}$ [°C]	P [µm/s]	K_A [mN/m]	σ_l [mN/m]	κ_c [10^{-19} J]
DMPC (diC14:0 PC)	23.6 [54]	83 [110]	234 [14]	2–3 [122]	0.56 [14]
POPC (C16:0-C18:1c9 PC)[a]	-2.5 [54]	130 [110]	213 [132]	7.4 [15]	0.77 [128]
DOPC (diC18:1c9 PC)	-18.3 [54]	158 [110]	265 [14]	9.9 [13]	0.85 [14]
DLPC (diC18:2c9c12 PC)[b]	-53 [133]	91 [13][e]	247 [14]	5.1 [13]	0.44 [14]
POPC/Chol 70:30 [mol%][c]	– [107]	68 [110][f]	354 [132]	9.4 [15]	3.57 [134][h]
PEO$_{40}$-b-PEE$_{37}$ (EO7)		2.5 [12]	120 [12]	22.8 [12]	1.4 [12]
PEO$_{26}$-b-PBD$_{46}$ (OB2)	-31 [99]	3.1 [99][g]	102 [67]	22.5 [135]	1.4 [103]
PEO$_{23}$-b-PMCL$_{50}$	-60 [136]	n.a.	n.a.	n.a.	n.a.

(a) Representative phospholipid for egg PC.
(b) Representative phospholipid for soy PC.
(c) Bilayers prepared from POPC/Chol 70:30 [mol%] are in the liquid-ordered phase state (L_0) and do not exhibit a solid-ordered-to-liquid-disordered phase transition [107].
(d) Glass transition temperature of the *hydrophobic* block moiety of the diblock copolymer.
(e) This is the *apparent* permeability coefficient P_{app} for DLPC bilayers. After correction, the authors estimated $P \approx 100\,\mu m/s$ [13].
(f) This is the permeability coefficient for DOPC/Chol 60:40 [mol%] bilayers.
(g) This is the permeability coefficient for a similar PEO-b-PBD (PEO$_{30}$-b-PBD$_{46}$).
(h) The values for the bending rigidity of cholesterol containing POPC bilayers reported in this study [134] are likely to be overestimated [128]. See [127, 128, 137] for the κ_c values of related PC/Chol systems. For instance, $\kappa_c = 1.44 \times 10^{-19}$ J for egg PC/Chol 70:30 [mol%] bilayers [137] and $\kappa_c \approx 1.1 \times 10^{-19}$ J for POPC/Chol 60:40 [mol%] bilayers [128].
n. a. = not available (not studied to our knowledge).

2.4.1 Phospholipids constituting lipid vesicles

Within the class of the universal, biomembrane constituting phospholipids, *glycero-phospholipids* represent the most abundant structural group. They consist of a glycerol backbone with two hydrophobic fatty acid chains esterified with the glycerol hydroxyl groups (–OH) at the carbon atoms C-1 and C-2, and a hydrophilic phosphate headgroup bound to the hydroxyl group at C-3 (see Tab. 4.3 for the chemical structures of the main glycerophosopholipids used in this work) [3].

Hydrophilic headgroup species and liposome surface charge: The type of phosphate headgroup in position C-3 defines the glycerophospholipid species and influences the surface properties and dynamics of pure or mixed lipid bilayers [97, 138, 139]. The charge-neutral ***phosphatidylcholines*** (PCs; $+/-$) characterized by a zwitterionic phosphocholine headgroup are the most widely used glycerophospholipids for the preparation of well-defined model membranes and vesicles. Surface charges can readily be introduced into lipid vesicle membranes by preparing them from mixtures of bilayer forming lipids, usually PCs, and smaller fractions of other glycerophospholipids or surfactants with charged headgroups. Negatively charged glycerophospholipids (at neutral pH), such as phosphatidylserine (PS; $-$), phosphatidylglycerol (PG; $-$), and phosphatitic acid (PA; $-$), are commonly used for the assembly of PC based, anionic liposomes. To obtain cationic liposomes, PC host bilayers can be doped for example with fatty acid amines, such as stearylamine (SA; $+$ at neutral pH) [3, 140].

Fatty acid composition and liposome membrane properties: Each glycerophospholipid species with a given hydrophilic phosphate headgroup comprises a large number of yet chemically different molecules based on the various combinations of fatty acid chains in positions C-1 and C-2. The nature of the hydrophobic fatty acid tails in the molecules constituting a lipid bilayer, particularly the number of double bonds per chain, greatly influences the basic bilayer properties, such as the thermotropic phase behavior (Sec. 2.3.1), permeability (Sec. 2.3.4), and elasticity (Sec. 2.3.5). In the following, this will be discussed for pure PC bilayer membranes, though the influence of the fatty acid composition on lipid bilayer properties is basically independent on the headgroup species.
The main phase transition temperature T_m of single-component PC bilayers increases with the length of the fatty acid residues and strongly decreases with the presence of *cis*-double bonds, which is the standard double-bond configuration in naturally occurring, unsaturated fatty acids (Tab. 2.1) [3]. The drop in T_m with increasing chain unsaturation is most pronounced when two or more alternating *cis*-double bonds are present in one or both fatty acid chains of the bilayer forming PC

molecule (polyunsaturated PC bilayers) compared to saturated or monounsaturated PC bilayers [13]. This reflects the high degree of disorder and fluidity of the polyunsaturated fatty acid chains above T_m which results in a low level of lipid packing density and cohesive interactions in liquid-disordered, polyunsaturated PC bilayers. As the permeability and mechanical strength of vesicle membranes are governed by membrane fluidity, packing density, and cohesion [11, 105, 122], the parameters for the permeability (P) and lysis tension (σ_l) of lipid bilayers correlate with T_m as a function of fatty acid composition (Tab. 2.1) [13]. Consequently, vesicles prepared purely from saturated/monounsaturated PCs are generally less permeable and tougher than those obtained from polyunsaturated PCs [13, 106, 141].

As for the elastic properties of phospholipid vesicle membranes, the bilayer compressibility as measured by the area expansion elastic modulus K_A is practically independent on fatty acid chain length and unsaturation (Tab. 2.1) [14]. On the other hand, the bending rigidity of saturated/monounsaturated PC bilayers slightly increases with fatty acid chain length as a result of the increased bilayer thickness (see values of the bending elastic modulus κ_c in Tab. 2.1). Again, an abrupt drop in bending rigidity is observed for polyunsaturated PC bilayers due to their increased fluidity and flexibility [14].

Functionalization of phospholipids and lipid vesicles: Apart from surface charge modification via the lipid headgroup charge, the well defined surface of lipid vesicles allows for a large variety of other chemical surface modifications. This is a powerful approach to amend the basic lipid bilayer properties with specific functionalities and control the biological behavior of liposomal vehicles. Multifunctional liposomes can be designed by separately or simultaneously incorporating lipids with headgroup-attached ligands, such as protective polymers, targeting ligands, diagnostic labels, stimuli-responsive polymers, and cell-penetrating peptides, into the lipid bilayer without affecting liposomal integrity [23, 35, 59, 142].

Phospholipid products: Lipid vesicles can be prepared from natural lipid extracts with different degrees of purification or from biologically derived, synthetic lipids with well-defined chemical structures. Egg yolk and soybeans contain large amounts of PCs in their plasma membranes establishing them as the cheapest commercial sources for PC isolation. The obtained egg yolk PCs (simply called **egg PC** in this work) and soybean PCs (**soy PC**) show a strong preference to form lyotropic lamellar phases in aqueous solution, i.e. vesicles in dilute systems (Fig. 2.5A) [143, 144]. The typical fatty acid distribution in egg PC is dominated by saturated and monounsaturated fatty acid chains, whereas soy PC primarily contains diunsaturated fatty acids [3, 140] (see also Tab. 4.2 for the fatty acid composition of the egg and soy PC isolates used in this work). More precisely, according to the predominant fatty acid

A

B
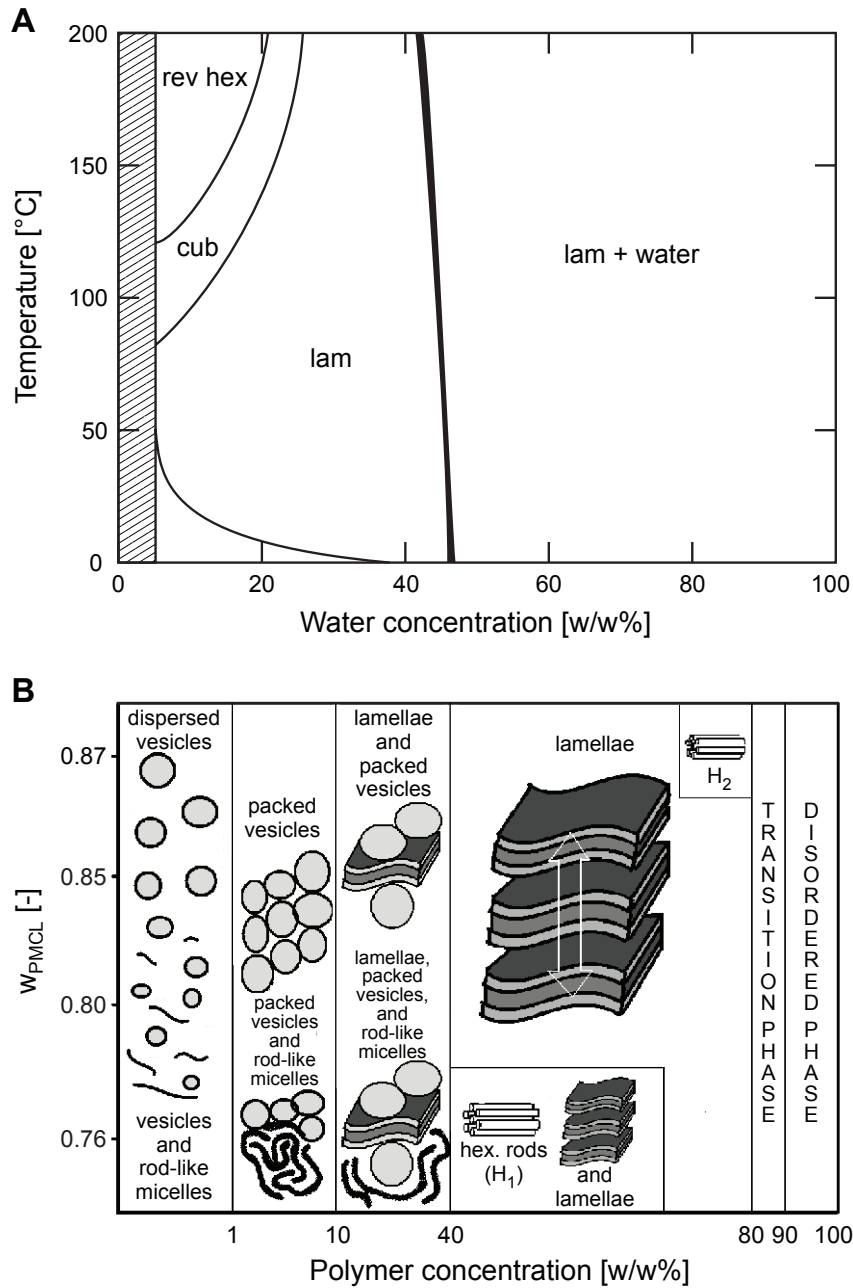
Figure 2.5: Phase diagrams of egg PC–water and PEO-*b*-PMCL–water mixtures. (A) Binary phase diagram of egg PC and water as a function of temperature. Adapted from Holmberg *et al.* [47] and Larsson [143]. (B) Binary phase diagram of PEO_{23}-*b*-$PMCL_m$ and water as a function of hydrophobic to hydrophilic block weight ratio (w_{PMCL}). Adapted from Braun *et al.* [52].

species in positions C-1 and C-2, the PCs isolated from egg yolk and soybeans are widely represented by the chemical structures of 1-palmitoyl-2-oleoyl-*sn*-glycero-3-phosphocholine (**POPC** or C16:0-C18:1*c*9 PC) and 1,2-dilinoleoyl-*sn*-glycero-3-phosphocholine (**DLPC** or diC18:2*c*9*c*12 PC), respectively (see Tab. 4.3 for the chemical structures of POPC and DLPC). Therefore, vesicles prepared from soy PC tend to be more flexible, more permeable, and less robust than pure egg PC vesicles as detailed above (Tab. 2.1) [145]. Furthermore, the polyunsaturated soy PCs are susceptible to lipid peroxidation induced by free oxygen radicals, whereas the saturated/monounsaturated egg PCs are practically insensitive [146, 147]. The resulting lipid chain breakdown would then further alter the mechanical stability and permeability of soy PC based vesicle membranes [146–148]. To avoid lipid oxidation in unsaturated lipids and their liposome preparations, it is recommended to store them in a closed container at $-20\,°C$ and/or under nitrogen atmosphere.

While egg PC has been widely used in early studies on the preparation and characterization of vesicles [105, 114, 149, 150], today, POPC is a common model lipid for basic lipid vesicle and bilayer research [3, 5]. For industrial vesicle applications, both egg PC and soy PC are largely employed. In this work, PC isolates from egg yolk and soybean were used for the development of new vesicle processing technologies, while POPC served as defined and well-known reference material.

2.4.2 Amphiphilic block copolymers constituting polymer vesicles

Since the late 1990s, advances in controlled polymerization techniques have allowed the design of defined amphiphilic block copolymers that mimic natural amphiphiles and their self-assembly structures, including vesicles [12, 151, 152].

Building blocks of polymer vesicles and polymer membrane conformations: In contrast to the naturally derived lipid vesicles, polymer vesicles (polymersomes) can be assembled from different copolymer architectures, such as diblock, triblock and multiblock copolymers, which give rise to various membrane conformations [65]. The majority of polymersomes is prepared from linear, cylindrically shaped AB diblock copolymers consisting of a hydrophilic (A) and a hydrobhobic (B) polymer chain. As presented in Figure 2.2B (Sec. 2.2), they self-assemble into the conventional amphiphilic bilayer structure in dilute aqueous solution which, based on their macromolecular nature, is usually thicker and highly entangled compared to the low molar mass and highly ordered lipid bilayers [16, 60, 65, 66, 68]. Furthermore, depending on chain flexibility, the hydrophobic chains in polymeric bilayers are typically interdigitated to various degrees as opposed to the well-separated phospholipid

bilayers [60]. Examples for bilayer forming AB diblock copolymers are the prototypical and most widely studied copolymers introduced by Discher and coworkers, namely poly(ethylene oxide)-*b*-poly(ethylethylene) (PEO-*b*-PEE) and poly(ethylene oxide)-*b*-polybutadiene (PEO-*b*-PBD) [12, 66–68, 99, 103, 123, 135].

In addition to the cylinder shaped AB diblock copolymers, bilayered polymersomes can also be obtained from U-shaped BAB triblock copolymers which form a loop in their hydrophilic middle chain upon self-assembly into bilayer membranes in excess water. In contrast, the more widely used ABA triblock copolymers can have two possible conformations within polymersome membranes: They can either stretch across the membrane in a cylindrical shape forming a monolayer or they can integrate into a bilayer by adopting a loop in their hydrophobic middle block (U-shape) so that the two hydrophilic chain ends extend to the same side of the bilayer. An example for the former, monolayer forming type of ABA triblock copolymer is poly(methyloxazoline)-*b*-poly(dimethylsiloxane)-*b*-poly(methyloxazoline) (PMOXA-*b*-PDMS-*b*-PMOXA)

which has been introduced and intensively investigated by Meier's group at the Universtity of Basel [4, 78, 117, 153]. Similarly, monolayered polymersome membranes can be prepared from a range of multiblock copolymers. Based on the individual adjustability of the chemical composition and length of each block in amphiphilic block copolymers, multiblock copolymers offer an extra level of control within polymersome membranes. As an example, ABC copolymers comprising two chemically different hydrophilic chain ends (A and C) and one hydrophobic middle block (B) are able to assemble into asymmetric membranes and, finally, into polymersomes with different internal and external surface chemistries.

The large variety of chemical compositions and molecular architectures of amphiphilic block copolymers that have been designed for the assembly of polymersomes is summarized in several recent reviews [7, 64, 65].

PEO-*b*-PMCL: In this work, a relatively new type of biocompatible and biodegradable AB copolymer, namely poly(ethylene oxide)-*block*-poly(γ-methyl-ε-caprolactone) (PEO-*b*-PMCL), was used for the preparation and characterization of food grade polymersomes (Chapter 3; see Fig. 3.1 for the chemical structure of PEO-*b*-PMCL). Its ability to self-assemble into vesicles at specific hydrophobic to hydrophilic block weight ratios in excess water was first demonstrated by Zupancich *et al.* (2006) [76]. The low T_g of the hydrophobic PMCL block ($\approx -60\,°C$) [136] allowed for the assembly of fluid and flexible vesicle membranes at room temperature.

Braun *et al.* then presented the full lyotropic phase behavior of vesicle forming PEO-*b*-PMCL copolymers at varying hydrophobic to hydrophilic block weight ratios (w_{PMCL}) in water [52]. The resulting binary phase diagram is shown in Figure 2.5B. Similar to binary egg PC–water mixtures (Fig. 2.5A), the phase diagram of PEO-*b*-PMCL with $w_{PMCL} > 0.8$ and water is dominated by lyotropic and isotropic

lamellar phases, i. e. vesicles, in concentrated and very dilute dispersions, respectively. For $w_{\mathrm{PMCL}} > 0.86$, the copolymer first self-assembles into an inverse hexagonal phase (H_2) before it transforms into the lamellar phase upon dilution.

Chemical copolymer constitution and polymersome membrane properties: The enormous versatility of block copolymer chemistry allows not only to adjust the physicochemical properties of polymersome membranes but also to introduce functionalities into the polymer vesicles via the molecular design of the constituting building blocks.

These design opportunities in the synthesis of amphiphilic block copolymers include the control over chemical block composition, block molecular weight and chain length, hydrophilic to hydrophobic block ratio, number of blocks, and the resulting overall molecular architecture. The different copolymer architectures can then be exploited for their influence on the structure of the self-assembled polymer membranes, such as the degrees of chain coiling, entanglement, and interdigitation, as well as the membrane thickness and its polarity profile, which, ultimately, determines the physicochemical membrane properties [7, 16, 65, 103].

Generally, polymer vesicles possess superior properties in terms of mechanical toughness and rheological robustness over lipid vesicles because of the increased thickness, the entangled structure, and, hence, the enhanced cohesion of polymer membranes. This has been characterized by measuring the lysis tension σ_l and the shear surface viscosity η_S of polymer vesicles in the fluid state prepared from flexible (coil–coil) diblock copolymers [12, 66, 67, 123, 135]. The values of σ_l for fluid polymer membranes exceed the characteristic ones for fluid lipid bilayers by at least a factor of 2 (Tab. 2.1). Furthermore, the lysis tension, i. e. toughness, of polymersomes was found to increase with increasing molecular copolymer weight and the resulting increased membrane thickness [67]. Based on the extremely high rheological parameters measured in polymer bilayers, polymersomes have also been referred to as hyperviscous vesicles [123]. At the same time, the enhanced mechanical and rheological stabilities of fluid polymersome membranes do not compromise their elastic nature, as characterized by the area expansion (K_A) and the bending (κ_c) elastic moduli [12, 67, 123, 135]. They fall in the range of values typical for lipid membranes (Tab. 2.1).

Due to the increased thickness of polymer membranes, polymersomes are generally described to be less permeable than their thin-walled lipid analogs in the polymersome literature [16, 65, 154]. However, the vast majority of these descriptions refer to the pioneering work by Discher *et al.* studying the permeability of fluid, but highly hydrophobic PEO-*b*-PEE membranes towards water [12]. Indeed, the obtained permeability coefficient P was considerably lower than those found for typical water permeabilities of fluid lipid bilayers (Tab. 2.1). A similar result has been reported for PEO-*b*-PBD membranes which are also characterized by a highly

hydrophobic and relatively rigid membrane interior [99, 103]. As summarized before (Sec. 2.3.4) and discussed in Section 3.3.2, the passive permeability of amphiphilic membranes towards polar solutes is not only dependent on membrane thickness, but also on a number of other factors, such as the fluidity, chain order, and relative hydrophobicity in the membrane. Consequently, polymersome permeability, in fact, varies over a broad range, depending on the chemical composition of the chosen amphiphilic building blocks and the resulting membrane architecture. For copolymers assembling into less hydrophobic [17] and/or more flexible membranes [99, 103], the membrane permeability towards hydrophilic molecules has been reported to be enhanced compared to conventional lipid bilayers.

The increased thickness and entangled structure of polymer membranes do constitute a high barrier against the transmembrane movement of amphiphiles (flip-flop), which is largely suppressed in polymersome bilayers [155, 156].

Functionalization of polymer vesicles: In polymersomes, there are many possibilities to further control vesicle permeability by assembling them from block copolymers that are responsive to external stimuli, such as pH, temperature, redox conditions, and light. Cargo release from such stimuli-responsive polymersomes can then be triggered by changing the external conditions and, thereby, switching the architecture or the stability of the polymer membrane as reviewed in [7, 22, 154, 157]. In analogy to liposome functionalization, further functionalities have been introduced to the surface of polymersomes by incorporating copolymers with functionalized hydrophilic blocks or with eng-group attached ligands into the polymer membrane [68, 158]. It has to be noted, however, that the presentation of surface functional groups by the hydrophilic polymer brush constituting the surface of polymersomes is less controlled compared to functionalized, well-defined headgroup surfaces of liposomes.

2.4.3 Cholesterol

Cholesterol is another amphiphilic biomembrane lipid that is enclosed in animal plasma membranes at relatively high molar fractions ($\approx$ 20–40 mol%). It belongs to the class of higher sterols, such as phytosterols (plant plasma membranes) and ergosterol (fungal plasma membranes). Insertion of cholesterol into lipid membranes induces a number of unique and substantial modulations in the structural and physical bilayer properties. These effects have been reviewed by several authors [107, 159, 160] and are summarized below.

Cholesterol is a uncharged amphiphile with a small hydrophilic –OH headgroup and a large hydrophobic body consisting of the steroid 4-ring framework and a short hydrocarbon side chain (see Tab. 4.3 for the chemical cholesterol structure). In the

case of predominantly saturated, mono-, and/or diunsaturated chain bilayers, the inverse-shaped cholesterol molecules ($p > 1$) intercalate in an upright conformation into lipid bialyers, with the –OH headgroup embedded in the hydrophilic surface layer [107, 159, 161].

On a *structural* level, the insertion of cholesterol into liquid-disordered bilayers (fluid or L_α phase state) leads to an increased lipid packing density so that the mainly hydrophobic cholesterol molecules are shielded from interactions with water by the neighboring phospholipid headgroups (umbrella model) [162]. The tighter molecular packing results in a decrease in the mean headgroup area per phospholipid molecule in the mixed phospholipid–cholesterol bilayer (condensing effect) [11, 110, 159]. At the same time, the conformational freedom and flexibility of the fatty acid chains are reduced and the total bilayer thickness increases (ordering and rigidifying effect) [107, 110, 163, 164]. In solid-ordered bilayers (gel or $L_{\beta'}$ phase state), the effects of cholesterol insertion are the opposite, promoting area dilation, disorder, and fluidity in the mixed bilayers [107, 165–167]. As a consequence, at sufficiently high cholesterol concentrations in a given phospholipid–cholesterol bilayer system, the phase transition between the solid-ordered ($L_{\beta'}$) and the liquid-disordered (L_α) phase state vanishes [160, 165] and gives rise to an intermediate, thermodynamically discrete state, the **liquid-ordered** phase state (L_0) [107, 168, 169]. Liquid-ordered bilayers have mechanical and permeation properties similar to solid membranes, as outlined below, while the fluidity and rapid diffusion in the plane of the bilayer are maintained.

On the *mechanistic* side, the condensing and ordering effects of cholesterol in fluid bilayers generally impart high barrier properties against transbilayer diffusion of both polar solutes (passive permeation) [107, 110, 170, 171] and membrane lipids (flip-flop) [95, 172]. Furthermore, cholesterol promotes a significant increase in overall mechanical membrane stability, as measured by the higher values of the area expansion modulus K_A [11, 110, 132, 173], the bending modulus κ_c [110, 127, 128, 137, 174], and the lysis tension σ_l [11, 15, 173] of cholesterol containing vesicle membranes (Tab 2.1). Consequently, the stiffer and tougher cholesterol containing vesicles obtained from a given mechanical treatment, such as extrusion or sonication, tend to be larger than their cholesterol-free analogues [15, 128, 137].

It has to be noted that the nature and magnitude of interactions between host membrane phospholipids and cholesterol and the resulting effects on bilayer properties depend on the chemical structure of the phospholipids [160]. The condensing and ordering effects of cholesterol decrease with increasing degrees of fatty acid chain unsaturation and are practically eliminated in bilayers consisting of polyunsaturated phospholipids with more than two *cis*-double bonds in each acyl chain [11, 159–161, 175].

In this study, cholesterol was incorporated into egg PC and soy PC bilayers to decrease the elasticity and increase the mechanical strength of vesicles processed by dynamically enhanced extrusion (Chapter 4).

2.4.4 Detergents

Surfactants ("surface active agents") are amphiphilic molecules that accumulate at interfaces, such as water-air and water-oil interfaces, thereby reducing their surface tension [47]. This definition comprises basically all amphiphilic molecules introduced in Section 2.1, including the cylinder shaped, virtually water insoluble, bilayer forming glycerophospholipids. In this section, we refer to micelle-forming surfactants (often called **detergents**), i. e. cone shaped amphiphiles that possess an aqueous solubility (critical micelle concentration) in the micro- to millimolar range above which they self-assemble into micellar aggregates. These include, among many other amphiphiles, synthetic surfactants such as sodium dodecyl sulfate (SDS) and Triton X-100, physiological surfactants such as the various bile salts, and monoacyl-glycerophospholipids (lysoglycerophospholipids) [82].

In liposome technology, detergents are used as additives (cosurfactants) to modulate bilayer properties [174, 176, 177], as templates for vesicle formation by the detergent depletion method [3], and as liposome solubilizing agents [178–180]. These principles and the underlying interactions of surfactants with lipid bilayers have been reviewed in detail by Heerklotz [82].

Vesicle solubilization by detergents: The solubilization of bilayered vesicles in the presence of excess detergent is also referred to as ***vesicle-to-micelle transformation***. For lipid vesicles, the process sequence of bilayer solubilization by detergents can almost generally be described by the three-stage model [82, 178, 179, 181], as schematically illustrated in Figure 2.6.

In stage I, detergent monomers partition into the vesicle bilayers without affecting vesicle integrity until the bilayers saturate with detergents. At saturation, the system enters stage II where mixed detergent-lipid micelles detach from the detergent-saturated bilayers. Hence, stage II is characterized by the coexistence of detergent-saturated bilayers and mixed micelles. By stage III, all membrane lipids are solubilized into mixed micelles and the vesicle-to-micelle transformation is complete.

According to this model, the detergent-induced solubilization of a given liposome suspension is characterized by the total detergent concentration (D_{tot}) required for the onset and completion of mixed micelle formation, $D_{\text{tot}}^{\text{sat}}$ and $D_{\text{tot}}^{\text{sol}}$, respectively. The corresponding parameters for the effective molar ratio of detergent to lipid in the vesicle bilayer at saturation and complete solubilization are $R_{\text{B}}^{\text{sat}}$ and $R_{\text{B}}^{\text{sol}}$, respectively (Fig. 2.6). A comprehensive list of experimental values of $R_{\text{B}}^{\text{sat}}$ and $R_{\text{B}}^{\text{sol}}$ for different aqueous detergent–lipid mixtures is given in [82]. For the aqueous PC/Triton X-100 and PC/sodium cholate systems used in this study, we referred to [178] and [176, 178, 182, 183], repectively.
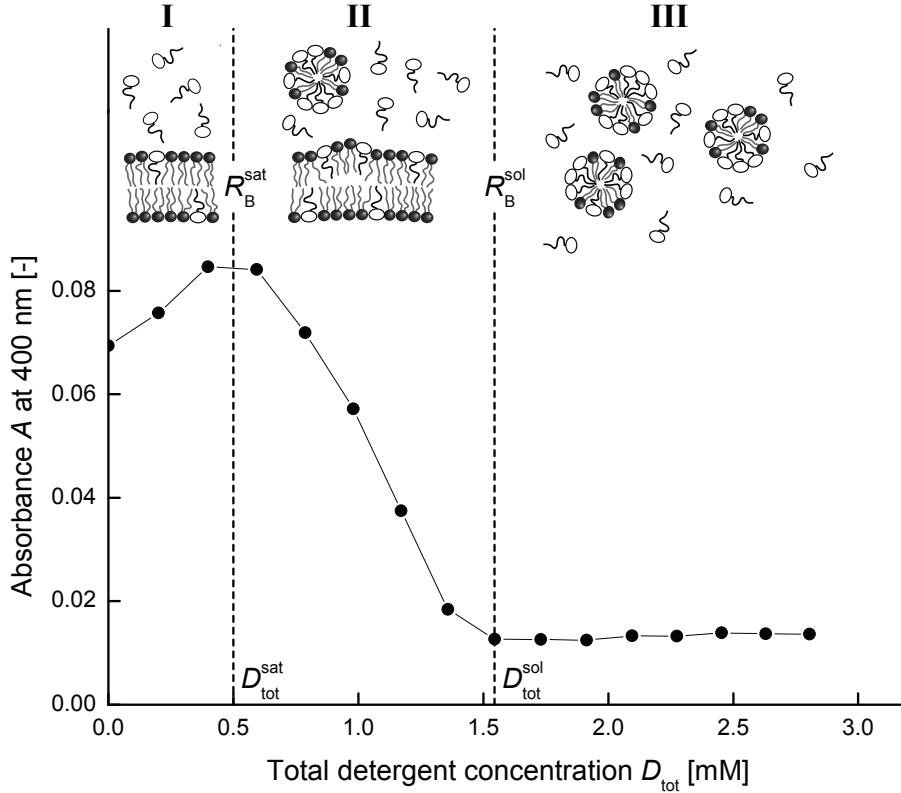
Figure 2.6: Three stages of bilayer solubilization by detergents. *Bottom*: Solubilization of vesicle bilayers by detergents shown through changes in turbidity of a LUVET$_{100}$ suspension as a function of total detergent concentration D_{tot} after sample equilibration. D_{tot}^{sat} and D_{tot}^{sol} mark the beginning and end of stage II, i.e. the onset and completion of vesicle solubilization, respectively. Composition of LUVET$_{100}$ suspension: 0.645 mM POPC/POPE 95:5 (mol/mol). Detergent: Triton X-100. *Top*: Schematic representation of stages I–III. Lipids and detergents are represented by filled and empty spheres (hydrophilic headgroups) with two and one connecting lines (hydrophobic chains), respectively. Adapted from Lichtenberg *et al.* [179].

To a first approximation, the three-stage model for detergent-induced vesicle solubilization applies to both lipid and polymer vesicles even though the mechanisms governing lipid and polymer membrane solubilization by detergents are different [155, 179]. These mechanisms are discussed in the frame of the bile salt-induced permeabilization and solubilization study of lipid and polymer vesicles presented in Section 3.3.2 of the present thesis. All experiments that rely on a fast and complete vesicle solubilization were conducted with an excess of the commonly utilized ethylene oxide detergent Triton X-100 for both lipid and polymer vesicles [155, 178, 179]. The detergent deplition method that is widely used for the preparation of membrane protein incorporating vesicles [3] is based on the reverse process of the vesicle-

to-micelle transformation, the *micelle-to-vesicle transformation* or vesicle reformation/reconstitution [82, 184].

Detergents as bilayer additives (cosurfactants):   Symmetric insertion of detergents into lipid host bilayers at molar ratios below saturation ($R_B < R_B^{sat}$; Fig. 2.6) induces changes in bilayer properties that are very much opposite to the effects of cholesterol on fluid bilayers described in Section 2.4.3.
On the structural level, the cone shaped detergents increase the conformational freedom and flexibility of the hydrophobic chains in the mixed bilayer and decrease the total bilayer thickness (disordering and fluidizing effect) [82]. On the mechanistic level, this results in enhanced transbilayer diffusion rates of both polar solutes (passive permeation) [82, 176] and host membrane lipids (flip-flop) [82, 185] across the fully equilibrated lipid–detergent membranes. In the case of an asymmetric distribution of guest detergents within the lipid host bilayer, membrane permeability towards polar solutes may be further increased by pore formation or mechanical failure in the mixed bilayer [82, 183]. Regarding the mechanical membrane properties, detergents act as softening agents in lipid bilayers inducing significantly lower bending rigidities and tensile strengths in the mixed bilayers. This has been quantified by the lower values of the bending elastic modulus κ_c [174, 181, 186] and the lysis tension σ_l [187], respectively, of detergent containing vesicle membranes.
In this study, the bile salt sodium cholate (SC) was used to decrease the bending rigidity of egg PC and soy PC vesicles and to increase the penetrability of nanopore membranes in dynamically enhanced vesicle extrusion (Chapter 4; see Tab. 4.3 for the chemical structure of SC). SC is commonly used to prepare ultraflexible lipid vesicles, the so-called *Transfersomes* [81, 188, 189].

2.5 Preparation of Vesicles

As introduced in Section 2.3.3, most vesicle structures are not a thermodynamically stable state. This means that their formation in aqueous solution does not occur truly spontaneously but requires the input of external energy [70, 94]. Therefore, the physical properties of the resulting kinetically trapped vesicles, including their mean size and lamellarity (see Fig. 2.2), depend not only on the chemical structure of the amphiphile (or amphiphile mixture) used and on the solution conditions, but particularly on the method of vesicle preparation [3].
The principle methods for the preparation of lipid vesicles have been summarized in the literature [3, 5, 36, 59]. For a detailed description on the preparation of nanometer- and micrometer-sized (lipid) vesicles and important related works, the

reader is referred to the reviews by Walde and coworkers [3, 5]. Experimental protocols for liposome preparation can be found in [142]. Please remember that the vesicle membranes need to be in their fluid state for all type of mechanical treatments carried out during vesicle preparation (Sec. 2.3.1). Therefore, it is recommended to follow the preparation protocols at a temperature at least 5 °C above T_m or T_g of the constituting lipids or block copolymers, respectively [3].

In general, the methods described for the preparation of lipid vesicles are also applicable to vesicle forming, synthetic amphiphiles with similar amphiphilicity to that of lipids, including amphiphilic block copolymers [4, 65, 77, 135]. However, the formation of polymersomes can be more complex and slower compared to liposomes, depending on T_g and the related flexibility of the block copolymer chains (see Sec. 2.3.1). For highly hydrophobic and/or high T_g copolymers, elevated temperatures or an apolar organic solvent are needed to fluidize polymer membranes and allow for polymersome formation [71, 75, 77].

In the following sections, the principles and characteristics of the vesicle preparation methods used in this work are summarized.

2.5.1 MLVs formed by thin amphiphile film hydration

Simple hydration of vesicle forming amphiphiles in excess aqueous solution under agitation yields multilamellar vesicles (MLVs). This is the easiest way to prepare vesicle suspensions and can be achieved by the relatively quick dispersion of a thin amphiphile film [3] or by prolonged stirring of the bulk amphiphile in the aqueous solution [190].

Principle of thin amphiphile film hydration: In the thin film hydration method, the vesicle forming amphiphile is first dissolved in a suitable organic solvent, usually chloroform. The obtained stock solution is then added to a round-bottom flask. Complete solvent removal by rotary evaporation followed by high vacuum drying overnight yields a dry thin amphiphile film on the glass surface of the flask as illustrated in Figure 2.7A.

The subsequent addition of an aqueous solution (hydration or swelling medium) at $T > T_m$ or T_g of the amphiphile used (Sec. 2.3.1) induces swelling of the dry film. This film swelling process proceeds through the hydration of the hydrophilic domains, formation of a lamellar phase, and increasing separation of the lamellae which eventually buckle and unbind to self-close into vesicles [57, 70, 192]. For the preparation of MLVs, the swelling process is accelerated by gentle (hand shaking) or vigorous shaking (vortex mixing). This promotes complete film dispersion in the aqueous solution in the form of bilayer to n-multilayer fragments resulting in the formation of mainly multilamellar vesicles (Fig. 2.7B). [3, 36, 142, 192].
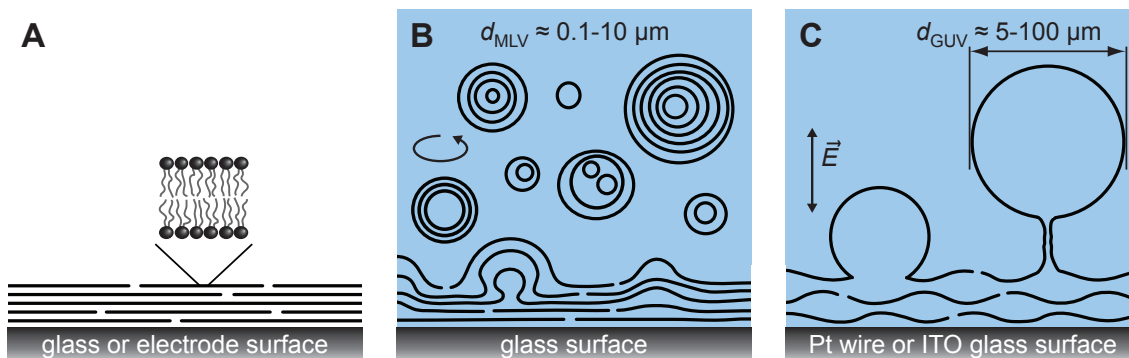
Figure 2.7: Schematic illustrations of the formation of MLVs and GUVs by thin film hydration. (A) Dry thin film of vesicle forming amphiphiles deposited onto a solid surface. (B) MLV formation by hydration of the thin amphiphile film in excess aqueous solution under shaking (indicated by the circular arrow). (C) GUV electroformation by hydration of the thin amphiphile film on the surface of an electrode in excess aqueous solution and in the presence of an ac electric field. $\vec{E}$ indicates the direction of the external electric field. Adapted from Shimanouchi *et al.* [191].

If the swelling process is initialized in an amphiphile film deposited on a flat surface and is allowed to occur under undisturbed conditions (strict avoidance of agitation) over a prolonged hydration time of several hours, mainly unilamellar giant vesicles are obtained. This is the so-called **gentle hydration (or spontaneous swelling) method** historically and currently used for the preparation of GUVs [5, 57, 135].

Characteristics of MLVs prepared by the thin film hydration method: The MLV suspensions obtained from thin film hydration are generally very heterogeneous in terms of size (typically 0.1–10 µm) and lamellarity [36, 192, 193]. On average, lipid MLVs are composed of at least 10 bilayers [190, 194], while their mean diameter is of the order of a few micrometers. Consequently, with respect to their large size, MLVs offer a relatively low internal aqueous volume for solute entrapment [36]. Furthermore, the preparation of MLVs by thin film hydration is not very reproducible. For a given amphiphile and solution composition, the obtained vesicle size, size distribution, and lamellarity depends on the quality of the dry film, including its thickness and the number of crystal defects, and on the energy input during agitation [3, 36, 192].

Due to these characteristics, unprocessed MLVs have limited use in research and industrial applications. However, MLV suspensions are widely used as pre-suspensions in the preparation of more defined vesicles by different homogenization techniques, such as extrusion (see Sec. 2.5.3), sonication [3, 194–196], fench press [3, 194, 197], high pressure valve homigenization [3, 198–200], and microfluidization [3, 201–203]. Based on the simple and little controlled formation of MLVs in excess aqueous solu-

tion, MLVs are often referred to as being formed spontaneously, including this work. Strictly and thermodynamically speaking, this is not the case as energy is supplied in the form of agitation to generate the MLVs from dry amphiphiles [70, 94].

2.5.2 MLVs subjected to freezing and thawing

Aqueous MLV suspensions, as obtained for example by the thin film hydration method (Sec. 2.5.1), are often taken through 5 to 10 freeze–thaw cycles prior to further homogenization, most commonly by the extrusion technique (Sec. 2.5.3). To do so, the MLV suspension is placed inside a thick-walled glass recipient, e. g. the round-bottom flask used for thin film dispersion, and subjected to repetitive complete freezing in liquid nitrogen at $T \approx -195\,°C$ followed by complete thawing in a water bath at $T > T_m$ or T_g of the amphiphile used (Sec. 2.3.1) [3, 36].

Effects of freeze–thaw cycles on vesicle suspensions: Although the process of freeze-thawing is not completely understood, it has proven to be useful to induce a number of equilibrating and slightly homogenizing effects in vesicle suspensions. Freeze–thaw cycles promote an even distribution of amphiphiles throughout the bilayers of mixed-component LUVs and MLVs. This is especially important for the preparation of functionalized vesicles incorporating for example marker lipids or head-group functionalized lipids in their matrix membrane [10, 204]. Equilibration is also achieved in the distribution of solutes between the aqueous domains of the vesicle interior and the external aqueous bulk solution. This results in significantly higher solute encapsulation efficiencies of freeze-thawed vesicle suspensions compared to their untreated analogues [3, 205, 206]. In MLV suspensions, the increase in encapsulation efficiency is especially pronounced as, in addition to equilibrating the solute distribution, freeze-thawing imparts significantly larger interlamellar spacings. This leads to lower degrees of mulitlamellarity and increased internal volumes in freeze-thawed MLVs [9, 205]. Finally, the freezing–thawing procedure eliminates very small vesicles (SUVs) possibly present in the initial MLV suspension through vesicle fusion, especially if the suspension medium is pure water [3]. Very small vesicles would not be affected in the subsequent extrusion process and would broaden the size distribution of the resulting homogenized vesicle suspension.

2.5.3 Conventional vesicle extrusion

The extrusion technique originally introduced by Olson *et al.* (1979) [150] is the most popular method to reproducibly prepare homogeneous vesicle suspensions with controlled mean size and lamellarity at the research level [3, 9, 15, 119, 193, 206].

Principle of the extrusion technique: The method consists of repetitively (at least 10 times) forcing a MLV suspension in the fluid state under moderate pressure through the well-defined, cylindrical pore channels of a track-etched polycarbonate filter membrane. The mean pore diameter of the membranes commonly used ranges from 30 to 400 nm [3, 9, 193]. Unilamellar or multilamellar vesicles that are larger than the mean diameter of the pore channels are reduced in size and lamellarity upon passage through the channels as schematically illustrated in Figure 2.8C [15, 119]. The resulting mean vesicle size reflects the mean diameter of the pores [9, 10, 15]. A closer description of the mechanism of vesicle extrusion is given in Section 2.6.

Usually, a MLV pre-suspension is first repetitively extruded 10 times through polycarbonate membranes with a relatively large mean pore diameter of 400 nm and/or 200 nm. Final extrusions through membranes with 100 nm, 80 nm, 50 nm, or even 30 nm pores are then repeated between 10 and 30 times. The obtained "Vesicles prepared by the Extrusion Technique" are abbreviated as VETs$_n$ where n indicates the mean pore diameter of the membrane used for final extrusions [3, 9].

Commercial extrusion devices: The most widely used commercial device for repetitive vesicle extrusion at laboratory scale is the LIPEX™ Extruder from Northern Lipids as illustrated in Figure 2.8 [207]. It is a heavy-duty vessel system that uses compressed nitrogen gas to force the fluid-state vesicles through the polycarbonate filter membrane in a batch-wise operation mode [193]. The applied pressures typically range from about 1.5 to 20 bar [15, 206, 208, 209]. Higher extrusion pressures of up to 55 bar can be built up in the LIPEX vessel to process even concentrated, viscous vesicle suspensions containing for example 400 mg ml^{-1} of lipids [9, 193]. The research scale LIPEX device as used in this thesis handles vesicle suspension volumes of 1.0–10 mL (Fig. 2.8). A larger LIPEX unit is also available from Northern Lipids to process preclinical volumes of 10–800 mL. Larger volumes of vesicle preparations may be processed by cycling them through the continuously operating Maximator® device from CPL Sachse [210–212]

For the preparation of research volumes (0.2–1.0 mL) of high value VET suspensions where low vesicle concentrations are acceptable, the syringe-based extrusion devices as supplied by Avestin (LiposoFast™; Ottawa, ON, Canada) [213] and Avanti Polar Lipids (Alabaster, AL, USA) [214] are best suited. They consist of two Hamilton syringes connected by a filter holder which allows for the manual back-and-forth extrusion of the sample [212, 215]. This extrusion system is limited by the pressure that can be applied manually and by the reduced back pressure tolerated by the syringe and filter holder setup.

It has to be noted that, for a given set of amphiphiles and pore diameter used, the generated vesicle size depends on the operation conditions in the extrusion device [212]. Higher extrusion pressures, i. e. higher pore flow rates, generally result in smaller vesicle sizes as predicted by the pressure-dependent models of vesicle extrusion
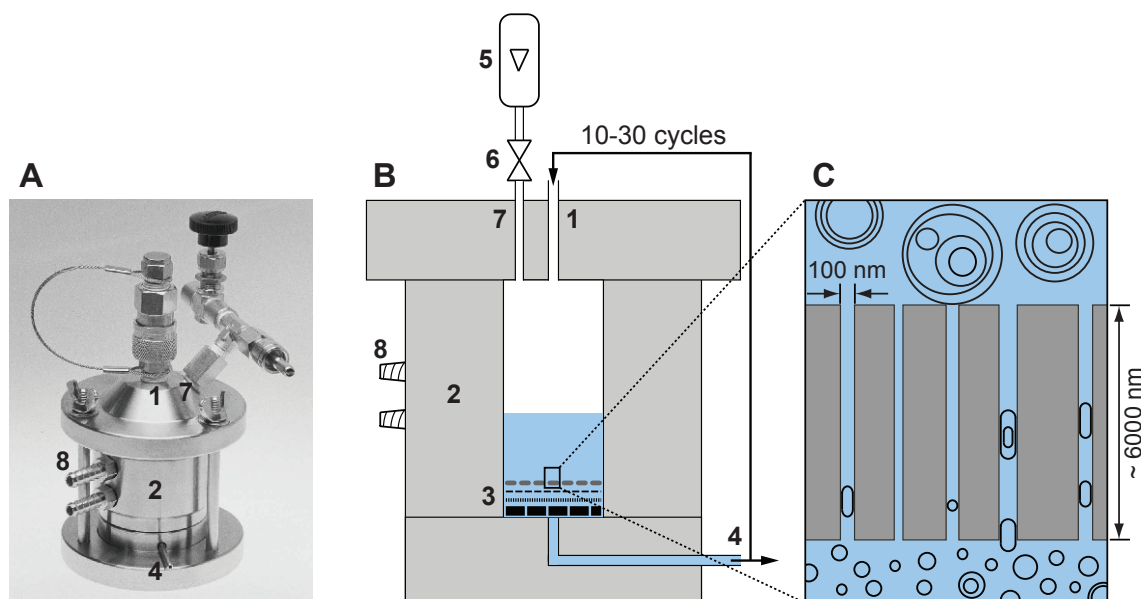
Figure 2.8: LIPEX device for repetitive vesicle extrusion. (A) Photograph and (B) schematic representation of the research scale LIPEX device showing the main functional components of the apparatus: (**1**) inlet of initial MLV or recycled vesicle suspension; (**2**) water-jacketed, robust vessel containing the to be extruded suspension; (**3**) track-etched polycarbonate membrane disc (*gray dashes*) placed on a polyester drain disc, a stainless steel support mesh, and a stainless steel support disc (from top to bottom); (**4**) outlet of extruded vesicle suspension; (**5**) compressed nitrogen gas cylinder; (**6**) adjustable pressure reduction valve; (**7**) nitrogen gas supply; (**8**) connectors to circulating water bath for optional heating when processing high T_m lipids or high T_g copolymers. (C) Close-up of the track-etched polycarbonate membrane with cylindrical, straight-through pore channels illustrating the principle of repetitive static vesicle extrusion. Drawing not to scale. Part (A) is reprinted from Mui *et al.* [216] with permission from Elsevier; Part (C) is adapted from Walde [3].

proposed by Patty and Frisken [15] and Bertrand and Joós [119] (Sec. 2.6).

Characteristics of vesicles prepared by the extrusion technique: The extrusion technique yields highly reproducible and rather homogeneous VET suspensions with an average vesicle size that corresponds, in a first approximation, to the mean pore diameter of the polycarbonate membrane used for final extrusions. This is especially true for VET_{100} suspensions which are characterized by mean vesicle diameters close to or slightly larger than 100 nm [15, 208, 209, 217] and predominant unilamellarity [9, 10, 204, 206, 218, 219]. Therefore, they are most commonly referred to as $LUVET_{100}$ suspensions.

Unilamellar VET systems can also be generated by final vesicle extrusions through

membranes with pore sizes smaller than $100\,nm$, e.g. VET_{80}, VET_{50}, and VET_{30} suspensions [9, 219]. In this case, the resulting mean vesicle diameter is generally larger than the pore size used [9, 15, 209]. This can be explained by the relaxation of the vesicles from a spherocylindrical to a quasispherical shape as they leave the pore channels during the final extrusion passages (see Fig. 2.11) [119].

VET_{200} and particularly VET_{400} preparations retain a significant population of oligolamellar vesicles and exhibit mean vesicle sizes that are smaller than the pore diameter used [9, 10, 217, 219]. The reason for this is the presence of uni- and oligolamellar vesicles considerably smaller than $400\,nm$ and smaller than $200\,nm$ in the initial MLV suspension which are not affected by the extrusion treatment. Based on the heterogeneity of MLV pre-suspensions, it is obvious that VET populations obtained from repetitive MLV extrusion through pore sizes larger than $100\,nm$ are increasingly heterogeneous in terms of size and lamellarity with increasing pore size, i.e. increasing cutoff of maximum vesicle size. As described in Section 2.5.2, this heterogeneity can be reduced by subjecting the MLV precursors to freeze–thaw cycles prior to extrusion, thereby eliminating very small vesicles and decreasing the degree of multilamellarity in the pre-suspension. Indeed, VET_{200} suspensions prepared from freeze-thawed MLVs exhibit a unilamellar character almost as high as that typically generated in $LUVET_{100}$ systems [9, 10].

2.5.4 Dynamically enhanced vesicle extrusion

The process of dynamically enhanced vesicle extrusion was introduced in the pursuit of the main objective of this work: The development of a scalable production process for the well controlled, reproducible, and gentle formation of nanometer-sized vesicle carriers for biomedical, cosmetic, and food applications (see Chapter 1 and Introduction in Chapter 4).

Principle of dynamically enhanced vesicle extrusion: Following the reliable but laborious and little scalable, static extrusion process (in terms of the various vesicle recirculations cycles through membranes with decreasing pore sizes; Sec. 2.5.3), the process of dynamically enhanced vesicle extrusion augments the conventional extrusion process with a defined shear flow field acting directly at the outlet of the nanopore membrane (see Fig. 2.9C). The shear forces are expected to shear off the leading bilyer to n-multilayer endcaps of spherocylindrical vesicles emerging from the nanopore channels. These endcap fragments would immediately self-close to form smaller, uni- to n-multilamellar vesicles upon leaving the pores. By selecting a defined pore diameter and controlling the applied shear rate, this would allow to specifically adjust the size and lamellarity of MLV precursors after a single, dynamically enhanced extrusion cycle, independently on the applied extrusion pressure and
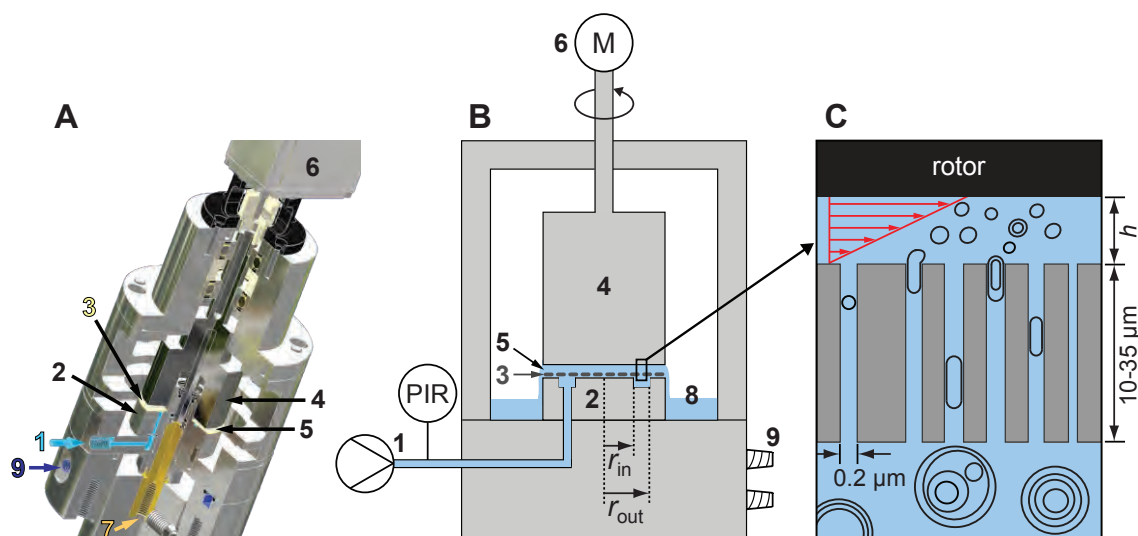
Figure 2.9: ROMER device for dynamically enhanced vesicle extrusion. (A) Technical drawing and (B) schematic representation of the research scale ROMER device with the main functional components of the apparatus: (**1**) MLV suspension inlet, (**2**) static, circular, planar membrane holder, (**3**) flat nanopore membrane disc glued onto membrane holder, (**4**) planar rotor, (**5**) shear gap between rotor and static membrane module with plate-plate shear geometry and shear gap height h, (**6**) motor for rotor speed adjustment, (**7**) µm-screw for shear gap height adjustment, (**8**) collection reservoir for dynamically extruded vesicle suspension, (**9**) connectors to circulating water bath for optional heating of the ROMER housing when processing high T_m lipids or high T_g copolymers. (C) Close-up of the plate-plate shear flow induced at the outlet of the freestanding, static nanopore membrane illustrating the principle of dynamically enhanced vesicle extrusion.

throughput.

If this principle will be proved successful in the frame of the present thesis, dynamically enhanced vesicle extrusion would, indeed, constitute a gentle, continuous and scalable process for the controlled generation of well-defined vesicle structures. Chapter 4 reports on the effect of dynamically enhanced MLV extrusion on vesicle size, lamellarity, and polydispersity as a function of the applied shear rate, nanopore shape, and vesicle membrane elasticity.

ROMER device: Continous, dynamically enhanced vesicle extrusion can be carried out using the so-called ROtating Membrane ExtrudeR (ROMER) as designed in the frame of this work (ROMER I; Figs. 2.9 and 4.1) and in the PhD thesis of Sebastian Holzapfel also carried out at the Laboratory of Food Process Engineering at ETH Zurich (ROMER II; Fig. 4.18) [220, 221].

For the present work, a research scale prototype of the ROMER device (ROMER I, simply called ROMER in this thesis) was constructed in collaboration with Bühler

AG (Uzwil, Switzerland) and built by Jan Corsano at the Laboratory of Food Process Engineering at ETH Zurich. Figure 2.9 schematically shows the setup and principle of the ROMER apparatus. In the following, the main functional components of the ROMER process are described by referring to the numbers indicated in Figure 2.9. Photographs of the experimental ROMER setup can be found in the Materials and Methods part of Chapter 4 (Fig. 4.1).

The core of the ROMER device is a rotor-stator system. The lower stator element consists of a circular, planar membrane holder with a circular recess between an inner and an outer radial distance of $r_{in} = 10.5\,\mathrm{mm}$ and $r_{out} = 12.5\,\mathrm{mm}$ (**2**). The recess houses the inlet for the to be extruded MLV suspension (**1**). Gluing a planar membrane disc (**3**) onto the membrane holder provides for a free-standing, active membrane ring above the circular recess with an inner and an outer radius of approximately $r_{in} = 10.5\,\mathrm{mm}$ and $r_{out} = 12.5\,\mathrm{mm}$ (Fig. 2.9B, see also photographs in Fig. 4.1). The shear flow acting directly at the outlet of the free-standing ring membrane is induced by the action of a planar rotor (**4**) located at a small distance above the planar membrane module and, hence, forming a plate-plate shear flow geometry (Fig. 2.9B and C). The shear rate $\dot{\gamma}(r)$ resulting in the shear gap (**5**) between the membrane and the rotor at a radial distance r is given by:

$$\dot{\gamma}(r) = \frac{v_x(r)}{h} = \frac{\omega r}{h} = \frac{(2\pi n)r}{h} \tag{2.5}$$

where h is the shear gap height, $v_x(r)$ the tangential velocity of the rotor at the radial distance r, ω the angular rotor velocity, and n the number of rotor revolutions. The ROMER apparatus allows adjusting the shear rate by precisely controlling the rotor speed n via a compact drive (**6**; 0–12 000 rpm) and the shear gap height h via a µm-screw (**7**; 0–2000 µm).

In all ROMER experiments reported in this thesis, we refer to the **representative shear rate** $\dot{\gamma}_{rep}$ acting at the radial center of the planar ring membrane, i.e. at $r_{rep} = (r_{in} + r_{out})/2 = 11.5\,\mathrm{mm}$. The deviation of the effective shear rate along the entire width of the ring membrane, i.e. between $r_{in} = 10.5\,\mathrm{mm}$ and $r_{out} = 12.5\,\mathrm{mm}$, from $\dot{\gamma}_{rep}$ is at the most $\pm 5\%$. The shear gap height h was typically set at 200 µm.

2.5.5 GUVs prepared by the electroformation method

The electroformation method developed by Angelova and Dimitrov [222–224] is currently the most widely used method to prepare giant unilamellar vesicles (GUVs) for vesicle and biomembrane research applications [5, 18, 225].

Principle and practical aspects of the electroformation method: Following the standard electroformation method, highly uniform GUVs can be obtained if the hydration of a thin amphiphile film as described in Section 2.5.1 is carried out in water
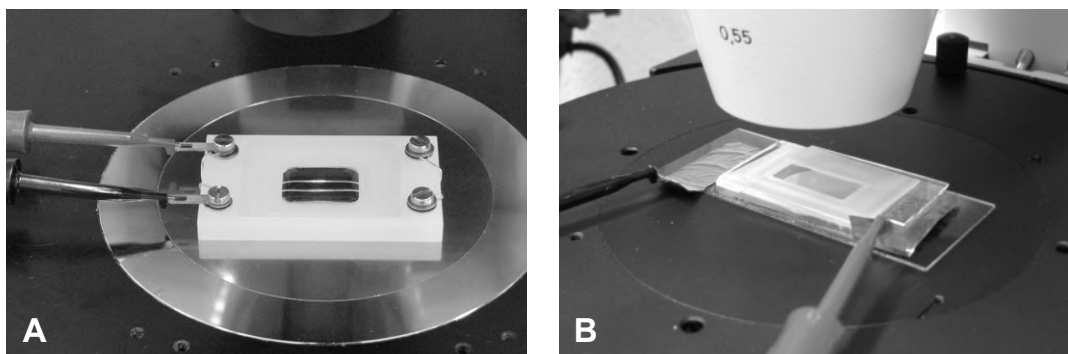
Figure 2.10: Electroformation chambers with a Pt wire or a ITO glass plate setup. The photographs show the two setups of electroformation chambers commonly used in GUV electroformation comprising (A) two parallel, cylindrical Pt wires or (B) two parallel, ITO coated glass plates separated by a spacer frame (here: PDMS spacer). The chamber is placed under an inverted microscope and connected to an external ac supply to monitor the swelling of the amphiphile film and the subsequent GUV growth during the electroformation experiment.

or in an aqueous solution of low ionic strength and in the presence of an alternating current (ac) electric field (see Fig. 2.7C) [191, 226, 227]. The mechanism of this electric field-induced GUV formation is not fully understood. However, it is generally recognized that the ac electric field and, in particular, the periodic electroosmotic motion of water molecules (electroosmotic vibration) enhance the swelling kinetics of the amphiphile film and promote bilayer separation. Therefore, during vesicle electroformation, the initial electro-*swelling* of a film of vesicle forming amphiphiles is followed by the controlled *growth* of unilamellar, giant vesicles as indicated in Figure 2.7C [57, 191, 223, 224, 227].

In an electroformation experiment, the amphiphile film is directly deposited from an organic stock solution on one or both surface(s) of two parallel electrodes assembled in an electroformation chamber. As illustrated in Figure 2.10, the setup of the electroformation chamber is most commonly based on (A) two parallel, cylindrical Pt wire electrodes [123, 191, 224, 226, 227] or on (B) two parallel, transparent electrode plates consisting of indium tin oxide (ITO) coated, electrically conductive glass slides. The ITO glass plates are usually separated by a silicon, a PDMS, or a teflon spacer [103, 227–231]. The chambers are designed such that they can be placed under an inverted microscope. After connecting the electroformation chamber to an external ac supply and filling in the hydration medium at $T > T_m$ or T_g of the amphiphile used, this allows to monitor film swelling and GUV growth, to adjust the applied electric field parameters accordingly, and, finally, to observe the obtained GUVs.

The growth behavior of GUVs and the final diameters of electroformed GUVs depend on a number of experimental conditions, including the amphiphile composition used,

the thickness and structure of the initial dry amphiphile film, the swelling medium, the membrane fluidity and bending rigidity, and the applied electric field parameters (voltage, frequency, duration). For electroformed lipid vesicles, these dependencies have been described in several detailed studies [191, 222–224, 226, 227, 229]. This work summarizes the relations between the driving voltages required for lipid and polymer GUV electroformation and the respective physicochemical membrane properties (Sec. 3.3.3).

The standard ac electric field parameters applied to lipid membranes consist of a voltage of 1–2 V (peak-to-peak value), a frequency of 10 Hz, and a total electroformation time of 60–120 min [191, 226, 227]. Polymer GUVs can also be obtained within 60–120 min by keeping the frequency at 10 Hz and applying somewhat higher driving voltages in the range of 4 to 10 V, depending on the fluidity of the polymer membrane [12, 57, 103, 123, 231, 232]. For extremely little fluid polymer membranes, the necessary electroformation time can extend to several hours [233, 234]. For the formation of both lipid and, in particular, the less dynamic polymer GUVs, it is recommended to start the electroformation experiment at lower voltage to allow for the initial film swelling before raising it to the driving voltages indicated above to promote GUV growth [123, 227, 232, 235] (see also Secs. 3.2.5 and 3.3.3 for the experimental protocols and a Results and Discussion part of the lipid and polymer GUVs prepared in this work).

Characteristics of GUVs prepared by the electroformation method: The giant vesicles obtained by the well controlled and reproducible electroformation method are rather homogeneous, uniformly spherical, and almost exclusively unilamellar [227, 230, 236, 237]. The diameters of a GUV population generated in a standard electroformation experiment typically range from around 5 to 50 µm for both lipid [191, 226, 230] and polymer GUVs [12, 65, 123]. Some vesicles can also easily grow to diameters of up to 100 µm or, occasionally, even to 200–300 µm, depending on the electroformation conditions used [226, 227, 236].

An important, desired or undesired, feature of electroformed vesicles is that they remain connected to the residual amphiphile film on the electrode through narrow membrane tubes (tethers) as indicated in Figure 2.7C [5, 230, 237]. This attachment to the electrode is highly advantageous for the subsequent (long term) investigation of individual GUVs, particularly if microneedles or micropipettes are involved for microinjection [5, 226, 238, 239] or micromanipulation applications [75, 123, 235]. For other applications, electroformed GUVs might be detached from the electrode by gently pipetting the entire suspension out of the electroformation chamber or by picking up individual GUVs with a micropipiette and transferring them in another observation chamber [5]. Generally, the attachment of GUVs to the electrode is stronger if they are formed on Pt wires rather than on ITO plates.

Furthermore, it has to be noted that electroformed GUVs tend to exhibit a small

membrane tension σ just after their formation. At this point, they possess no excess area ($\Delta = 0$) and, hence, do not undergo thermal shape fluctuations (Sec. 2.3.5). Upon storage for a few hours to days, electroformed GUVs become increasingly relaxed and fluctuating [227, 228]. This peculiarity should be kept in mind when using electroformed GUVs for the characterization of mechanical membrane properties, particularly the membrane bending rigidity (κ_c) as extracted from thermal shape fluctuations (Sec. 2.3.5) [127]. On the other hand, freshly electroformed, tense GUVs are advantageous for the perforation of vesicle membranes in the microinjection experiments mentioned above.

In contrast to the procedure of thin film hydration under agitation (Sec. 2.5.1; Fig. 2.7B), the electroformation method generally does not allow for an efficient, passive encapsulation of water-soluble macromolecules and charged compounds into the lumen of GUVs during their formation (Fig. 2.7C). This is due to the fact that large and charged molecules hardly permeate into the amphiphile film and between the lamellae during the relatively short time of film swelling. The same applies to the formation of GUVs by the gentle hydration method (Sec. 2.5.1) [5].

Finally, it has to be mentioned that, in the case of electroformed lipid GUVs, there are some concerns about partial oxidation of the lipid acyl chains induced by the applied electric fields. This has been confirmed for electroformed GUVs prepared from di-polyunsaturated PCs comprising two or more alternating *cis*-double bonds in each fatty acid chain [146]. The authors of this study assumed that lipid bilayers consisting of saturated/monounsaturated PCs are practically insensitive to lipid oxidation, as reported earlier [147]. The oxidation-induced chemical breakdown of fatty acid chains incorporated into vesicle membranes is known to alter a number of physicochemical bilayer properties, such as the bilayer fluidity, permeability, and mechanical stability [146–148]. This has to be considered when using GUVs composed of polyunsaturated lipids and prepared by the electroformation method for research applications.

Applications of electroformed GUVs: The micrometer-sized and highly unilamellar GUVs obtained from electroformation are suitable model systems for the light microscope-assisted real time observation and analysis of individual vesicles and their membranes. Therefore, electroformed GUVs are widely used in different research application as reviewed in [5, 18, 225].

Electroformed GUVs are for example used to study the lateral structure and dynamics of lipid membranes by fluorescence microscopy [225, 240], as well as the mechanical and rheological membrane properties by micropipette aspiration, falling ball viscosimetry, and tether pulling experiments [75, 123]. Furthermore, the membrane permeability to water can be determined from the osmotic swelling and shrinking of electroformed GUVs [99, 241]. The dynamics of entire vesicles have been studied by monitoring the deformation behavior of electroformed GUVs, e. g. in the

presence of external electric fields [120, 121] and in external shear flows [74, 90]. Based on the characteristics of electroformed GUVs summarized in the previous section, the preparation of freely suspended and/or flaccid GUVs by the electroformation method is a delicate task. Such GUVs can more easily be obtained by the spontaneous swelling (gentle hydration) method, however, at the expense of sample homogeneity in terms of GUV size and unilamellarity [5]. The important works by Evans, Needham, and coworkers on the mechanical properties of lipid bilayers have for example been carried out by micropipette aspiration of spontaneously formed GUVs [11, 13, 14, 122]. Finally, larger amounts of suspended GUVs which, in addition, allow for high encapsulation efficiencies of any type of solute molecule can preferably be prepared by the methods that are based on initial w/o or w/o/w emulsions. Because the presence of residual oil in the obtained vesicle membranes is very likely, these GUV systems are, in turn, not suitable for the study of membrane properties and vesicle dynamics [5].

2.6 Mechanism and models of the vesicle extrusion process

Despite the extensive use of the extrusion technique (Sec. 2.5.3), the actual mechanism by which relatively large MLVs break up into smaller and predominantly unilamellar vesicles upon repetitive extrusion through narrow pore channels is only slowly being elucidated [15, 119, 208, 209, 242].

The straight-through pore channels of the track-etched polycarbonate membranes most commonly used for vesicle extrusion have a uniform, cylindrical shape [243, 244]. They are relatively long (6–10 µm) and narrow with the well-defined mean pore diameter typically ranging from 30 to 400 nm [3, 9, 15, 193, 209]. It is clear that forcing an order of magnitude larger MLV into such a nanopore channel must lead to a process of membrane rupture and resealing along the channel which then results in the observed reduction in vesicle size and lamellarity [208]. A thorough understanding of this process and of the influence of different process and material parameters on the vesicles generated has been the objective of the studies listed above. Ultimately, three models have been proposed to describe the process of vesicle extrusion and to predict the final vesicle size given the influencing parameters of the extrusion system [15, 119, 242]. They are all based on bilayered phospholipid vesicles.

2.6.1 Model for shear-dependent vesicle breakup inside the pore channel or at the pore exit

The first consideration about a possible mechanism for LUV formation by the extrusion technique has been theoretically described by Clerc and Thompson (1994) [242]. They proposed a shear-induced breakup of long phospholipid bilayer cylinders inside the pore channel or at the pore exit based on the Rayleigh instability.

The derived model only predicts the dependency of the final vesicle radius (R_V) on the pore radius (R_P) following $R_\mathrm{V} = \pi^{1/2} R_\mathrm{P}$ and does not quantitatively account for different extrusion conditions. However, since the shear-induced breakup of a given vesicle membrane in the pore depends on the velocity of the vesicle suspension through the pore channel, Clerc an Thompson suggested that the final vesicle size is also influenced by the flow rate of the suspension resulting from the applied extrusion pressure.

In general, the model by Clerc and Thompson predicts a final vesicle size larger than observed in subsequent systematic extrusion experiments [15, 208, 209].

2.6.2 Systematic experimental studies on vesicle extrusion

The predominant flow rate dependency of the final vesicle size obtained by repetitive vesicle extrusion through a given pore diameter as suggested by Clerc and Thompson [242] was not confirmed in subsequent numerical and experimental extrusion studies. This was evaluated by doubling the length of a pore channel, i. e. reducing the pore flow rate by half, while keeping the extrusion pressure constant. The experiments showed no significant change in the final vesicle sizes generated at the varying pore flow rates in the case of relatively low extrusion pressures applied ($\lesssim 7\,\mathrm{bar}$ for $R_\mathrm{P} = 50\,\mathrm{nm}$) [119, 209].

Instead, the average size of extruded vesicles was found to depend on the extrusion pressure, particularly in the low pressure range evaluated in the flow rate studies mentioned above. Generally, the final vesicle size decreases as the applied extrusion pressure increases for all pore diameters commonly used in vesicle extrusion (evaluated range: 50–200 nm) [15, 119, 208, 209]. Furthermore, there is a minimum pressure related to the lysis tension of the vesicle membrane below which the vesicles cannot be extruded successfully [209].

These detailed experimental studies of the effects of the various extrusion parameters on vesicle size as reported by Frisken and coworkers have led to the formulation of the following pressure-dependent extrusion models.

2.6.3 Static model for pressure-dependent vesicle breakup at the pore entrance

Based on their finding that the average size of sequentially extruded vesicles depends on the applied extrusion pressure rather than on the induced pore flow rate [208, 209], Frisken and coworkers proposed a pressure-dependent breakup mechanism of large vesicles at the entrance of the pore channels as follows (see Fig. 2.11A). A to be extruded vesicle in suspension, i. e. at rest and at equilibrium, is characterized by a quasispherical shape, constant internal volume, practically zero membrane tension, and finite bilayer membrane expansibility (Secs. 2.3.3 and 2.3.5). As, during the initial extrusion passages, a large vesicle is pushed almost quasistatically into the narrow pore channel, the area of the vesicle membrane expands and a membrane tension σ is induced (Fig. 2.11A). If the pressure difference $\Delta P = P_1 - P_0$ applied across the entering vesicle is large enough, the induced membrane tension exceeds the lysis tension σ_l of the vesicle membrane. Consequently, the vesicle bursts at the neck of the cylindrical channel, thereby reducing its volume and entering the pore.

Patty and Frisken described this initial entry of a large vesicle into the pore channel using the analogy of blowing a bilayer bubble into a small circular opening ("bubble blowing model" 2003) [15]. This static description suggests an axisymmetric rupture of the entering vesicle at the pore opening such that the cylindrical bilayer portion in the pore entrance separates from the main vesicle (Fig. 2.11A) and proceeds through the channel in the form of a spherocylindrical vesicle (Fig. 2.11B).
The derived model predicts the dependency of the final vesicle radius (R_V) on

  (i) the pore radius R_P used,

 (ii) the applied extrusion pressure ΔP, and

(iii) the lysis tension σ_l of the vesicle membranes being extruded

according to the relation:

$$R_V \sim \sqrt{\frac{R_P \sigma_l}{2\Delta P}} \tag{2.6}$$

The bubble blowing model successfully fits experimental data for repetitive extrusion of large vesicle precursors with lysis tensions ranging from 2.9 to 9.4 mN/m (e. g. ceramide-doped, plain, and cholesterol-doped POPC vesicles) through pore diameters of 50 to 100 nm applying extrusion pressures of roughly 1.5 to 25 bar [15]. However, the model is not consistent with data for vesicles sequentially extruded through 200 nm pore membranes. Furthermore, it is not valid in the limit of the final extrusion passages where the vesicle size approaches the diameter of the pore and the vesicles slip in and out of the pore channels without breaking. The reason for this is that the bubble blowing model is based on a static description of the initial passages of vesicle extrusion which does not fully reflect the physics of the repetitive extrusion process.
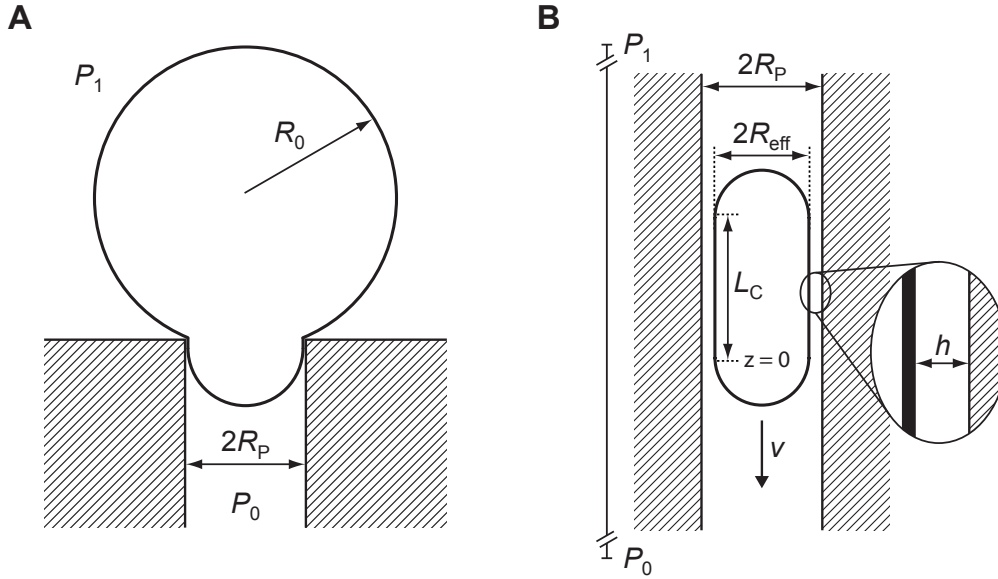
Figure 2.11: Mechanism of repetitive vesicle extrusion. Idealized schematic diagram of (A) the initial passages and (B) the final passages of vesicles through cylindrical pore channels in the repetitive extrusion process. (A) Large vesicle of initial radius R_0 being pulled into the cylindrical pore of radius R_P under a pressure difference $\Delta P = P_1 - P_0$ applied across the entering vesicle. (B) Spherocylindrical vesicle flowing through the cylindrical pore channel of radius R_P under a pressure difference $\Delta P = P_1 - P_0$ applied across the channel. The vesicle moves at a velocity v and is separated from the channel wall by a lubrication layer of thickness h. The spherocylinder has a cylinder length L_C and an endcap radius R_{eff}. Adapted from Hunter and Frisken [208] and Bruinsma [245].

2.6.4 Dynamic model for pressure-dependent vesicle breakup at the pore entrance

To date, the most complete description of the process of repetitive vesicle extrusion through nanopore channels is provided by the recent study by Bertrand and Joós (2012) [119]. It includes a flow model and molecular dynamics simulations to further exploit the behavior of vesicles flowing through the pore channels.

The proposed model builds on the pressure-dependent breakup mechanism of large vesicles at the pore entrance as introduced by Frisken and coworkers [15, 208, 209] and described in the previous section (Sec. 2.6.3 and Fig. 2.11A). However, in contrast to the static bubble blowing model developed by Patty and Frisken [15], the flow model by Bertrand and Joós is based on a dynamic, i.e. rheological, description of the final pore passages of vesicles in the repetitive extrusion procedure [119]. It is composed of (A) a simple geometrical argument and (B) elements of a previous theory for spherocylindrical vesicles flowing through narrow channels developed by Bruinsma [245].

(A) Geometric argument: Area and volume constraints. During the final extrusion passages, the vesicles characterized by predominant unilamellarity, constant internal volume, and finite bilayer expansibility (Secs. 2.3.3 and 2.3.5) flow in and out of the pore channels of a given mean diameter without rupturing. Thereby, their shape is assumed to transform back and forth from a relaxed quasisphere outside of the channel to a stretched spherocylinder inside (Fig. 2.11B). Due to the larger surface area of the spherocylinder compared to the quasisphere of equal volume, a membrane tension σ is induced in the vesicles as they enter the pore channel, i.e. as their membrane area expands. Consequently, the final vesicle size resulting from repetitive extrusion corresponds, to a first approximation, to the critical vesicle size above which the vesicle membrane can not tolerate this area difference and ruptures. Remember that vesicle rupture occurs at the lysis tension σ_l of its bilayer membrane induced by the critical bilayer area expansion α_{crit} (Sec. 2.3.5).

These considerations were developed into a simple geometrical argument comprised in the flow model by Bertrand and Joós. It already gives an estimation of the final size of repetitively extruded vesicles for a given pore radius R_{P} used and for the critical area expansion α_{crit} of the vesicle membranes being extruded [119].

(B) Flow of vesicles in a cylindrical pore channel: To account for the pressure dependency of the final vesicle size, Bertrand and Joós combined their geometrical argument with elements of Bruinsma's description for the flow of spherocylindrical vesicles through narrow, cylindrical channels [245] (see also the studies by Frisken and coworkers for a summary of Bruinsma's theory in relation to vesicle extrusion [208, 209]). Figure 2.11B schematically shows a spherocylindrical vesicle flowing through a cylindrical pore channel which corresponds to the assumed situation of the final extrusion passages. The key variables of Bruinsma's analytical flow description are indicated in the scheme.

The vesicle moves through the pore channel of radius R_{P} at a velocity v. A lubrication layer of thickness h separates the vesicle surface from the channel wall so that the vesicle essentially travels through a channel of effective radius R_{eff}:

$$R_{\mathrm{eff}} = R_{\mathrm{P}} - h \tag{2.7}$$

The thickness of the lubrication layer h increases with increasing vesicle velocity v which then further decreases the effective pore radius R_{eff}. Bruinsma has given the following expression for the estimation of the lubrication layer thickness h as a function of v [245]:

$$h(v) \cong 2.05 R_{\mathrm{P}} \left(\frac{\eta_{\mathrm{ext}} v}{\sigma} \right)^{2/3} \tag{2.8}$$

where η_{ext} is the viscosity of the external fluid.
As for the membrane tension σ of the spherocylindrical vesicle bilayer, Bruinsma

shows that an additional membrane tension is induced by viscous stresses as the vesicle flows through the pore. This results in a tension profile along the vesicle axis (z-coordinate) following [245]:

$$\sigma(z) = \sigma(z_0) - \frac{\eta_{\text{ext}}v}{h(v)}z \tag{2.9}$$

where $\sigma(z_0)$ is the membrane tension at the frontal endcap of the spherocylinder (at $z = 0$; see Fig. 2.11B). This predicts a linear decrease of the membrane tension along the cylindrical lubrication region from front to back.

Finally, Bruinsma found that the flow rate Q of spherocylindrical vesicles through a narrow pore channel resulting from the applied pressure difference obeys Darcy's law. The standard form of Darcy's law describes the laminar flow of a viscous fluid through a cylindrical channel by:

$$\eta Q = K\left(\frac{\Delta P}{\Delta L}\right) \tag{2.10}$$

where η is the fluid viscosity, Q the volume flow rate, K the permeability of the channel, ΔP the pressure difference applied across the channel, and ΔL the channel length. In the case of vesicle extrusion, ΔL corresponds to the length of the pore channel L_{P}. For the flow of a homogeneous fluid through a cylindrical pore channel, the permeability K is a purely geometrical factor given by $K = \pi R_{\text{P}}^4/8$ [208, 209]. The presence of vesicles in the fluid leads to viscous dissipation as the vesicles are pushed through the channel. Therefore, Bruinsma argues that each vesicle traveling in the channel at a given time reduces the pressure difference ΔP across the entire channel which leads to an effective channel permeability [245]:

$$K_{\text{eff}} = \frac{\pi R_{\text{P}}^4}{8 + 0.233(nL_{\text{C}})(L_{\text{C}}/R_{\text{eff}})^2} \tag{2.11}$$

where $n = N/L_{\text{P}}$ is the number of vesicles N per unit length in the pore channel and L_{C} the length of the cylindrical portion of the spherocylindrical vesicle. Hence, the channel permeability is no longer purely geometrical, but depends on the number density of vesicles inside the channel which is determined by the amphiphile concentration of the vesicle suspension.

Complete dynamic extrusion model: Extending the simple geometrical argument (A) with the elements of Bruinsma's flow description of spherocylindrical vesicles in a pore channel (B) yields the complete dynamic extrusion model developed by Bertrand and Joós [119].

The model predicts the average final size of repetitively extruded vesicles given

  (i) the pore radius R_{P} and

(ii) the length L_P of the pore channels used,

(iii) the applied extrusion pressure ΔP, and

(iv) the lysis tension σ_l and related approximate critical area expansion α_crit of the vesicle membranes being extruded.

Fitting this model to experimental data of vesicles repetitively extruded through pore diameters ranging from 50 to 100 nm (from Patty and Frisken [15]) showed good agreement between the predicted and experimental values, except for the lowest extrusion pressures applied. In addition, the flow model was systematically applied to a wider range of extrusion parameters compared to that evaluated in the previous experimental extrusion studies by Frisken and coworkers[15, 208, 209].

Combining the results from these earlier experimental studies and from the flow model of Bertrand and Joós [119], including their molecular dynamics results, leads to the following current conclusions about the **dependency of the final vesicle size on different extrusion parameters**.

Pore diameter $2R_\text{P}$: The pore size used is the primary determinant for the average final size of vesicles produced by the repetitive extrusion technique. Due to the volume conservation and finite membrane expansibility characteristic to vesicle structures, the pore entrance imposes a geometrical constraint on the vesicles as they are forced through the channel. Smaller pore diameters induce larger area expansions in the entering vesicle membranes as they transform from a quasispherical shape outside the channels to a spherocylindrical shape inside during the final extrusion passages. For a given bilayer composition, this results in smaller critical, i. e. final, sizes of vesicles that are able to slip in and out of the channels without rupturing [119].

Lysis tension σ_l: The lysis tension of a vesicle membrane is characteristic to its bilayer composition and measures the tensile strength of the membrane (Sec. 2.3.5). Tougher vesicle membranes tolerate larger area expansions before rupturing. This explains the increased final size of vesicles exhibiting higher lysis tensions and prepared by repetitive extrusion at otherwise constant extrusion conditions [15, 128].

Extrusion pressure ΔP: Increasing pressure differences ΔP applied across a given pore geometry leads to higher flow rates Q (Eq. 2.10) and, hence, higher velocities v of the spherocylindrical vesicles traveling inside the pore channels during the final extrusion passages (Fig. 2.11B). This results in a thickening of the velocity-dependent lubrication layer $h(v)$ surrounding the vesicles as they flow through the pores (Eq. 2.8). Consequently, the effective diameter $2R_\text{eff}$ available for the vesicles to move through the channels diminishes (Eq. 2.7) and the final vesicle size decreases due to the geometrical constraints described above [119].

Pore length L_P: The vesicle flow rate inside the pore channel can also be varied through the length of the pore channel L_P while keeping the applied pressure difference ΔP constant (Eq. 2.10). As mentioned earlier, the final vesicle size was found

not to depend on the pore flow rate for relatively low extrusion pressures applied ($\lesssim 7$ bar for $R_\text{P} = 50$ nm) [119, 209]. However, the flow model of Bertrand and Joós predicts that, at higher extrusion pressures, the final mean vesicle size significantly decreases with increasing pore flow rate (or decreasing channel length at constant ΔP) [119]. This can be attributed to the membrane tension induced in the vesicle bilayer during its flow through the pore channel as described by Bruinsma (Eq. 2.9) [245] and confirmed by the molecular dynamics simulations of Bertrand and Joós [119]. Indeed, their simulation results revealed a frequent rupture of spherocylindrical vesicles near the critical size inside the channel. This shear-induced rupture always occurred just behind the frontal endcap where the membrane tension along the vesicle axis was found to be maximal [119].

The effect of the shear-induced membrane tension on the final vesicle size adds up to the effect of the velocity-dependent lubrication layer as they both originate from the vesicle flow rate in the pore channel.

Amphiphile concentration c: A slight variation in the vesicle flow rate inside the pore channels results also from variations in amphiphile concentration of the vesicle suspension being extruded. A higher amphiphile concentration leads to a greater number density of vesicles per channel which reduces the pore flow rate (Eq. 2.11). In this case, the lubrication layer thickness decreases and the average vesicle size produced is slightly increased as observed by Frisken and coworkers [209] and predicted by the flow model of Bertrand and Joós [119].

2.7 Analysis of submicrometer-sized vesicles

2.7.1 Scattering techniques

Scattering techniques, such as light, neutron, and X-ray scattering, are essential tools for the structural characterization of a material in the submicrometer size range. The basic principle of all scattering experiments is schematically shown in Figure 2.12. It consists of a monochromatic incident beam of single wavelength λ that is scattered by the sample. The intensity of the scattered radiation is measured as a function of the scattering angle θ with respect to the transmitted beam. The most important variable of scattering experiments is the scattering vector $\boldsymbol{q}$ whose magnitude is then given by [246]:

$$q = \frac{4\pi \sin(\frac{\theta}{2})}{\lambda} \tag{2.12}$$
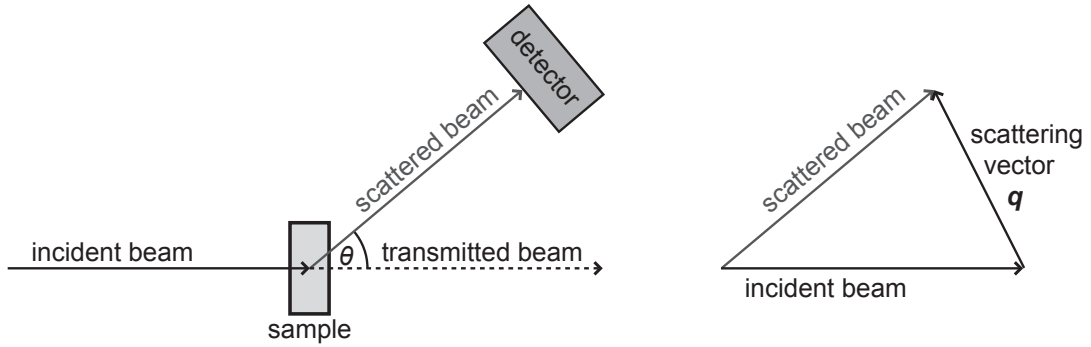
Figure 2.12: Principle of scattering techniques. An incident beam of single wavelength λ is scattered by the sample and the scattered beam is detected at the scattering angle θ relative to the transmitted beam. Adapted from Richardson [246].

Dynamic light scattering (DLS)

Dynamic light scattering (DLS) is also known as quasi-elastic light scattering (QELS) or photon correlation spectroscopy (PCS). It is extensively used to estimate the mean diameter and size distribution of submicrometer-sized vesicles because it involves simple sample preparation, the measurement is non-invasive, and time for analysis is relatively short [195, 217, 247–252]. DLS instruments basically measure the diffusion coefficient of colloidal particles in solution undergoing Brownian motion and relate this to particle size. Detailed descriptions of the PCS technique can be found in the literature [253–255].

Theory of dynamic light scattering: Autocorrelation function. In a typical DLS setup, a defined sample volume is illuminated by an incident laser beam that is scattered by the dispersed particles. Due to the continuous Brownian motion of the dispersed particles, the intensity of the scattered light detected at the scattering angle θ will fluctuate over time (Fig. 2.12). Analysis of these time-dependent intensity fluctuations provides information on particle motion and ultimately particle size. This information is extracted from the time autocorrelation function of the scattered light intensity as constructed by a digital autocorrelator. For a given delay time τ, the normalized intensity–intensity time autocorrelation function is given by [255]

$$g^{(2)}(\tau) = \frac{\langle I(t)I(t+\tau)\rangle}{\langle I(t)\rangle^2},\tag{2.13}$$

where $I(t)$ and $I(t + \tau)$ are the intensities of the scattered light measured at times t and $t + \tau$, respectively, and the symbol $\langle...\rangle$ indicates averaging of the enclosed quantity over t. The second order intensity–intensity time autocorrelation function

$g^{(2)}(\tau)$ (Eq. 2.13) can also be expressed in terms of the first order time autocorrelation function of the scattered electric field $g^{(1)}(\tau)$ using the so-called Siegert relation [256]:

$$g^{(2)}(\tau) = B + \beta[g^{(1)}(\tau)]^2. \tag{2.14}$$

In Eq. 2.14 the factor β is an optical constant that depends on the experimental geometry, while the parameter B is the long-time value of $g^{(2)}(\tau)$, commonly referred to as the baseline of the correlation function. The correlation function decreases with increasing delay time τ and approaches the constant background value B as correlation is lost. The decay rate Γ of correlation is higher, the faster the dispersed particles move, i.e. the smaller the particles are.

Monodisperse systems: For monodisperse particles in Brownian motion the field–field time autocorrelation function can be described by a single exponential decaying function $g^{(1)}(\tau) = \exp(-\Gamma\tau)$. The translational diffusion coefficient of the particles D is then obtained from the derived decay rate Γ [257]

$$\Gamma = Dq^2, \tag{2.15}$$

where q is the magnitude of the scattering wave vector $\boldsymbol{q}$ (Fig. 2.12) given by

$$q = \frac{4\pi n \sin\left(\frac{\theta}{2}\right)}{\lambda_0}. \tag{2.16}$$

Here, n represents the refractive index of the solvent and λ_0 is the wavelength of the laser in vacuum.

Finally, the measured diffusion coefficient D can be translated into a hydrodynamic radius R_h using the Stokes-Einstein relation which assumes that particles are spherical, non-interacting and have smooth surfaces [257]:

$$D = \frac{k_{\mathrm{B}}T}{6\pi\eta R_h}, \tag{2.17}$$

where k_{B} is Boltzmann's constant, T is the absolute temperature, and η is the dynamic viscosity of the suspension liquid.

Polydisperse systems: In most cases, samples are polydisperse and $g^{(1)}(\tau)$ can no longer be treated as a single exponential but must be generalized to a sum or an integral over a distribution function $G(\Gamma)$ of decay rates Γ corresponding to each of the particle species in the population. $g^{(1)}(\tau)$ is then represented as the Laplace transform of the distribution function $G(\Gamma)$ [254]:

$$g^{(1)}(\tau) = \int_0^\infty G(\Gamma)\exp(-\Gamma\tau)\mathrm{d}\Gamma. \tag{2.18}$$

Recovering $G(\Gamma)$ from $g^{(1)}(\tau)$ using DLS data, either analytically or numerically, is a very complex task, especially with regard to the noise associated with the data [258].

Method of cumulants: One commonly employed method to characterize $G(\Gamma)$ consists of fitting the measured autocorrelation function $g^{(1)}(\tau)$ using the cumulant expansion first described by Koppel (1972) [259] and revisited by Frisken (2001) for data analysis of polydisperse vesicle samples [250]. Unless stated otherwise, the method of cumulants was used to analyze DLS data of vesicle suspensions collected in this thesis. It is based on expanding the logarithm of the field–field autocorrelation function $g^{(1)}(\tau)$ in terms of the cumulants $\kappa_m(\Gamma)$ of the distribution giving a polynomial in the delay time τ:

$$\ln[g^{(1)}(\tau)] = -\bar{\Gamma}\tau + \frac{\kappa_2}{2!}\tau^2 - \frac{\kappa_3}{3!}\tau^3 + \frac{\kappa_4}{4!}\tau^4 - \cdots . \tag{2.19}$$

The first cumulant describes the average decay rate $\kappa_1(\Gamma) = \bar{\Gamma}$ and yields the average diffusion coefficient $\bar{D} = \bar{\Gamma}/q^2$ from Eqs. 2.15 and 2.12. The mean hydrodynamic radius R_h of the polydisperse sample can then be derived from $\bar{D}$ using the Stokes-Einstein expression (Eq. 2.17). The second cumulant is identical to the second moment about the mean $(\kappa_2(\Gamma) = \mu_2)$ and corresponds to the variance of the distribution of decay rates. The normalized second cumulant, commonly referred to as polydispersity index *PDI*, is a useful measure to describe the relative width of the size distribution. It is calculated on basis of the first and second cumulants $\bar{\Gamma}$ and μ_2, respectively:

$$PDI = \frac{\mu_2}{\bar{\Gamma}^2}. \tag{2.20}$$

PDI values of 0.02 or less are generally obtained for nearly monodisperse or monodisperse, clean preparations [253].

The method of cumulants is appropriate only for small delay times τ and monomodal $G(\Gamma)$, but yields reliable results for a $PDI \leq 0.3$ [250, 254]. The validity of cumulant analysis has been demonstrated by scattering from both known mixtures of monodisperse polystyrene latex spheres and from defined LUVET$_{100}$, VET$_{200}$ and VET$_{400}$ suspensions [217, 250, 257]. It is not recommended to use parameters beyond μ_3, because over-fitting of data with many parameters in a power-series expansion will render all the parameters, including $\bar{\Gamma}$ and μ_2, less precise [254]. Frisken [209] has shown that the use of μ_3 has not changed the values of the other parameters significantly in the fits of different versions of the cumulant function evaluated for data analysis of extruded vesicle suspensions.

In this work, the cumulant function with terms up to the second moment about the mean μ_2 was directly fitted to the data of the intensity–intensity autocorrelation

function $g^{(2)}(\tau)$. Using the Siegert relation (Eq. 2.14) and replacing the second cumulant $\kappa_2(\Gamma)$ by the second moment about the mean μ_2, the basic cumulant function (Eq. 2.19) can be written as

$$g^{(2)}(\tau) = B + \beta \exp(-2\bar{\Gamma}\tau + \mu_2\tau^2), \qquad (2.21)$$

where B, β, $\bar{\Gamma}$ and μ_2 are fitting parameters.

The cumulant expansion has the advantage of providing information on $G(\Gamma)$ in terms of $\bar{\Gamma}$ and μ_2 without *a priori* knowing the form of $G(\Gamma)$. On the other hand, it does not give information on the shape of the size distribution without having to assume a functional form of $G(\Gamma)$, such as lognormal, 2-exponential, Gaussian and Schulz distributions [252–254]. According to Patty and Frisken (2006) [252], the asymmetric Schulz distribution provides a good estimate of the number-weighted size distribution of extruded vesicles. If the form of the distribution function $G(\Gamma)$ is known to be bimodal or broad unimodal, it is more appropriate to analyze DLS data by direct numerical inversion of the autocorrelation function using inverse Laplace transform algorithms [217, 258], such as the non-negatively constraint least square (NNLS) analysis [247, 260], exponential sampling [261], or the Provencher algorithm, also known as CONTIN [128, 262].

Advantages and limitations of particle sizing by DLS: It has to be noted that hydrodynamic diameters D_h and *PDI* values extracted from light scattering data are intensity-weighted averages that scale with the particle radius to the power of six (r^6) [263]. Therefore, particle sizing by DLS is very sensitive to the presence of large particles, i. a. dust, which predominate the scattering patterns. Intensity-weighted averages can be converted to volume-weighted averages (scaling with r^3) using the Mie theory [264, 265], if the refractive index of the particle is known. This conversion is, however, only applicable for solid spheres with a homogeneous density, a requirement which is not fulfilled for the geometry of vesicles. In the latter case, a coated sphere model with identical refractive indices of lumen and medium would be more appropriate [247, 266].

Particles with diameters significantly smaller than the wavelength of the illuminating laser (typcially less than $d = \lambda_0/10$) show an isotropic scattering pattern (Rayleigh theory) and can be well characterized by single-angle DLS measurements. In contrast, the scattering function of larger particles with diameters in the range of the wavelength of the incident beam shows an angular dependence characteristic to particle size (Mie theory) and DLS results become dependent on the detector position with respect to the scattering angle θ [217].

Since DLS measures the diffusion coefficient D and not the particle diameter, the determination of Stokes-Einstein diameters (Eq. 2.17) can be distorted by attractive and repulsive particle interactions, which become stronger with increasing particle

concentration. Another concentration effect is multiple scattering occurring at relatively high particle concentrations and leading to a faster dacay of $g^{(2)}(\tau)$ than that predicted by the Brownian motion of dispersed particles. This results in an underestimation of particle size and is the reason for perfomring DLS experiments on diluted samples [257].

Although the limitations of DLS in terms of model-dependent distribution characterization, limited shape information, intensity-weighted results, and data analysis for broad size distributions are apparent, it remains a useful technique for comparing different samples on a relative size scale provided all measuring conditions, such as particle concentration, scattering angle, and nature of dispersing agent, are kept constant.

Small angle neutron scattering (SANS)

Small angle neutron scattering (SANS) is a powerful technique for the *in-situ* characterization of the structure and dynamics of self-assembled supramolecular aggregates, including lipid membranes. Model-based analysis of SANS data yields quantitative information on the distribution of structural features, their sizes, shapes and correlation lengths in a range of $\sim$ 1-1000 nm [246, 267].

For unilamellar and multilamellar vesicles, typical structural parameters obtained from SANS measurements include mean size, size distribution, and multilamellarity parameters of the vesicle population. Furthermore a number of structure and material parameters can be derived on the level of the bilayer membrane, such as the lamellar repeat distance, bilayer thickness, molecular surface area, thicknesses of the bilayer polar and hydrophobic regions, area compressibility, and the degree of hydration of the lipid headgroup [219, 268–273].

In contrast to light and X-rays, neutrons are scattered by protons in the atomic nucleus rather than by electrons surrounding the nuclei. Therefore, SANS is independent on the atomic number of elements and, thus, well suited for the study of soft and biological materials which are inherently rich in light elements.

In addition, neutron scattering cross sections do not only change from element to element, but can also differ between the element's isotopes, giving SANS a remarkably different sensitivity to hydrogen and its isotope, deuterium. This unique scattering behavior of neutrons allows to separate and enhance the scattering contributions of e. g. bilayer components of interest by specific deuteration of lipid constituents and/or variation of the H_2O/D_2O ratio in the solvent under minimal perturbation of the host membrane. The extra information obtained from such contrast variation experiments allows, for example, to improve the validity of phospholipid structural parameters [274, 275] and to assess lateral heterogeneity and domain formation in model membranes [276, 277].

While X-rays can be generated for every day use in the laboratory, even though at

orders of magnitude smaller intensities than those from a synchrotron source, neutrons in adequate quantities for SANS experiments are exclusively available from central reactor or spallation sources [246]. Due to the limited access to beamtime at such large-scale facilities, SANS is not suitable for routine sample analysis. Instead, the valuable information on aggregate morphologies, sizes and size distributions obtained from SANS measurements is restricted to a few selected and representative samples.

2.7.2 TNBS assay for external vesicle surface area determination

The TNBS assay as optimized in the frame of this thesis and published in *Analytical Biochemistry* 442, 262-271 (2013) is a simple and reliable chemical assay to quantify the proportion of phospholipids present in the outermost monolayer of lipid vesicles [10]. It gives an average value for the relative external surface area E of a liposome suspension which is a practical estimate for its degree of lamellarity.

Estimation of liposome lamellarity via determination of the relative external surface area: The relative external surface area E (or proportion of phospholipids constituting the outermost monolayer) of lipid vesicles can be measured by several chemical assays [140, 204, 218, 278–280], including the TNBS assay [10, 204]. They all use a particular marker lipid that is embedded in the liposomal bilayers during their preparation. The marker lipids exposed in the outermost monolayer of the vesicles are then quantified by reaction with a specific externally added reagent and by recording the concomitant spectroscopic signal change. Normalization of this signal change to that caused by reaction of all marker lipids present in the liposomal analyte suspension (100% signal) gives the relative external surface area E [140].
For unilamellar vesicles comprising a single bilayer membrane and having a diameter of $\gtrsim 100$ nm (LUVs), E is approximately 50%. Even higher E values ($> 50\%$) are typically found in small unilamellar vesicles with diameters below 100 nm (SUVs) because of the asymmetric lipid distribution across their highly curved bilayer membranes. For multilamellar vesicles (MLV), E is lower than 50% and decreases with increasing degree of multilamellarity [140].

Principle of the TNBS assay: In the TNBS assay, the marker lipid is simply a naturally occurring aminolipid, usually phosphatidylethanolamine (PE), and the external reagent is TNBS (2,4,6-trinotrobenzene sulfonate) as schematically shown in Figure 2.13 [10].
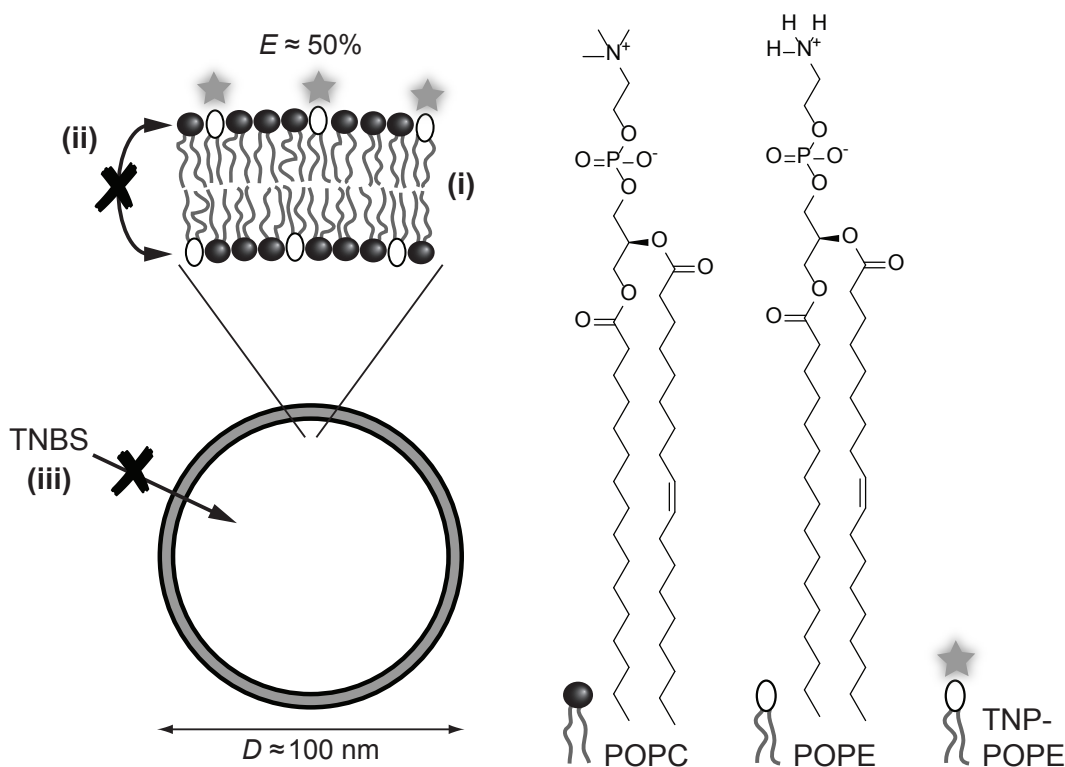
Figure 2.13: Principle of the TNBS assay for external vesicle surface determination using POPE as marker lipid in a POPC host membrane. The extent of outer lipid labeling is proportional to the UV/Vis absorbance increase at $\lambda_{\mathrm{max}} = 344\,\mathrm{nm}$ upon reaction of the primary amine of exposed POPE headgroups with externally added TNBS yielding trinitrophenyl-POPE (TNP-POPE). The assay relies on (i) an even distribution of marker lipids throughout all bilayer leaflets of MLVs and LUVs and on negligible rates of (ii) marker lipid flip-flop and (iii) reagent permeation across the vesicle membranes.

The primary amine of an exposed PE headgroup reacts in its nucleophilic, non-protonated form with externally added TNBS yielding a colored, trinitrophenyl (TNP)-labeled product with an absorption maximum at $\lambda_{\mathrm{max}} = 344\,\mathrm{nm}$ [281, 282]. Under suitable assay conditions, the amount of TNP-labeled PE formed in an intact and Triton-solubilized vesicle sample, respectively, is proportional to the UV/Vis absorbance increase at $\lambda_{\mathrm{max}} = 344\,\mathrm{nm}$, which allows for the direct determination of E [10].

For mechanistic details of the trinitrophenylation reaction and their translation into an optimum TNBS assay protocol for external vesicle surface area determination, the reader is referred to our publication in [10]. The derived protocol as applied in this thesis is also described in the Materials and Methods part of Chapter 4 (Sec. 4.2.6). Compared with earlier versions of the TNBS assay [140, 204, 283], our optimized protocol consumes considerably less marker lipids and reduces the amount

of samples to be prepared and measured, while the accuracy is maintained or even improved.

Accuracy and applicability of the TNBS assay: The results obtained from the chemical assays introduced above, including the TNBS assay, reflect true external vesicle surface area only if the following criteria are fulfilled (see also Fig. 2.13 for criteria (i–iii)) [10]:

  (i) Even distribution of the marker lipids throughout all bilayers of the liposomal analyte suspension [204].

 (ii) Negligible transbilayer diffusion (flip-flop) of marker lipids during the incubation time of reaction [204].

(iii) Negligible membrane permeability of the externally added reagent during the time of analysis [204].

 (iv) Proper consideration of a possible background reaction of the reagent [10].

  (v) Equal extent of marker lipid modification in the outer surface of intact vesicles and in mixed micelles formed on vesicle solubilization with detergent to obtain the 100% signal from all marker lipids present in the sample [204].

With respect to criterion (i), different marker lipids are known to be randomly distributed between the two monolayers of the bilayer(s) in LUVs and MLVs, especially when taking them through freeze-–thaw cycles during their preparation (Sec. 2.5.2) [204, 205, 284, 285]. However, geometric packing constraints in the highly curved bilayers of SUVs typically lead to asymmetric lipid distributions in mixed lipid SUVs with a preferential partitioning of phospholipids with small headgroup volumes in the inner monolayer [149, 284]. For this reason, marker lipids have been observed to distribute nonrandomly between the outer and inner membrane surfaces of SUVs. No reliable results are obtained for such SUVs if external surface quantification is based on the chemical quantification of marker lipids [204, 218].

During the development of our optimized TNBS assay, we evaluated the five criteria listed above and showed that they were all fulfilled when applying the proposed protocol to well-defined vesicles (VETs$_{100-400}$) prepared from POPC/Chol/POPE 65:30:5 (mol/mol). In these reference vesicles, the presence of cholesterol in the bilayer membranes ensures negligible rates of both PE flip-flop (criterion (ii)) and TNBS permeation (criterion (iii)) across the vesicle membranes during time of analysis (see Sec. 2.4.3 for the effects of cholesterol on bilayer properties) [95, 107, 170, 172]. Accurate external surface area results can also be obtained for cholesterol-free lipid vesicles if their membrane fluidity is decreased simply by slightly increasing the PE content, e. g. to POPC/POPE 91:9 (mol/mol). Finally, the optimized TNBS assay can successfully be applied to plain liposomes prepared from commercial egg PC isolates which typically retain a large enough fraction of egg PE ($\approx 9\,\text{mol}\%$ in the egg

PC product used in this thesis; Tab. 4.1) [10]. With no need of incorporating extra marker lipids, natural egg PC isolates offer an inexpensive and easy-to-use model system for the development and control of new liposome processing technologies as implemented in this work (Chapter 4).

Advantages and limitations of the TNBS assay and related chemical assays:
It must be noted that, in contrast to SANS and electron microscopy techniques, external surface area measurements do not provide absolute quantities regarding the average number of lamellae in a liposome preparation. The weight of internal lipids is the same for a vesicle with a few lamellae closely associated with the outside bilayer as for a vesicle comprising a larger number of lamellae in its center.
On the other hand, the analysis of external vesicle surface areas involves simpler technologies that are less invasive, less costly in terms of labor and equipment, and available on a daily basis. These are important advantages for a systematic evaluation of vesicle samples during the development and optimization of vesicle preparation protocols, liposome formulations, and processing technologies. External surface area assays allow monitoring of vesicle integrity and provide comparative and representative average values for the degree of lamellarity of vesicles generated at varying process and material parameters.

3 Vesicles from food grade amphiphilic block copolymers

3.1 Introduction

Based on the long-standing goal to enhance drug efficacy and minimize adverse side effects in biomedical applications, vesicles have moved a long way from traditional pharmaceutical carriers to stimuli-responsive drug delivery vehicles with controlled release properties in terms of location, time, and dose [22–24]. While the *in vivo* performance of vesicular drug carriers is usually tested after intravenous injection [23], special vesicle formulations have also been developed for alveolar [35], transdermal [286, 287], and oral drug administration [35, 288, 289].

Yet, the promising strategies of 'smart', stimuli-responsive vesicles developed in the field of (oral) drug delivery have not been transferred to the design of personalized foods, which aim at improving human nutrition, preventing diseases, and promoting public health [290]. Following the concepts of 'smart' drug delivery vehicles [23, 289], vesicles have great potential to deliver nutrients and nutraceuticals to a target site of the gastrointestinal (GI) tract and control cargo release under particular stimuli conditions, thereby greatly increasing the absorption and bioavailability of the encapsulated agents.

Previous studies on the application of vesicles in foods have mainly reported on the use of traditional, unfunctionalized liposomes that release cargo by passive diffusion or in response to global environmental changes. Nevertheless, they have been shown to offer advantages e. g. in cheese manufacturing, food supplementation and fortification, flavor control, and food preservation [6, 41, 42].

The incorporation of vesicle carriers in a food matrix for specific and efficient oral delivery of encapsulated bioactive agents to the site of absorption is a challenging task. A prerequisite for the successful delivery via the ingested food product is the protection of the vesicle-entrapped compound in its active form from enzymatic and chemical degradation, as well as from temperature, ionic strength, and pH variations at all stages of food processing, transport, storage, and preparation. After food consumption, the vesicle structure should still be stable under the harsh conditions of the GI tract and show controlled release properties when reaching the target site to

confer high bioavailability to the bioactive ingredient [42, 288].

Polymersomes are particularly attractive to design stimuli-responsive, delivery-release carriers for the purpose described above. Due to the higher molecular weight of vesicle-forming amphiphilic block copolymers (BCP) compared to their naturally occurring lipid analogues, polymeric vesicle membranes tend to be thicker, tougher, and often less permeable than conventional lipid bilayers [12, 16, 67, 99]. As a consequence, polymer vesicles may have superior properties in terms of stability and load retention. Furthermore, the versatility of block copolymer chemistry, e. g. chemical composition, block length, hydrophilic to hydrophobic block ratio, and crosslinking, surpasses the design flexibility of lipid vesicles and allows to extensively tailor the polymer membrane properties to specific applications [4]. The successful assembly and controlled destabilization of a large number of stimuli-responsive polymersome formulations have been summarized in recent reviews within the biomedical field [22, 154, 157], whereas no such systems have been reported for food applications.

Aim: The motivation of this study is to assemble food grade polymersomes that can serve as templates for the encapsulation, protection, targeted delivery, and controlled release of nutritional and health supplements in functional or personalized foods.

Approach: To that end, a biocompatible and biodegradable amphiphilic diblock copolymer, namely poly(ethylene oxide)-*block*-poly(γ-methyl-ε-caprolactone) (PEO-*b*-PMCL), is considered for vesicle formation [52, 76, 291]. In contrast to PCL-based amphiphiles that have semicrystalline character in bulk [292], the hydrophobic PMCL block has a low glass transition temperature T_g of approximately $-60\,°C$ and, hence, is in an amorphous state at room temperature [136]. This allows the formation of self-assembly structures, including spherical and worm-like micelles, as well as vesicles, from PEO-*b*-PMCL of varying PMCL block molecular weights in water without excessive heating and without the use of a cosolvent, as demonstrated for the first time by Zupancich *et al.* (2006) [76].

Earlier efforts to generate self-assembled structures from PEO-*b*-PMCL in aqueous phase reported on the formation of spherical micelles only [293, 294]. Vesicle structures were obtained in a number of studies from dilute dispersions of semicrystalline PEO-*b*-PCL , however, their formation involved the use of cosolvents and/or heating above $T_g \approx 60\,°C$ [79, 291, 292]. The resulting PEO-*b*-PCL vesicles are typically rigid and leaky [292].

The ability of PEO-*b*-PMCL to form biocompatible and biodegradable fluid-phase vesicles under physiological conditions is a prerequisite to create edible polymersome carriers for sensitive food supplements. Recently, a full binary phase diagram of PEO-*b*-PMCL block copolymers in water has been published for varying hydrophobic PMCL block lengths across the whole concentration range from bulk polymer to dilute aqueous solution [52] (Fig. 2.5). Based on these data and on previous morphological studies of dilute PEO-*b*-PMCL dispersions in water [76, 295], we focus on dilute aqueous solutions of PEO-*b*-PMCL amphiphiles ($\leq 1\,w/w\%$) with a hy-

drophobic to hydrophilic block weight ratio (w_{PMCL}) larger than 0.8, as this favors the formation of vesicles (Fig. 2.5).

Outline: This chapter describes the ability of selected PEO-*b*-PMCL block copolymers (PEO$_{23}$-*b*-PMCL$_{50}$ with $w_{\mathrm{PMCL}} = 0.86$ and PEO$_{23}$-*b*-PMCL$_{63}$ with $w_{\mathrm{PMCL}} = 0.88$) to form vesicles in aqueous solution. Furthermore, the efficiency of the generated food grade polymersomes to encapsulate and retain a molecular cargo under undisturbed conditions, as well as their release properties under GI stress conditions are reported.

The spontaneous self-assembly of PEO-*b*-PMCL into vesicle structures is induced upon hydration of a dry polymer film in excess water at room temperature. Following thin film hydration, both 100 nm-sized large unilamellar vesicles (LUVETs$_{100}$) and micrometer-sized giant unilamellar vesicles (GUVs) are prepared using the common and highly reproducible methods of vesicle extrusion and electroformation, respectively. Dynamic light scattering (DLS) and light microscopy (LM) imaging are used to characterize the mean size and size distribution of the obtained LUVETs$_{100}$ and GUVs, respectively. The vesicle structure is further demonstrated by encapsulating hydrophilic molecules in the aqueous vesicle lumen. LUVETs$_{100}$ are loaded with a self-quenched fluorescent dye, calcein, and the permeability coefficient of the PEO-*b*-PMCL membrane towards calcein is determined under undisturbed storage conditions by monitoring the increase in fluorescence intensity with the efflux and dilution of calcein into the external medium. Accordingly, the release properties of PEO-*b*-PMCL LUVETs$_{100}$ in the presence of gastrointestinal bile salts are studied. To our knowledge, this is the first study to report on the release properties of PEO-*b*-PMCL vesicles and to quantitatively measure calcein permeability from polymersomes in general.

The behavior of the PEO-*b*-PMCL block copolymer throughout vesicle formation and the subsequent release studies is compared to that of the most widely studied vesicle forming phospholipid, POPC. This allows to discuss the obtained results in the context of the structure-property relationships of novel PEO-*b*-PMCL polymersomes and conventional lipid vesicles (Fig. 1.1).

3.2 Materials and methods

3.2.1 Materials

The phospholipid used was 1-palmitoyl-2-oleoyl-*sn*-glycero-3-phosphocholine (POPC; $> 99\%$; $25\,\mathrm{mg\,mL^{-1}}$ solution in chloroform) from Avanti Polar Lipids (Alabaster, AL, USA). The food grade, amphiphilic diblock copolymer poly(ethylene oxide)-*block*-poly(γ-methyl-ε-caprolactone) with the block lengths $\mathrm{PEO_{23}}$-*b*-$\mathrm{PMCL_{50}}$ ($\bar{M}_n = 7400$ $\mathrm{g\,mol^{-1}}$, $w_{\mathrm{PMCL}} = 0.86$) and $\mathrm{PEO_{23}}$-*b*-$\mathrm{PMCL_{63}}$ ($\bar{M}_n = 9050\,\mathrm{g\,mol^{-1}}$, $w_{\mathrm{PMCL}} = 0.88$) was synthesized and provided by our collaborator Jörg Braun (Department of Chemistry, Universtiy of Basel, Switzerland) [52, 76]. Figure 3.1 presents the molecular formula of $\mathrm{PEO_n}$-*b*-$\mathrm{PMCL_m}$, while the chemical structure of POPC is included in Table 4.3 (see Chapter 4).

All other solvents and chemicals, namely chloroform ($\geq 99.8\%$; stabilized with ethanol), diethyl ether ($\geq 99.8\%$), methanol ($\geq 99.8\%$), calcein disodium salt (2,4-bis-(*N,N*'-di(carboxymethyl) aminomethyl)fluorescein) disodium salt), sodium chloride (NaCl; $\geq 99.8\%$), sodium phosphate monobasic dihydrate ($\mathrm{NaH_2PO_4 \cdot 2H_20}$; $\geq 99.0\%$), sodium phosphate dibasic dihydrate ($\mathrm{Na_2HPO_4 \cdot 2H_20}$; $\geq 99.0\%$), 4-(2-hydroxyethyl)piperazine-1-ethanesulfonic acid (HEPES; $\geq 99.5\%$), ethylenediamine-tetraacetic acid (EDTA; $\geq 98.5\%$), Triton X-100 (simply called Triton in this work), bile salts ($\geq 95\%$), and Sepharose 4B, were of analytical grade and purchased from Sigma-Aldrich (Buchs, Switzerland). All aqueous solutions were prepared using ultrapure water from a Synergy water purification system (Merck Millipore, Billerica, MA, USA) and stored at $4\,°\mathrm{C}$.
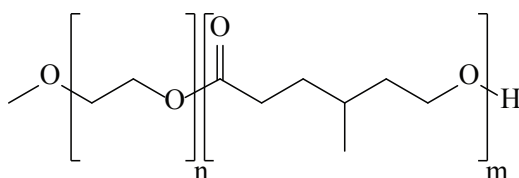
Figure 3.1: Chemical structure of the amphiphilic diblock copolymer PEO$_\mathbf{n}$-*b*-PMCL$_\mathbf{m}$. The subscripts n and m indicate the average number of monomer units in the hydrophilic PEO chain and in the hydrophobic PMCL chain, respectively.

3.2.2 Preparation of calcein-entrapped large unilamellar vesicles

For the bilayer permeability experiments, LUVETs$_{100}$ were prepared from POPC and $\mathrm{PEO_{23}}$-*b*-$\mathrm{PMCL_{63}}$, respectively, containing the fluorescent dye calcein at self-
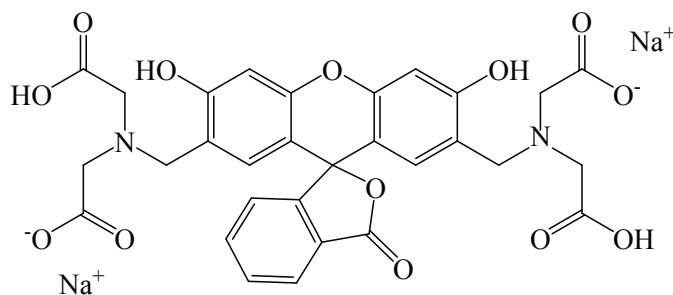
Figure 3.2: Structure and pH dependent valency of calcein. Chemical structure and pKa values of the fluorescent dye calcein with a disodium salt form as used in this study. Carboxyl pKa$_1$ = 2.1 and pKa$_2$ = 2.9; hydroxyl pKa$_3$ = 4.2 and pKa$_4$ = 5.5; methylimino pKa$_5$ = 10.8 and pKa$_6$ = 11.7 [297].

quenching concentration (80 mM) [296] (Fig. 3.2 and 3.4). Both types of amphiphilic molecules were taken through the vesicle preparation procedures commonly used in liposome technology, including the thin film hydration method, freeze–thaw cycles, and the extrusion technique [3, 9, 193, 206].

A stock solution of 5 w/w% PEO$_{23}$-b-PMCL$_{63}$ was prepared in chloroform, while POPC was used as obtained (25 mg mL^{-1} solution in chloroform). The amphiphile stock solution and excess chloroform were added to a 50 mL round-bottom flask to form a thin film by rotary evaporation. Residual solvent was removed under high vacuum overnight. The dry film was then hydrated with an appropriate amount of calcein-containing buffer solution (80 mM calcein, 10 mM sodium phosphate buffer, pH 7.4) to yield an amphipihle concentration of 5 mM POPC and 1 w/w% PEO$_{23}$-b-PMCL$_{63}$ ($\sim$ 1.1 mM), respectively. While the lipid film was dispersed within seconds under gentle agitation, the BCP film was allowed to hydrate for another 24 h by reconnecting the round-bottom flask to the rotary evaporator at atmospheric pressure, 120 rpm, and 25 °C. Subsequently, the amphiphile suspension was vortexed until complete film dispersion and subjected to ten cycles of freezing and thawing from liquid nitrogen to 50 °C. To obtain LUVETs$_{100}$, the dispersion was sequentially extruded 10 times through polycarbonate membranes with 400-, 200-, and, finally, 100-nm pore diameters (Whatman, Kent, UK) using a LIPEX extruder (Northern Lipids, BC, Canada) and compressed nitrogen gas (purity grade 4.5, 99.995%; PanGas, Dagmersellen, Switzerland) [193]. Extrusion was performed at room temperature where both POPC and PEO$_n$-b-PMCL$_m$ bilayers are in a fluid state (POPC: $T_m = -2.5$ °C; PMCL: $T_g \approx -60$ °C) [54, 136].

The calcein-containing vesicles were separated from the non-entrapped dye molecules by size exclusion chromatography (SEC) using a Sepharose 4B column (diameter: 1 cm, length: 26 cm) and an iso-osmotic elution buffer (190 mM NaCl, 10 mM sodium phosphate, pH 7.4). The equivalent osmolality between the external and internal buffer solutions was verified with an osmometer (Advanced Micro-Osmometer,
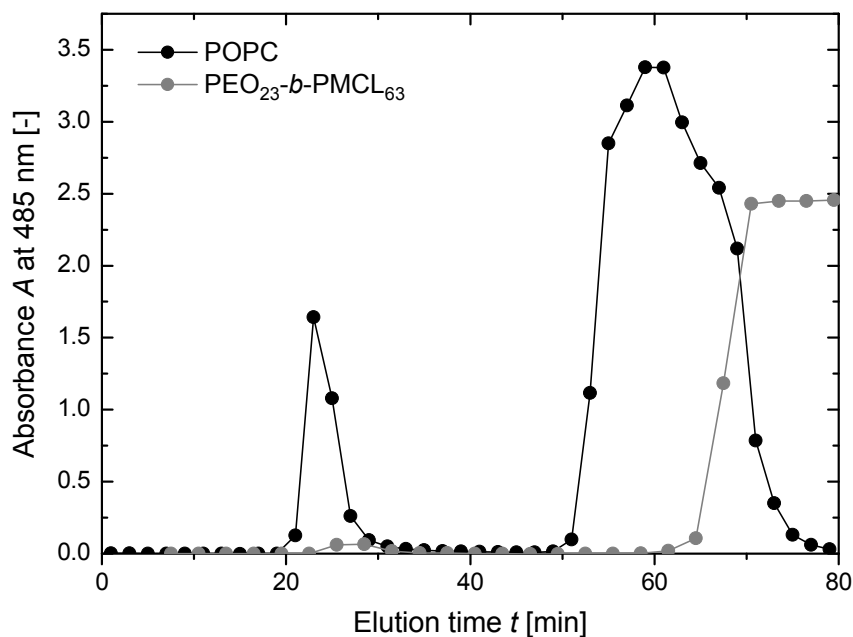
Figure 3.3: Separation of calcein-entrapped LUVETs$_{100}$ from free calcein by SEC. SEC elution profiles of calcein-entrapped LUVETs$_{100}$ (first peaks) and free calcein molecules (second peaks) after loading the calcein-containing LUVET$_{100}$ suspensions prepared from POPC (●) or PEO$_{23}$-*b*-PMCL$_{63}$ (●) on the column. Sepharose 4B column: 1×26 cm. Sample loading: $500\,\mu$L. Flow rate: $0.33\,$mL min^{-1}. LUVET$_{100}$ suspension before SEC: $[$POPC$] = 5\,$mM; $[$PEO$_{23}$-*b*-PMCL$_{63}] = 1\,$w/w%; $[$calcein$] = 80\,$mM. Absorbance A was measured at $\lambda = 485\,$nm using a BioTek PowerWave XS microplate reader (POPC) or a PerkinElmer Lambda 19 spectrophotometer (PEO$_{23}$-*b*-PMCL$_{63}$).

Model 3MO, Advanced Instruments, Norwood, MA, USA) and was found to be around $365\,$mOsm/kg. A sample volume of $0.5\,$mL was loaded to the SEC column and the flow rate was controlled at $0.33\,$mL min^{-1} using a peristaltic pump (Pharmacia Peristaltic Pump P-3, Pharmacia, London, UK). The calcein-containing vesicle fractions were identified by UV/Vis spectrophotometry at $485\,$nm. According to the obtained separation curve (Fig. 3.3), samples were collected and combined during an elution time interval of 17-31 min (total volume: $\approx 4.6\,$mL) and 22-33 min (total volume: $\approx 3.6\,$mL) for the lipid and BCP vesicle fractions, respectively. The POPC concentration in the combined, eluted lipid vesicle suspension was approximately $135\,\mu$M as determined by the Steward assay for 3 independent samples (see Sec. 4.2.7 for a close description of the Stewart assay protocol) [142, 298]. The PEO$_{23}$-*b*-PMCL$_{63}$ concentration in the BCP eluate was not analyzed.

Calcein-entrapped vesicles were stored after the extrusion step in the calcein-containing buffer solution at $4\,$°C in the dark and used within 1 week after preparation. Prior to release experiments, a $0.5\,$mL aliquot of the vesicle suspension was passed down the SEC column and immediately used for fluorescence leakage measurements.

3.2.3 Calcein release measurements

The release of vesicle-entrapped calcein across lipid and BCP bilayers was evaluated according to previous vesicle permeability studies by Lafleur and coworkers [296, 299].

The calcein-loaded liposome suspension collected after column separation was further diluted with iso-osmotic elution buffer (190 mM NaCl, 10 mM sodium phosphate, pH 7.4) by a factor of 175 to obtain a POPC concentration of approximately 0.77 µM in the cuvette. Considering an internal aqueous volume of $V_{int} = 3.3$ µL/µmole lipid calculated for the collected POPC LUVETs$_{100}$ assuming a mean vesicle diameter of 112 nm (Fig. 3.6), an average headgroup area of 0.68 nm^2, and a bilayer thickness of 3.7 nm [36, 300], this POPC concentration ensured the maximum calcein concentration in the bulk solution after total dye release from all the vesicles not to exceed 200 nM. 200 nM of calcein in the external buffer solution denoted the upper concentration limit of the linear region identified in our standard curve of fluorescence intensity versus free calcein concentration (Fig. 3.4C). At the high end of encapsulated calcein concentration (80 mM), the fluorescence intensity of the dye was highly quenched, resulting in low background fluorescence intensity of the calcein-entrapped vesicle suspensions (Fig. 3.4A).

Based on the minor fraction of PEO$_{23}$-*b*-PMCL$_{63}$ vesicles collected (Fig. 3.3) and on preliminary fluorescence measurements of calcein-loaded, intact and Triton-solubilized BCP vesicles, the polymersome suspension was used as obtained after column separation, i. e. without further dilution. Eluted and diluted samples were allowed to equilibrate for 1 h in the measuring cuvette to prevent initial leakage artifacts associated to small variations in osmotic pressures and/or temperatures between the internal and external buffer solutions [301–303].

The release of calcein from the vesicles over time was directly monitored by the increase in fluorescence intensity as the dye leaked into the external buffer solution where it was diluted to below self-quenching concentrations.

For the spontaneous release measurements under undisturbed conditions, 3 mL of calcein-entrapped vesicle suspension was added to a 1 cm – 3 mL quartz fluorescence cuvette and steady-state fluorescence spectra were recorded at 1-h time intervals over a total storage time of 10 h. The excitation wavelength was set at $\lambda_{ex} = 490$ nm and the data was analyzed at an emission wavelength of $\lambda_{em} = 515$ nm. Between measurements, samples were stored at room temperature in the dark. The percentage of calcein released after storage time t ($R(t)$) was calculated according to:

$$R(t) = 100(I(t) - I_0)/(I_{total} - I_0) \tag{3.1}$$

where I_0 is the background fluorescence intensity of the calcein-entrapped vesicle suspension at the beginning of the experiment ($t = 0$), $I(t)$ is the fluorescence intensity at time t, and I_{total} corresponds to the total fluorescence intensity after total
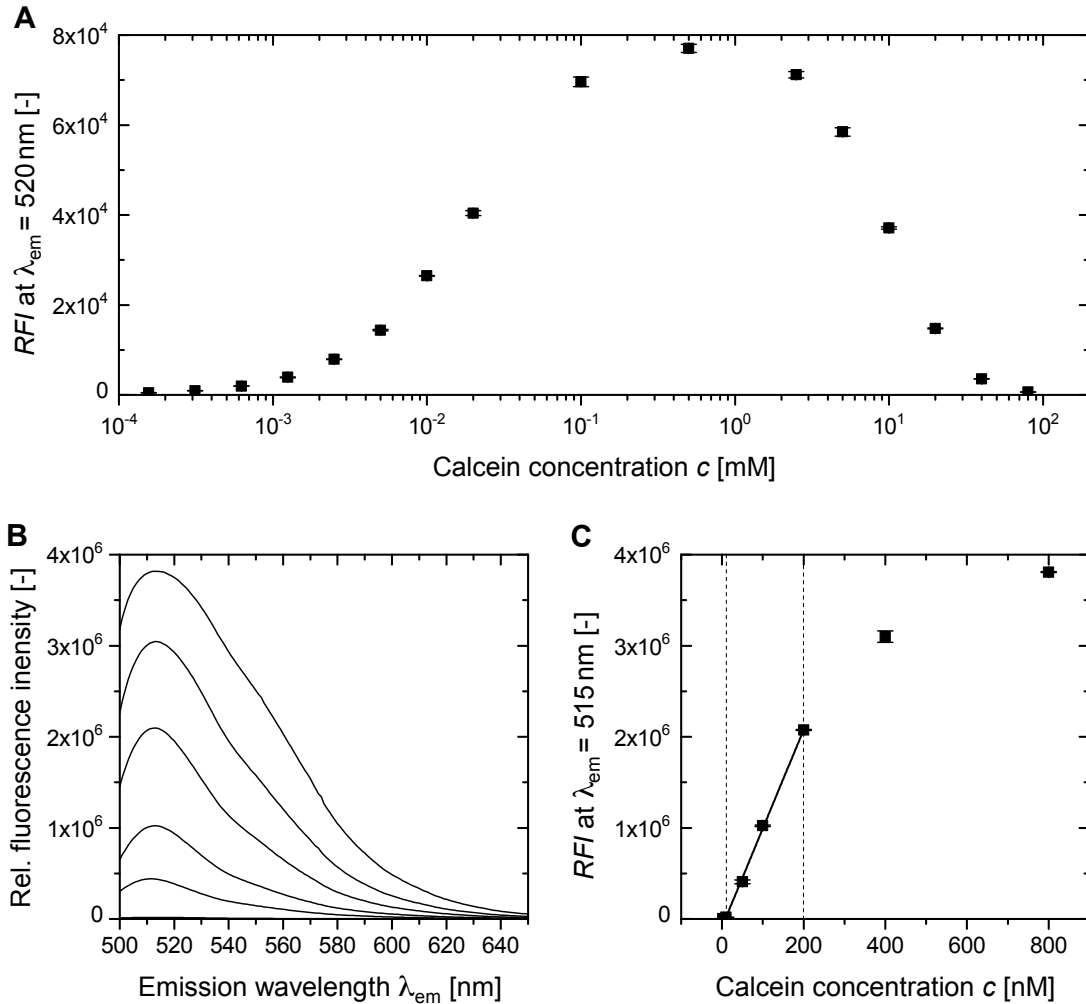
Figure 3.4: Fluorescence and self-quenching properties of calcein. (A) Relative fluorescence intensity RFI of calcein at $\lambda_{em} = 520\,nm$ as a function of sub-quenching and quenching calcein concentration in the elution buffer (190 mM NaCl, 10 mM sodium phosphate, pH 7.4). (B) Fluorescence spectra of the elution buffer containing different sub-quenching concentrations of calcein (0, 10, 50, 100, 200, 400, 800 nM) after appropriate dilution of the iso-osmolar calcein solution (80 mM calcein, 10 mM sodium phosphate, pH 7.4). The RFI increases with increasing calcein concentration in the measured range of sub-quenching dye concentrations. (C) Dependence of RFI of the elution buffer at $\lambda_{em} = 515\,nm$ on the concentration c of calcein below the self-quenching concentration. Line represents linear least-square fit between 10 and 200 nM of calcein:
$RFI = 1.083 \times 10^4 c - 8.888 \times 10^4$; $R^2 = 0.9999$. $\lambda_{ex} = 490\,nm$.

dye release from all the vesicles. I_{total} was measured after complete vesicle solubilization by the addition of 20 µL of 5 w/v% Triton to the analyte suspension at the end of the experiment (total volume in cuvette: 3020 µL). The percentage of released calcein was plotted as a function of storage time.

Time courses of bile salt-induced calcein release were recorded continuously by performing time scan fluorescence measurements of the calcein-entrapped vesicle suspensions upon bile salt addition. 2970 µL of calcein-entrapped vesicle suspension was added to a 1 cm – 3 mL quartz fluorescence cuvette and the background fluorescence intensity I_0 was measured for 300 s. The release experiment was then initiated by adding 30 µL of a 300 mg mL^{-1} bile salt solution in elution buffer (190 mM NaCl, 10 mM sodium phosphate, pH 7.4) to achieve a total sample volume of 3000 µL with an external bile salt concentration of 3 mg mL^{-1}. Bile salt-induced release kinetics were monitored for 40 min, before the total fluorescence intensity I_{total} was determined by adding 20 µL of 5 w/v% Triton. In each case of surfactant solution addition, mixing was achieved by withdrawing the vesicle suspension from the cuvette and redelivering it into the cuvette with an Eppendorf pipette and the same polypropylene tip used for bile salt solution and Triton solution addition. The fluorescence intensity was monitored at 3-s time increments for a total measuring time of 3600 s and the excitation and emission wavelengths were set at $\lambda_{\text{ex}} = 490$ nm and $\lambda_{\text{em}} = 515$ nm, respectively.

The calcein calibration curve (Fig. 3.4B-C) and fluorescence release measurements were recorded on a SPEX Fluorolog 2 instrument from HORIBA Jobin Yvon (UK). The excitation wavelength was set at $\lambda_{\text{ex}} = 490$ nm and the emission was usually recorded between $\lambda_{\text{em}} = 500$ nm and 650 nm. Excitation and emission bandpath widths were set at 1 mm and 3 mm, respectively. The spectrofluorometer was not equipped for sample stirring or temperature control.

The self-quenching properties of calcein evaluated over a broad range of calcein concentrations of about 10^{-4} to 10^2 mM (Fig. 3.4A) was demonstrated on a Bio-Tek FL600 fluorescence microplate reader (Bio-Tek Instruments, Winooski, VT, USA) using black 96-well polystyrene plates with a sample volume of 400 µL/well. Excitation and emission wavelengths were set at $\lambda_{\text{ex}} = 490$ nm and $\lambda_{\text{em}} = 520$ nm. All fluorescence measurements were carried out at room temperature.

3.2.4 DLS

The mean size, polydispersity and size distribution of calcein-entrapped vesicles before and after separation by SEC were analyzed by dynamic light scattering (DLS) using a Zetasizer Nano ZS (Malvern Instruments, UK). The measurements were performed in the backscattering mode at a scattering angle of $\theta = 173°$ and the measuring temperature was controlled at 25 °C.

Calcein-loaded LUVET$_{100}$ suspensions collected before and after column separation were diluted with elution buffer (190 mM NaCl, 10 mM sodium phosphate, pH 7.4) by a factor of 50 and 2, respectively. For the lipid vesicle suspensions, this resulted in a POPC concentration of around 50 to 100 µM in the cuvette. Diluted samples were placed in a 1.5 mL disposable polystyrene cuvette and the measurement of each sample was repeated three times to check for reproducibility and sample stability. The intensity time autocorrelation functions were analyzed using the Multiple Narrow Modes algorithm incorporated in the Malvern DTS software (version 5.10), which is based on a non-negatively constraint least square fit (NNLS; see Sec. 4.2.5 in the Background Chapter) [260, 304]. In addition to the intensity weighted results of average hydrodynamic diameters and poyidspersity indices (scaling with r^6), volume weighted size distributions (scaling with r^3) are displayed after conversion of the intensity weighted size distributions using Mie theory [264]. It has to be mentioned that the conversion of intensity to volume weighted averages basically assumes a particle geometry of homogeneous solid spheres, which is not fully consistent with that of vesicles.

3.2.5 Preparation of giant unilamellar vesicles (GUVs)

GUVs were formed from POPC and PEO$_{23}$-*b*-PMCL$_{50}$, respectively, following the electroformation method with a Pt wire setup [123, 222, 224, 226]. The homemade formation and investigation chamber used is illustrated in Figure 2.10A. A detailed description of its components and dimensions is given in Bucher *et al.* [226]. The two parallel Pt wire electrodes in the chamber had a diameter of 0.5 mm and a distance of 3 mm.
POPC and PEO$_{23}$-*b*-PMCL$_{50}$ stock solutions were prepared at 0.2 mg mL^{-1} in chloroform (263 µM POPC) and 2.0 mg mL^{-1} in chloroform/diethyl ether/methanol 2:7:1 (v/v) (270 µM PEO$_{23}$-*b*-PMCL$_{50}$), respectively. To form thin amphiphile films on the electrode surface, the stock solutions were deposited on the two Pt wires using a 10 µL Hamilton syringe as follows: 2 µL of the POPC solution (526 pmol) was deposited in two different areas of each of the two Pt wires to create a total of four thin film regions for GUV formation and subsequent investigation. The PEO$_{23}$-*b*-PMCL$_{50}$ solution was deposited as a single 1 µL droplet (270 pmol) onto the center of each of the two Pt wires. Special care was taken to avoid sliding during solution deposition at a specific spot as this promotes the formation of a uniform thin film which, in turn, is important for the successful formation of a controlled amount of spherical GUV close to the electrode surface [226]. The films were subsequently dried by placing the chamber under reduced pressure overnight in a desiccator.
Prior to start the electroformation experiment, the chamber containing the dried amphiphile films was taped onto the microscope stage to allow the direct monitoring of vesicle growth. A function generator (Agilent 33120A, Agilent Technologies,

CA, USA) was connected to the Pt wires and an ac electric field with a sinusoidal waveform was applied at a frequency of 10 Hz and an initial voltage of 0.1 V (peak-to-peak value). The electro-osmotically controlled swelling of the lamellar films was initiated by carefully adding 1.2 mL of buffer solution (0.5 mM HEPES, 0.5 mM EDTA, pH 7.4, room temperature) to the working chamber under prevention of agitation and air inclusions. For the formation of POPC GUV, the voltage was increased to 2 V and kept constant for 90 min before switching the ac field off. GUV formation from the PEO_{23}-b-$PMCL_{50}$ film was induced by gradually increasing the voltage from 0.1 to 2 V during the first 60 min and keeping it constant for another 60 min. GUV growth was then promoted by further increasing the voltage to 3 V within 30 min and keeping it for an additional 90 min. The ac field was switched off after a total electroformation time of 4 h. All electroformation experiments were carried out at room temperature.

3.2.6 GUV imaging and characterization

GUVs were observed under an inverted light microscope (Nikon DIAPHOT-TMD) in the phase contrast mode using a 60x long working distance objective lens (LWD Plan 60 / 0.7-1.7 Ph3DL, Nikon). Images were acquired, processed, and analyzed using a digital camera (Nikon DS-Fi1) and the Nikon NIS-Elements D3.0 imaging software.

For lipid and polymer GUVs obtained after the electroformation experiment, size distribution functions and their characteristic parameters were calculated using a Matlab code written by Tim Althaus at the Laboratory of Food Process Engineering, ETH Zurich. The GUV size x was defined by its diameter parallel to the Pt wire which was manually measured for each GUV observed on the wire. As this characterization of GUV size by image analysis can be regarded as a counting technique, the collected values of GUV diameters were equally weighted by considering the size distribution functions based on the number of GUVs [305]. The number weighted logarithmic density distribution function $q_0(\lg x)$ was calculated according to

$$q_0(\lg \bar{x}_i) = \frac{n_i}{\sum_{k=1}^{\infty} n_k} \frac{1}{\Delta x_i} \frac{\bar{x}_i}{\lg(\exp(1))} \tag{3.2}$$

and plotted against the GUV diameter x in a semi-logarithmic plot with logarithmic abscissa. n_i is the number of all GUVs in the size range from $\bar{x}_i - \Delta x_i/2$ to $\bar{x}_i + \Delta x_i/2$ where Δx_i is the interval width and $\bar{x}_i$ is the mean value of the interval.

The cumulative number distribution function

$$Q_0(x_i) = \frac{\sum_{k=1}^{i} n_k}{\sum_{k=1}^{\infty} n_k} \tag{3.3}$$

was calculated to determine the number weighted median diameter $x_{50,0}$ ($Q_0(x_{50,0}) = 0.5$), as well as the limiting diameters $x_{10,0}$ ($Q_0(x_{10,0}) = 0.1$) and $x_{90,0}$ ($Q_0(x_{90,0}) = 0.9$). They denote those GUV diameters where 50%, 10% and 90%, respectively, of the GUVs in number are smaller than the given diameter. A useful measure to compare the width of size distributions is the so-called *span* value given by

$$span_0 = \frac{x_{90,0} - x_{10,0}}{x_{50,0}} \tag{3.4}$$

in the case of number based distribution characteristics.

3.3 Results and discussion

3.3.1 Large unilamellar vesicles prepared from PEO-*b*-PMCL

Calcein-entrapped LUVETs$_{100}$ were prepared from PEO$_{23}$-*b*-PMCL$_{63}$ to study the ability of the food grade diblock copolymer to (i) form uniform nanometer-sized vesicles, (ii) to encapsulate and retain hydrophilic molecules in the aqueous vesicle core under undisturbed storage conditions, and (iii) to show controlled release properties under GI stress conditions.

According to earlier systematic studies on aggregate morphologies from PEO$_{n}$-*b*-PMCL$_{m}$ in water at varying PMCL block lengths [52, 76], the chosen PEO$_{23}$-*b*-PMCL$_{63}$ block copolymer architecture with $w_{PMCL} = 0.88$ was very likely to predominantly self-assemble into lamellar sheets and vesicles in concentrated and dilute dispersions, respectively (Fig. 2.5).
With this perspective, the methods originally described for liposome preparation could be applied to the vesicle forming synthetic amphiphile [64, 65, 77, 135]. More specifically, we adopted the most commonly used combination of thin film hydration, freeze-thawing and repetitive extrusion through, ultimately, 100-nm pore membranes to prepare LUV structures with controlled sizes, i. e. LUVETs$_{100}$, both from POPC and PEO$_{23}$-*b*-PMCL$_{63}$ [3, 9, 193, 206]. The hydrophilic fluorescent marker calcein was added to the hydration medium in which the vesicles were formed. Finally, the presence and size of calcein-entrapped LUVETs$_{100}$ before and after separation of free dye molecules by SEC were evaluated by DLS measurements.
For phosphatidylcholines, including the intensively studied model lipid POPC, this preparation protocol is well known to yield homogeneous and mostly unilamellar liposomes with a mean diameter that reflects the 100-nm nominal pore diameter of the filter membrane [9, 15, 208, 209, 219, 299].

TEM: In the frame of this thesis, the reproducible results of the extrusion technique for liposome preparation have been confirmed in our laboratory [10]. An example of a well defined POPC LUVET$_{100}$ suspension as prepared for comparison in the present study is shown by the cryo-TEM micrograph in Figure 3.5A provided by Paul Beck [306].
Cryo-TEM images were also recorded of LUVETs$_{100}$ prepared from 0.1 w/w% PEO$_{23}$-*b*-PMCL$_{63}$ solutions in water following the imaging procedure described in Section 4.2.8. However, at the low polymer concentration of the isotropic regime of PEO-*b*-PMCL vesicle dispersions (< 1 w/w%; Fig. 2.5) [52], no aggregate structures were found in the small sample volume of the cryo-TEM specimen. Figure 3.5 includes a TEM micrograph of an analogous 0.1 w/w% PEO$_{23}$-*b*-PMCL$_{54}$ LUVET$_{200}$ suspension ($w_{PMCL} = 0.87$) recorded by our project partner Jörg Braun at the Zentrum
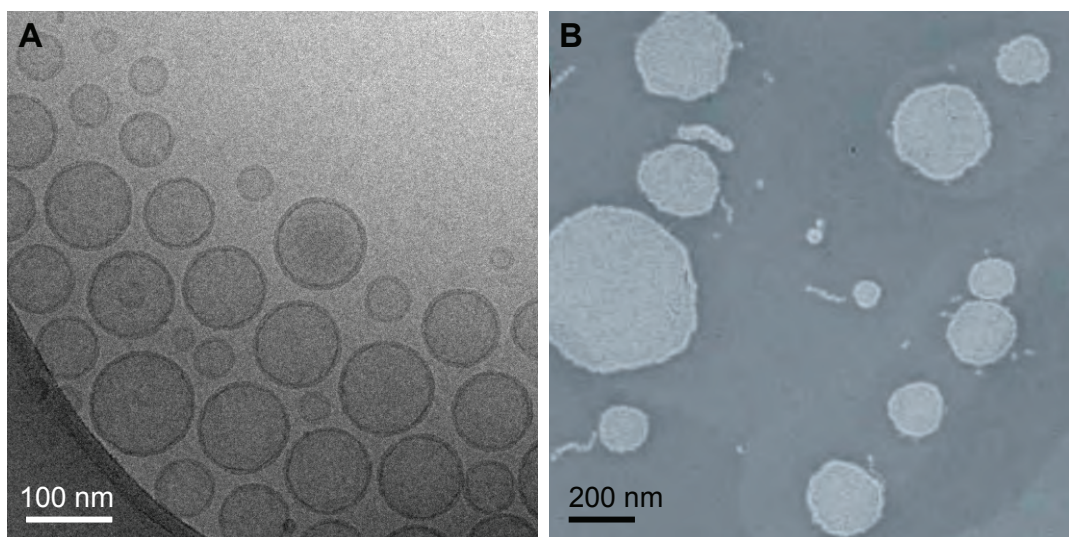
Figure 3.5: Cryo-TEM and TEM micrographs of POPC and PEO-*b*-PMCL large unilamellar vesicles. (A) Cryo-TEM micrograph of LUVETs$_{100}$ prepared from POPC using a 100-nm pore polycarbonate membrane for final extrusion cycles. 15 mM POPC in Millipore water. (B) TEM micrograph of LUVETs$_{200}$ prepared from PEO$_{23}$-*b*-PMCL$_{54}$ using a 200-nm pore polycarbonate membrane for final extrusion cycles. 0.1 w/w% PEO$_{23}$-*b*-PMCL$_{54}$ in Millipore water. $w_{PMCL} = 0.87$. Part (B) is adapted from Braun *et al.* [52] with permission from John Wiley & Sons Inc.

für Mikroskopie, University of Basel (ZMB), instead [52]. Despite the collapsed state of vesicles in dried TEM specimens, the image clearly reveals spherical vesicle structures as the predominant species in isotropic PEO-*b*-PMCL dispersions with $w_{PMCL} > 0.8$ [52, 76, 295]. As described by Braun *et al.* [52] and other authors studying the same BCP system [76, 295], a few worm-like micelles and membrane fragments coexist with the bilayered vesicles.

DLS: In this study, the presence of mixed morphologies was also evident from the DLS results of calcein-entrapped LUVETs$_{100}$ prepared from a calcein containing 1 w/w% PEO$_{23}$-*b*-PMCL$_{63}$ solution (Fig. 3.6).
The volume-weighted size distribution of the PEO$_{23}$-*b*-PMCL$_{63}$ vesicle suspension recorded before separation of free dye molecules by SEC was broad and multimodal. Its primary peak at 106 nm represents the predominant LUVET$_{100}$ population, while the small peak at 35 nm indicates the coexistence of a few micellar structures. The shoulder arising from aggregate sizes of around 200 to 700 nm can most probably be attributed to packed vesicle clusters as the dispersion was prepared at the upper polymer concentration limit of the isotropic regime, i.e. at 1 w/w% (Fig. **??**) [52]. Packed vesicles have previously been observed for semi-dilute aqueous block copoly-
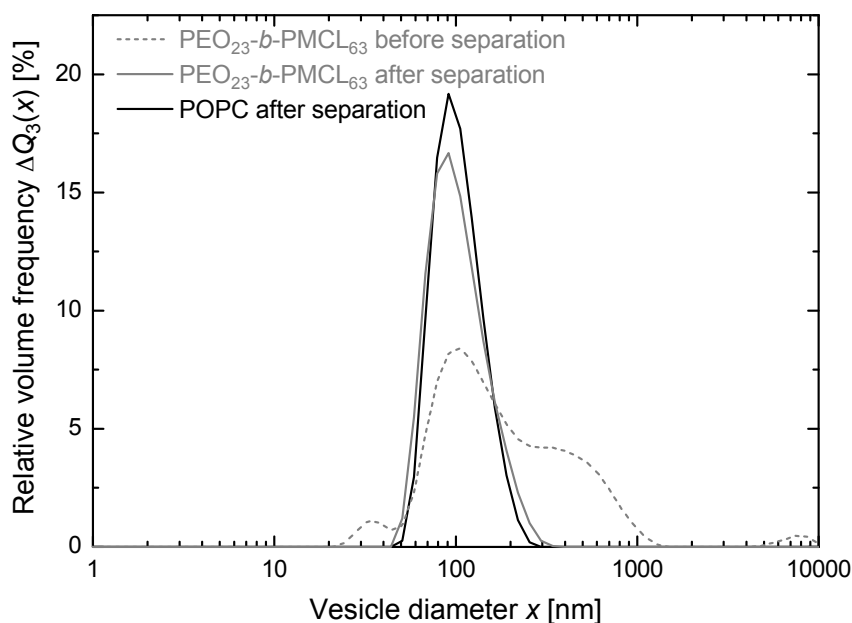
Figure 3.6: Size distributions of calcein-entrapped POPC and PEO-*b*-PMCL LUVETs$_{100}$. Volume-weighted size distributions of calcein-entrapped LUVETs$_{100}$ from POPC (*black line*) and PEO$_{23}$-*b*-PMCL$_{63}$ (*gray line*) before (*dotted line*) and after (*solid line*) separation of free dye molecules by SEC. Amphiphile concentration before separation: 5 mM POPC; 1 w/w% PEO$_{23}$-*b*-PMCL$_{63}$. Amphiphile concentration after separation: $\approx$ 135 µM POPC; $\ll$ 1 w/w% PEO$_{23}$-*b*-PMCL$_{63}$.

mer solutions. Only at very low concentrations around or even below 1 w/w%, they were reported to detach from each other to form very stable isotropic dispersions [51, 52, 56].

The average size of the minor micelle population at around 35 nm was in good agreement with the cross-sectional diameters of spherical and wormlike PEO-*b*-PMCL micelles described in literature [76, 293]. The persistence of mixed aggregate morphologies resulting from the self-assembly of vesicle forming PEO-*b*-PMCL in water was probably influenced by the polydispersity of the polymer molecules comprising the aggregates [307, 308]. Depending on the hydrophobic block molecular weight, aggregate morphologies have been reported to progress from spherical to worm-like micelles and, finally, to bilayers as the number of monomer repeat units in the PMCL block was increased [76]. This is the classic evolution of aggregate morphologies as described for other polymeric amphiphile systems in water [309–311]. Additionally and more importantly than block length polydispersity, the strong hydrophobicity of bilayer forming block copolymers and the inability of macromolecular exchange between aggregates are thought to be responsible for the coexistence of mixed morphologies. The aggregate structures initially formed upon hydration of the bulk polymer in water are kinetically trapped systems that have not reached global equi-

librium [307, 312, 313].

After separation of non-entrapped calcein molecules by SEC, the size distribution of the calcein-loaded PEO_{23}-*b*-$PMCL_{63}$ $LUVET_{100}$ suspension practically overlaid with the narrow, monomodal distribution function of the well defined and analogously prepared POPC sample (Fig. 3.6). This indicates that the passage of the initial PEO_{23}-*b*-$PMCL_{63}$ $LUVET_{100}$ preparation over the Sepharose column not only successfully separated free dye molecules but also micellar aggregates from the calcein-entrapped vesicle population. Also, the vesicle clusters detected in the initial $1\,w/w\%$ PEO_{23}-*b*-$PMCL_{63}$ $LUVET_{100}$ dispersion separated into stable isotropic vesicles upon dilution on the column to a polymer concentration of $\ll 1\,w/w\%$ [51]. The intensity-weighted mean hydrodynamic diameters D_h of the calcein-entrapped $LUVET_{100}$ suspensions from POPC and PEO_{23}-*b*-$PMCL_{63}$ as obtained from DLS measurements were 112 nm and 115 nm, respectively. In accordance to the narrow size distributions in Figure 3.6, the corresponding polydispersity indices *PDI* were low and accounted for 0.06 and 0.11 for the phospholipid and polymer sample, respectively. Narrow size distributions, i.e. low *PDI* values, and controlled mean vesicle sizes that are close to or slightly larger than the filter pore size used for final extrusions are characteristic for $LUVET_{100}$ suspensions both from phospholipids [3, 9, 10, 15, 208, 209] and amphiphilic block copolymers [65, 135, 314, 315].

Summary: The previous morphological studies on PEO-*b*-PMCL aggregate structures by Zupancich *et al.* and Braun *et al.* [52, 76] and our DLS results for calcein-loaded POPC and PEO_{23}-*b*-$PMCL_{63}$ $LUVET_{100}$ suspensions, including the overlaying monomodal size distributions and the consistent mean hydrodynamic diameters, confirm the successful formation of defined $LUVETs_{100}$ from PEO_{23}-*b*-$PMCL_{63}$ by the applied preparation procedure.

3.3.2 Release properties of large unilamellar PEO-*b*-PMCL vesicles

The vesicular structure of PEO_{23}-*b*-$PMCL_{63}$ $LUVETs_{100}$ was further demonstrated by its ability to encapsulate highly hydrophilic substances in the membrane-confined aqueous core. Due to the selective permeability of the self-assembled amphiphilic bilayer, the negatively charged and water-soluble fluorescent dye calcein could be entrapped in the aqueous interior of osmotically balanced vesicles at a high self-quenching concentration. As described earlier [19, 117, 296, 299, 301, 315], this allowed to directly monitor the permeation of calcein across the vesicle membrane as an increase in fluorescence intensity upon release and dilution, i.e. dequenching, of the dye into the external medium.

The following two sections present the release kinetics of the marker molecule calcein from PEO_{23}-b-$PMCL_{63}$ and standard POPC $LUVETs_{100}$ measured under undisturbed and gastrointestinal stress conditions, respectively.

Passive permeability of polymeric PEO-*b*-PMCL and standard POPC vesicle membranes

The ability of PEO_{23}-b-$PMCL_{63}$ polymersomes to retain a molecular cargo during storage was examined by measuring the spontaneous release of calcein from PEO_{23}-b-$PMCL_{63}$ $LUVETs_{100}$ under undisturbed conditions. The observed stability in terms of load retention was compared to that of conventional phospholipid $LUVETs_{100}$ prepared from POPC.

Results: Figure 3.7 shows the time courses of the percentage of passive calcein release from the calcein-entrapped POPC and PEO_{23}-b-$PMCL_{63}$ $LUVETs_{100}$ during a storage time of 10 hours at room temperature. Following the lipid membrane permeability study by Shimanouchi *et al.* [19], the behavior of calcein release from the bilayered vesicles was analyzed by a first-order kinetic according to:

$$R(t) = R_{\max}(1 - \exp(-kt)) \qquad (3.5)$$

The apparent rate constant k for calcein permeation across the vesicle membrane was extracted from the best fit of Eq. 3.5 to the experimental data (Fig 3.7). It was found to be $9.4 \times 10^{-5}\,\mathrm{s}^{-1}$ and $6.9 \times 10^{-5}\,\mathrm{s}^{-1}$ for the POPC and PEO_{23}-b-$PMCL_{63}$ membranes, respectively. The corresponding apparent permeability coefficient P to calcein was then calculated from the relation $P = (D_h/6)k$ derived from a common model for solute permeation across vesicular membranes [115, 118, 316]. As described in the previous section, the mean hydrodynamic diameter D_h was $112\,\mathrm{nm}$ and $115\,\mathrm{nm}$ for the POPC and PEO_{23}-b-$PMCL_{63}$ $LUVET_{100}$ samples, respectively. The results for passive calcein permeability across POPC and PEO_{23}-b-$PMCL_{63}$ vesicle membranes, measured at room temperature and pH 7.4, were $1.7 \times 10^{-3}\,\mathrm{nm\,s}^{-1}$ and $1.3 \times 10^{-3}\,\mathrm{nm\,s}^{-1}$, respectively.

Passive permeability obtained for POPC vesicles vs. literature values: The P value obtained for passive calcein permeation through the POPC membrane was almost one order of magnitude higher than that reported by Shimanouchi *et al.* for the same loaded vesicle system under comparable experimental conditions (pH 7.5, $T = 25\,°C$; $P = 1.9 \times 10^{-4}\,\mathrm{nm\,s}^{-1}$) [19].
Increased temperatures during repeated exposure of the analyte solution to the light
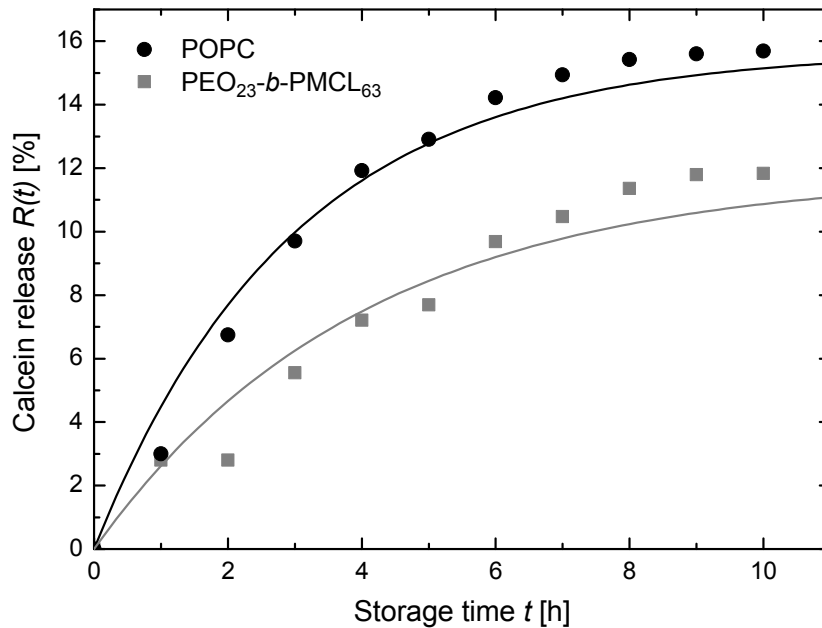
Figure 3.7: Passive permeability of POPC and PEO-*b*-PMCL vesicles. Time courses of the percentage of passive calcein release (Eq. 3.1) from calcein-entrapped LUVETs$_{100}$ from POPC (●) and PEO$_{23}$-*b*-PMCL$_{63}$ (■). pH = 7.4; $T \approx$ room temperature. Fluorescence spectra recorded at $\lambda_{\text{ex}} = 490\,$nm and analyzed at $\lambda_{\text{em}} = 515\,$nm. Analyte solution in the cuvette before addition of $20\,\mu$L $5\,$w/v% Triton: Total volume $= 3000\,\mu$L; [POPC] $\approx 0.77\,\mu$M; [PEO$_{23}$-*b*-PMCL$_{63}$] $\ll 1\,$w/w%; internal [calcein] $= 80\,$mM, total [calcein] $\approx 200\,$nM. Solid lines represent best fit curves to the experimental data using Eq. 3.5 with $R^2 = 0.981$ (POPC; ▬) or $R^2 = 0.947$ (PEO$_{23}$-*b*-PMCL$_{63}$; ▬). Results represent the values of a single experiment.

source of the fluorescence spectrometer have probably contributed to a slightly enhanced calcein permeablility measured in the present work [19, 100, 104]. However, the considerable discrepancy between the P values for POPC membranes reported here and in literature can not solely be attributed to the lack of temperature control during fluorescence measurements. This becomes apparent from the literature values of calcein permeability from POPC LUVETs$_{100}$ measured at elevated temperatures (e. g. $T = 50\,°$C, $P \approx 1.2 \times 10^{-3}\,$nm s^{-1}) [19] which were still lower than our result obtained at room temperature ($P = 1.7 \times 10^{-3}\,$nm s^{-1}). Apart from incubation temperature, solution pH, and the resulting valency of slightly acidic marker molecules, including calcein, carboxyfluorescein, and 5,5'-dithiobis-2-nitrobenzoic acid (DTNB) [17, 112, 317], the permeability of such a marker molecule across a specific vesicle bilayer is influenced by a number of other factors. Among these are the composition and ionic strength of the internal and external buffer solutions [112, 301, 317, 318], the resulting bilayer surface charges [109], the presence of an osmotic gradient across the bilayer [301, 319, 320], as well as counter ion permeability in the case of charged

marker species [100, 321].

Indeed, the lower permeability coefficient of calcein across POPC membranes reported by Shimanouchi *et al.* was determined from isotonic release measurements using the tetra sodium salt form of calcein [19], whereas calcein disodium salt was used in the otherwise similar experimental protocol of the present study. At the neutral pH of the employed buffer solutions (pH 7.5 and pH 7.4, respectively), both calcein forms carried approximately the same amount of multiple negatively charged groups (see Fig. 3.2 for the structure and pKa values of calcein) [317]. Therefore, it can be assumed that the encapsulated calcein molecules themselves did not differ in permeation rate-determining hydrophilicity and solubility in the POPC bilayer. However, the apparent permeability coefficient P of calcein with a tetra sodium salt form was very likely to be decreased due to its association with a larger amount of Na^+ counterions which permeate lipid membranes at considerably lower rates ($P \approx 10^{-7}$–$10^{-5}\,\mathrm{nm\,s^{-1}}$) [100, 113, 114]. The permeation of anionic fluorescent dye and charged molecules, in general, across lipid bilayers is always coupled to the movement of counterions which restore transmembrane electrical balance. As a consequence, the permeability of counterions substantially influences the flux rate of the diffusing dye [100, 321].

For the same reason of the dependence of ion permeation on counterion permeability, the release rate of vesicle-encapsulated calcein is also dependent on internal and external buffer compositions [112, 317, 321], which were different in the iso-osmotic systems investigated by Shimanouchi *et al.* and in the present study [19]. Compared to their experimental setup exhibiting a large inward Na^+ concentration gradient, our system disposed of practically balanced Na^+ concentrations, a larger outward Cl^- concentration gradient, and a reduced inward gradient in terms of ionic strength. All of these gradients further contribute to enhanced release rates of calcein from lipid vesicles as they promote the permeation of more mobile Cl^- counterions into the vesicles ($P \approx 10^{-4}\,\mathrm{nm\,s^{-1}}$) instead of the calcein-coupled efflux of less permeable Na^+ from the vesicles to maintain electroneutrality [100, 114].

Given that the experimental conditions were not exactly the same (salt form of calcein, buffer compositions), the calcein permeability from POPC LUVETs$_{100}$ determined as reference value for lipid vesicles in this study ($P = 1.7 \times 10^{-3}\,\mathrm{nm\,s^{-1}}$) can be taken as comparable with that reported by Shimanouchi *et al.* ($P = 0.2 \times 10^{-3}\,\mathrm{nm\,s^{-1}}$) [19]. Our result was also in line with the P values of egg PC VETs$_{200}$ to the less negatively charged trivalent anion 5(6)-carboxyfluorescein ($P \approx 0.5 \times 10^{-3}\,\mathrm{nm\,s^{-1}}$) [109], as well as to the smaller divalent anion DTNB ($P = 60 \times 10^{-3}\,\mathrm{nm\,s^{-1}}$) [17], both also determined at neutral pH and $T = 25\,°\mathrm{C}$.

Passive permeability of PEO-*b*-PMCL vs. POPC vesicle membranes: As for the PEO$_{23}$-*b*-PMCL$_{63}$ membrane, calcein permeabilty was found to be decreased by a factor of 1.3 compared to that measured across the POPC bilayer ($P =$

$1.3 \times 10^{-3} \, \text{nm s}^{-1}$ and $1.7 \times 10^{-3} \, \text{nm s}^{-1}$, respectively). With a first regard to the 12-fold higher molecular weight of PEO_{23}-b-$PMCL_{63}$ than that of POPC, one would expect the permeability of PEO_{23}-b-$PMCL_{63}$ vesicles to be reduced by several factors rather than being within the P range of POPC vesicles.

Owing to the increased membrane thickness resulting from the self-assembly of high molar mass copolymers, polymersomes are often described to be less permeable to small hydrophilic solutes than their thin-walled phospholipid analogs [12, 16, 65, 78, 117, 154, 322, 323]. Among the generally limited number of polymersome permeability studies, this assumption can be evaluated by comparing the various permeability coefficients to water reported in liposome and polymersome literature, as has been done by Discher *et al.* and Carlsen *et al.* [12, 99]. Indeed, the P values for water across polymer membranes with hydrophobic core thicknesses of $d_C \approx 10 \, \text{nm}$ formed from PMOXA-b-PDMS-b-PMOXA ($P = 0.8 \, \mu\text{m s}^{-1}$) [78, 322], PEO-$b$-PEE ($P = 2.5 \, \mu\text{m s}^{-1}$) [12], and PEO-$b$-PBD ($P = 3.1 \, \mu\text{m s}^{-1}$) [99] were found to be at least ~ 1 order of magnitude below those reported for lipid membranes in the fluid state composed purely of mono- and dimono-unsaturated PCs with acyl chain lengths of 14 to 18 carbon atoms ($d_C \approx 3 \, \text{nm}$, $P \approx 20\text{-}80 \, \mu\text{m s}^{-1}$) [13, 108, 300]. Similarly, the release of doxorubicin from PS-b-PAA vesicles with a wall thickness of approximately $30 \, \text{nm}$ was described to be considerably smaller than that measured earlier from egg PC liposomes [323, 324].

It has to be noted, however, that none of the studies mentioned above have reported on quantitative permeability results for both polymeric and lipidic membranes to a specific solute under constant experimental conditions which would allow for a more direct comparison of polymersomes and liposomes in terms of load retention. Also, the assumption of decreased membrane permeabilities of polymersomes has especially been confirmed for polymers comprising a hydrophobic block moiety with a relatively high glass transition temperature. These polymers self-assemble into stiff vesicle membranes [99] that are, in the case of T_g > room temperature, even in a glassy state during release measurements at room temperature [323]. In contrast, more flexible polymer membranes, e. g. from PEO-g-PDMS with $d_C \approx 5 \, \text{nm}$ and $T_g = -123 \, \text{°C}$, exhibited comparable water permeabilities to those of lipid membranes in the fluid state ($P = 28 \, \mu\text{m s}^{-1}$) [99]. PEO-$b$-PBO and PEO-$b$-PBO-$b$-PEO vesicles were even shown to be one order of magnitude more permeable to DTNB than egg PC liposomes at neutral pH, which was attributed to the more hydrophilic nature of the polyether membranes [17].

The wide range of permeability coefficients reported for polymersomes relative to those of liposomes indicates that permeation of a specific solute across polymer membranes is not only influenced by the well-known effect of molecular polymer weight and resulting membrane thickness. Polymersome permeability also depends on the fluidity [99, 103, 115, 323, 325] and the relative polarity of the hydrophobic membrane core [17, 103, 115, 117], as well as on the polymeric membrane structure,

including the degree of coil formation, chain entanglement, and interdigitation within the membrane as opposed to a stretched and ordered bilayer structure [17, 60, 99]. All of these factors enter the simple solubility-diffusion model that describes the passive permeation of solutes across vesicle membranes following Fick's first law and considering the bilayer as a homogeneous barrier of thickness d_B [101, 326, 327]:

$$P = \frac{SD}{d_B} \tag{3.6}$$

Here, S is the solubility or partition coefficient of the solute between the membrane and the aqueous phase, while D represents its diffusion coefficient within the membrane. According to Eq. 3.6, the solubility-diffusion model considers the entry of a specific solute into the membrane and its diffusion through the membrane as possible rate-limiting steps for permeation, as measured by S and D, respectively. While the fluidity and order of the vesicle membrane primarily influence vesicle permeability via D, the S dependence of P is mainly determined by the relative polarity profile of the membrane interior.

Fickian diffusion behavior of anionic marker molecules similar to calcein through vesicle membranes, with the permeation rate being inversely proportional to the membrane thickness at a given chemical composition of amphiphiles, has been demonstrated for both polymersomes [17] and liposomes [328]. Also, water-soluble fluorescence probes with multiple negative charges, including calcein, have been suggested to permeate lipid vesicle membranes in the gel or liquid-crystalline state by the simple solubility-diffusion mechanism rather than through transient pores or lipid packing defects within the bilayer [19, 329]. This allows us to discuss the permeability results for POPC and PEO_{23}-b-$PMCL_{63}$ vesicles obtained from the spontaneous release of calcein based on the considerations outlined above.

Following the linear scaling of the hydrophobic membrane thickness d_C with the number of PMCL units described for PEO_{23}-b-$PMCL_m$ lamellar phases, d_C and d_B of the PEO_{23}-b-$PMCL_{63}$ membrane can be estimated to be around 17 nm and 23 nm, respectively [52, 152]. The corresponding literature values for POPC bilayers are $d_C = 2.7$ nm and $d_B = 3.7$ nm [300]. If the permeation rate across the two membrane systems was only dependent on total or hydrophobic membrane thickness, the permeability of PEO_{23}-b-$PMCL_{63}$ membranes would be expected to be approximately 6 times lower than that of POPC bilayers. This is not the case as indicated by the small factor of 1.3 found between the P values of PEO_{23}-b-$PMCL_{63}$ and POPC $LUVETs_{100}$.

According to the solubility-diffusion model (Eq. 3.6), the effect of the increased bilayer thickness of PEO_{23}-b-$PMCL_{63}$ vesicles on membrane permeability is compensated by higher partition and diffusion coefficients for calcein within the polymer membrane compared to those resulting in the interior of the POPC membrane. The higher partition coefficient of the PEO_{23}-b-$PMCL_{63}$ system can be rationalized in terms of the weaker hydrophobicity of the polyether membrane compared to the

aliphatic lipid membrane (Fig. 3.1 and Tab. 4.3). At the same time, diffusion of small solutes through the PEO_{23}-b-$PMCL_{63}$ membrane seems to be facilitated due to differences in the polymeric and lipidic membrane structures. In a previous study on PEO_{23}-b-$PMCL_m$ lamellar phases with m ranging from 25 to 54, the hydrophobic chains within the lamellae were considered to be in a partially stretched conformation, but showed a tendency to coiling at higher numbers of PMCL units [52]. With m = 63 in the PEO_{23}-b-$PMCL_m$ polymer under investigation, the hydrophobic blocks within the PEO_{23}-b-$PMCL_{63}$ membrane can be assumed to be partially coiled. Chain coiling leads to a lower packing density of the self-assembled block copolymers and promotes the entanglement and interdigitation of the hydrophobic chains in the membrane core [60]. As a consequence, the diffusion coefficient of small molecules in the more disordered and less densely packed PEO_{23}-b-$PMCL_{63}$ membrane is increased compared to ordered lipid bilayers.

Summary: This is the first example to our knowledge in which the passive permeabiltiy of PEO-PMCL vesicles has been analyzed, and the first to quantitatively measure calcein permeability from polymersomes in general. Although the molecular weight and the membrane thickness of the PEO_{23}-b-$PMCL_{63}$ membrane studied in this work were several times larger than those of a conventional POPC bilayer, the permeability coefficients obtained for the two vesicle systems were rather similar ($P = 1.3 \times 10^{-3}\,\mathrm{nm\,s^{-1}}$ and $1.7 \times 10^{-3}\,\mathrm{nm\,s^{-1}}$, respectively). This revealed the influence of the nature of the hydrophobic block moiety and the architecture of the self-assembled polymer membrane on polymersome permeabiltiy as discussed in this section.

Bile salt-induced permeability of polymeric PEO-*b*-PMCL and standard POPC vesicle membranes

The controlled release of encapsulated active components from vesicle carriers is equally important in delivery-release applications than their ability to retain the cargo during storage and transport to the site of activation. Therefore, after studying the passive permeabiltiy of PEO_{23}-b-$PMCL_{63}$ vesicles, we tested the release properties of the food grade polymersomes under gastrointestinal stress conditions. More specifically, the calcein-entrapped PEO_{23}-b-$PMCL_{63}$ $LUVETs_{100}$ were exposed to bile salts added to the external iso-osmotic buffer solution and the bile salt-induced release kinetics of calcein were followed by fluorescence spectroscopy. The concentration of bile salts in the external medium was set at $7\,\mathrm{mM}$ which reflects the lower and upper range of bile salt concentrations in the human duodenum after ingestion of a meal and in the fasted state, respectively [330, 331]. The bile salts employed consisted of an approximate 1:1 mixture of sodium cholate and sodium
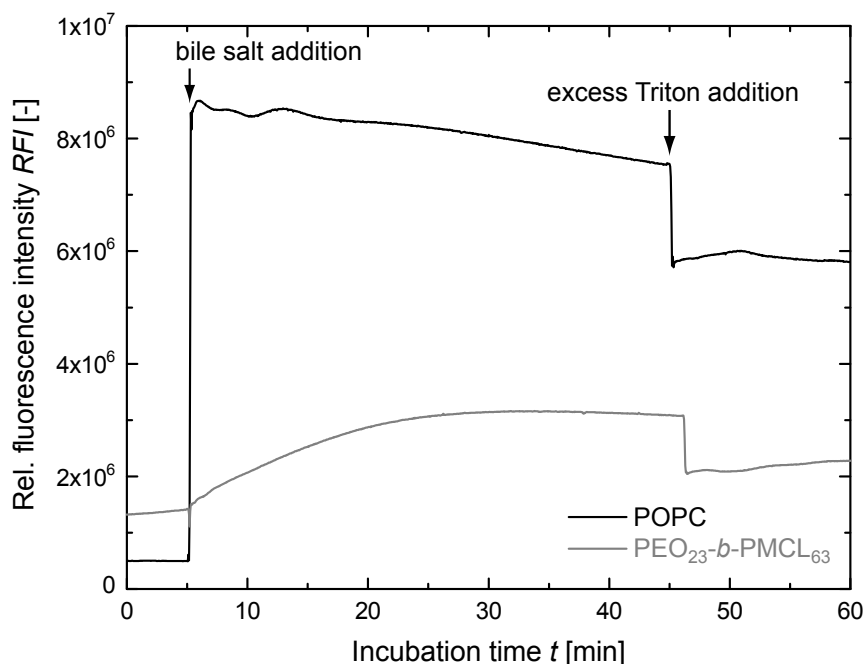
Figure 3.8: Bile salt-induced permeability of POPC and PEO-*b*-PMCL vesicles. Time-courses of calcein release induced by the addition of bile salts to calcein-entrapped LUVET$_{100}$ suspensions from POPC (——) and PEO$_{23}$-*b*-PMCL$_{63}$ (——). pH = 7.4, $T \approx$ room temperature. Fluorescence intensity measured at $\lambda_{ex} = 490$ nm, $\lambda_{em} = 515$ nm, and 3 s time intervals. Analyte solution in the cuvette after bile salt addition: Total volume = 3000 µL; [POPC] ≈ 0.76 µM; [PEO$_{23}$-*b*-PMCL$_{63}$] $\ll 1$ w/w%; internal [calcein] = 80 mM, total [calcein] ≈ 200 nM; [bile salts] = 7.08 mM. [Triton] = 0.53 mM after addition of 20 µL 5 w/v% Triton.

deoxycholate which, in addition to chenodeoxycholate, make up the major components of bile salts in humans [332].

Again, the results obtained for the polymer vesicles were compared to the bile salt-induced release behavior of standard POPC vesicles measured under the same experimental conditions.

Results: Figure 3.8 shows the time courses of calcein release induced by the addition of bile salts to the calcein-entrapped POPC and PEO$_{23}$-*b*-PMCL$_{63}$ LUVETs$_{100}$ over an incubation time of 40 min at room temperature. In addition to the bile salt-induced release kinetics reflected by the increase in fluorescence intensity ($I(t)$; $t = 5$-45 min), the measurement curves include the constant background and total fluorescence intensities of the calcein-entrapped vesicle suspensions before bile salt addition (I_0; $t = 0$-5 min) and after excess Triton addition (I_{total}; $t = 45$-60 min), respectively.

The time course obtained from the POPC sample had the form of a step function with the fluorescence intensity of the calcein-loaded vesicle suspension abruptly jumping to a maximum value upon bile salt addition. Increasing incubation time did not lead to further increase in fluorescence intensity. Instead, the curve slowly decayed with time, possibly due to photobleaching of the fluorescence dye under the continuous exposure to light. The addition of excess Triton to ensure total calcein release at the end of the experiment resulted in a shift of the fluorescence intensity to a lower plateau reflecting a simple dilution effect due to Triton solution addition. The overall time course shows that the addition of external bile salts at duodenal concentration triggered an immediate and complete release of trapped material from the POPC vesicles in the analyte solution.

In contrast, the release profile of calcein from the PEO_{23}-b-$PMCL_{63}$ LUVETs$_{100}$ revealed a gradual release behavior of molecular cargo from the polymer vesicles in the presence of external bile salts following a first-order kinetic over an incubation time of approximately 30 min. The fraction of calcein released 30 min after the addition of bile salts also corresponded to the total amount of initially loaded calcein. This was indicated by the plateau of the fluorescence intensity at incubation times > 30 min, as well as by the shift of this plateau to a lower value upon excess Triton addition.

Interactions of bile salts with POPC membranes: The presented release measurements were performed on very dilute vesicle suspensions due to the high sensitivity of fluorescence measurements and the requirement of performing quantitative calcein release experiments in the linear range of fluorescence intensity vs. total calcein concentration (see Sec. 3.2.3 and Fig. 3.4 in Materials and Methods). This resulted in a very high bile salt to lipid molar ratio R in the POPC analyte solution after addition of bile salts at duodenal concentration ($R \approx 9300$), which is well known to induce lipid bilayer solubilization ([181] and references therein; see also Background Sec. 2.4.4). For various mixtures of phosphatidylcholine vesicles and the bile salt sodium cholate, the effective bile salt to lipid molar ratio in the vesicle bilayer resulting in complete vesicle solubilization, R_B^{sol}, was reported to be smaller than 1 [176, 178, 182, 183]. Therefore, with the molar ratio of bile salt to POPC in the analyte solution being far above unity, the fast and complete calcein release detected from the POPC vesicles can directly be related to complete bile salt-induced vesicle solubilization.

The immediate and strong response of the fluorescence intensity of the calcein-entrapped POPC vesicle suspension to bile salt addition (Fig. 3.8) also shows that the transition kinetics for this vesicle-to-micelle transformation were very fast in the case of POPC vesicles. This can be attributed to the high membrane fluidity of PC bilayers in the liquid-crystalline state and to a fast transbilayer movement (flip-flop) of bile acids across these bilayers. The latter process is a critical step

in the mechanism described for a relatively rapid detergent-induced solubilization of lipid bilayers: It is initialized by a fast penetration of detergents into the outer monolayer and proceeds through the flip-flop mediated transmembrane equilibration of detergents between the two monolyers to bilayer saturation and, finally, to bilayer solubilization [179, 184, 333].

Interactions of bile salts with PEO-*b*-PMCL membranes: The exact concentration of PEO_{23}-*b*-$PMCL_{63}$ in the polymer analyte solution was not known, since this parameter had not been analyzed in the purified, calcein-entrapped polymersome suspension collected after separation and concomitant dilution on the SEC column. However, considering the concentration of PEO_{23}-*b*-$PMCL_{63}$ in the initial unpurified vesicle suspension ($\sim 1.1\,\text{mM}$) and that of bile salts subsequently added to the purified vesicle suspension ($7\,\text{mM}$), the molar ratio of bile salts to vesicle-forming BCPs in the PEO_{23}-*b*-$PMCL_{63}$ analyte solution can be estimated to also be well above unity. Therefore, it is very likely that the PEO_{23}-*b*-$PMCL_{63}$ vesicles in the investigated suspension were also solubilized in the presence of external bile salts at duodenal concentration.

With this regard, the gradual release profile of calcein observed from the PEO_{23}-*b*-$PMCL_{63}$ vesicles can be explained by much slower kinetics of the bile salt-induced vesicle-to-micelle transformation of polymer membranes compared to those involved in the fast detergent solubilization of lipid bilayers. Apparently, the structure of the PEO_{23}-*b*-$PMCL_{63}$ membrane did not allow for the fast flip-flop-mediated mechanism of bilayer solubilization. It was rather disintegrated by a slow process that proceeds via formation and detachment of mixed micelles from the outer monolayer [179, 181, 184]. The shedding of mixed micelles from closed vesicles results in partial vesicle solubilization, i. e. increased membrane permeability, as indicated by the release behavior of the PEO_{23}-*b*-$PMCL_{63}$ vesicles in the presence of bile salts [179]. The recorded bile-salt induced leakage profile does, however, not allow to draw any conclusion on whether or not the PEO_{23}-*b*-$PMCL_{63}$ vesicles were completely solubilized by the time of complete calcein release at $t \approx 30\,\text{min}$.

Summary: The comparison of the release behavior of PEO_{23}-*b*-$PMCL_{63}$ and POPC vesicles in the presence of bile salts again demonstrated the role of bilayer architecture in the permeability properties of vesicle membranes. The obtained results confirm the less ordered and entangled structure, as well as the higher resulting rigidity of the thicker PEO_{23}-*b*-$PMCL_{63}$ membrane compared to the highly ordered, fluid-like POPC bilayer. All of these structural and physical properties decrease the mobility of bile salts in the polymer membrane and prevent its fast flip-flop mediated solubilization.

Closing remarks: Some important remarks about the release studies described in this section need to be added. In the bile salt-induced release measurements, the decrease in fluorescence intensity detected upon Triton addition was considerably larger than that expected from the small decrease in calcein concentration due to sample dilution (dilution factor: 1.007) (Fig. 3.8). This singularity was not observed in the previous release experiments under undisturbed conditions and can not be explained at this stage. The apparent mismatch in linearities between fluorescence intensity and free calcein concentration did not allow to draw any quantitative conclusions from the bile salt-induced release measurements. Nevertheless, the bile salt-induced calcein release profiles clearly indicated that the encapsulation efficiency of the PEO_{23}-b-$PMCL_{63}$ $LUVET_{100}$ suspension was much lower compared to its POPC analogue (Fig. 3.8). In fact, the encapsulation efficiency of calcein into PEO_{23}-b-$PMCL_{63}$ vesicles was very low, considering the dilutions of the calcein-entrapped POPC and PEO_{23}-b-$PMCL_{63}$ $LUVET_{100}$ suspensions by factor 175 and 1, respectively, prior to release measurements.

The poor loading efficiency of hydrophilic cargo into the PEO_{23}-b-$PMCL_{63}$ vesicle suspension can partially be attributed to the formation of micellar structures and membrane fragments, in addition to the predominant vesicle morphology, upon hydration of PEO-b-PMCL with $w_{PMCL} > 0.8$ in aqueous solution (Fig. 3.5) [52, 76, 295]. Here, the low encapsulation efficiency was also the result of a small overall yield of calcein-entrapped PEO_{23}-b-$PMCL_{63}$ $LUVETs_{100}$ obtained from the preparation protocol used. The small yield is indicated by the minor peak in the elution profile of the PEO_{23}-b-$PMCL_{63}$ vesicle fraction compared to that recorded from the eluted POPC vesicles (Fig. 3.3.). It is likely that the hydration time of 24 h did not allow for the complete hydration and dispersion of the lamellar polymer film in the aqueous phase. Previous works studying the self-assembly structures of amphiphilic block copolymers, including PEO-b-PMCL, in aqueous solution allowed for sample hydration and equilibration of at least 1 week [52, 56, 76]. Optimization of the protocols used in this study, both for the synthesis of PEO-b-PMCL polymers and for the subsequent preparation of nanometer-sized vesicle suspensions, should be considered to gain control over the self-assembly of the amphiphiles into well-defined vesicle structures and to increase encapsulation efficiency.

3.3.3 Giant unilamellar vesicles prepared from PEO-*b*-PMCL

The ability of PEO-b-PMCL copolymers with $w_{PMCL} > 0.8$ to self-assemble into vesicle membranes in aqueous solution was further evidenced by generating and directly visualizing micrometer-sized GUVs from PEO_{23}-b-$PMCL_{50}$ with $w_{PMCL} = 0.86$.

Vesicle samples were prepared both from standard POPC and from the food grade diblock copolymer using one of the most popular, established, and reproducible

methods for GUV formation, i.e. the electroformation method [5, 222, 227] (Sec. 2.5.5). The homemade investigation chamber used contained two parallel Pt wire electrodes where GUV growth was induced from a thin amphiphile film in aqueous solution and in the presence of an ac electric field [226] (Fig. 2.10). This allowed the real time observation of the swelling of the amphiphile film, of the eventual bending of lamellar sheets and, finally, of the growth of GUVs by light microscopy [191, 223]. Whereas the lipid GUVs from POPC were easily obtained by setting the electric field parameters within the range typically applied for phospholipids (10 Hz, 2 V, 90 min in this study) [191, 226, 334], the synthetic GUVs from PEO_{23}-b-$PMCL_{50}$ could only be formed after adjusting the standard electroformation protocol as follows. The polymer film was hydrated at relatively low voltage for a prolonged swelling time by gradually increasing the voltage from 0.1 to 2 V during the first 60 min and keeping it constant for another 60 min. GUV growth was then promoted at higher voltage for a second period of 2 hours by further increasing the voltage from 2 V to 3 V within 30 min and holding it at 3 V for the next 90 min. The frequency of the ac electric field was kept constant at 10 Hz throughout all electroformation experiments.

The obtained GUVs were visualized by phase contrast LM and characterized by statistical image analysis in terms of number-weighted vesicle size distributions.

Results: Figure 3.9 shows highly uniform, spherical GUVs that were successfully formed at the surface of the Pt wires, not only from conventional POPC (Fig. 3.9 A-B) but also from the PEO_{23}-b-$PMCL_{50}$ copolymer (Fig. 3.9 C-D), using the standard and adapted electroformation protocols, respectively. The obtained lipid and polymer GUVs were similar in size with diameters usually ranging from about 3 to 50 µm (Fig. 3.10). In some experiments, the giant POPC vesicles even grew up to a maximum diameter of around 90 µm. These observations are consistent with previous reports on the size range of electroformed liposomes [191, 226, 230] as well as polymersomes [12, 65, 335].

The number-weighted diameter distributions of populations of POPC and PEO_{23}-b-$PMCL_{50}$ GUVs detected and analyzed after one representative electroformation experiment are shown in Figure 3.10. They were rather narrow and monomodal, as expected for electroformed vesicles [65, 191, 230]. The derived distribution parameters, including the number-weighted median diameter $x_{50,0}$ and $span_0$ value (Eqs. 3.3 and 3.4), were comparable for the lipid and polymer GUV populations. They accounted for 12.4 µm and 14.3 µm and for 1.51 and 1.74, respectively.

Pathways of GUV formation from PEO-*b*-PMCL and POPC films: The observed formation of GUVs from the dry amphiphile films is a direct proof for the ability of both POPC and PEO_{23}-b-$PMCL_{50}$ to self-assemble into lamellar phases and vesicle membranes in concentrated and dilute aqueous solutions, respectively,
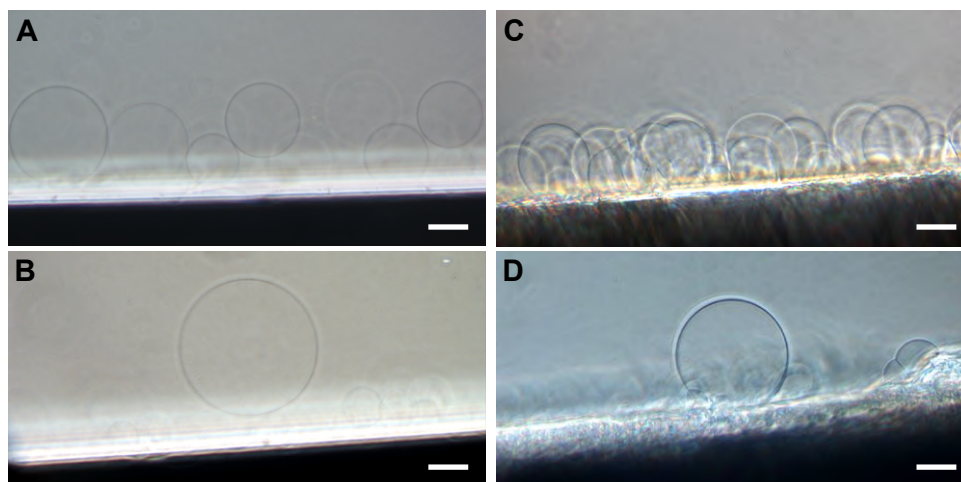
Figure 3.9: LM micrographs of electroformed POPC and PEO-*b*-PMCL GUVs.
GUVs electroformed on a Pt wire from POPC (A-B) and PEO$_{23}$-*b*-PMCL$_{50}$ (C-D) in buffer
solution (0.5 mM HEPES, 0.5 mM EDTA, pH 7.4). Electroformation POPC: 10 Hz, 2 V,
90 min. Electroformation PEO$_{23}$-*b*-PMCL$_{50}$: 10 Hz; 60 min at 0.1-2 V, 60 min at 2 V,
30 min at 2-3 V, and 90 min at 3 V. T = room temperature. Scale bar = 20 µm.
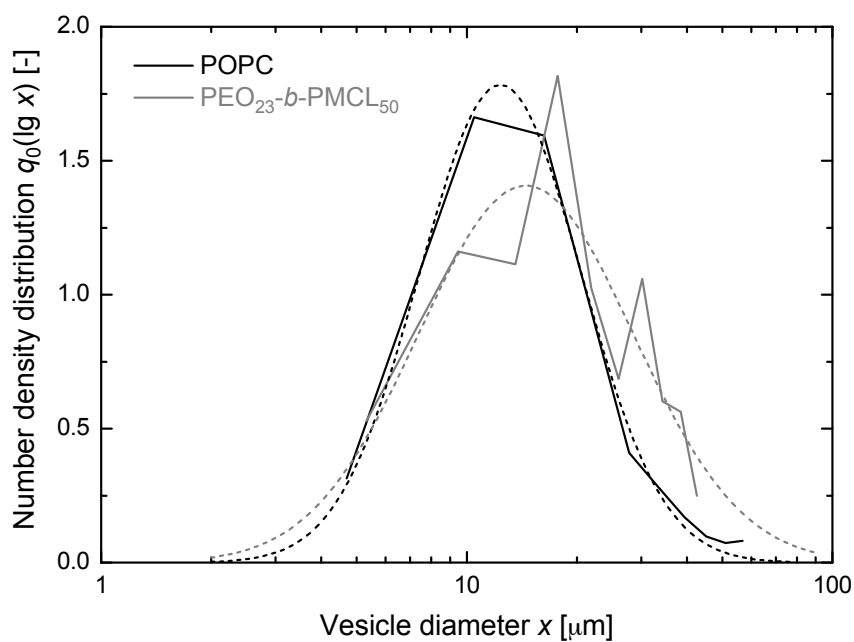
**Figure 3.10: Size distributions of electroformed POPC and PEO-*b*-PMCL
GUVs.** Number-weighted size distributions of the electroformed GUVs prepared from
POPC (*black line*) and PEO$_{23}$-*b*-PMCL$_{50}$ (*gray line*) and shown in Figure 3.9. *Solid
lines*: Distribution functions calculated from statistical image analysis of LM micrographs.
Dotted lines: Lognormal fits to the measured data.

as illustrated in the corresponding phase diagrams of equilibrated amphiphile-water mixtures as a function of concentration (Fig. 2.5) [47, 52].

According to earlier studies on the hydration kinetics of thin films of vesicle forming block copolymers by Battaglia and coworkers [57, 336], hydrating amphiphile films proceed through the entire phase sequence described for the corresponding amphiphile-water mixtures under equilibrium conditions as water diffuses into the film, both in the absence and presence of an ac field. Thereby, the initial swelling rate is controlled not only by the diffusion of water into the amphiphile assembly but also by the series of phase transitions that take place within the film as the water content increases. For the PEO_{23}-b-$PMCL_{50}$ copolymer investigated here, these phase transitions lead from the disordered polymer melt through (i) an inverse hexagonal phase to (ii) a lyotropic lamellar phase, before the stacked lamellae unbind to transform into vesicles, that is (iii) an isotropic lamellar phase (Fig. 2.5B) [52]. In contrast, the morphologies of low molar mass phosphatidylcholines only evolve into (i) lyotropic and (ii) isotropic lamellar phases, i.e. vesicles, upon diffusion of water into the bulk phase (Fig. 2.5A) [47]. Application of an ac electric field during thin film hydration facilitates GUV formation by strongly enhancing both the diffusion of water into the amphiphile film and the unbinding of lamellae for subsequent GUV growth [57, 191, 223, 227].

Kinetics of GUV formation from PEO-*b*-PMCL and POPC films – Polymer and lipid membrane properties: The longer hydration time required in our electroformation experiments for the initial swelling of the PEO_{23}-b-$PMCL_{50}$ film compared to the almost immediate hydration of the POPC film can be explained based on the pathways and mechanisms of vesicle formation upon thin film hydration outlined above. The diffusion and phase transition processes within the amphiphile film were much slower for the high molecular weight copolymer because of its higher hydrophobic content and lower mobility. In addition, PEO_{23}-b-$PMCL_{50}$ proceeds through a larger number of necessary phase transitions from the bulk amphiphile to unbound lamellae than POPC which further slowed down the initial swelling kinetics of the polymer film [57].

To promote the growth of GUVs from the swollen lamellae the PEO_{23}-b-$PMCL_{50}$ film had to be subjected to a higher driving voltage (3 V) than that typically applied to phospholipids (1-2 V) [191, 226, 334]. This higher resistance of the polymer membrane to vesicle growth can directly be related to its increased thickness, the higher bending rigidity, and the lower membrane fluidity as described in a previous study on the growth behavior of GUVs during electroformation [191]. The higher rigidity of the PEO_{23}-b-$PMCL_{50}$ membrane became also directly apparent from microscopic observations of growing GUVs during the electroformation experiments. Adjacent polymer GUVs were more resistant to electric field-induced lateral fusions than the thin-walled, fluid-like GUVs from POPC (see for example the closely joined

PEO$_{23}$-*b*-PMCL$_{50}$ GUVs at the right side of Figs. 3.9C and D) [228].

Relation of membrane properties and electroformation conditions required for GUV formation: The relations between the driving voltage required for electroformation, the resulting growth behavior of GUVs, and the physicochemical properties of vesicle membranes are also revealed from earlier electroformation protocols reported in literature.

Phospholipid GUVs are not formed under standard electroformation conditions (10 Hz, 1-2 V) if the bilayers are in the gel state, that is if the temperature T during electroformation is below the main phase transition temperature T_{m} of the phospholipid used [191]. Similarly, the electroformation method is inefficient in generating giant polymersomes from glassy lamellar films ($T < T_{\mathrm{g}}$) composed for example of rigid (rod–rod) or rigid-flexible (rod–coil) diblock copolymers with high T_{g} hydrophobic chains [75]. On the other hand, the energy supplied by the ac electric field of appropriate voltage allows to overcome the kinetic barrier to vesicle formation from lipid and polymer films if the membranes are in a fluid state, i. e. $T > T_{\mathrm{m}}$ and T_{g}, respectively. This was the case for the POPC ($T_{\mathrm{m}} = -2.5\,°\mathrm{C}$) and PEO-*b*-PMCL ($T_{\mathrm{g}} \approx -60\,°\mathrm{C}$) amphiphiles used in this study [54, 136] (see Background Section 2.3.1 for the temperature dependent phase states of lipid and polymer bilayers).

As observed and discussed in the frame of our own experiments, the necessary driving voltage for the electroformation of more resistant polymer GUVs is usually higher than that commonly applied to phospholipids (1-2 V) [191, 226, 334]. Depending on the fluidity of the polymer membrane, the typical voltages range from 4 to 10 V, while the frequency is kept at 10 Hz as for phospholipids [12, 57, 103, 123, 231, 232]. Rodríguez-García *et al.* applied for example 9 V to highly hydrophobic PEO-*b*-PBD to form relatively rigid and little permeable giant polymersomes, whereas flexible and highly permeable GUVs from water soluble PEO-*b*-PPO-*b*-PEO (Pluronics) were already obtained at 5 V [103]. Similarly, increasing driving voltages of 3.6-8.0 V have been applied to a set of PEO-*b*-PBD polymers of increasing molecular weights to generate GUVs that were characterized by increasing bilayer thicknesses and decreasing susceptibility to electrodeformation [231]. In addition to the energy input from the ac electric field, the highest M_w sample had to be heated to 60 °C to allow for vesicle formation, while the low M_w polymersomes were grown at room temperature. In contrast, Reiner *et al.* reported on the electroformation of GUVs from an even manifold higher M_w PEO-*b*-PBD at 10 V without the necessity of heating. However, this was only possible after an extensive electroformation time of 18 h and after increasing the fluidity of the high M_w PEO-*b*-PBD membrane by incorporating a small fraction of the detergent-like Pluronic F-127 (PEO-*b*-PPO-*b*-PEO) [233]. Dimova and coworkers also prepared and characterized GUVs from PEO-*b*-PBD but with a relatively low molecular weight. These GUVs formed within less than 30 min at room temperature and at a driving voltage of 9 V as described in their widely used

electroformation protocol for the preparation of giant polymersomes [123]. Application of lower voltages close to those typically used for phospholipids ($\approx 800\,\mathrm{mV}$) also yielded giant PEO-*b*-PBD vesicles, but the growing times were significantly longer (about 3 h) and the resulting GUVs were smaller.

Based on these earlier electroformation reports, the total electroformation time of 4 h required for the preparation of PEO$_{23}$-*b*-PMCL$_{50}$ GUVs under the electroformation conditions used here could probably be reduced by increasing the driving voltage during the growth phase from 3 V to around 10 V. This would likely result in a shorter growth time which currently accounts for 2 h. The initial swelling of the PEO$_{23}$-*b*-PMCL$_{50}$ film is still recommended to be conducted at gentle voltages of up to 2 V for a swelling time of around 2 h as suggested by the protocol developed in this study.

Summary and outlook: In addition to the dye encapsulation and release studies on PEO$_{23}$-*b*-PMCL$_{63}$ LUVETs$_{100}$ reported in the first part of this chapter, the ac electric flied-assisted growth of GUVs from the PEO$_{23}$-*b*-PMCL$_{50}$ film presented in this section was another, this time direct and visual, proof of the ability of the investigated PEO-*b*-PMCL polymers to self-assemble into vesicle membranes in excess aqueous solution.

At the same time, this work provides the first protocol for the successful electroformation of GUVs based on the biocompatible and biodegradable PEO-*b*-PMCL diblock copolymer. An earlier study has already reported the formation of giant PEO-*b*-PMCL polymersomes using the w/o/w double emulsion transformation method [5]. It involved the production of a well defined, polymer stabilized w/o/w double emulsion in a microfluidic flow focusing device, followed by evaporation of the volatile oil phase [337]. This method generally allows a precise control over the final size of the giant vesicles and a highly efficient encapsulation of water soluble molecules, including macromolecules, in the vesicle lumen [338–340]. However, the obtained vesicle membranes are often heterogeneous in terms of lamellarity, amphiphile aggregates associated with the membrane, and residual solvent trapped inside the membrane and, hence, show altered membrane properties [5, 337–339].

In contrast, the electroformation technique is well known to generate homogeneous, spherical, and unilamellar giant vesicles consisting of a plain amphiphile membrane. Therefore, it is currently the most widely used method for the preparation and characterization of model membranes [5, 18] (Background Sec. 2.5.5). Accordingly, our adapted electroformation protocol for the routine formation of PEO-*b*-PMCL GUVs gives access to numerous experimental techniques to further characterize the membrane properties and dynamics of these food grade polymersomes towards specific applications. The widely used micropipette aspiration technique allows for example to determine the stretching and bending elasticities (K_A and κ_c), tensile strength (σ_l), permeability, and shear surface viscosity (η_S) of GUV membranes (Background

Sec. 2.3.5) [13, 14, 75]. Further rheological membrane properties have been directly measured by falling ball viscosimetry and tether pulling experiments [123]. Fluorescence recovery of fluorescent probes incorporated into GUVs after photobleaching gives quantitative information regarding the membrane fluidity [68, 240]. Finally, the visibility of GUVs under the optical microscope allows to measure membrane permeability by the osmotic swelling and shrinking of GUVs [99, 241] and to monitor the deformation behavior of GUVs under osmotic stress conditions [339], in the presence of external electric fields [120, 121], and in external flow fields [74, 88, 90].

3.4 Conclusions

The aim of this study was to assemble food grade polymersomes and demonstrate their potential as controlled delivery-release nanocapsules of functional components in food applications.

Biocompatible and biodegradable PEO-*b*-PMCL diblock copolymers with $w_{PMCL} > 0.8$ were evaluated for their ability to

(i) form vesicle structures in aqueous solution under physiological conditions,
(ii) encapsulate and retain hydrophilic molecules in the aqueous vesicle lumen under undisturbed conditions, and
(iii) show controlled release properties under GI stress conditions.

All experiments were amended with standard phospholipid vesicles prepared from POPC for comparison.

(i) The PEO-*b*-PMCL amphiphiles studied were able to self-assemble into lamellar vesicle structures by the hydration of a thin polymer film in excess aqueous solution at room temperature. The use of an organic cosolvent and/or elevated temperatures for membrane fluidization was not necessary.

This was well evidenced by the direct LM visualization of micrometer-sized GUVs prepared from PEO$_{23}$-*b*-PMCL$_{50}$ using the electroformation method ($x_{50,0} = 14.3\,\mu$m). The alternating electric field-induced growth of GUVs from the dry polymer film upon water addition could be observed in real time.

Thin film hydration under agitation allowed the spontaneous formation of nanometer-sized PEO-*b*-PMCL vesicles in aqueous solution. Well-defined vesicles with a mean hydrodynamic diameter of 115 nm, i.e. LUVETs$_{100}$, were obtained by repetitive extrusion of spontaneously formed PEO$_{23}$-*b*-PMCL$_{63}$ vesicles through 400 nm, 200 nm, and finally 100 nm pore membranes. The vesicle structure of nanometer-sized PEO-*b*-PMCL aggregates was verified by TEM. A few micelles, worm-like micelles and membrane fragments coexisted with the predominant species of spherical vesicles.

(ii) Further proof of the PEO-*b*-PMCL vesicle structure was shown by passively encapsulating the strongly hydrophilic fluorescent dye, calcein, at high self-quenching concentration into the aqueous core of PEO_{23}-*b*-$PMCL_{63}$ $LUVETs_{100}$. Compared to POPC $LUVETs_{100}$, the encapsulation efficiency of calcein into the polymer LUVETs$_{100}$ was, however, very small.

Both POPC and PEO_{23}-*b*-$PMCL_{63}$ vesicles exhibited first-order release kinetics of encapsulated calcein under osmotically balanced, undisturbed storage conditions. The derived permeability coefficients P of calcein across POPC and PEO_{23}-*b*-$PMCL_{63}$ vesicle membranes were $1.7 \times 10^{-3}\,\mathrm{nm\,s^{-1}}$ and $1.3 \times 10^{-3}\,\mathrm{nm\,s^{-1}}$, respectively. In other words, the ability of PEO_{23}-*b*-$PMCL_{63}$ vesicles to retain hydrophilic molecular cargo under undisturbed conditions was only 1.3 times higher compared to standard POPC vesicles, despite of the membrane thickness of PEO_{23}-*b*-$PMCL_{63}$ vesicles exceeding that of POPC bilayers by approximately factor 6.

(iii) Exposure of calcein-entrapped POPC $LUVETs_{100}$ to external bile salts at duodenal concentration triggered an immediate, complete, and uncontrolled release of encapsulated cargo. In contrast, calcein release from PEO_{23}-*b*-$PMCL_{63}$ $LUVETs_{100}$ under the same GI stress conditions followed a first-order release kinetic and was only complete after an incubation time of 30 min.

The behavioral differences of PEO-*b*-PMCL and POPC vesicles during the preparation procedures and the release experiments described in this study provided further insight into the structure-property functions of the investigated vesicle systems.

During electroformation, PEO-*b*-PMCL membranes required higher voltages to grow and were more resistant to lateral fusion than lipid membranes indicating a higher rigidity of the polymer membrane.

As for the release studies, the small difference between the permeability coefficients obtained for the thick PEO-*b*-PMCL membrane ($d_B \approx 23\,\mathrm{nm}$) and the thin POPC bilayer ($d_B = 3.7\,\mathrm{nm}$) originated from the less hydrophobic nature of the PMCL membrane core compared to the aliphatic lipid membrane. Furthermore, coiling and entanglement of the long PMCL chains lowered the amphiphile packing density in the PEO-*b*-PMCL membrane and facilitated the permeation of small molecules across the polymer membrane as opposed to the highly ordered and densely packed POPC membrane. On the other hand, the less ordered and entangled structure, as well as the lower fluidity of the PEO-*b*-PMCL membrane prevented its fast solubilization by the penetration and transmembrane equilibration of duodenal bile salts. These comparative observations highlighted that, in addition to the well-known effect of membrane thickness, vesicle permeability is also influenced by the fluidity, the relative polarity profile, and the architecture of the vesicle membrane. All of these structural and physical membrane properties need to be taken into account when designing vesicle carriers for controlled delivery-release applications.

The controlled destabilization of PEO-*b*-PMCL vesicles under gastrointestinal stress conditions renders these food grade polymersomes promising candidates for the delivery of functional food components to the site of absorption at increased bioavailability. The versatility of block copolymer chemistry and the adjustability of vesicle membrane properties offer many possibilities to further develop the PEO-*b*-PMCL carriers towards 'smart', stimuli-responsive vehicles for food applications. Additional functions could be introduced, e.g. for specific targeting, triggered release, and enhanced intestinal permeability, to maximize the absorption rate and bioavailability of the encapsulated agent. The adjusted electroformation protocol described in this work for the preparation of GUVs from PEO-*b*-PMCL polymers gives access to a wide range of characterization methods on the single vesicle and membrane level. They can be useful for the assessment of new PEO-*b*-PMCL vesicle formulations during further development steps. With regard to practical implementations, the synthesis protocol of aqueous PEO-*b*-PMCL dispersions should be further optimized in terms of reducing coexisting mixed morphologies and improving encapsulation efficiency.

4 Process development and investigation of dynamically enhanced vesicle extrusion

4.1 Introduction

The large variety of functional vesicle formulations suggested and, in some cases, implemented in the fields of biomedicine [21, 35], cosmetics [6], and foods [6, 41, 42] requires close control over the physicochemical properties of vesicle templates prepared for the different applications.

For delivery-release applications, vesicle size and lamellarity are key parameters to be controlled during the assembly of nanometer-sized vesicle carriers. They influence important characteristics of the carrier, including the density of surface functionalization, the amount of internal volume, the entrapment efficiency, as well as the release behavior of encapsulated cargo across one ore more bilayers, depending on whether the vesicles are uni- or oligolamellar [19, 35, 36, 341]. In the case of unilamellar lipid vesicles, the release characteristics across the single bilayer are still dependent on vesicle size as this influences the fluidity and, hence, the permeability of the vesicle membrane [19]. For intravenous applications of liposomes as drug delivery vehicles, unilamellar vesicles with a diameter of around $100\,\mathrm{nm}$ are considered optimal, e.g. for prolonged blood circulation life-times *in vivo* and for maximum accumulation at the sites of disease [38, 342–344].

The extrusion technique originally introduced by Olson *et al.* (1979) [150] is the most popular method to control the mean size and lamellarity of nanometer-sized vesicle suspensions in fundamental and applied research applications [3, 9, 10, 193, 206]. It consists of repetitively (at least 10 times) forcing spontaneously formed multilamellar vesicles (MLVs) through track-etched polycarbonate membranes with defined pore diameters, typically ranging from 30 to $400\,\mathrm{nm}$. The method yields highly reproducible and rather homogeneous VET (vesicles prepared by the extrusion technique) suspensions with a mean vesicle size that reflects the mean pore diameter of the filter membrane used. This is especially true when using $100\,\mathrm{nm}$ pore membranes for final extrusions yielding so-called LUVETs$_{100}$ with predominantly unilamellar

character [3, 9, 10]. The well-defined and homogeneous LUVETs$_{100}$ represent the vesicle structure of choice for controlled delivery-release applications. However, their preparation requires up to 30 recirculations cycles through membranes with decreasing pore sizes (Sec. 2.5.3) which is time consuming and not suitable for industrial large-scale production as outlined in the following [45].

The most widely used device for repetitive vesicle extrusion at the research level is the LIPEX™ Extruder from Northern Lipids [207]. It is a vessel system that operates at medium pressures of up to ≈ 55 bar (800 psi) and is marketed for the batch-wise processing of vesicle suspensions from bench volumes (0.1-10 mL) to preclinical scales (10-800 mL) [9, 193, 206]. For clinical and industrial applications (> 1 L), high pressure filter holders have also been incorporated into continuously operating extrusion processes with recycling options [45, 193, 345]. This has for example been realized in the Maximator® device from CPL SACHSE [210–212]. Limited surface areas and clogging of the nanopore membranes pose, however, serious technical limitations in the large-scale processing of liposome suspensions by continuous, repetitive vesicle extrusion [45, 193, 211].

Currently, the homogenizing techniques employed in industrial liposome manufacturing [41, 45] are adopted from emulsion processing [346] and include mainly microfluidization [201, 202, 347] and high-pressure valve homogenization of coarse MLV pre-suspensions [198–200]. These devices operate at high homogenizing pressures of around 200-2000 bar generating rather polydisperse populations of SUVs with limited loading efficiencies. Furthermore, high energy dissipation and concomitant local temperature increase in the high-pressure process chambers can lead to degradation of both vesicle constituents and sensitive encapsulated components [45, 203].

The vesicle preparation methods based on replacement of organic solvents by aqueous media, including reverse-phase evaporation and enthanol injection, do not require homogenization devices [3]. They are gentle and easy to scale up, thereby offering attractive alternatives to the high-pressure homogenization techniques [45]. Furthermore, reverse-phase evaporation and ethanol injection allow for high encapsulation efficiencies of water-soluble and ethanol-soluble substances, respectively. However, the obtained vesicle suspensions are rather polydisperse and usually contain significant populations of oligolamellar vesicles. Even more compromising is the presence of residual solvent in the final vesicle suspensions which seriously limits their application in pharamceutical and food products [45].

Aim: The aim of the present study was to develop new, scalable processing technologies to generate nanometer-sized, loaded vesicle carriers in a well controlled, reproducible and gentle manner for pharmaceutical, cosmetic, and food applications. The lack of such processing technologies is still one of the major challenges to bridge the gap between the increasing variety of suggested vesicle formulations at the research level and their appearance on the market [35, 45].

Approach: Our approach was to combine the reliable technique of vesicle extru-

sion with the beneficial principles of dynamically enhanced membrane emulsification [220]. The latter technology has been introduced, systematically studied, and optimized for the gentle and controlled production of narrow drop size distributions in emulsion systems at the Laboratory of Food Process Engineering at ETH Zurich [220, 348, 349]. Accordingly, a research scale prototype of the so-called ROtating Membrane ExtrudeR (ROMER) has been designed and built in collaboration with Bühler AG (Uzwil, Switzerland) in the frame of this work.

The core of the ROMER device consists of a plate-plate shear flow cell with a nanopore membrane integrated in the lower plate allowing for continuous, dynamically enhanced vesicle extrusion (see Sec. 2.5.4 for a closer description of the setup). A defined and adjustable shear flow field can be induced at the outlet of the nanopore membrane by precisely controlling the rotational speed of the upper plate and by adjusting the shear gap height at the micrometer-scale.

Depending on the applied shear rate, the ROMER device shall allow for the gentle and controlled shearing-off of extruded vesicles to specifically adjust vesicle size and lamellarity to a given application after a single extrusion cycle. This principle has previously been demonstrated in a microfluidic cross-flow channel [350] which can be regarded as a single pore model of dynamically enhanced membrane extrusion [221]. Ota *et al.* reported on the formation of monodisperse giant unilamellar vesicles by shearing off the leading edge of a deformed planar bilayer in a microfluidic T-junction [350].

Outline: This chapter studies the efficiency of dynamically enhanced vesicle extrusion in homogenizing lipid MLV suspensions using the new ROMER device at varying material and process parameters. The process-structure relationships of the dynamically extruded vesicles are described (Fig. 1.1).

The MLV precursors are prepared by thin film hydration using pharmaceutical grade phosphatidylcholine (PC) isolates from egg yolk and soybean. Optionally, cholesterol (Chol) or sodium cholate (SC) is incorporated in the lipid host membrane to vary bilayer elasticity. Commercially available nanopore membranes with rated pore diameters of 200 nm are evaluated, including track-etched polymer membranes from polycarbonate (PC200) and polyethylene therephthalate (PET200), as well as a sintered ceramic membrane (Cer200). The pore size distributions and porous structures of the membranes are characterized using scanning electron microscopy (SEM) and statistical image analyses of the electron micrographs.

In preliminary experiments, the conventional LIPEX extruder is used to test the performance of the nanopore membranes in static vesicle extrusion. The LIPEX extruder is also used to benchmark MLV homogenization after 1 to 10 static extrusion cycles through the nanopore membranes selected for subsequent systematic ROMER experiments. Finally, the efficiency of the ROMER device in MLV homogenization is studied as a function of the applied shear rate, pore shape, and bilayer elasticity. The extent of MLV homogenization in terms of vesicle size, polydispersity, and

lamellartiy is routinely analyzed by dynamic light scattering (DLS) and an optimized protocol of the TNBS assay for relative external vesicle surface area determination. Morphological studies of vesicles obtained from static and dynamically enhanced extrusion are carried out by cryo transmission electron microscopy (cryo-TEM) and, in the latter case, complemented by small angle neutron scattering (SANS).

The chapter closes with a discussion on the deformation and break-up behavior of lipid vesicles in dynamically enhanced extrusion based on dimensionless numbers and on the results presented in this work.

4.2 Materials and methods

4.2.1 Materials

The naturally occurring synthetic phospholipids 1-palmitoyl-2-oleoyl-*sn*-glycero-3-phosphocholine (POPC; 25 mg mL^{-1} solution in chloroform) and 1-palmitoyl-2-oleoyl-*sn*-glycero-3-phosphoethanolamine (POPE; powder) were purchased from Avanti Polar Lipids (Alabaster, AL, USA). Pharmaceutical grade phosphatidylcholines (PCs) purified from soybean (LIPOID S100, abbreviated as S100 in this work; coarse agglomerates) and from egg yolk (LIPOID E80, abbreviated as E80 in this work; coarse agglomerates) were obtained from Lipoid (Ludwigshafen, Germany) and used without further purification. Chloroform (99.9%; stabilized with ethanol) was a product of ECSA Centonze (Balerna, Switzerland), ethanol absolute (99.9%) of Scharlab (Barcelona, Spain), HCl fuming (37%) of Merck (Darmstadt, Germany) and D(+)-sucrose of AppliChem (Darmstadt, Germany). All other chemicals, namely cholesterol (Chol; 99%), sodium cholate hydrate (SC; from ox or sheep bile, 99%), 2,4,6-trinitrobenzene sulfonate (TNBS; 5 w/v% solution in H$_2$O, BioReagent), Triton X-100 (simply called Triton in this work), boric acid (99.5%), sodium hydroxide (98%), iron(III) chloride hexahydrate (98%), ammonium thiocyanate (99%) and deuteriumoxide (D$_2$O; 99.9 atom% D), were of analytical grade and obtained from Sigma-Aldrich (Buchs, Switzerland).
Stock solutions of 1 w/w% POPE in chloroform, 1 w/w% Chol in chloroform and 0.1 w/w% SC in ethanol were prepared and stored at −20 °C. All aqueous solutions were prepared using ultrapure water from a Synergy water purification system (Merck Millipore, Billerica, MA, USA) and stored at 4 °C.

The chemical compositions and fatty acid distributions of the PC isolates E80 and S100 as provided by the distributor are listed in Tables 4.1 and 4.2, respectively. Table 4.3 shows the chemical structures of the predominant phospholipid species of S100 and E80, as well as of the synthetic phospholipids, sterols and co-surfactants used. The nominal specifications and short names of the commercial nanopore membranes used are summarized in Table 4.4.

4.2.2 Preparation of regularized MLV pre-suspensions

Regularized MLV pre-suspensions for subsequent ROMER experiments and for nanopore membrane performance tests in conventional extrusion were prepared using the thin film hydration method, followed by freeze–thaw cycles, and the conventional extrusion technique [3, 9, 193, 206] (Sec. 2.5.1–2.5.3). The vesicle membrane matrix was formed from E80 or S100 phospholipids. In the case of the addition of

Table 4.1: Chemical composition of E80 and S100 PC isolates. Chemical composition of the phosphatidylcholine isolates E80 (source: egg yolk) and S100 (source: soybean) used in this work, accoring to the distributor Lipoid (Ludwigshafen, Germany).

Component	E80 [w/w%]	S100 [w/w%]
Phosphatidylcholine	81.8	96.3
Lysophosphatidylcholine	2.0	1.0
Phosphatidylethanolamine	8.2	< 0.1
Lysophosphatidylethanolamine	< 0.5	n. a.
N-acylphosphatidylethanolamine	n. a.	< 0.1
Phosphatidylinositol	n. a.	< 0.1
Cholesterol	0.6	n. a.
Sphingomyelin	2.5	n. a.
Triglycerides	2.6	0.6
Non-polar lipids	n. a.	1.4
Free fatty acids	< 0.05	< 0.05
DL-α-tocopherol	0.08	0.19
Water	0.4	0.5
Ethanol	< 0.2	< 0.2

n. a. = not analyzed. Components not analyzed by the distributor represent minor fractions or lack completely in the respective egg yolk or soybean sources.

Table 4.2: Fatty acid distribution of E80 and S100 PC isolates. Fatty acid (FA) composition in % to total fatty acids of the phosphatidylcholine isolates E80 (source: egg yolk) and S100 (source: soybean) used in this work, accoring to the distributor Lipoid (Ludwigshafen, Germany).

Fatty acid (trivial name)	Abbreviation	E80 [%]	S100 [%]
Palmitic acid	C16:0	28-34	12-17
Stearic acid	C18:0	12-15	2-5
Oleic acid	C18:1c9	26-30	11-15
Linoleic acid	C18:2c9c12	13-18	59-70
α-Linolenic acid	C18:3c9c12c15	$\leq$ 1.0	3-7
Polyunsaturated FAs C 20 and higher		6-10	n. a.

n. a. = not analyzed. Components not analyzed by the distributor represent minor fractions or lack completely in the respective egg yolk or soybean sources.
Note: The abbreviation 18:1c9, for example, indicates that the linear fatty acid has 18 carbon atoms with one *cis* double bond starting at position 9, where the carboxy C atom is carbon number 1.

Table 4.3: Biologically occurring lipids and surfactants used in this work. Abbreviation, nomenclature according to IUPAC, chemical structure, and molecular weight of the phospholipids, sterols, and co-surfactants used.
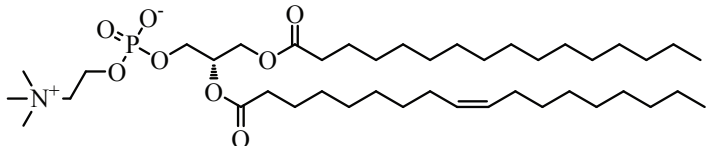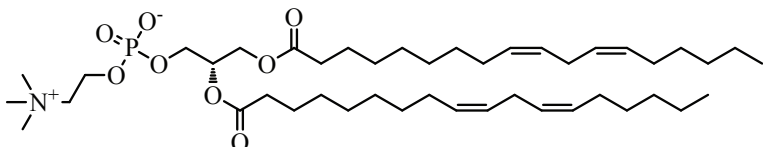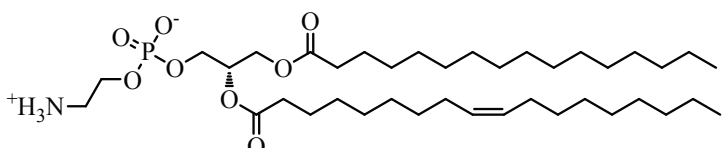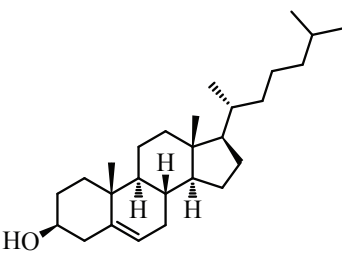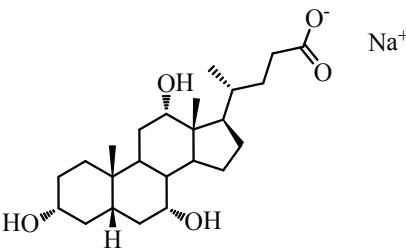
Abbreviation	IUPAC nomenclature and chemical structure	M_w [g/mol]
POPC (E80)	1-palmitoyl-2-oleoyl-*sn*-glycero-3-phosphocholine	760.076
DLPC (S100)	1,2-dilinoleoyl-*sn*-glycero-3-phosphocholine	782.082
POPE	1-palmitoyl-2-oleoyl-*sn*-glycero-3-phospho-ethanolamine	717.996
cholesterol	(3β)-cholest-5-en-3-ol	386.654
sodium cholate	$3\alpha,7\alpha,12\alpha$-trihydroxy-5β-cholan-24-oic acid sodium salt	430.553

Table 4.4: Nominal specifications of nanopore membranes used in this work, as provided by the manufacturer.

Short name	PC800	PC200	PET210	Cer200
Manufacturer	Whatman (Kent, UK)	Whatman (Kent, UK)	Oxyphen (Wetzikon, Switzerland)	Fraunhofer IKTS (Dresden, Germany)
Product name	Nucleopore®	Nucleopore®	RoTrac®	Mikrofiltrations-flachmembran
Material	Polycarbonate (PC)	Polycarbonate (PC)	Polyethylene therephthalate (PET)	Aluminium oxide (Al_2O_3)
Porous structure	Track-etched channels	Track-etched channels	Track-etched channels	Sintered particles
Pore diameter [nm]	800	200	210	200 (support: 2.5 µm)[a]
Pore density [10^6 cm^{-2}]	30	300	50	n. a.
Membrane thickness [µm]	9	10	35.5	10 (support: 1 mm)[a]
Air flow rate [L min^{-1} cm^{-2} bar^{-1}]	40.6	5.1	0.7	n. a.

n. a. = not available.

[a] The ceramic sinter membrane is asymmetric and consists of a coarse support and a thin active membrane layer.

bilayer stiffening or softening components, 30 mol% Chol or 10 mol% SC, respectively, was included in the lipid mixtures. For external surface area determinations, 5 mol% POPE was incorporated in the lipid vesicles prepared from S100 matrix membranes, whereas E80, which naturally contained 8.8 mol% PE, was used as obtained.

Appropriate amounts of lipid stock solutions (Sec. 4.2.1) and E80 or S100 agglomerates were weighed in a 100 mL round-bottom flask and dissolved in additional chloroform. A thin lipid film was formed by rotary evaporation, followed by residual solvent removal under high vacuum overnight. Unless otherwise stated, the dry lipid film was hydrated in ultrapure water to yield a total lipid concentration of 6.45 mM (corresponding to 5 mg mL^{-1} S100) and vortexed until complete film dispersion. The MLV suspension obtained was taken through 10 freeze–thaw cycles to promote an even distribution of lipids throughout the bilayers and to reduce the extent of multilamellar character, as well as the amount of limit size vesicles [3, 9, 205].

To improve the quality and reproducibility of DLS measurements, the MLV suspension was cleaned and regularized by pre-extruding it three times through a PC800 nanopore membrane using the conventional LIPEX extruder from Northern Lipids (Burnaby, BC, Canada) and compressed nitrogen gas (purity grade 4.5, 99.995%; PanGas, Dagmersellen, Switzerland) [209, 257]. Static and dynamic extrusion experiments were carried out at room temperature, which is well above the main phase transition temperatures T_m of soy PC (-15±5 °C) [351] and egg PC (-5.8±6.5 °C) [54]. Finally, the obtained VET$_{800}$ suspension was diluted with Millipore water to a total lipid concentration of 0.645 mM. This was the working concentration of ROMER and membrane performance experiments carried out on the day of vesicle preparation. Typically, around 150 mL of VET$_{800}$ suspension was prepared for an experimental ROMER series using one nanopore membrane type and testing four shear rate settings in triplicate.

For cryo-TEM studies of defined vesicles prepared by the conventional extrusion technique, LUVETs$_{100}$ were prepared at a total lipid concentration of 10 mM in MilliQ water following the procedure described in Section 3.2.2. ROMER samples for cryo-TEM imaging were prepared at a total lipid concentration of 20 mM. Samples for SANS measurements were prepared at the standard concentration of ROMER experiments (0.645 mM) but using D$_2$O instead of H$_2$O as hydration medium.

4.2.3 ROMER experiments

The design and principle of the ROMER device (Sec. 2.5.4) allowed to study the effect of a shear field at the membrane outlet on the homogenization of MLVs by dynamically enhanced pore extrusion. Systematic ROMER experiments were performed at varying shear rates using two types of commercial, track-etched nanopore

Table 4.5: Vesicle membrane compositions studied in systematic ROMER experiments.

Lipid mixture	Molar ratio [mol/mol]
S100/POPE	95:5
S100/Chol/POPE	65:30:5
S100/SC/POPE	85:10:5
E80	100
E80/Chol	70:30
E80/SC	90:10

membranes (PC200 and PET210; Tab. 4.4) and different vesicle membrane compositions of varying bilayer elastic properties (Tab. 4.5).

Figure 4.1 illustrates the experimental setup of the ROMER process as implemented in our laboratory and described below. Prior to an experimental ROMER series, in which one combination of membrane type and vesicle bilayer composition was studied at varying shear rates, 16 units of static membrane modules were prepared by gluing flat membrane discs (**1**) onto the planar membrane holders (**2**, Fig. 4.1A) using a two-component adhesive (Scotch-Weld™ DP 610 for PC membranes, Scotch-Weld™ DP 810 for PET membranes; 3M Deutschland, Germany). The adhesive bond was allowed to harden for 2-4 hours at $60\,°C$, followed by curing for at least 3 days at room temperature.

Four discrete shear rate settings ($\dot{\gamma}_{rep} = 0\,s^{-1}$, $6021\,s^{-1}$, $30\,107\,s^{-1}$, and $60\,214\,s^{-1}$; see Sec. 2.5.4 for the definition of $\dot{\gamma}_{rep}$) were tested by controlling the rotational speed of the rotor (**4**) at 0, 1000, 5000, and $10\,000\,rpm$ and keeping the shear gap height (**5**) constant at $200\,\mu m$ (Fig. 4.1B). A feeler gauge (**6**) was used to adjust the shear gap height via the μm-screw in the fully assembled ROMER device (**0**) by preliminarily omitting the insertion of the product reservoir (**3**) to allow access of the feeler gauge to the shear gap (Fig. 4.1B and C). The rotor speed was controlled via a compact drive (**9**; MCD EPOS 60 W) with its associated software (EPOS User-Interface version 2.31) from Maxon Motor (Sachseln, Switzerland). The VET$_{800}$ pre-suspension was pumped from the reserve polypropylene syringe (**7**; BD Plastipak™ Luer Lok 20 mL, Becton Dickinson, Allschwil, Switzerland) via connecting polyvinyl chloride tubing (Becton Dickinson) through the membrane and into the shear gap using a syringe pump (**8**; PHD 2000 Infusion, Harvard Apparatus, MA, USA) at a controlled flow rate of $1\,mL\,min^{-1}$. A piezoresistive pressure sensor (**9**; XTM-190 3.5 bar or 18 bar, Kulite Semiconductor, Kaiserslautern, Germany) was inserted at the membrane inlet to detect possible membrane defects developing during extrusion experiments. Pressure data were visualized and recorded using the LabVIEW software (version 8, National Instruments) (Fig. 4.1C).

Each shear-enhanced extrusion experiment at a specific shear rate setting was run
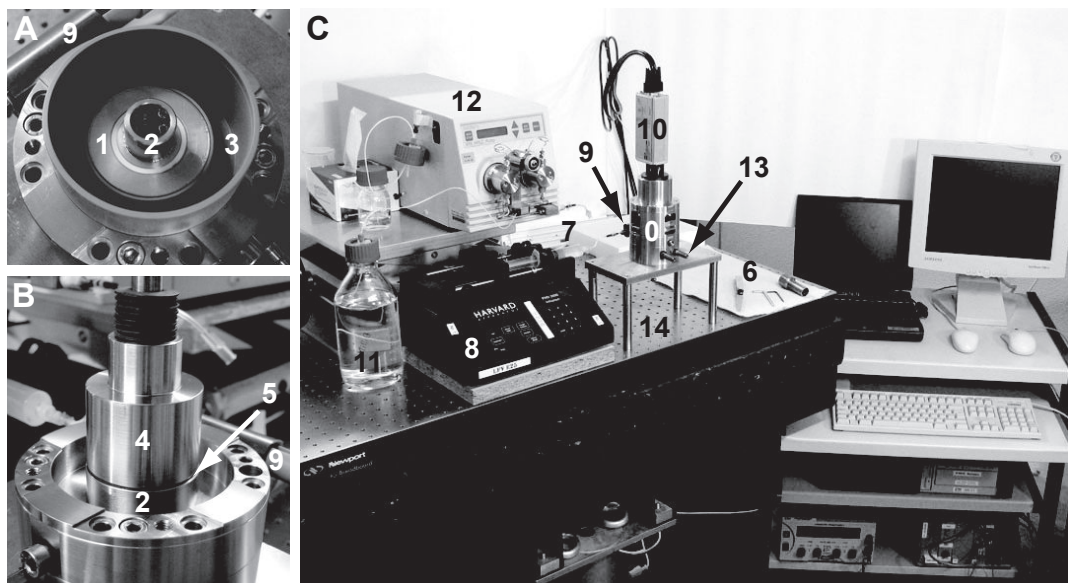
Figure 4.1: Photograph of the experimental setup of the ROMER device (0).
The key components of the process and associated elements are highlighted. (A) Top
view of the membrane module with the circular flat nanopore membrane (**1**) glued onto
the static membrane holder (**2**). The product reservoir (**3**) is inserted for subsequent
sample collection. (B) Side view of the shear-enhanced extrusion chamber with the rotor
(**4**) situated above the static membrane module (**2**). The shear gap height (**5**) between
membrane and rotor was adjusted using a feeler gauge (**6**). (C) ROMER process including
a reservoir syringe containing the initial VET$_{800}$ suspension (**7**), a flow rate-controlled
syringe pump (**8**), a pressure sensor at the membrane inlet (**9**), the motor of the ROMER
device (**10**), a Millipore water container (**11**) and HPLC pump (**12**) for rinsing, and
connectors to optional thermostat controller (waterbath) of the ROMER housing (**13**).
The device was installed on a vibration-free optical table (**14**).

.

for 400 s and carried out in triplicate. Extruded samples were collected from the
product reservoir (**3**). Between every extrusion experiment, the membrane module
was replaced, the inlet tubing was rinsed with Millipore water (**11**) using a HPLC
pump (**12**; 515 HPLC Pump, Waters Corporation, MA, USA), and the product
reservoir (**3**) and rotor (**4**) were cleaned and dried.

The structure of dynamically extruded vesicle populations was systematically ana-
lyzed off-line using DLS and the TNBS assay to measure their mean hydrodynamic
diameter D_h and polydispersity index *PDI*, as well as the average relative external
surface area E, respectively. Mean values and standard deviations of the means of
these structural parameters (D_h, PDI, E) were calculated, normalized to the cor-
responding values of the initial VET$_{800}$ suspension ($D_{h,0}$, PDI_0, E_0), and plotted as
a function of shear rate.

4.2.4 SEM and characterization of membrane pore structures

For the surface characterization of pore shape and pore size, nanopore membranes were visualized by scanning electron microscopy (SEM). Two-dimensional micrographs of membrane surfaces were taken by Sebastian Holzapfel on a Ultra 55 scanning electron microscope from Carl Zeiss (Oberkochen, Germany) at the Frontiers In Research: Space & Time (FIRST) center at ETH Zurich. Prior to examination, samples were coated with a thin layer ($\approx 10\,\text{nm}$) of gold-platinum alloy using a sputter system (SCD-050, BAL-TEC AG, Liechtenstein) to increase surface conductivity. This reduces loading of the sample with electrons and subsequent imaging artifacts. For each membrane type, around 100 micrographs of adjacent membrane areas were acquired to allow for a statistical analysis of mean pore size and pore size distribution of at least 750 pores.

Surface pore areas were derived from the pore perimeters measured manually using a touch screen and the image processing software ImageJ (version 1.43r). Thereby, single pore openings were distinguished from surface pore clusters to separately calculate the size distribution functions, including their characteristic parameters, of the single pore population and of the total pore population.

The pore size x was defined by the diameter of an equivalent circular pore area. Since pore size characterization by the analysis of SEM micrographs is based on a counting technique, all measured pore sizes were equally weighted by considering the distribution functions based on the number of pores [305]. The number-weighted logarithmic density and cumulative distribution functions $q_0(\lg x)$ and $Q_0(x)$, respectively, as well as the corresponding distribution parameters $x_{50,0}$, $x_{10,0}$, $x_{90,0}$, and $span_0$ were then calculated as described in Section 3.2.6.

4.2.5 DLS

Vesicle size and polydispersity were analyzed by dynamic light scattering (DLS) as outlined in Section 4.2.5. The light scattering instrument used for most DLS measurements was a BI-200SM research goniometer (Brookhaven Instruments, NY, USA) that was equipped with a diode laser (DPY315M-100, Coherent, CA, USA) operating at a wavelength of 532 nm. The temperature of the refractive index matching naphthalene bath surrounding the sample holder was maintained at 25 °C and the scattering angle θ was set to 90°.

Vesicle suspensions were diluted in their suspension medium (Millipore water) to approximately 0.1 mM total lipids and placed in a 5 mL cylindrical glass vial. For each sample, the intensity time autocorrelation function was recorded five times for a period of 2 min to check reproducibility and sample stability. The collected data was combined and analyzed with the method of cumulants (Eq. 2.21, see Sec. 4.2.5)

[259] to extract the intensity-weighted average hydrodynamic diameter D_h and poly-dispersity index *PDI* using the Brookhaven particle sizing software BI-9000 (version 4.02). Three independent identical samples were analyzed following this procedure and the corresponding sample mean values and standard deviations of the means were calculated.

Volume-weighted size distributions of a few example liposome suspensions were determined on a Zetasizer Nano ZS (Malvern Instruments, UK) in the backscattering mode (scattering angle $\theta = 173°$) and at $T = 25\,°C$.
Vesicle suspensions were diluted in their suspension medium (Millipore water) to approximately 0.2 mM total lipids and placed in a 1.5 mL disposable polystyrene cuvette. Two to three independent identical samples were analyzed and the measurement of each sample was repeated three times.
The intensity time auto correlation functions were analyzed using the Multiple Narrow Modes algorithm incorporated in the Malvern DTS software (version 5.10), which is based on a non-negatively constraint least square fit (NNLS; Sec. 4.2.5) [260, 304]. The obtained intensity-weighted size distributions (scaling with r^6) were converted into volume-weighted size distributions (scaling with r^3) using Mie theory [264], even though Mie theory applies to homogeneous solid spheres only which do not precisely represent the geometry of vesicles.

4.2.6 TNBS assay

The degree of vesicle lamellarity was estimated by measuring the relative external surface area E of PE-doped vesicles using the TNBS assay described earlier by Gruber and Schindler [204] and optimized in the frame of this thesis [10]. In principle, the ratio of outermost monolayer lipid to total vesicle membrane lipid was derived from the spectroscopic signal change induced by the reaction of exposed aminolipids with external TNBS and normalized to the signal change for reaction of all aminolipids present (see Section 2.7.2 for a closer description of the assay principle).
The TNBS *reagent solution*, a 0.1 w/v% TNBS solution, was freshly prepared before use by diluting the commercially available 5 w/v% TNBS solution in H_2O with borate buffer (0.2 M boric acid, pH 8.5). For external aminolipid labeling, 300 µL of vesicle suspension (containing 0.645 mM total lipids, typically with 5 mol% POPE) was mixed with 100 µL of start buffer (0.2 M boric acid, 1 M sucrose, pH 9.0) to reach a reaction pH of 9.7. The labeling reaction was then started by adding 25 µL of TNBS *reagent solution*. After incubation for 40 min at room temperature, the reaction was stopped by adding 15 µL of 3 M HCl and the externally labeled vesicles were solubilized with 10 µL of 5 w/v% Triton to obtain a clear, mixed micellar

sample solution (450 µL, no turbidity). For total aminolipid labeling, the corresponding *total solution* was prepared by first adding 100 µL of start buffer (0.2 M boric acid, 1 M sucrose, pH 9.0) containing 0.5 w/v% Triton to a 300-µL aliquot of the same vesicle suspension which leads to vesicle solubilization. Then 25 µL of TNBS *reagent solution* was added to start the labeling of all aminolipids present and, after 40 min at room temperature, the reaction was stopped with 15 µL of 3 M HCl. Finally, the mixture was diluted by adding 10 µL of Millipore water to obtain the mixed micellar *total solution* (450 µL, no turbidity). The *sample blank solution* and the *total blank solution* were prepared following the same protocols as described above, but in the absence of lipids, i. e. using Millipore water in place of the vesicle suspension.

The *sample solution*, the *total solution* and the two *blank solutions* were prepared in triplicate. Their absorption spectra were measured at room temperature against a matrix blank between 280 and 600 nm using a Hitachi U-2800 double beam UV/Vis spectrophotometer and 1-cm, 0.7-mL quartz cuvettes. The absorbance at $\lambda_{\max} = 344$ nm (A_{344}) was used to calculate the relative external surface area

$$E\ (\%) = 100 \frac{A_{344}^{\text{sample}} - A_{344}^{\text{sample,blank}}}{A_{344}^{\text{total}} - A_{344}^{\text{total,blank}}}, \tag{4.1}$$

where A_{344}^{sample}, $A_{344}^{\text{sample,blank}}$, A_{344}^{total}, and $A_{344}^{\text{total,blank}}$ are the average absorbance values of the three repeat *sample solutions*, the *sample blank solutions*, the *total solutions*, and the *total blank solutions* at $\lambda_{\max} = 344$ nm, respectively. Linearity between A_{344} and POPE concentration was demonstrated in DHPC/POPE micellar solutions with POPE concentrations ranging from 5 to 45 µm.

4.2.7 Stewart assay

Phospholipid concentrations in the liposomal S100 suspensions were determined following a recent version of the colorimetric assay described by Stewart [142, 298]. The method is based on the ability of phospholipids to form a colored complex with ammonium ferrothiocyanate which is readily soluble in chloroform and exhibits an absorption maximum around $\lambda_{\max} = 488$ nm. In contrast to the Bartlett assay [352], which measures total inorganic phosphate after acid digestion of the phospholipid, the presence of inorganic phosphate from buffer solutions does not interfere with the Stewart assay.

A 0.1 M ammonium ferrothiocyanate solution was prepared by dissolving 30.40 g of ammonium thiocyanate and 27.03 g of ferric chloride hexahydrate in Millipore water and making up to 1 liter. The solution is stable at room temperature for several months. An aliquot (typically 150 µL) of the liposome suspension (containing $\approx$ 0.5 mg mL^{-1} total lipids) was added to a polypropylene centrifuge tube, followed
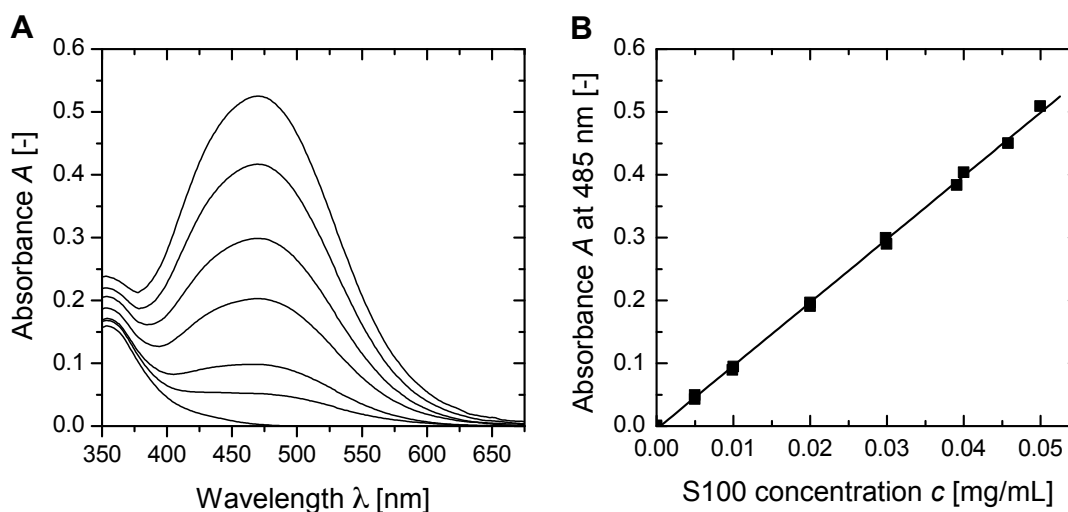
Figure 4.2: Quantification of total phospholipids by the Stewart assay. (A) Absorption spectra of S100 phosphilipids reacted with ammonium ferrothiocyanate at different concentrations of S100 in chloroform (0.005, 0.01, 0.02, 0.03, 0.04, and 0.05 mg mL^{-1}), measured against chloroform. (B) Dependence of the absorbance A at $\lambda = 485$ nm on the concentration c of complexed S100 phospholipids in the chloroform phase. Line represents linear least-square fit between 0 and 0.05 mg mL^{-1}: $A = 10.079c - 0.005$; $R^2 = 0.9989$.

by 2.0 mL of chloroform and 2.0 mL of the ammonium ferrothiocyanate solution. The test tube was vigorously vortexed for 15 s to extract the colored complex into chloroform and centrifuged for 5 min at 1000 rpm to get a clear separation of the biphasic system. The resulting complexed phospholipid concentration in the chloroform phase was approximately 0.04 mg mL^{-1}. The absorption spectrum of the chloroform layer was acquired against a chloroform blank between 350 and 700 nm using a Hitachi U-2800 double beam UV/Vis spectrophotometer and 1-cm, 1.4-mL quartz cuvettes. The absorbance at $\lambda = 485$ nm was compared to a calibration curve (Fig. 4.2 B) to find the phospholipid concentration in the liposome suspension. For each sample, the analysis was conducted in triplicate. The calibration curve was generated from a 0.1 mg mL^{-1} S100 stock solution in chloroform that was prepared in duplicate and diluted to a concentration range of 0.005 to 0.05 mg mL^{-1} (Fig. 4.2). It has to be noted that the slope of absorbance vs. complex concentration standard curves varies for different phospholipid head groups and has to be determined for every single species or mixture of phospholipids used. Since the Stewart assay requires a positive charge to be present in the lipid, it is unresponsive to negatively charged phospholipids, such as phosphatidic acids and phosphatidylglycerol.

4.2.8 cryo-TEM

Morphological studies of Millipore water based 10-20 mM liposome suspensions were carried out by cryo-transmission electron microscopy (cryo-TEM) at the Electron Microscopy Center ETH Zurich (EMEZ). Specimens were prepared and analyzed by Takashi Ishikawa (Department of Biology, ETH Zurich and Biomolecular Research Laboratory, PSI Villigen) following the procedure described earlier [353].

A 3.5 μL drop of the liposome suspension was adsorbed on a holey carbon grid (Quantifoil Micro Tools, Jena, Germany), blotted at controlled temperature (room temperature) and humidity ($\sim 95\%$) to form a free spanning aqueous thin film, and plunged in liquid ethane using a Vitrobot apparatus (FEI, Eindhoven, Netherlands). At the high cooling rate of water during freezing in liquid ethane, the aqueous specimen is vitrified and can subsequently be analyzed at liquid nitrogen temperatures of around $-162\,°C$. This was done in a 626 cryo-holder from Gatan (Pleasanton, CA, USA) using a Tecnai G2 F20 microscope (FEI) that was equipped with a field emission gun and Tridem energy filter (Gatan) operated at an accelerating voltage of 200 kV. The data were recorded by a 2048×2048 CCD camera (Gatan) at an underfocus of 5–10 μm to enhance the poor absorption contrast typical for biological samples. Small, contrast rich particles appearing in many of the micrographs stem from ice crystal contaminations formed during the freezing procedure.

4.2.9 SANS

SANS was used to extract quantitative information on vesicle morphology, lamellar structure and bilayer interactions in polydisperse liposome suspensions generated by dynamically enhanced pore extrusion. VET_{800} pre-suspensions for ROMER experiments and subsequent SANS measurements were hydrated and extruded in D_2O following the protocol described in Section 4.2.2. D_2O addition maximizes the scattering contrast between the protonated bilayers and the deuterated dispersion medium thus creating best conditions for membrane thickness evaluation [272]. Samples were prepared and analyzed at the standard lipid concentration of ROMER experiments (0.645 mM) using pure POPC. At this concentration (≈ 0.05 w/w%), there is no long-range order between the bilayers of different vesicles [219].

SANS measurements were conducted by Marianne Liebi on the SANS-I beam line at the Paul Scherrer Institute (PSI, Villigen, Switzerland). The neutron wavelength was fixed at 8 Å. Data were collected on a two-dimensional ^{3}He position-sensitive detector at sample-to-detector distances of 2 m, 6 m, and 18 m covering a momentum transfer of $0.003 \leq q \leq 0.15\,\text{Å}^{-1}$. All scattering patterns collected were azimuthally isotropic. After correcting the data for background signal from the empty setup, sample transmission, and detector efficiency, the two-dimensional intensity maps were radially averaged to obtain the one-dimensional intensity functions $I(q)$. The

commonly called scattering curves were obtained by plotting the scattering intensity $I(q)$ over the magnitude of the scattering vector q in a double-logarithmic graph. The scattering intensity functions $I(q)$ were described as the product of the size averaged form factor $F(q)$ and the structure factor $S(q)$ following [268, 354, 355]:

$$I(q) = \langle F^2 \rangle(q)S(q) \tag{4.2}$$

For fitting of the scattering curves, the software package SASfit was used as described in Results and Discussion [355]. All fits included a constant incoherent background.

4.3 Results and discussion

4.3.1 Vesicles prepared from the commercial soybean and egg yolk phosphatidylcholine isolates E80 and S100

With regard to the development of a continuous processing of tailored vesicles at pilot scale, ROMER experiments were conducted using pharmaceutical grade phosphatidylcholines (PCs) purified from egg yolk and soybean. They belong to the cheapest and most established commercial sources for the isolation of phosphatidylcholines at large quantities.

The lipid and fatty acid compositions of the respective E80 and S100 products used in this work are summarized in Tables 4.1 and 4.2 (see Materials and Methods). According to their typical fatty acid distributions (Tab. 4.2), the predominant phosphatidylcholine proportions present in E80 ($\approx 83\,\mathrm{mol\%}$ PC) and S100 ($\approx 95\,\mathrm{mol\%}$ PC) can be widely represented by the chemical structures of POPC and DLPC, respectively (Tab. 4.3). In this regard, vesicles prepared from E80 or S100 are probably similar in many respects to pure POPC or DLPC vesicles, but the presence of minor fractions of the various lipidic components other than PCs in the natural isolates (Tab. 4.1) may significantly alter physical bilayer properties [145].

LUVET$_{100}$ suspensions prepared from E80 and S100 PC isolates

In a first step, the ability of E80 and S100 to form well-defined vesicle structures was evaluated by following the most common and highly reproducible protocols for the preparation of 100 nm-sized unilamellar vesicles. They include thin film hydration, freeze-thawing, and sequential static extrusion through, ultimately, 100 nm-pore polycarbonate membranes as described in the Background Sections 2.5.1–2.5.3 and in the Experimental Section 3.2.2.

The morphologies of the resulting E80 and S100 LUVETs$_{100}$ were evaluated by cryo-TEM imaging. Subsequent image analysis allowed to calculate the cumulative volume distribution functions $Q_3(x)$ (Eq. 3.3 with the vesicle number n being replaced by the vesicle mass, i.e. vesicle volume, m) and to extract the volume-weighted median diameters $x_{50,3}$ (see Sec. 3.2.6). DLS measurements were performed to determine the vesicle mean sizes and size distributions in terms of average hydrodynamic diameters D_h and polydispersity indices *PDI*.

Results: The cryo-TEM micrographs in Figure 4.3 show that the application of the conventional extrusion protocol to E80 and S100 suspensions led to the expected formation of mostly unilamellar vesicles with a mean diameter close to that of the pore size used, i.e. 100 nm [3, 9, 193, 206]. The average hydrodynamic diameters of
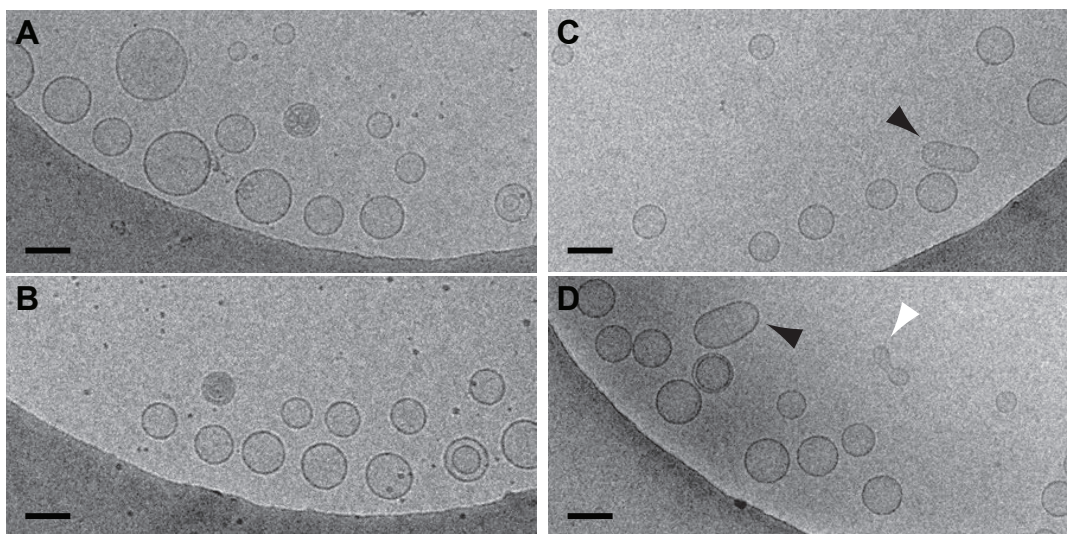
Figure 4.3: Cryo-TEM micrographs of LUVETs$_{100}$ prepared from E80 and S100. LUVETs$_{100}$ were prepared from commercial, pharmaceutical grade phosphatidylcholines purified from egg yolk (E80; A-B) and soybean (S100; C-D) using track-etched polycarbonate membranes with 100 nm pore diameters for final extrusions. *Black arrows:* prolate vesicle shapes. *white arrow:* oblate vesicle shape. Total lipid concentration: 10 mM. Scale bar = 100 nm.

E80 and S100 LUVETs$_{100}$ prepared at an extrusion pressure of approximately 12-14 bar were 119 nm and 97 nm, respectively (Tab. 4.6). This is in good agreement with DLS results reported in literature for LUVETs$_{100}$ prepared in a comparable pressure range using egg PC ($D_h = 139\pm36$ nm) [9], POPC ($D_h \approx 126$ nm) [15], soy PC ($D_h = 100–125$ nm) [218], and DOPC ($D_h \approx 94$ nm) [217].

Size of E80 vs. S100 LUVETs$_{100}$: The larger size and uniform sphericity of LUVETs$_{100}$ from E80 (Fig. 4.3A-B) compared to those prepared from S100 (Fig. 4.3C-D) is most likely the result of an increased membrane cohesion induced by some of the lipidic residues present in the E80 isolate but absent in the S100 product (Tab. 4.1). Cholesterol (≈ 1.2 mol% in E80), for example, is well known to have a condensing effect in lipid bilayers, especially in coexistence with sphingomyelin (≈ 2.7 mol% in E80) [11, 172]. Increasing fractions of phoshatidylethanolamine (≈ 8.8 mol% in E80) were also reported to considerably increase the lipid packing density in various mixed PC/PE vesicle formulations because of the smaller volume of the PE headgroup and its hydrogen bonding capability (Tab. 4.3) [10, 138, 356, 357]. Finally, the abundance of unsaturated acyl chains with two or more alternating *cis* double bonds is considerably lower in E80 phospholipids than in S100 phospholipids (Tab. 4.2) resulting again in increased lipid ordering and higher rigidity in E80 bilayers [13, 14, 106, 141].

All these characteristic E80 components, including cholesterol, sphingomyelin, phosphatidylethanolamine and saturated/monounsaturated chain PCs, contribute to an increased lysis tension σ_l [13, 15, 141] and a higher elastic bending modulus k_c [14, 128, 137] in the vesicle membrane. An increase in both of these material parameters has previously been shown to result in larger sizes of LUVETs$_{100}$ and sonicated unilamellar vesicles prepared from POPC and egg PC, respectively [15, 128, 137].

Shape of E80 vs. S100 LUVETs$_{100}$: The surface of the LUVETs$_{100}$ from E80 was rather smooth and spherical (Fig. 4.3A–B) as typically observed in extruded vesicles prepared from egg PC [9, 193, 358].

The deflated, non-spherical shapes adopted by some of the visualized S100 LUVETs$_{100}$ correspond to well-described stationary shapes of vesicles disposing of excess membrane area, i.e. having a reduced volume of $v < 1$ (Eq. 2.2, Background Sec. 2.3.2). According to the spontaneous-curvature model for vesicles consisting of single-component, symmetric bilayers with spontaneous curvature $C_0 = 0$, vesicles with $v \lesssim 1$ are most stable, i.e. confine minimum bending energy, by adopting prolate ellipsoid shapes (black arrows in Fig. 4.3C–D). For $v < 0.65$, the bending energy becomes minimal for oblate ellipsoids corresponding to the vesicle shape indicated by the white arrow in Fig. 4.3D [73, 84]. Hence, the observed non-sphericity of S100 LUVETs$_{100}$ can primarily be attributed to vesicle excess area and is not necessarily related to the S100 bilayer's lower elastic energy barrier to bending and concomitant thermally induced surface undulations or even membrane invaginations [81].

Cryo-TEM vs. DLS: Due to the different weighting of measured vesicle sizes, the volume-weighted median diameters $x_{50,3}$ (scaling with r^3) calculated from cryo-TEM image analysis were slightly smaller than the intensity-weighted average diameters D_h (scaling with r^6) obtained from DLS experiments (Tab. 4.6). The small shift between volume and intensity-weighted size distribution parameters and the low *PDI* values of both E80 and S100 LUVET$_{100}$ suspensions indicate rather homogeneous monomodal size distributions which is intrinsic to the extrusion method using 100 nm-pore filters [3, 15].

Cryo-TEM allows the undistorted direct visualization and authentic size determination of individual vesicles, but statistically firm and true size distributions can only be derived from a large number of independent micrographs, provided that the frozen liquid film across the holey grid contains a representative vesicle population as present in the bulk. DLS, on the other hand, is an experimentally simple, fast, and easily accessible *in-situ* measurement technique that averages over the whole sample volume providing good sample statistics. Therefore, DLS was used to compare average sample sizes and polydispersities in the following systematic parameter studies using the ROMER device, bearing the limitations of the indirect and model-dependent light scattering technique, including its sensitivity to large particles, in mind (see Sec. 4.2.5) [248].

Table 4.6: Structural parameters of LUVET$_{100}$, VET$_{800}$ and MLV suspensions prepared from E80 and S100 matrix membranes with and without the addition of cholesterol (Chol) and sodium cholate (SC). LUVETs$_{100}$ and VETs$_{800}$ were prepared by the conventional repetitive extrusion technique using track-etched polycarbonate membranes with nominal pore diameters of 100 nm and 800 nm, respectively, for final extrusions. Shown are the average hydrodynamc diameter D_h and polydispersity index PDI obtained from DLS measurements, the volume-weighted median diameter $x_{50,3}$ calculated from cryo-TEM image analysis and the relative external surface area E determined by the TNBS assay.

Vesicle suspension	Lipid composition	Molar ratio [mol%]	D_h [nm]	PDI [–]	$x_{50,3}$ [nm]
LUVET$_{100}$	E80[1]	100	119.1 ± 0.2	0.09	113.7
	S100[1]	100	96.8 ± 0.2	0.05	85.3

Vesicle suspension	Lipid composition	Molar ratio [mol%]	D_h [nm]	PDI [–]	E [%]
VET$_{800}$	E80[4]	100	349.8 ± 11.8	0.20	22.5 ± 1.5
	E80/Chol[1]	70:30	542.9 ± 7.3	0.18	26.4 ± 1.3
	E80/SC[1]	90:10	323.5 ± 4.4	0.26	48.3 ± 7.1
	S100/POPE[4]	95:5	875.5 ± 22.7	0.23	14.9 ± 1.7
	S100/Chol/POPE[1]	65:30:5	717.6 ± 0.5	0.27	18.1 ± 0.8
	S100/SC/POPE[1]	85:10:5	353.8 ± 8.2	0.31	41.9 ± 0.6
MLV	E80[3]	100	448.7 ± 9.1	0.30	n. a.
	S100[3]	100	1978.7 ± 182.1	0.35	n. a.

n. a. = not analyzed.

[n =] Number of samples used for averaging data.

[n = 1] Results represent mean values ± standard deviations of the means of 3 independent measurements of n = 1 identical samples.

[n > 1] Results represent mean values ± standard deviations of the means of n independent preparations of identical samples.

Note: Standard deviations of the means of *PDI* results are omitted for reasons of clarity.

115

VET$_{800}$ pre-suspensions prepared from E80 and S100 PC isolates

To compare the extents of vesicle homogenization by shear-enhanced pore extrusion at varying material and process parameters on relative scales, the structural parameters of dynamically extruded vesicles will be normalized to the corresponding values of the initial VET$_{800}$ suspensions. Table 4.6 includes the size distribution parameters D_h and *PDI* as well as the relative external surface areas E obtained from DLS measurements and TNBS assays, respectively, for the different VET$_{800}$ pre-suspensions used as starting material for ROMER experiments.

The pre-suspensions were obtained by extruding heterogeneous MLV precursors three times through PC800 membranes using the LIPEX device as described in Section 4.2.2. Since aminolipids are practically absent in soybean isolates (Tab. 4.1), S100 vesicles were doped with a small fraction of POPE (5 mol%) to allow for subsequent external surface area analysis with TNBS. The addition of POPE marker lipids was not observed to influence the mean size of VET$_{800}$ suspensions based on S100 (data not shown).

Plain phospholipid VETs$_{800}$: The pre-extruded VET$_{800}$ suspensions prepared from plain E80 and S100/POPE had an average diameter of approximately 350 nm and 880 nm, respectively, and were generally fairly polydisperse ($PDI \approx 0.2$). As expected, the corresponding values of relative external surface area E inversely correlated with vesicle size, i.e. E decreased with increasing vesicle diameter due to a higher degree of lamellarity (E80 VETs$_{800}$: $E = 22.5\%$; S100/POPE VETs$_{800}$: $E = 14.9\%$).

Effect of cholesterol insertion: In contrast, both the diameter and relative external surface area of E80 VETs$_{800}$ increased upon incorporation of the membrane stiffening component cholesterol ($D_h \approx 540$ nm; $E = 26.4\%$). This can be explained by the higher resulting bilayer bending modulus leading not only to increased vesicle sizes [128, 137] but also to larger interlamellar distances, which in turn decrease vesicle lamellarity [107]. The concomitant increase in vesicle size and external surface area upon cholesterol incorporation was not apparent for S100/POPE VETs$_{800}$. This is most probably due to the higher degree of lipid chain unsaturation in the S100 membranes, which is known to reduce the ordering and rigidifying effects of cholesterol [159, 359].

Effect of sodium cholate insertion: Inclusion of cone-shaped sodium cholate (SC) in E80 and S100 bilayers, on the other hand, considerably decreased the equilibrium size of both VET$_{800}$ systems to $D_h \approx$ 320-350 nm. This can be explained by the smaller spontaneous radii of bilayer curvature resulting from such phospholipid–SC mixtures [81]. The corresponding external surface area results ($E > 40\%$) were close to the values expected for predominantly unilamellar vesicle populations [9, 10]. However, at the average vesicle diameter of more than 300 nm, these E values are strongly believed to be overestimated due to contributions of internal lipid labeling

following TNBS permeation through the soft and less ordered phospholipid–SC vesicle membranes [10, 176, 182].

Plain phospholipid MLVs: The large difference in mean sizes between plain E80 and S100/POPE VETs$_{800}$ prepared in the absence of membrane interacting compounds was unexpected and can not fully be explained. However, it is apparent that the obtained VET$_{800}$ sizes directly originated from the average diameters of the corresponding MLV precursors as listed in Table 4.6. At constant swelling conditions, pure E80 spontaneously formed relatively small MLVs upon thin film hydration ($D_h \approx 450\,\text{nm}$), while S100 self-assembled into very large MLVs ($D_h \approx 2\,\mu\text{m}$) of comparable polydispersity.
Having a mean diameter of $D_h > 1\,\mu\text{m}$, S100 MLVs cannot accurately be characterized by DLS since measurements are affected by multiple scattering and/or a fluctuating number of low concentrated particles in the measuring volume [257]. After the pre-extrusion step, the resulting S100 VETs$_{800}$ fell into a range of sizes and polydispersities that just allowed a reliable analysis of size distribution parameters using DLS and the method of cumulants [254, 257], while offering a heterogeneous initial system for ROMER experiments.

All ROMER experiments reported in Section 4.3.5 have been carried out using both E80 and S100 vesicle formulations as listed in Table 4.6. They basically showed the same behavior and trends in the systematic studies of dynamically enhanced pore extrusion, but the effects of varying shear rates on the initially larger S100 systems were more pronounced. Therefore, the results presented in this chapter are restricted to vesicles prepared from S100 matrix membranes.

4.3.2 Characterization of nanopore membranes

The selection of adequate membrane properties, including the material, the design, and the membrane pore characteristics (pore size and size distribution, pore geometry, pore density), is key to process efficiency and product quality of any membrane-based process technology. While the choice of membrane shape, dimensions, material and the resulting thermal, mechanical, and chemical stabilities is governed by the configuration of the apparatus and the processing conditions, the product properties are very much influenced by the membrane pore characteristics. In dynamically enhanced vesicle extrusion, uniform cylindrically shaped pore channels are expected to allow for a most effective and controlled shearing-off of the frontal endcap of liposomal spherocylinders emerging from such pore channels (see Fig. 2.9 in the Background Section).
To study the pore characteristics of different types of commerical planar nanopore membranes suitable for mounting in the ROMER device, their surface pore structure was analyzed by SEM and compared to the nominal membrane specifications

provided by the manufacturer (Tab. 4.4). The nominal pore diameters of all membranes evaluated and used for ROMER experiments were around 200 nm.

Track-etched polymer membranes

SEM: The SEM micrographs in Figure 4.4 illustrate the surface pore structures of the track-etched polycarbonate and polyethylene therephthalate membranes PC200
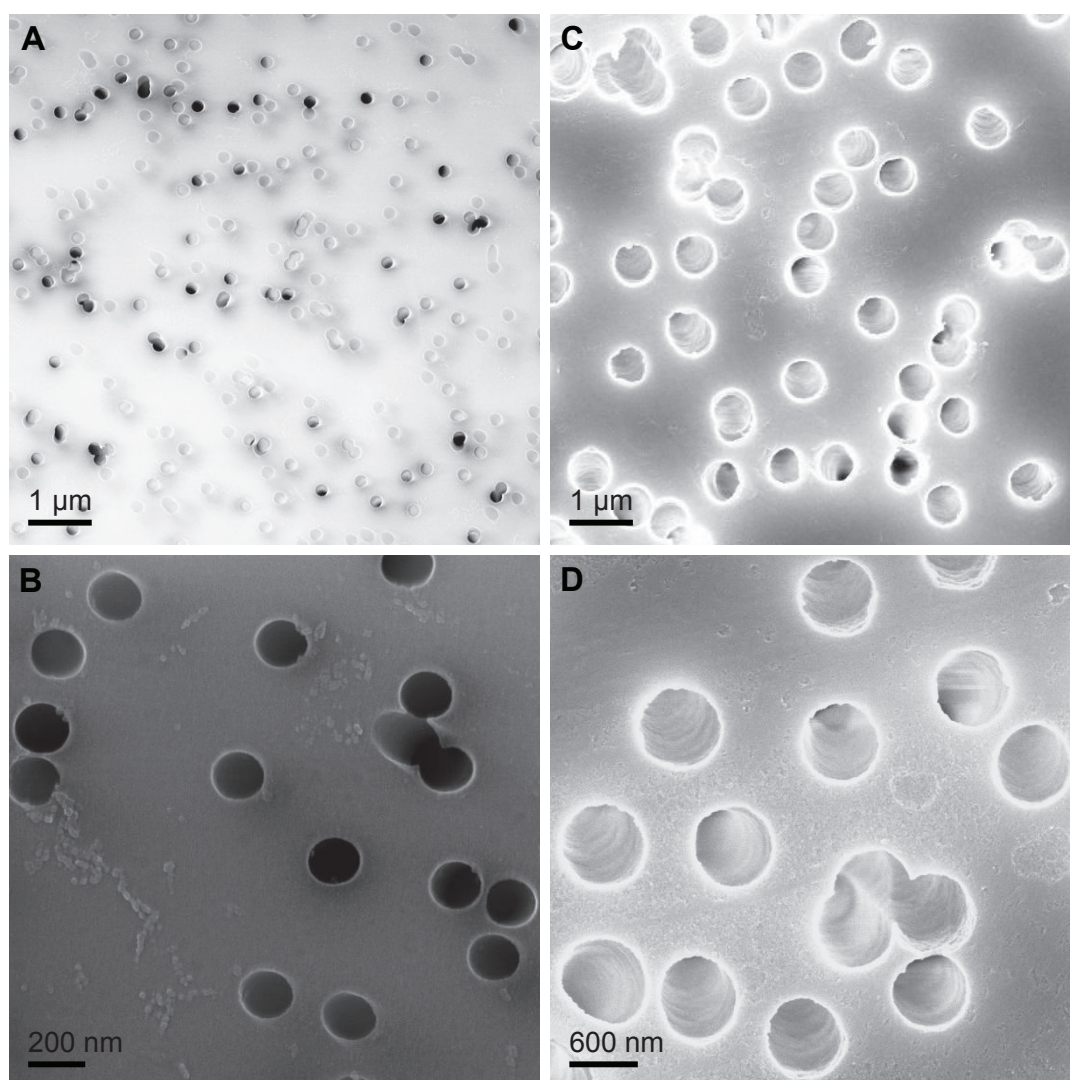
Figure 4.4: SEM micrographs of track-etched PC200 and PET210 membranes. Visualized are the membrane surfaces of track-etched nanopore membranes based on polycarbonate (PC; A-B) and polyethylene therephthalate (PET; C-D) with nominal pore diameters of 200 nm (PC200) and 210 nm (PET210), respectively.

(Fig. 4.4A-B) and PET210 (Fig. 4.4C-D), respectively, at different magnifications. The observed well-defined circular pore openings are characteristic for track-etched membranes as they are fabricated by irradiating thin polymer films with heavy-ion beams followed by uniform chemical etching along the created latent tracks. For both PC and PET films, the processes of track formation and etching are well studied. This allows the production of precise membrane structures with roughly cylindrical pore channels spanning from surface to surface. Pore density, pore size, and pore shape can be adjusted almost independently by controlling the irradiation and etching conditions [243, 360].

Pore size distribution and pore shape: In a statistical analysis of the collected SEM micrographs, the pore areas at the surface of PC200 and PET210 membranes were measured to calculate the corresponding pore size distributions shown in Figure 4.5 and summarized in Table 4.7.

The median diameter $x_{50,0}$ of the single pore population (no overlapping pore openings) measured on the surface of the PC200 membrane was in perfect agreement with its nominal 200-nm pore diameter x_0 indicating the presence of uniform cylindrical pore geometries (see sketch in Fig. 4.5). In contrast, the median diameter $x_{50,0}$ of the single pore openings determined for the PET210 membrane was as large as 662 nm. This is more than three times the rated pore diameter $x_0 = 210$ nm derived from air flow measurements by the manufacturer. Apparently, the pore channels in the PET210 membrane are strongly biconically shaped. This is most likely a direct consequence of the prolonged etching time required to develop the ion tracks in the thicker PET210 film (35.5 μm) compared to that needed for breakthrough and pore size adjustment in the thin PC200 foil (10 μm). In addition, the latter polymer material is more sensitive to the alkali etch solution [243].

The pore cone angle and resulting surface pore diameter in PET210 membranes could probably be reduced by optimizing the etching conditions such that the ratio of track etch rate to bulk (radial) etch rate is high and the formation of cylindrical pore shapes is favored [243]. To increase the track etch rate in PET films, the ion tracks are often sensitized by UV treatment or the addition of alcohols to the etchants [243, 361]. Due to different activation energies of the track etching and bulk etching processes, a simple increase in temperature during etching can also be used to elevate the etch rate ratio towards cylindrical pore formation [243, 362]. Indeed, the controlled generation of cylindrical pore shapes has been described for thin films (≈ 10 μm) based on both PC and PET using standard alkali etch solutions at 60 °C [244, 363], while well-defined conically shaped pores have been formed in PET films by one-side etching at room temperature [362, 364].

Due to the biconical pore shape, a higher percentage of overlapping pore openings, i. e. lower relative total single pore area, was found on PET210 surfaces than on the cylindrically perforated PC200 membrane (Tab. 4.7), even though the nominal pore density of the latter membrane type was higher (Tab. 4.4). Including these
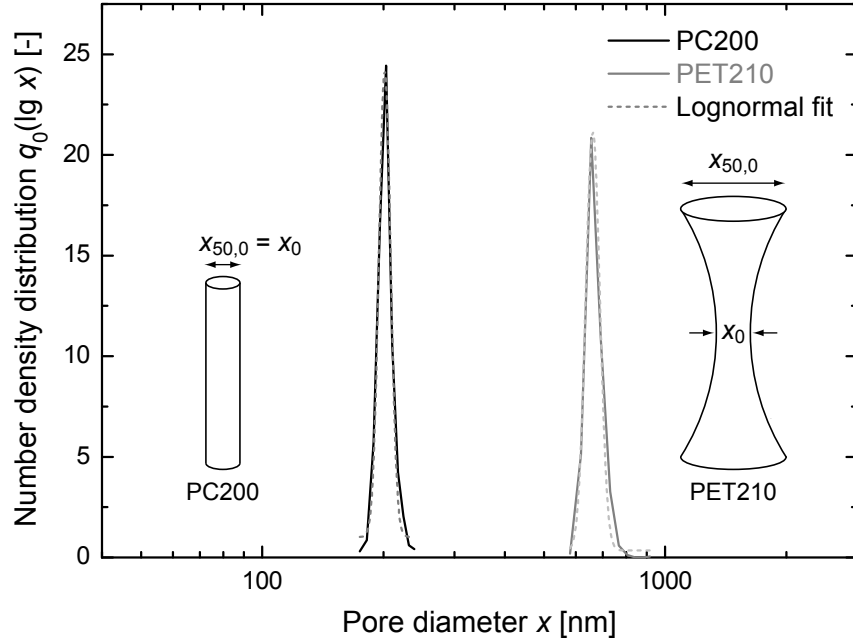
Figure 4.5: Pore size distributions of PC200 and PET210 membrane surfaces. Number-weighted pore size distributions of single pore openings on the surface of the track-etched nonapore membranes PC200 (*black line*) and PET210 (*gray line*). *Solid lines*: Distribution functions calculated from statistical image analysis of SEM micrographs. *Dotted lines*: Lognormal fits to the measured data. *Schematic illustrations* of the derived pore shapes including the nominal pore diameter x_0 and the measured number-weighted median diameter $x_{50,0}$ of the single pore opening. Drawing not to scale.

Table 4.7: Pore size distribution characteristics of PC200 and PET210 membrane surfaces. Included are the number-weighted pore size distribution parameters $x_{50,0}$ (median diameter) and $span_0$ (distribution width) for the single pore population and the total pore population (including both single pore openings and merged pore openings).

Short name of membrane type		PC200	PET210
Nominal pore diameter x_0	[nm]	200	210
Total number of pores measured	[-]	891	1453
Total number of single pores measured	[-]	751	1111
Relative total area of single pore openings	[%]	71	61
Median diameter $x_{50,0}$ of single pore openings	[nm]	202	662
Median diameter $x_{50,0}$ of total pore openings	[nm]	209	672
$span_0$ value of single pore openings	[-]	0.11	0.13
$span_0$ value of total pore openings	[-]	0.48	0.57

clusters of merged pore openings in the calculation of pore size distributions resulted only in a minor shift of the number-weighted median pore diameter $x_{50,0}$ to larger pore sizes for both PC200 and PET210 membranes (see single vs. total pore size distribution parameters in Tab. 4.7). However, the presence of surface pore clusters significantly influenced the distribution widths as indicated by the strong increase in the corresponding $span_0$ values.

The very narrow pore size distributions of the single pore openings in both PC200 and PET210 membranes shown in Figure 4.5 and represented by the low $span_0$ values in Table 4.7 are characteristic to track-etched membranes [243]. The monomodal, logarithmic single pore size frequencies $q_0(\lg x)$ derived from SEM image analysis could be well described by lognormal distribution functions (Fig. 4.5).

Potential of track-etched polymer membranes in dynamic vesicle extrusion:
Even though both polycarbonate and polyethylene therephthalate films are widely used for track-etched membrane production [243], the nanopore membranes used in conventional (static) vesicle extrusion are almost exclusively based on track-etched polycarbonate membranes [3, 15, 193, 365]. Indeed, the PC200 membrane showed a precise porous structure with well-defined cylindrical pore channels which is most suitable for static vesicle extrusion and probably also for dynamically enhanced vesicle extrusion.

On the other hand, the biconical pore shape and the relatively large proportion of merged pore openings observed in PET210 membranes is expected to reduce the efficiency of shear forces at the membrane outlet in dynamic vesicle extrusion. However, the thicker PET210 membrane offers an advantage over the PC200 foils in terms of pressure resistance. While the extrusion pressures in the ROMER setup using PC200 membranes were limited to a range of 1 to 1.5 bar, PET210 membranes resisted trans-membrane pressures of up to 4 bar.

It has to be noted that the pressure resistance of both track-etched membrane types during ROMER experiments was, in most cases, limited by the adhesive bond between the polymer foil and the stainless steel membrane holder (Fig. 4.1) and not by the burst pressure of the membrane itself.

Ceramic sinter membranes

With regard to the ultimate goal of large-scale processing of concentrated vesicle suspensions by dynamically enhanced membrane extrusion at high throughput rates, a ceramic sinter membrane based on Al_2O_3 was also evaluated for potential use in the ROMER device. Ceramic membranes are widely used in micro- and ultra-filtration applications because of their high pressure resistance and excellent durability against high temperature processing and corrosive feed stocks, especially relevant for cleaning procedures.
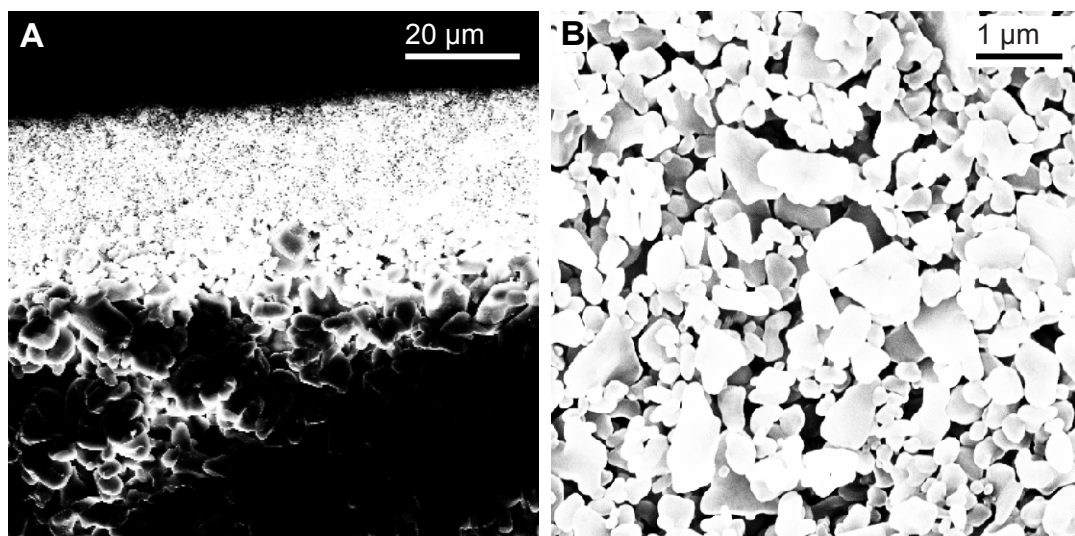
Figure 4.6: SEM micrographs of asymmetric ceramic sinter membrane Cer200.
The Cer200 membrane is an asymmetric, sintered nanopore membrane based on ceramic Al_2O_3 particles with a nominal pore diameter of 200 nm. (A) Cross-sectional fracture showing the coarse membrane support with 2.5-µm pores and the thin ($\approx 10\,\mu m$) active membrane layer with 200-nm pores. (B) Surface of active nanopore membrane with 200-nm pores.

Potential of ceramic sinter membranes in dynamic vesicle extrusion: In conventional vesicle extrusion, controlled vesicle size reduction has been achieved using ceramic sinter membranes despite their typical irregular pore shapes and tortuous paths as opposed to the straight-through pore channels of track-etched polymer membranes [193, 345].

Sinter membrane modules usually consist of the mechanically strong, self-supporting membrane itself. This eliminates the need of a membrane holder and concomitant issues with membrane detachment due to insufficient bonding of the active membrane to its support as frequently observed for composite membrane modules in the ROMER device. Furthermore, sinter membrane modules generally allow for high throughput operations and back-flushing of cleaning solutions.

As for the extrusion of vesicles, liposome suspensions can alternatively be passed through a sinter membrane in opposite directions to maintain the membrane in an unclogged condition, even when processing concentrated samples [345]. Back-flushing is not possible when using track-etched polymer membranes because of a different filter housing configuration and, more importantly, because of their limited membrane thickness and pressure resistance based on the restricted penetration depth of accelerated heavy ions through the polymer films. Therefore, clogged track-etched membranes usually have to be replaced which may compromise the cleanliness of the extrusion procedure.

To avoid the build-up of high back pressures, asymmetric sintered nanopore membranes are often employed. They consist of a thin active membrane layer that is sinter bonded onto a coarse membrane support of the same alloy.

SEM: The SEM micrographs in Figure 4.6 show the cross-section and the active membrane surface of the asymmetric, sintered ceramic membrane Cer200 evaluated in this work. It consisted of a $10\,\mu m$ active membrane layer with a rated pore diameter of 200 nm and a membrane support with 2.5-µm pores, both formed from Al_2O_3 particles. The total thickness of the sinter membrane was 1 mm.

4.3.3 Performance of nanopore membranes in conventional extrusion

Prior to ROMER experiments, the performances of the considered nanopore membranes were studied by inserting them in the static LIPEX extruder (Fig. 2.8) and analyzing the vesicle structures obtained from the most commonly applied extrusion procedure (Background Section 2.5.3) [3, 9, 193, 206]. The extrusion technique has been studied in detail, especially for track-etched polycarbonate membranes, and is well known to effectively size down MLVs upon passage through well-defined cylindrical pore channels [9, 15]. Therefore, track-etched polycarbonate membranes served as reference membrane in the nanopore membrane performance tests described in this section.

VET$_{200}$ suspensios prepared using track-etched PC and PET membranes

To verify the rated 210-nm pore diameter of the PET210 membrane and to evaluate the performance of its biconical pores in conventional extrusion, a VET_{200} suspension was prepared by sequentially extruding a S100 MLV pre-suspension 10 times through a PET210 membrane using the LIPEX extruder. The resulting vesicle size distribution measured by DLS on the Malvern Zetasizer NS was compared to that of a VET_{200} suspension obtained by taking the same MLV pre-suspension through the same extrusion procedure but using the reference PC200 membrane.

DLS results: Despite the pronounced biconical pore shape and surface pore diameters of around 660 nm (Fig. 4.5 and Tab. 4.7), the PET210 membrane was found to allow for an effective down-sizing of MLVs similar to that achieved by the cylindrical 200-nm pores of the PC200 membrane. This was revealed by the DLS results of the obtained VET_{200} suspensions presented in Figure 4.7. The good agreement between the peak positions of the monomodal size distributions resulting from repetitive MLV extrusion through PET210 and PC200 membranes confirms that the mean
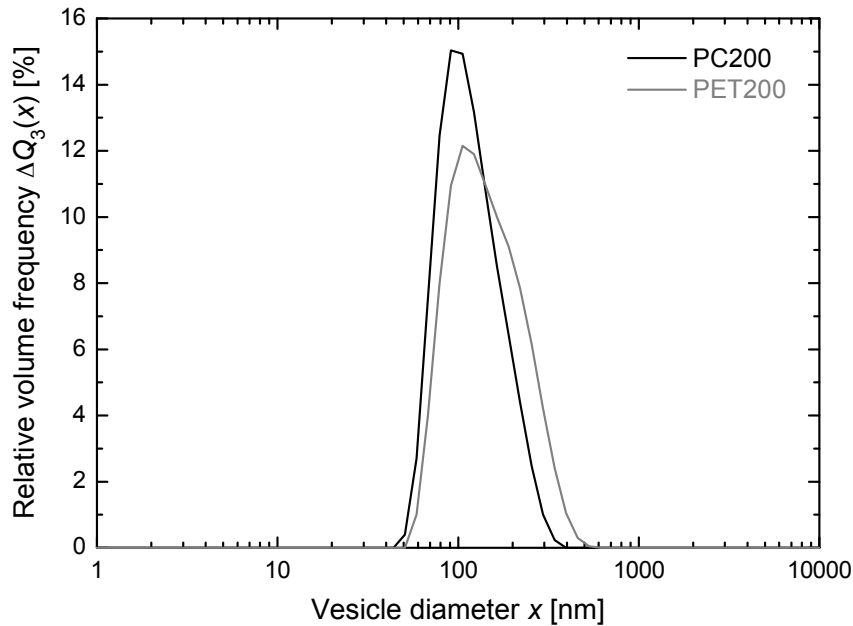
Figure 4.7: Size distributions of VET$_{200}$ suspensions produced with track-etched PC200 and PET210 membranes. The VET$_{200}$ suspensions were obtained by sequential extrusion of a S100 MLV pre-suspension 10 times through a track-etched PC200 (——) or a PET210 (——) membrane. S100 concentration: 0.645 mM.

pore diameter at the center of the PET210 membrane is, indeed, close to 200 nm as indicated by the manufacturer.

Mechanism of vesicle breakup in cylindrical and biconical pore channels: The results of the PC200 and PET210 membrane performance tests support the models for the conventional extrusion process by Patty and Frisken (Sec. 2.6.3) [15] and Bertrand and Joós (Sec. 2.6.4) [119]. They describe the mechanism of vesicle size reduction in conventional extrusion by a pressure-induced breakup at the pore entrance rather than by a shear-induced fissioning of the spherocylinder inside the pore channel or at the pore exit (Sec. 2.6.1) [242].

According to these pressure dependent models, the final vesicle size is, to a first approximation, only dependent on the geometrical constraints of the pore diameter imposed on the vesicles due to volume conservation and finite bilayer expansibility. As a large vesicle is pushed almost quasistatically into a channel during the initial extrusion passes, the bilayer area expands inducing a membrane tension in the vesicle membrane (Fig. 2.11A). The vesicle bursts upon reaching a critical membrane tension σ_{crit} equal to the lysis tension σ_l of the vesicle membrane with the neck region being the most probable location for vesicle rupture.

Our experiment shows that vesicles rupture to similar extents during multiple extrusion passes through straight-through pore channels whether this neck region is

located at the entrance of cylindrical pores or in the center of biconical pores as in the case of track-etched PC200 and PET210 membranes, respectively.

The larger volume fraction of vesicles $> 200\,\text{nm}$ present in the VET_{200} population obtained from the PET210 membrane compared to that produced by the PC200 membrane (Fig. 4.7) is most likely the effect of the gradual contraction of the biconical pore channels. This gradual contraction induces lower membrane tensions in the neck region of vesicle bilayers entering the biconical pores and, as a consequence, allows for the passage of larger vesicles through these pores of a given nominal diameter without bursting.

In contrast, the sharp edges of the entrances of cylindrical pores quickly lead to the build-up of high membrane tensions in the neck region locally exceeding the lysis tension and inducing pore nucleation in the bilayer followed by vesicle membrane rupture [119]. Ultimately, this results in smaller critical vesicle sizes that can persist during the final extrusion passes through PC200 membranes. Additional flow-induced rupture events of spherocylindrical vesicles traveling through cylindrical pore channels were frequently observed near this critical vesicle size [119]. This is probably the reason for the larger volume fraction of vesicles $< 100\,\text{nm}$ formed by multiple MLV extrusion through the PC200 membrane (Fig. 4.7).

LUVETs$_{100}$ prepared using asymmetric ceramic sinter membranes

The suitability of asymmetric ceramic sinter membranes for vesicle extrusion was evaluated by following the conventional extrusion protocol for the preparation of LUVET$_{100}$ suspensions using the LIPEX extruder (Sec. 3.2.2) and planar, asymmetric ceramic membrane discs.

To avoid possible interactions between the Al_2O_3 membrane surface and charged compounds of the S100 PC isolate, the MLV pre-suspension was prepared from zwitterionic, synthetic POPC. The MLV suspension was sequentially extruded 10 times through a Cer200 membrane with a rated pore diameter of $200\,\text{nm}$, followed by 10 extrusion cycles through a Cer100 membrane with a rated pore diameter of $100\,\text{nm}$. The Cer100 membrane used for final extrusions was inserted in the LIPEX extruder such that the position of the active nanoporous membrane layer was varied between the membrane inlet and the membrane outlet. The obtained vesicle morphologies were analyzed in terms of size distributions and vesicle shapes by DLS measurements (Fig. 4.8) and cryo-TEM imaging (Fig. 4.9), respectively.

DLS results: In contrast to the typical monomodal size distributions of LUVETs$_{100}$ obtained by repetitive vesicle extrusion through standard track-etched PC membranes, MLV homogenization by repetitive extrusion through sintered ceramic membranes of the same nominal pore diameters resulted in broad bimodal size distributions for both Cer100 configurations tested (Fig. 4.8).

125
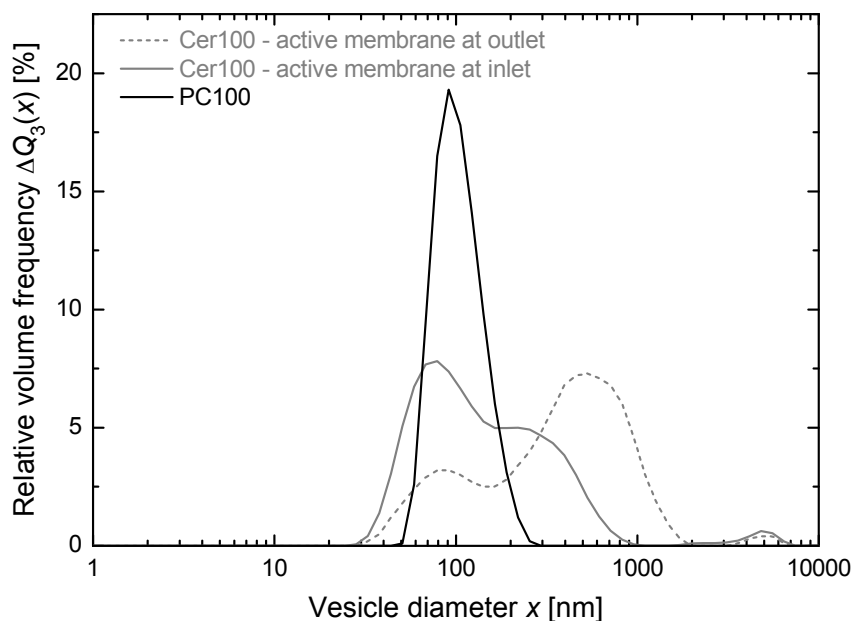
Figure 4.8: **Size distributions of LUVETs$_{100}$ produced with asymmetric ceramic sinter membranes and standard polymeric track-etched membranes.** The LUVET$_{100}$ suspensions were obtained by sequential extrusion of a POPC MLV suspension 10 times through 200 nm pores and 10 times through 100 nm pores of track-etched PC membranes (PC200 and PC100; *black line*) and asymmetric sintered ceramic membranes (Cer200 and Cer100; *gray lines*). The position of the active membrane layer of the Cer100 membrane was varied between the membrane inlet (*gray solid line*) and the membrane outlet (*gray dashed line*). POPC concentration: 10 mM.

Interestingly, a rather successful downsizing of MLVs was only achieved by forcing them through the active membrane layer directly at the inlet of the asymmetric Cer100 membrane as demonstrated by the maximum of the primary peak of the resulting vesicle size distribution at 80 nm. This primary peak was even slightly shifted towards smaller vesicle diameters compared to the predominant vesicle size of 90 nm measured in the homogeneous LUVET$_{100}$ suspension after analogous MLV extrusion through the reference PC200 and PC100 membranes. Processing the MLV pre-suspension in the opposite membrane direction, i.e. from the coarse membrane support at the inlet to the active membrane layer at the outlet of the Cer100 membrane, resulted in a very limited downsizing of vesicles and a primary peak maximum of the corresponding size distribution at around 500 nm (Fig. 4.8).

Mechanism of vesicle breakup upon passage through porous sinter membranes: According to the proposed pressure-induced mechanism of vesicle breakdown upon extrusion through nanochannels (Background Secs. 2.6.3–2.6.4) [15, 119, 208], multiple contractions along the tortuous path through nanoporous sinter membranes

and high related transmembrane pressures are likely to be the reason for the observed generation of relatively small vesicles upon multiple passages through the Cer100 membrane with the nanoporous layer being at the membrane inlet.

Increasing extrusion pressures are known to decrease the size of extruded vesicles for a given bilayer composition and pore diameter using conventional track-etched membranes [15, 119, 208, 209]. This has been explained by the higher flow rates resulting in the pore channels which leads to a thickening of the lubrication layer surrounding the spherocylindrical vesicles as they flow through the channels, and, hence, to a decreased effective pore diameter (see Fig. 2.11B and Eqs. 2.7–2.8 in Sec. 2.6.4) [119, 208, 245]. A similar phenomenon of reduced effective diameter of the pore entrance due to high transmembrane pressures required for sinter membrane processing could be responsible for the extensive breakdown of vesicles at the nanopore inlet of Cer100 membranes.

Nevertheless, a considerable amount of vesicles with diameters > 200 nm remained in the LUVET$_{100}$ suspension produced by the Cer100 membrane with the active membrane layer at the membrane inlet. The resulting shoulder of the corresponding bimodal size distribution (Fig. 4.8) can be attributed to the absence of defined surface to surface channels in sinter membranes, i. e. reduced pore lengths, which would promote an additional flow-induced breakup of vesicles inside the channel during the final extrusion cycles [119].

Cryo-TEM: The cryo-TEM micrographs in Figure 4.9 confirm the presence of two vesicle size populations in the LUVET$_{100}$ sample collected after final extrusion passes through the Cer100 membrane with the active membrane layer facing the vesicle feed. Uniform vesicles with diameters ranging from 50 to 100 nm coexisted with approximately 200 nm-sized vesicles. The former population of small vesicles was predominantly unilamellar and spherical in shape, comparable to the well-defined
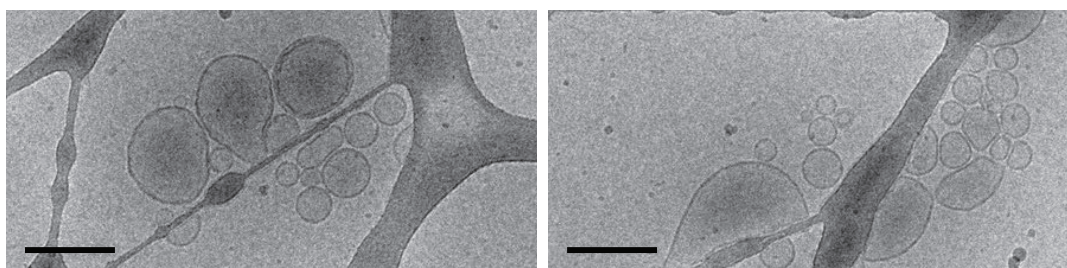
Figure 4.9: Cryo-TEM micrographs of LUVETs$_{100}$ produced with asymmetric ceramic sinter membranes. The LUVET$_{100}$ suspension was prepared by sequential extrusion of a POPC MLV suspension 10 times through 200 nm pores and 10 times through 100 nm pores of the asymmetric ceramic sinter membranes Cer200 and Cer100, respectively. The active membrane layer of the Cer100 membrane was at the membrane inlet. POPC concentration: 10 mM. Scale bar = 200 nm.

LUVET$_{100}$ suspensions produced with conventional track-etched PC membranes (Fig. 4.3). In contrast, the less downsized vesicles, while also being mostly unilamellar, seemed to have large excess areas leading to the observed deflation of the quasi-spherical vesicle shape [73]. This excess area explains the larger final size adopted by these flaccid vesicles since it allows them to tolerate larger area expansions without rupturing during the final passes through the 100-nm pore membrane [119, 366]. Likewise, the pre-stretching and creation of excess area of unsized vesicles while passing the coarse membrane support before entering the nanoporous layer towards the exit of the Cer100 membrane largely prevented vesicle breakdown when operating in the opposite filter direction (Fig. 4.8). Unsuccessful downsizing of vesicles was also reported in a ceramic extrusion setup using a cylindrical, asymmetric membrane module with the active membrane lining the inner wall and operating in an outside-to-inside direction [345].

Recovery of vesicle constituents after passage through nanopore membranes

Total lipids and lipid compositions of initial MLV suspensions are known to be recovered after conventional extrusion through polycarbonate membranes using different devices [15, 212, 367]. However, these static extrusion setups are usually operated at higher extrusion pressures than those tolerated by the free-standing membrane configuration of the ROMER device. The different nanopore membranes were, therefore, tested for possible lipid retention during a single passage of unsized vesicles through the ROMER membrane module under the standard conditions of subsequent ROMER experiments.

VET$_{800}$ suspensions prepared from an initial S100 concentration of $0.5\,\mathrm{mg\,mL^{-1}}$ were pumped through the various membrane types mounted onto the ROMER membrane holder at controlled flow rates. The total phospholipid concentration was quantified before and after extrusion using the Stewart assay and the recovered phospholipid fraction was plotted as a function of extrusion pressure (Fig. 4.10).

Track-etched PC200 and PET210 membranes: No significant loss of lipids was detected after one extrusion cycle through the track-etched polymer membranes, in spite of the moderate transmembrane pressures of around 1.3 bar and 1.8 bar resulting from low volumetric VET$_{800}$ extrusion at $1\,\mathrm{ml\,min^{-1}}$ through the pressure-sensitive PC200 and PET210 membranes, respectively (Fig. 4.10). The recovery of phospholipids after VET$_{800}$ extrusion through the PET210 membrane was slightly lower than that measured after the PC200 membrane. This is probably caused by the higher degree of merging and branching channels within the thicker PET210 membrane resulting from different surface angles of track-etched pores fluctuating around normal angle [243]. Nevertheless, approximately 89% and even 94% of total
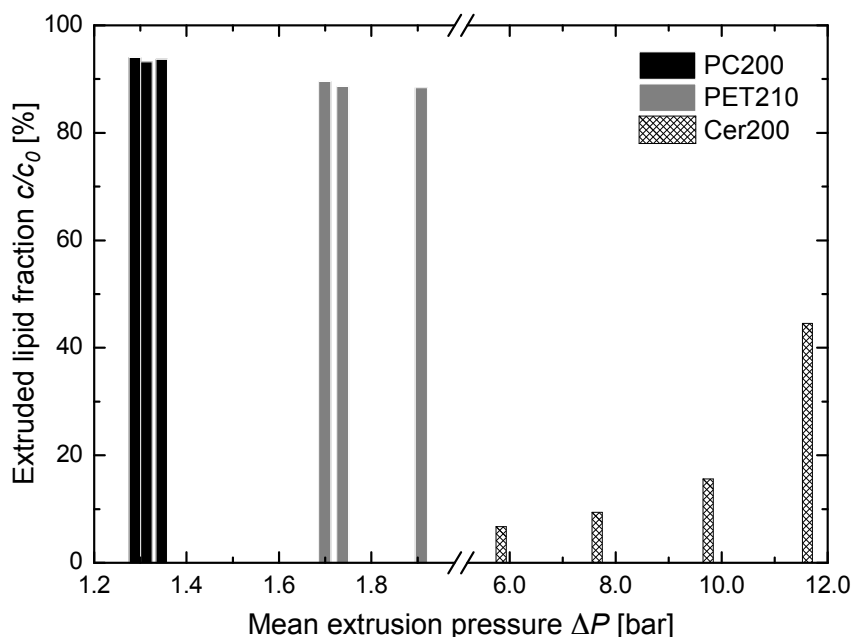
Figure 4.10: Recovery of total phospholipids after one VET$_{800}$ extrusion cycle through different nanopore membranes. S100 VET$_{800}$ precursors were passed 1 time through the track-etched polymer membranes PC200 and PET210 and through the ceramic sinter membrane Cer200 using the ROMER device at increasing extrusion pressures. Initial S100 concentration c_0: 0.645 mM.

phospholipids were recovered after extrusion through the straight-through channels of PET210 and PC200 membranes, respectively. This is in the upper range of lipid recovery reported previously for conventional liposome extrusion through polycarbonate membranes [367].

Ceramic sinter membrane Cer200: The filter resistance and extent of lipid retention by the ceramic sinter membrane was drastically increased compared to the track-etched polymer membranes. The transmembrane pressures resulting from VET$_{800}$ extrusion at 2 ml min^{-1} through the Cer200 membrane were in a range of 6-8 bar, whereas the corresponding lipid recoveries were < 10% (Fig. 4.10). Even when increasing the extrusion pressure to 10-12 bar by controlling the flow rate of the vesicle feed at 8 ml min^{-1}, the amount of the recovered phospholipid fraction remained below 50%. It can be assumed that a large fraction of pores, especially the smaller ones, was inactive under the investigated extrusion conditions leading to the entrapment of vesicles along the tortuous path through the Cer200 membrane. Additional lipid loss was probably caused by the adsorption of lipids to the negatively charged surface of Al$_2$O$_3$ particles as surface forces dominated over the flow forces through the depth-type sinter membrane.

Summary of nanopore membrane performance tests: The performance of the track-etched PET210 membrane in conventional vesicle extrusion was comparable to the reference polycarbonate membrane PC200 despite its biconical pore channels as opposed to standard cylindrical pore shapes. The use of both track-etched membrane types will allow to study the influence of pore shape on the efficiency of dynamically enhanced vesicle extrusion in subsequent systematic ROMER experiments. Static vesicle extrusion through asymmetric ceramic sinter membranes resulted in broad bimodal vesicle size distributions, deflated vesicle shapes, and low lipid recovery rates. As a consequence, the Cer200 membrane was not further considered for ROMER experiments.

Homogenization of MLVs by repetitive extrusion through track-etched PC and PET membranes: Benchmarking the vesicle extrusion process

In a last preliminary experiment prior to ROMER experiments, structural vesicle parameters were recorded after 1 to 10 extrusion passes of a standard VET_{800} pre-suspension based on S100 through the selected PC200 and PET210 membranes using the conventional LIPEX extruder. Since the repetitive extrusion procedure is one of the most popular techniques to reproducibly homogenize MLV suspensions in terms of vesicle size, polydispersity and lamellarity [9, 216], this data set will be used to benchmark the new ROMER process. Structural vesicle parameters measured after a single passage through the ROMER device at controlled shear rates will be compared to those obtained here after n static extrusion cycles.

Figure 4.11 shows the structural vesicle parameters, including the hydrodynamic diameter D_h, the relative external surface area E, and the polydispersity index *PDI*, all normalized to the corresponding initial values, of a VET_{800} suspension as a function of the number of extrusion passes through PC200 and PET210 membranes, respectively. The extrusion pressure was kept constant at 6 bar throughout the repetitive extrusion procedure using both types of track-etched nanopore membranes. As the phospholipid proportion in the outermost vesicle monolayer detected by external surface area analysis inversely relates to the degree of vesicle lamellarity (Sec. 2.7.2), the results of the normalized external surface area E/E_0 were plotted as reciprocal values. This helps to illustrate the concomitant changes in vesicle size and lamellarity upon sequential extrusion (Fig. 4.11A and 4.11B).

General results: Overall, the mean size (Fig. 4.11A), degree of lamellarity (Fig. 4.11B) and polydispersity (Fig. 4.11C) of the VET_{800} suspension rapidly decreased with increasing numbers of extrusion cycles through both PC200 and PET210 membranes during the initial extrusion passes. These data are consistent with previous studies on vesicle size reduction and the related increase in relative external surface area, i.e. decrease in vesicle lamellarity, for egg PC MLVs extruded between 1 to 10
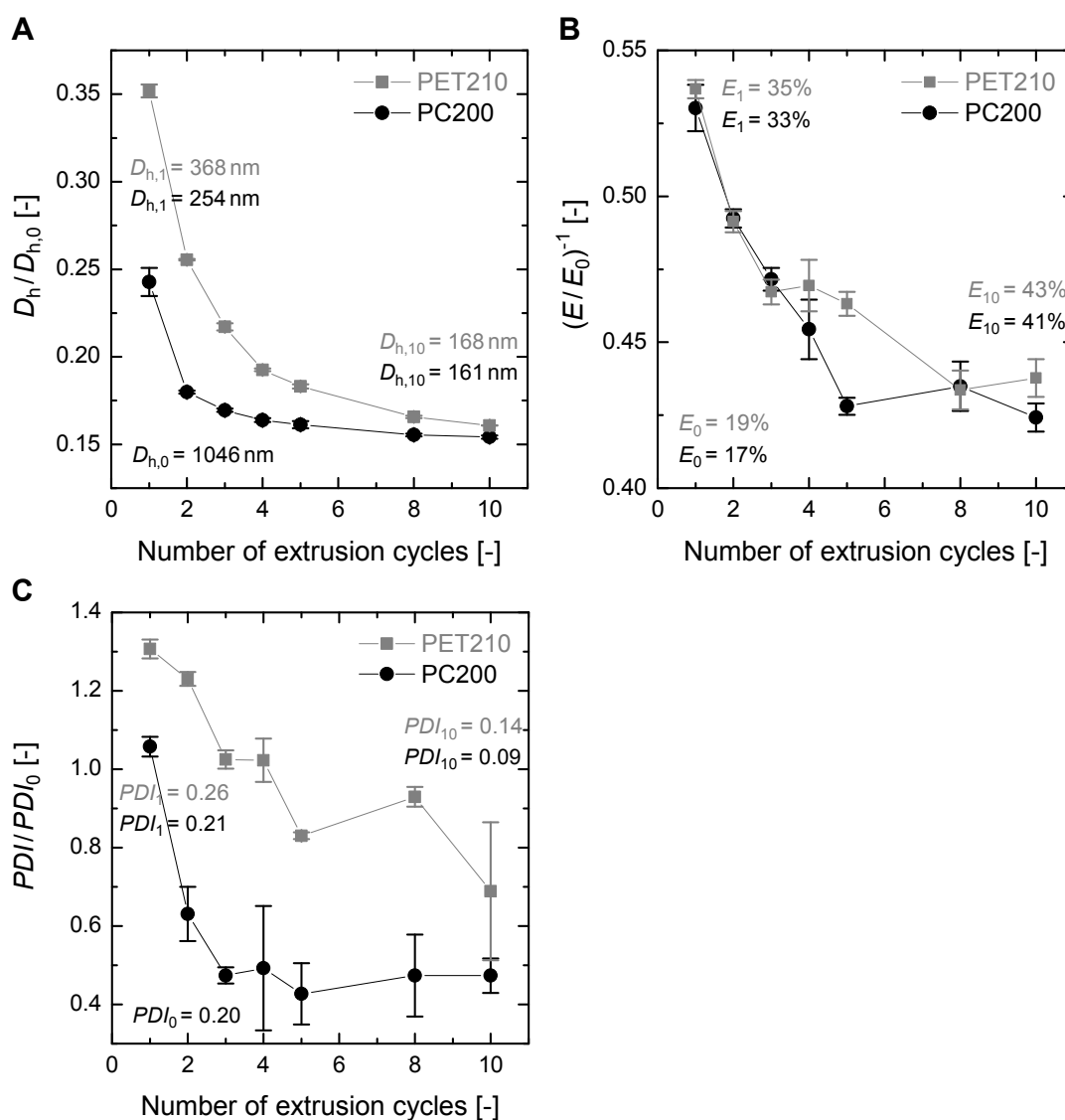
Figure 4.11: Homogenization of MLVs by repetitive, static extrusion using the LIPEX device. Hydrodynamic diameter D_h (A), relative external surface area E (B), and polydispersity index PDI (C), normalized to the respective initial values $D_{h,0}$, E_0, and PDI_0, of a VET_{800} suspension passed the indicated number of extrusion cycles through a PC200 ($\bullet$) or a PET210 membrane ($\blacksquare$) using the LIPEX device. Extrusion pressure: 6 bar. VET_{800} precursors were prepared by pre-extruding a MLV suspension from S100/POPE 95:5 (mol/mol) 3 times through a PC800 membrane. Total lipid concentration: 0.645 mM. Results represent mean values and standard deviations of the means of two (4-10 cycles) to three (1-3 cycles) independent extrusion experiments using the same VET_{800} pre-suspension. The lines are drawn to guide the eye.

times through polycarbonate membranes with 30-, 50-, 100-, 200- and 400-nm pore diameters [9, 216].

Homogenization of MLVs using PC200 vs. PET210 membranes: Whereas the structural parameters of extruded S100 vesicles remained already unchanged after 5 passes through the PC200 membrane, the final vesicle morphology after repetitive extrusion through the PET210 membrane was only reached after 8–10 cycles. This can again be attributed to the less effective pressure-induced breakdown of vesicles at the conically shaped entrance of PET210 pores compared to that triggered by the cylindrical pore openings of the PC200 membrane as described earlier.
After 8-10 extrusion cycles, the values of the mean sizes and relative external surface areas of the $VETs_{200}$ obtained from repetitive extrusion through PC200 and PET210 membranes converged (Fig. 4.11A and B). This is a result of the constant extrusion pressure applied and of the comparable geometrical constraints imposed by the entrance or the center of the cylindrical PC200 and biconical PET210 pore channels, respectively [119].

Obtained VET_{200} suspensions vs. literature reports: The indicated final vesicle diameters (PC200: 161 nm; PET210: 168 nm) and final relative external surface areas (PC200: 40.7%; PET210: 43.0%) were in good agreement with previous results for $VETs_{200}$ prepared by passing frozen and thawed egg PC MLVs 10–20 times through 200-nm pore PC membranes [9, 10].
Due to the fact that the model by Patty and Frisken predicting the final vesicle size as a function of pore size, extrusion pressure and vesicle lysis tension (Eq. 2.6) was only consistent with data for vesicles extruded through pore sizes ranging from 50 to 100 nm and not with those obtained from 200-nm pores (Sec. 2.6.3) [15], our results for final VET_{200} diameters could not be verified with this model. Nevertheless, the final diameter of 161 nm measured after 10 extrusion cycles through the PC200 membrane at 6 bar compared well with the experimental data reported by Patty and Frisken for POPC $VETs_{200}$ prepared under the same extrusion conditions ($D_h \approx 180$ nm). The small variation in the observed VET_{200} diameters is based on the different bilayer compositions used here (S100) and in the study by Patty and Frisken (POPC). This can still be explained by their general model: S100 contains a considerably higher percentage of unsaturated acyl chains with two or more alternating *cis*-double bonds than POPC (Tab. 4.3 and 4.2) conferring a lower lysis tension to the S100 bilayers (Tab. 2.1) [13] and, hence, resulting in smaller sizes of extruded vesicles (Eq. 2.6) [15].

Polydispersity of VET_{200} suspensions: The *PDI* values (Fig. 4.11C) of the VET_{200} suspensions prepared with increasing numbers of extrusion cycles through the PET210 membrane did not approach the baseline values of the reference PC200 samples as quickly as the series of vesicle size (Fig. 4.11A) and lamellarity (Fig. 4.11B). Moreover, it has to be noted that the results for these *PDI* values obtained from

DLS measurements were generally subject to large variations, even within repeat measurements of an individual sample. This is reflected by the large standard deviations of the mean *PDI* results indicated in Figure 4.11C.

According to a detailed study of the method of cumulants for DLS data analysis of VET_{200} samples by Frisken [250], the observed instability of *PDI* results is based on the limited robustness of the traditional cumulant fit to the measured intensity–intensity autocorrelation function $g^{(2)}(\tau)$ (Sec. 2.7.1, Eq. 2.21). Traditional cumulant fitting functions are derived from the standard expansion of the logarithm of the field–field autorrelation function $g^{(1)}(\tau)$ in terms of the cumulants $\kappa_m(\Gamma)$ of the distribution of decay rates $G(\Gamma)$ about the delay time $\tau = 0$ (Eqs. 2.19 and 2.21). Frisken reported that such traditional cumulant fits give unstable results for all fitting parameters derived from data analysis of VET_{200} suspensions. In particular, they do not allow for a satisfactory determination of the *PDI* value that is defined on the basis of the first and second cumulants $\kappa_1(\Gamma) = \bar{\Gamma}$ and $\kappa_2(\Gamma) = \mu_2$, respectively (Eq. 2.20) [250]. More robust fitting functions and consistent results of fitting parameters for polydisperse samples could be obtained by following a modified version of the original cumulant method as reformulated by Frisken in terms of the moments μ_m of the distribution about the mean rather than of the cumulants $\kappa_m(\Gamma)$ about $\tau = 0$ [250].

4.3.4 Morphology of vesicles prepared by dynamically enhanced extrusion

Prior to systematic ROMER experiments, the integrity and morphology of vesicles produced by dynamically enhanced membrane extrusion in the evaluated shear rate range were analyzed by cryo-TEM imaging and SANS measurements. VET_{800} pre-suspensions were pumped through the ROMER device using PC200 membranes and applying the standard ROMER settings at the minimum and maximum shear rates tested in this study ($\dot{\gamma}_{rep,min} = 6021\,s^{-1}$ and $\dot{\gamma}_{rep,max} = 60\,214\,s^{-1}$; see Sec. 4.2.3 in Materials and Methods).

Due to the very small sample volume of cryo-TEM specimens, the total lipid concentration of samples prepared from S100 for cryo-TEM investigation was increased to 20 mM (15.5 mg mL^{-1} S100). Samples for SANS measurements were prepared at the standard lipid concentration of ROMER experiments (0.645 mM; 0.5 mg mL^{-1} POPC), but using pure POPC instead of S100 phospholipids for better comparability with literature data.

According to a number of studies on conventional vesicle extrusion, the concentration of total lipids has no effect on the scattering behavior [368], the vesicle size [9, 128, 217], and the extent of multilamellarity [9] of $LUVET_{100}$, VET_{200} and VET_{400} suspensions prepared at lipid concentrations between 0.1 and 400 mg mL^{-1}.

Therefore, it can be assumed that the results obtained here from cryo-TEM and SANS experiments are comparable even though the samples have been prepared at different lipid concentrations. Nevertheless, it has to be taken into account that the known influence of lipid film thickness, i. e. lipid concentration at film hydration, on the properties of the initial MLV suspension is probably not fully overcome after the three pre-extrusion cycles applied through coarse 800 nm-pore membranes followed by a single pass through the PC200 membrane in the ROMER device [3].

cryo-TEM

Indeed, the recorded cryo-TEM micrographs show rather heterogeneous vesicle suspensions obtained from ROMER processing of S100 VETs$_{800}$ both at low (Fig. 4.12A–C) and high shear rates (Fig. 4.12D–F). Both samples contained the desired unilamellar (A and D) and oligolamellar (B, E and F) vesicles, but also large multilamellar and multivesicular structures (C and F). The latter dense lipid structures were not disintegrated after a single pass through the PC200 membrane, even when applying a strong shear flow field at the membrane outlet (F). High shear forces did, however, slightly reduce the size of unilamellar (A $\rightarrow$ D) and multilamellar vesicles (C $\rightarrow$ F) compared to the corresponding structures collected after dynamically enhanced membrane extrusion at low shear rates.

At the same time, strongly deformed, elongated vesicles with a tendency to budding were generated by the action of high shear stresses as revealed by Figure 4.12E. It can be assumed that the VET$_{800}$ precursors of these vesicles disposed of excess membrane area as already suggested for the deflated S100 LUVETs$_{100}$ visualized in the cryo-TEM images of Figure 4.3C–D. An initial excess membrane area relative to a sphere (Δ, Eq. 2.3) is known to strongly enhance vesicle deformation in a given shear flow [90, 92, 366]. The development of buckling instabilities and growing endcaps as observed in Figure 4.12E has previously been reported for strongly deformed vesicles under shear in the case of large initial excess areas [366]. Additionally, an inhomogeneous shear flow field as it is likely to develop at the maximum rotor speed applied was suggested to promote tip formation in deformed vesicles [366]. Both stable and undulating tube-like lipid structures have also been observed following exposure of liposomes to the large velocity gradients and resulting shear flow fields induced by sonication [195].
The shape transformation and preservation of vesicle integrity in spite of the large bilayer deformation observed here was probably also supported by a stress-induced lateral demixing of the S100 components, such that the components with a high affinity for highly curved bilayers accumulated at the strongly deformed edges. The polyunsaturated lipid tails of DLPC, which is the predominant phospholipid species in S100, were, for example, found to stabilize both positive and negative regions

of curvature in highly curved DPPC/DLPC vesicles [369]. Similar spontaneous adjustments of local bilayer composition and elasticity in response to stress- or temperature-induced shape transformations have been reported for other mixed lipid vesicles [73, 141, 188, 195, 287].
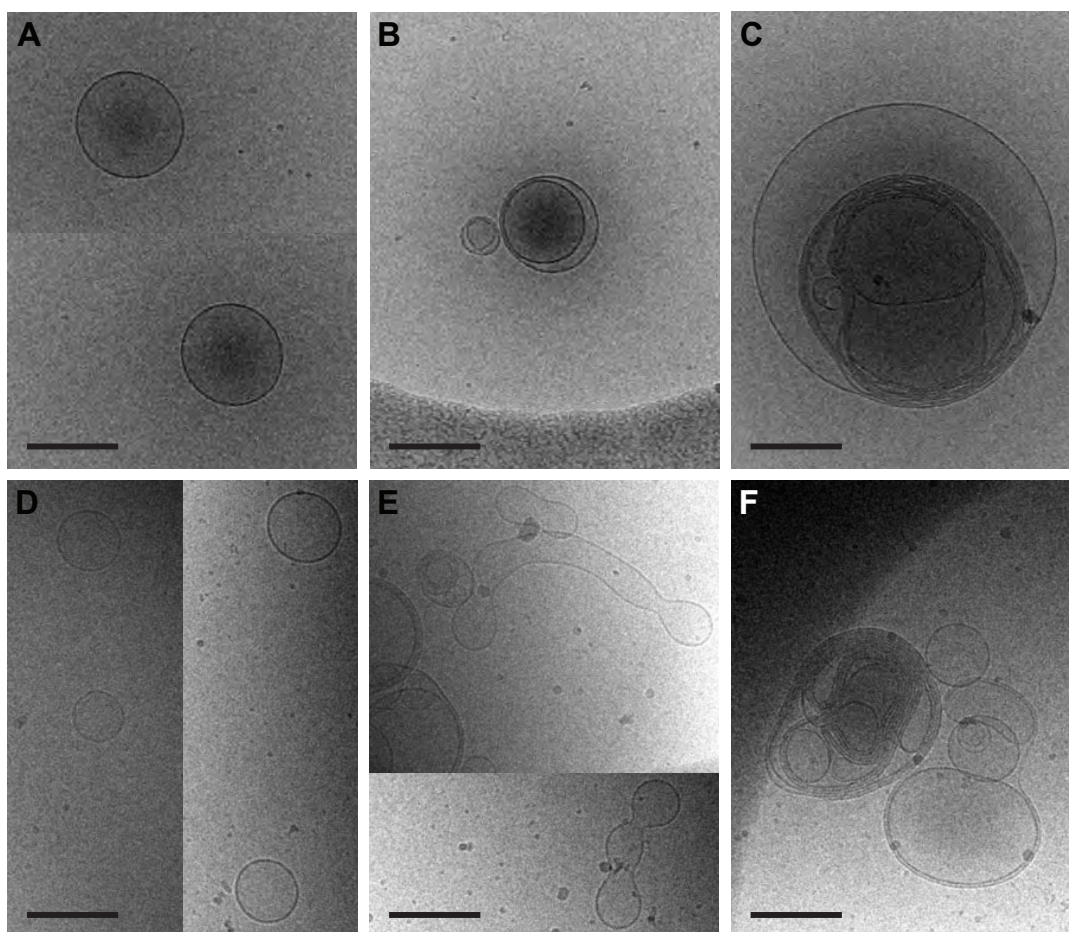
Figure 4.12: Cryo-TEM micrographs of dynamcally extruded vesicles. VET_{800} precursors were dynamically extruded 1 time through a PC200 membrane using the ROMER device and applying low ($\dot{\gamma}_{rep} = 6021\,s^{-1}$; A-C) and high shear rates ($\dot{\gamma}_{rep} = 60\,214\,s^{-1}$; D-F), respectively. Flow rate: $1\,ml\,min^{-1}$. Shear gap height: $200\,\mu m$. Rotor speed: $1000\,rpm$ (A-C) and $10\,000\,rpm$ (D-F). $VETs_{800}$ were prepared by pre-extruding a MLV suspension from S100 3 times through a PC800 membrane using the LIPEX device. Total lipid concentration: $20\,mM$. Scale bar = $200\,nm$.

SANS

In accordance to cryo-TEM observations, SANS measurements revealed no significant influence of the applied shear rate on the structural properties of a POPC VET_{800} suspension after dynamically enhanced extrusion through PC200 membranes. The shape of the recorded scattering curves was the same for samples generated at zero, low, and high shear rates as shown in Figure 4.13.

Model-independent analysis of SANS curves: For the characterization of the overall particle size, a preliminary model-independent analysis of SANS curves is often done by the Guinier approximation [246, 355, 370]. It relates the low q-range scattering from a dilute dispersion of three-dimensional objects, including liposomes [269], to the radius of gyration R_G without assuming a specific particle shape: $I(q) = I_0 \exp(-R_G^2 q^2/3)$. The value of R_G can then be determined from the so-called Guinier plot of $\ln I(q)$ versus q^2 that has a slope of $-R_G^2/3$ in the linear Guinier region at low q-values ($q < 1/R_G$).

In the case of the investigated ROMER samples, the linear Guinier region of vesicle size was not accessible within the q-range probed by the experimental SANS setup. This is indicated by the pronounced region of power-law decay of the scattering functions in the log-log plots presented in Fiugre 4.13 which extends down to the lowest q values measured. Apparently, the vesicle structures present in the ROMER samples were in a range of large diameters that scattered to low q values outside of the accessible q-range.

Complementary DLS measurements of the same ROMER suspensions revealed mean hydrodynamic diameters ranging from 374 nm to 368 nm for samples generated at zero and high shear rates, respectively. The minor size reduction detected at increasing shear rates confirms the negligible effect of the shear flow field at the membrane outlet on the structure of relatively large POPC vesicles obtained after one ROMER passage under the chosen process conditions.

In the following, the model-dependent analysis of the recorded SANS curves is discussed on the basis of the fitting results for the high shear sample only.

Model-dependent analysis of SANS curves I considering a population of weakly ordered membrane stacks: As the bilayers of large vesicles collected from the ROMER device represent local disc-like structures in the measured q-range, the recorded scattering curves could be fitted well with a form factor based on Porod's approximation for flat cylinders [355, 371]. The cylinder length L corresponds to the bilayer thickness d_{B}, while the radius R was chosen such that the diameter of the cylinder stretched beyond the distances probed in the SANS experiment. To account for polydispersity, the form factor for flat cylinders was combined with a
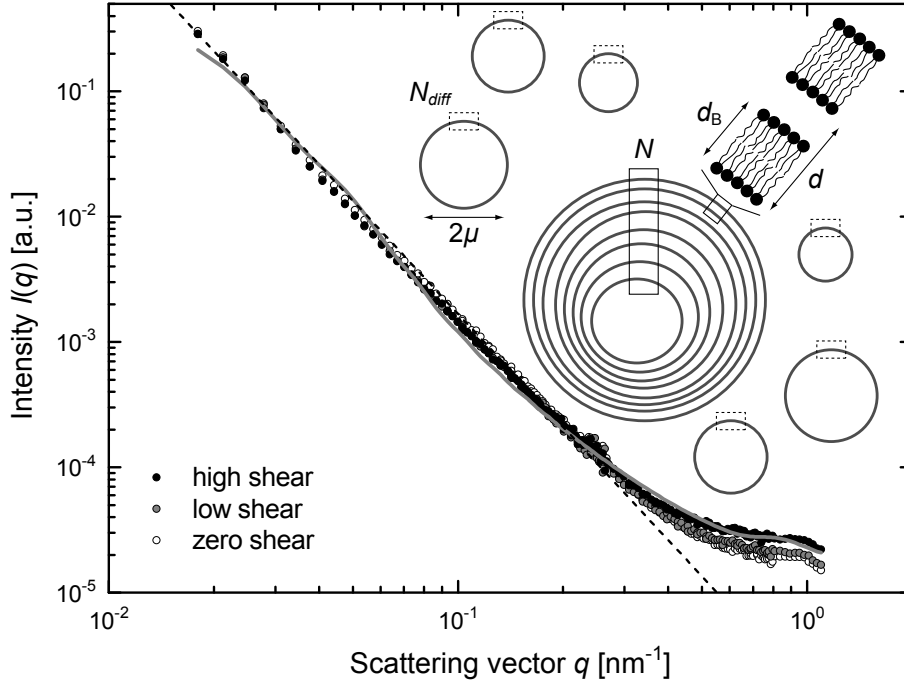
Figure 4.13: Radially averaged SANS curves of dynamcally extruded vesicles.
VET_{800} precursors were dynamically extruded 1 time through a PC200 membrane using
the ROMER device and applying zero (○), low ($\dot{\gamma}_{rep} = 6021\,s^{-1}$; ◉), and high shear rates
($\dot{\gamma}_{rep} = 60\,214\,s^{-1}$; ●). Flow rate: $1\,ml\,min^{-1}$. Shear gap height: $200\,\mu m$. Rotor speed:
$0\,rpm$, $1000\,rpm$, and $10\,000\,rpm$, respectively. $VETs_{800}$ were prepared by pre-extruding
a MLV suspension from POPC 3 times through a PC800 membrane using the LIPEX
device. Total lipid concentration: $0.645\,mM$. *Solid gray line*: model-dependent fit curve
to the SANS data of the high shear sample (●) considering a population of weakly ordered
membrane stacks. *Dashed black line*: q^{-3} power-law fit to the SANS data of the high
shear sample. *Diagram:* ROMER vesicle suspension with fitting parameters for bilayer
thickness d_B, lamellar repeat distance d, number of coherent scattering bilayers in the
membrane stack N, number of diffuse scattering bilayers N_{diff}, and median diameter 2μ
of the unilamellar vesicle population.

Delta size distribution which simply scales the form factor with a constant particle
number density n.
The scattering curves from dilute dispersions of disc-like structures, such as the con-
sidered planar bilayers, are well known to exhibit a power-law behavior of q^{-2} at
$q > 1/R_G$ [246]. However, this was not in agreement with the slope of -3 extracted
from the power-law region of the log-log plots presented in Figure 4.13 (see q^{-3} fit
curve). The intermediate q^{-3} decay of the scattering curves from ROMER samples
between that typically observed for discs (q^{-2}) and the Porod scattering from sharp
interfaces of dense structures (q^{-4}) [246] can be assigned to the presence of both
uni-/oligolamellar vesicles and dense multilamellar structures in the heterogeneous

ROMER suspensions. These two vesicle populations have also been observed by cryo-TEM imaging (Fig. 4.12).

Sample multilamellarity and the resulting steeper slope of the scattering curves could be well described by including a structure factor of weakly ordered membrane stacks [372]. Disorder was considered by the so-called stacking disorder caused by small variations in bilayer separations and described within the paracrystalline theory [268, 373, 374]. A Gaussian distribution of the number of bilayers in the stack N was introduced to account for the polydispersity of the stack size without affecting the form factor and the stacking separation, i. e. the lamellar repeat distance d [354]. With respect to the morphology of large vesicles, the number of coherent scattering bilayers in the stack N represents the mean number of bilayers per multilayer vesicle, while the additional diffuse scattering term N_{diff} accounts for the number of single, uncorrelated bilayers outside of the scattering domain, i. e. unilamellar vesicles [190].

The best full q-range fit to the SANS curve of the high shear sample including the form factor of flat cylinders and the structure factor of weakly ordered membrane stacks was obtained with a bilayer thickness of $d_{\mathrm{B}} = 4.1\,\mathrm{nm}$, a mean stacking number of $N = 8.4$ with a lamellar repeat distance of $d = 6.3\,\mathrm{nm}$, and a mean number of uncorrelated scattering bilayers of $N_{diff} = 7.4$ (see schematic illustration in Figure 4.13). The results for bilayer thickness d_{B} and lamellar repeat distance d in the ROMER sample prepared from pure POPC are in good agreement with literature values extracted from SAXS and SANS scattering data of fully hydrated POPC MLVs [190, 219, 300].

According to the numbers of coherent ($N = 8.4$) and diffuse scattering bilayers ($N_{diff} = 7.4$), the vesicle population of the investigated high shear sample consisted of approximately 85% unilamellar and 15% multilamellar vesicles comprising an average number of 8 lamellae per MLV. The estimated proportion of unilamellar vesicles was comparable or even higher than that typically reported for homogeneous LUVET$_{100}$ and VET$_{200}$ suspensions, which, however, are characterized by a lower mean number of lamellae per MLV of 2 to 3 [9, 10, 193, 219, 341]. This indicates that the MLV population in the studied ROMER suspension, while being relatively small, probably contained so-called lipid-rich liposomes with a large number of tightly packed bilayers. Such lipid-rich liposomes with practically uncountable numbers of lamellae were already observed in the cryo-TEM micrographs in Figures 4.12 C and F [341].

With respect to the applied pre-extrusion cycles through PC800 membranes followed by the single passage of the VET$_{800}$ suspension through the PC200 membrane in the ROMER device, the measured mean number of 8 lamellae per MLV is reasonable compared to the average stack size of $N \approx 25$ and $N \approx 3$ reported for fully hydrated MLVs and VETs$_{200}$, respectively [190, 219].

Model-dependent analysis of SANS curves II considering a population of weakly ordered membrane stacks and a population of unilamellar vesicels: The obtained fitting results were verified by a second approach for the global fit to the same scattering data, which included a population of unilamellar vesicles, in addition to the population of stacked bilayers as described above. The unilamellar vesicle population was represented by introducing a second form factor for spherical shells with an inner radius R and a shell thickness ΔR corresponding to the vesicle bilayer thickness d_B [355]. The spherical shell model was convoluted with a lognormal size distribution for the vesicle core radius R [355]:

$$p(R, \sigma, \mu) = (R\sqrt{2\pi\sigma^2})^{-1} \exp \frac{(\ln R - \ln \mu)^2}{2\sigma^2} \qquad (4.3)$$

where μ and σ represented the location and width parameters, respectively.

The best fit including the co-existing populations of stacked bilayers and unilamellar vesicles was obtained with a global bilayer thickness of $d_B = 4.3\,\text{nm}$ (fit curve not shown in Fig. 4.13). This is in good agreement with the corresponding value derived from the previous fitting procedure including the population of weakly ordered membrane stacks only ($d_B = 4.1\,\text{nm}$). The lognormal distribution parameters of the vesicle population were $\mu = 97\,\text{nm}$ for the median radius and $\sigma = 0.32$ for the geometric standard deviation reflecting the pore size of the PC200 membrane used for ROMER sample preparation.

While the stacking number of the stacked bilayer population revealed a mean number of lamellae per MLV of $N = 6.9$, the diffuse scattering term N_{diff} was close to one as the single, uncorrelated bilayers were now represented by the unilamellar vesicle population. Calculating the total bilayer areas in the stacked membrane and unilamellar vesicle populations confirmed the proportions of stacked to uncorrelated bilayers, i.e. multi- to unilamellar vesicles, identified in the high shear sample by the previous fitting approach.

Summary: Vesicle morphologies and dimensions of the high shear ROMER suspension as extracted from experimental SANS data using the two fitting procedures are summarized in the schematic illustration of Figure 4.13.

It has to be noted that the indicated structural parameters and their mean values reported in the text above were generally associated with broad statistical distribution functions. Heterogeneity in the ROMER suspensions was also reflected by the line shape of their diffuse scattering curves exhibiting only a weak signature of one quasi-Bragg reflection (Fig. 4.13). In contrast, the diffraction patterns of fully hydrated MLVs from a single lipid species in the L_α phase are known to exhibit two to three robust orders of Bragg peaks [372, 375]. The observed decrease in Bragg peak intensity accompanied by peak broadening indicates a high degree of stacking

disorder in the MLV population of ROMER suspensions as already revealed by the cryo-TEM micrographs in Figures 4.12C and F [372, 375].

From the cryo-TEM and SANS experiments reported in this section it can be concluded that the ROMER samples prepared from phospholipid VET_{800} pre-suspensions under standard process conditions were rather heterogeneous in terms of size and lamellartiy, irrespective of the applied shear rate.

4.3.5 Effectivity of dynamically enhanced vesicle extrusion at varying material and process parameters

Finally, the efficiency of the shear flow field in the ROMER prototype on the homogenization of MLVs was systematically studied as a function of nanopore shape and vesicle bilayer composition in the shear rate range between 0 and $60\,214\,\mathrm{s}^{-1}$.

Influence of pore shape in dynamically enhanced vesicle extrusion

The influence of pore shape on the homogenizing effect of dynamically enhanced vesicle extrusion was studied by passing VET_{800} pre-suspensions through the ROMER device at varying shear rates using the two track-etched polymer membranes PC200 and PET210 with cylindrical and biconical pore channels, respectively. Both membrane types have a nominal pore diameter of around $200\,\mathrm{nm}$ and have been shown to perform similarly in the conventional, repetitive extrusion process using the static LIPEX device, despite their different pore shapes (Secs. 4.3.2 and 4.3.3).

Experimental ROMER series were carried out using the standard device configuration at four increasing shear rate settings ($\dot{\gamma}_{\mathrm{rep}} = 0$, 6021, 30107, and $60\,214\,\mathrm{s}^{-1}$) as described in Materials and Methods (Sec. 4.2.3). The VET_{800} pre-suspensions were prepared from S100/POPE 95:5 (mol/mol) and the feed rate was controlled at $1\,\mathrm{mL\,min}^{-1}$ resulting in average transmembrane pressures of $1.4\,\mathrm{bar}$ and $1.8\,\mathrm{bar}$ for the PC200 and PET210 membranes, respectively.

The initial VET_{800} and the dynamically extruded vesicle suspensions were analyzed by DLS measurements and the TNBS assay to obtain the structural vesicle parameters as summarized in Figure 4.14. Shown are the hydrodynamic diameter D_h (Fig. 4.14A), the relative external surface area E (Fig. 4.14B), and the polydispersity index PDI (Fig. 4.14C), all normalized to the corresponding initial structural parameters, of S100 $VETs_{800}$ after dynamically enhanced extrusion through the PC200 and PET210 membranes as a function of the applied shear rate. Absolute values of the structural parameters of the initial VET_{800} suspension (index 0) and of the extruded suspensions collected after exposure to zero (index $\dot{\gamma}0$) and to maximum shear (index $\dot{\gamma}$max) are also indicated in Figure 4.14.
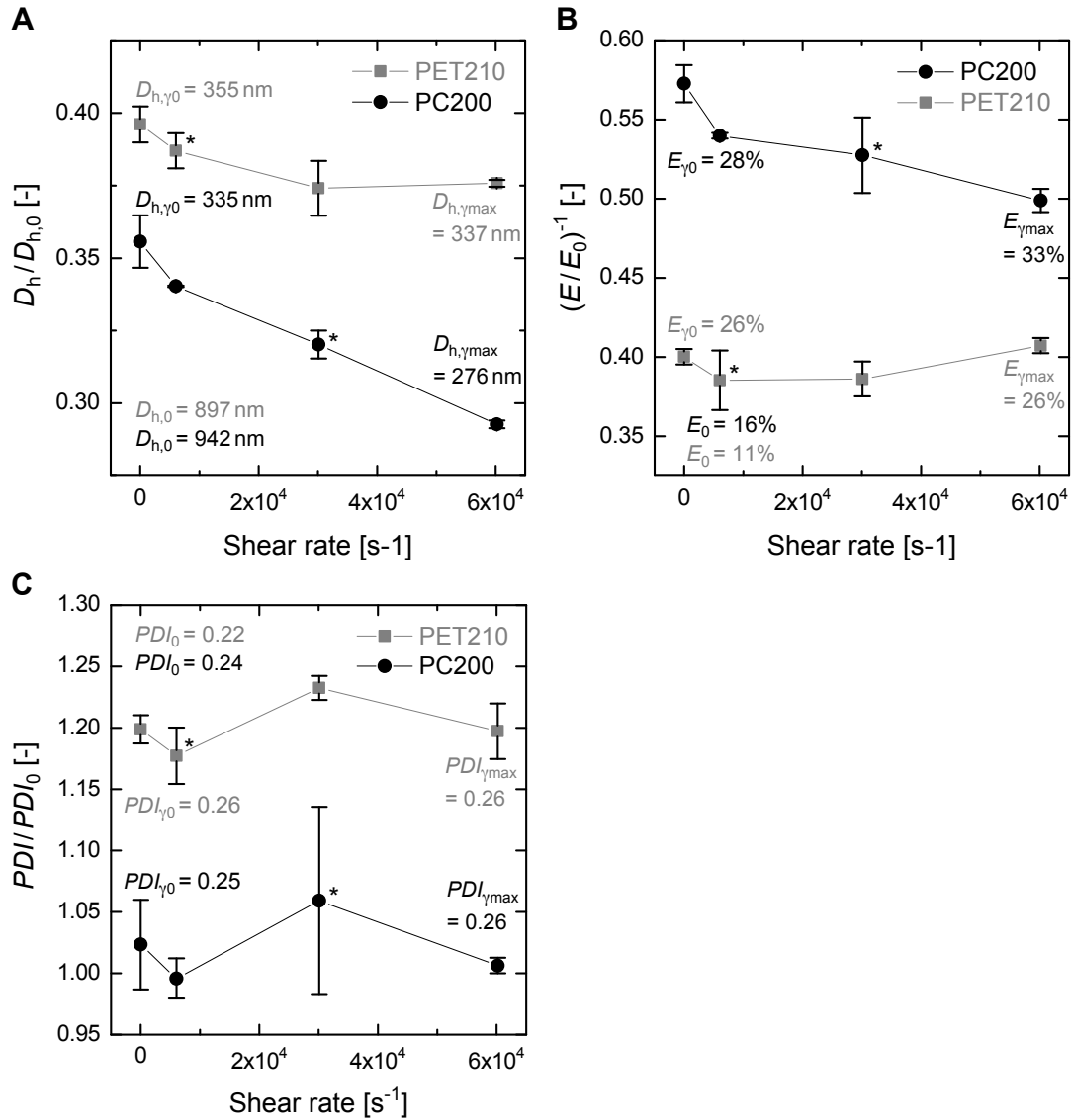
Figure 4.14: Homogenization of MLVs by dynamically enhanced extrusion using the ROMER device – effect pore shape. Hydrodynamic diameter D_h (A), relative external surface area E (B), and polydispersity index PDI (C), normalized to the respective initial values $D_{h,0}$, E_0, and PDI_0, of VETs$_{800}$ after one dynamically enhanced extrusion cycle through PC200 (cylindrical pores; ●) or PET210 membranes (biconical pores; ■) using the ROMER device at increasing shear rates ($\dot{\gamma}_{rep} = 0\text{-}60\,214\,\text{s}^{-1}$). Flow rate: $1\,\text{ml}\,\text{min}^{-1}$; resulting mean extrusion pressure: $1.4\,\text{bar}$ (PC200) and $1.8\,\text{bar}$ (PET210). Extrusion time: $400\,\text{s}$. Shear gap height: $200\,\mu\text{m}$. Rotor speed: $0\,\text{rpm}$, $1000\,\text{rpm}$, $5000\,\text{rpm}$, and $10\,000\,\text{rpm}$. VET$_{800}$ precursors were prepared by pre-extruding a MLV suspension from S100/POPE 95:5 (mol/mol) 3 times through a PC800 membrane using the LIPEX device. Total lipid concentration: $0.645\,\text{mM}$. Results represent mean values and standard deviations of the means of three (* two) independent ROMER experiments using the same VET$_{800}$ pre-suspension for each membrane type tested. Lines are drawn to guide the eye.

Dynamically enhanced homogenization of MLVs using cylindrical vs. biconical pore membranes: Dynamically enhanced VET_{800} extrusion through the cylindrical pores of the PC200 membrane allowed a reduction of the average vesicle diameter from 335 nm to 276 nm at increasing shear rates between 0 and $60\,214\,\mathrm{s^{-1}}$. In contrast, inserting the PET210 membrane with biconical pore channels under the same processing conditions did not result in a significant shear-induced vesicle size reduction (Fig. 4.14A). The evolution of vesicle lamellarity as a function of the applied shear rate was directly reflected by the observed size changes. The lamellarity decreased, i.e. the relative external surface area increased, as vesicles were downsized with increasing shear rates using the PC200 membrane, while size and lamellarity were not influenced by the shear flow at the outlet of the PET210 membrane (Figs. 4.14A and B).

It has to be noted that the size reduction as a function of shear rate obtained with the PC200 membrane was relatively small compared to the initial vesicle size. This is indicated by the normalized values of mean hydrodynamic vesicle diameters plotted in Figure 4.14A. The vesicle size after simple extrusion through the PC200 membrane in the absence of a shear field ($\dot{\gamma}_{\mathrm{rep}} = 0\,\mathrm{s^{-1}}$) accounted for 36% of the initial VET_{800} size. This corresponds to a vesicle size reduction of 64% by the conventional extrusion component of the ROMER process, whereas the shear flow at the membrane outlet contributed to an additional down-sizing of only 6% at the maximum shear rate tested ($\dot{\gamma}_{\mathrm{rep}} = 60\,214\,\mathrm{s^{-1}}$).

The performances of the PC200 and PET210 membranes in dynamically enhanced vesicle extrusion could not be distinguished in terms of sample polydispersity as the *PDI* values were not influenced by the applied shear rate for either membrane type used (Fig. 4.14C). Apart from the anyhow small variation in mean vesicle size as a function of shear rate (Fig. 4.14A), this can be explained by the instability of *PDI* results for polydisperse samples obtained from the traditional cumulant fit to the measured DLS data as already discussed in Section 4.3.3 [250]. Indeed, the *PDI* values of ROMER sampels were as high or slightly higher than those of the initial VET_{800} suspensions resulting in relative *PDI* values around and above unity, respectively (Fig. 4.14C). This shows that a single passage of the heterogeneous VET_{800} pre-suspension through the ROMER device broadens the vesicle size distribution, irrespectively of the applied shear rate. The increase in sample polydispersity during ROMER processing was comparable to that generated by a single extrusion cycle through the static LIPEX device using the same vesicle and membrane systems (Figs. 4.14C and 4.11C).

Homogenization of MLVs by dynamically enhanced vs. repetitive static extrusion: Due to the minor influence of the ROMER shear flow on the structure of dynamically extruded vesicles, varying shear rates did not allow to specifically adjust vesicle morphology, for example to the well defined $VET_{100\text{-}400}$ structures obtained

from the conventional extrusion procedure [3, 9, 193]. The mean diameter and external surface area of the ROMER suspension generated with the PC200 membrane at maximum shear rate ($D_{h,\dot{\gamma}\text{max}} = 276\,\text{nm}$; $E_{\dot{\gamma}\text{max}} = 33\%$) compared just well to the structure of VETs$_{400}$ prepared by 10 static extrusion cycles through 400-nm pore PC membranes [9, 10].

Inserting the same type of 200-nm pore membranes in the dynamic and static extrusion devices showed that, under the applied extrusion conditions, the dynamically enhanced ROMER process was slightly less efficient in the homogenization of S100 VET$_{800}$ precursors than the static LIPEX device (Figs. 4.11 and 4.14). Even at the maximum shear rate tested, the relative vesicle diameters obtained by ROMER processing ($D_{h,\dot{\gamma}\text{max}}/D_{h,0} = 0.29$ for PC200; $D_{h,\dot{\gamma}\text{max}}/D_{h,0} = 0.38$ for PET210) were slightly larger than those measured after a single extrusion cycle through the LIPEX device ($D_{h,1}/D_{h,0} = 0.24$ for PC200; $D_{h,1}/D_{h,0} = 0.35$ for PET210) for both PC200 and PET210 membrane types used. The larger extent of vesicle size reduction achieved by static extrusion can be assigned to the larger extrusion pressure of 6 bar applied to the LIPEX device compared to the transmembrane pressures of $< 2\,\text{bar}$ resulting from the low throughput of $1\,\text{mL}\,\text{min}^{-1}$ through the PC200 and PET210 membranes during ROMER processing.

In other words, the well known downsizing effects of increased pressures and higher resulting flow velocities through the pores in the conventional extrusion process (Sec. 2.6) [15, 119, 208, 209] were not overcome by the shear flow field induced at the membrane outlet of the ROMER device.

Mechanism of vesicle breakup in dynamically enhanced pore extrusion: The observations described above confirm the pressure-dependent models of vesicle extrusion through a given pore diameter as suggested by Patty and Frisken (Sec. 2.6.3) [15] and Bertrand and Joós (Sec. 2.6.4) [119]. Based on their models describing a pressure-induced mechanism of vesicle breakup at the entrance of cylindrical pores and on the collected ROMER data (Fig. 4.14), we are able to summarize the rupture events at the inlet, inside and at the outlet of nanopore channels during ROMER processing as follows (see also Fig. 4.15 for a schematic summary).

Large VET$_{800}$ precursors are primarily broken up at the inlet of the static ROMER membrane. The applied pressure and the geometrical constraints imposed by the 200-nm orifice of cylindrical PC200 and biconical PET210 pores induce a membrane tension that exceeds the rupture tension of the S100 bilayer as the VETs$_{800}$ are pushed into the pore. Cevc and coworkers have determined a critical vesicle to nanopore radius ratio of $R_V/R_P = 1.5$ for pure soy PC vesicles above which the lipid bilayer is not able to tolerate the deformation and concomitant area expansion during pore penetration without bursting [188]. With a ratio of initial vesicle radius to nominal pore radius $R_{h,0}/R_P$ of 4.3–4.7 during the presented ROMER experiments using either membrane type (Fig. 4.14A), S100 VETs$_{800}$ were, indeed, very

likely to rupture at the pore inlet (Fig. 4.15). Vesicle breakdown at the 200-nm pore orifice becomes also apparent from the larger extent of vesicle size reduction (i.e. smaller relative vesicle diameters $D_h/D_{h,0}$) with increasing initial VET$_{800}$ sizes (i.e. increasing $R_{h,0}/R_P$ values) by ROMER processing over the entire shear rate range (Figs. 4.14A and 4.16A). In analogy to conventional pressure extrusion, this shows that the mean vesicle size produced by the ROMER device is mostly defined by the geometrical constraints of the pore diameter rather than by the applied shear rate [15, 119].

The bilayer fragments released into the pore and drifting through the channel upon vesicle breakup self-close into smaller vesicles which are then hardly affected by the shear flow field at the membrane outlet (Fig. 4.14A). This can be rationalized especially in the case of a *stochastic rupture* of large vesicles via multiple pore nucleation in the neck region of the pore channels. Stochastic vesicle rupture gives rise to bilayer sheets flowing along the channel as observed in the simulations by Bertrand and Joós [119]. In their study, the flat bilayer fragments are proposed to fold and self-close into smaller vesicles at the pore exit under a simultaneous loss of internal volume, that is under creation of excess surface area. Such deflated vesicles would be even less susceptible to a subsequent shear-induced breakup at the membrane outlet of the ROMER device since flaccid vesicles easily deform in the presence of high shear forces until the reservoir of excess area becomes zero [366, 376]. Only upon further deformation, the vesicle membrane area would expand and induce a membrane tension in the bilayer that would eventually reach its lysis tension.

In contrast to a stochastic breakup mechanism, the static description of vesicle extrusion by Patty and Frisken proposes an *axisymmetric rupture* of large vesicles at the opening of cylindrical pores such that hemispherical bilayer fragments are separated from the entering vesicles ("bubble blowing model"; Fig. 2.11A) [15]. In this case, the vesicle fragments are assumed to immediately self-close and travel through the pore channel in the steady-state shape of a spherocylinder, before they relax into a spheroid outside of the channel [119, 208, 245]. The spherocylinder has a greater surface area and, hence, higher membrane tension than the sphere of equal volume. Furthermore, additional membrane tension has been described to build up by viscous stresses as the spherocylindrical vesicle flows through the pore channel such that the tension decreases from front to back of the spherocylinder (Eq. 2.9 and Fig. 2.11B) [119, 245]. According to this, the frontal endcap of vesicles exiting cylindrical pore channels in the form of a spherocylinder is more likely to be sheared off in dynamically enhanced vesicle extrusion.

Summary: Indeed, the pre-stretched state of a spherocylindrical vesicle membrane and the confining wall effects of well-defined cylindrical pore exits seem to be a prerequisite for vesicle breakup by the shear forces at the membrane outlet in dynamically enhanced vesicle extrusion (Fig. 4.15). This is indicated by the shear-induced
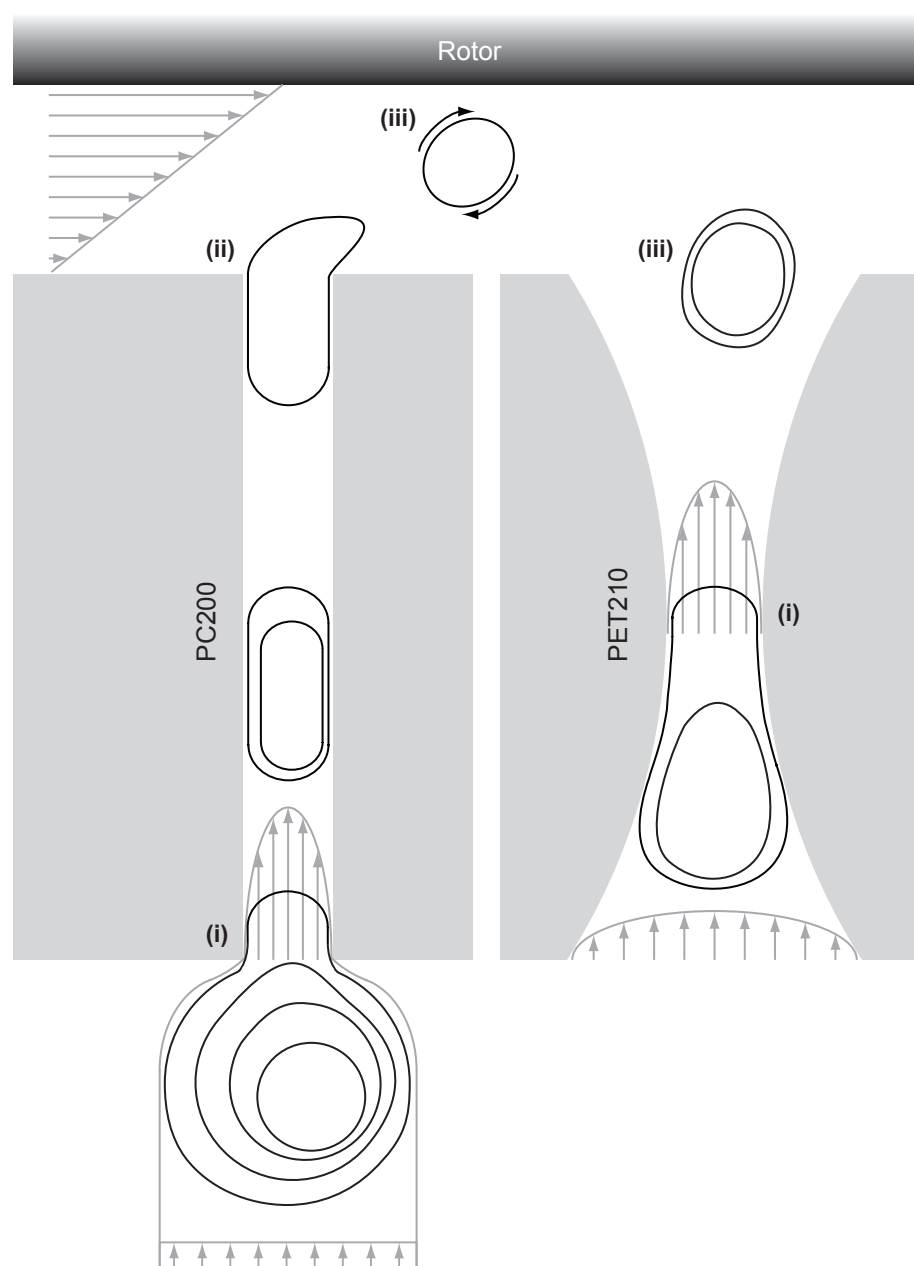
Figure 4.15: Summary of vesicle breakup events in dynamically enhanced pore extrusion. Schematic illustration of dynamically enhanced vesicle extrusion through cylindrical (PC200) and biconical nanopore channels (PET210) by the ROMER device, including characteristic flow patterns and breakup mechanisms of vesicles along the process sequence (not drawn to scale). (i) Extensive pressure-induced breakup of large vesicles in the uniaxial elongation flow at the entrance constriction of the pore channel. (ii) Small extent of vesicle breakup in the simple shear flow at the pore exit in the case of confined and deformed emerging vesicles. (iii) No vesicle breakup in simple shear flow in the case of free-flowing, quasispherical vesicles.

reduction in vesicle size and lamellarity achieved by ROMER processing of VETs$_{800}$ using the PC200 membrane with cylindrical pore channels (Figs. 4.14A and B). Due to the extensive pressure-induced VET$_{800}$ breakdown at the inlet of the 200-nm pores, the effect of the shear flow field at the membrane outlet was, however, small. In contrast, the structure of vesicles exiting the conical openings of the PET210 membrane was not significantly influenced by the ROMER shear flow in the evaluated shear rate range (Fig. 4.14). As reported previously, vesicles being forced through the biconical PET210 channels break up to similar extents at the central PET210 constriction as those entering cylindrical PC200 pore channels, but they seem to quickly relax into spheroids as they exit the conical channels. The ROMER results for the PET210 membrane show that vesicles entering the simple shear flow at the membrane outlet in an unconfined, quasispherical state are not broken up by the viscous flow forces (Fig. 4.15).

The flow behavior of vesicles in the simple shear flow of the ROMER device, as well as at the inlet and outlet of cylindrical pores is discussed in further detail in Section 4.3.6.

Influence of vesicle membrane elasticity in dynamically enhanced vesicle extrusion

In order to reduce the extent of vesicle breakdown at the pore inlet, the bilayer softening agent sodium cholate (SC) was added to the initial S100-based vesicle suspension following the original Transfersome formulations by Cevc [177, 189, 377]. Typical Transfersomes consist of a soy PC matrix membrane with 11–13 w/w% SC. They are known to be extremely deformable and have been shown to penetrate pores at vesicle to pore radius ratios of $R_V/R_P \leq 5$ without bursting [188, 378].

According to this, VET$_{800}$ pre-suspensions were prepared from S100/SC/POPE 85:10:5 (mol/mol) which corresponds to a total phospholipid/SC weight/weight ratio of approximately 94:6. This is clearly below the saturation and solubilization limit of similar phosphatidylchline/cholate bilayer systems [176, 178, 181–183]. Systematic ROMER experiments were carried out under standard process conditions as described in the previous section and in Materials and Methods (Sec. 4.2.3) but using the PC200 membrane only. The aim of these experiments was to study the possibly larger effect of the ROMER shear flow on the breakdown of highly deformed but intact VETs$_{800}$ at the exit of cylindrical 200-nm pore channels.

Figure 4.16 again shows the results in the form of relative extruded vs. initial structural vesicle parameters as a function of the applied shear rate for S100 vesicles with and without the incorporation of SC. For reasons of clarity, only the absolute values of the initial VET$_{800}$ parameters (index 0) are included in the figure.
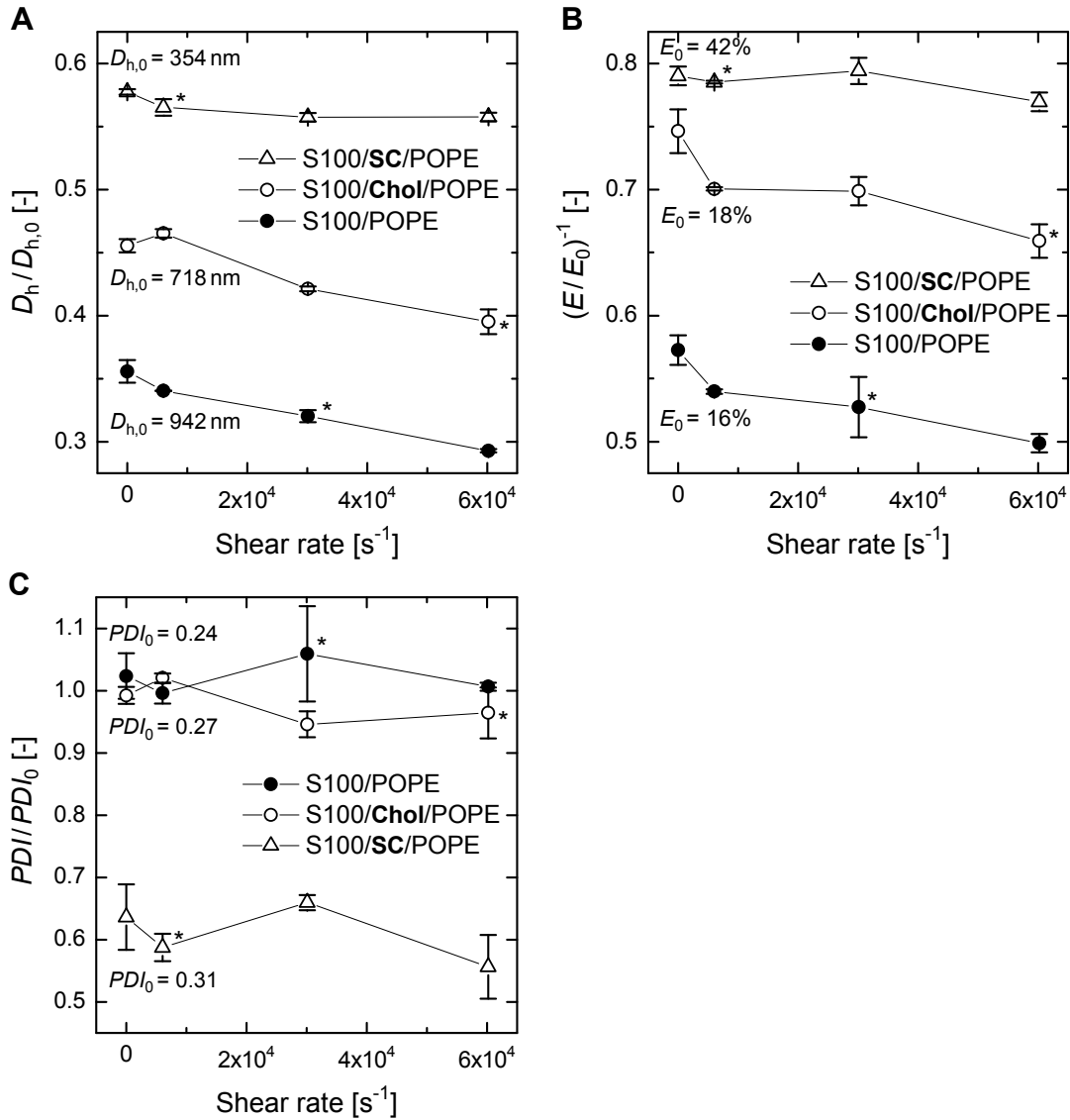
Figure 4.16: Homogenization of MLVs by dynamically enhanced extrusion using the ROMER device – effect vesicle membrane elasticity. Hydrodynamic diameter D_h (A), relative external surface area E (B), and polydispersity index PDI (C), normalized to the respective initial values $D_{h,0}$, E_0, and PDI_0, of VETs$_{800}$ from S100/POPE 95:5 (mol/mol) (●), S100/Chol/POPE 65:30:5 (mol/mol) (○), and S100/SC/POPE 85:10:5 (mol/mol) (△) after one dynamically enhanced extrusion cycle through PC200 membranes using the ROMER device at increasing shear rates ($\dot{\gamma}_{rep}$ = 0–60 214 s^{-1}). Flow rate: 1 ml min^{-1}; resulting mean extrusion pressure: 1.4 bar (S100/POPE), 1.2 bar (S100/Chol/POPE), and 1.1 bar (S100/SC/POPE). Shear gap height: 200 μm. Rotor speed: 0 rpm, 1000 rpm, 5000 rpm, 10 000 rpm. VET$_{800}$ precursors were prepared by pre-extruding a MLV suspension 3 times through a PC800 membrane using the LIPEX device. Total lipid concentration: 0.645 mM. Results represent mean values and standard deviations of the means of three (* two) independent ROMER experiments using the same VET$_{800}$ pre-suspension for every bilayer composition tested. The lines are drawn to guide the eye.

147

Homogenization of soft MLVs by dynamically enhanced extrusion: Apart from an increased bilayer elasticity, the incorporation of edge-active SC in the S100 host membrane inevitably led to higher spontaneous membrane curvatures as already mentioned in Section 4.3.1 [81, 181, 187]. This resulted in significantly smaller equilibrium sizes of the initial VETs$_{800}$ with a mean $D_{h,0}$ of 354 nm (Tab. 4.6). Considering the low value of the resulting initial vesicle to pore radius ratio $R_{h,0}/R_\mathrm{P}$ of 1.8 and the increased bilayer elasticity, it is not surprising that SC-doped vesicles were, indeed, only broken up to small extents during passage through the PC200 membrane (Fig. 4.16A). Their structure, including vesicle size, lamellarity and polydispersity, was practically insensitive to the subsequent ROMER shear flow (Figs. 4.16A–C), even though the energy required for the fragmentation of more deformable lipid membranes is known to be lower [15, 187–189].

This shows again that lipid bilayer membranes are not broken up by the simple ROMER shear flow if the degree of vesicle deformation at the pore exit is small, in this case due to the small initial vesicle to pore radius ratio. Furthermore, it has to be noted that mixed PC/SC vesicles with high bilayer elasticites often adopt non-spherical shapes with surface undulations under the influence of thermal motion [81, 177, 181]. The increased thermal fluctuations in such mixed fluid bilayers "hide" excess area that can easily be pulled out by the ROMER shear flow thereby deforming the soft vesicles without reaching their otherwise low lysis tension [89, 187, 188]. For the same reason of non-spherical shape fluctuations that are not resolvable with dynamic light scattering, the *PDI* values of the SC-containing VET$_{800}$ presuspensions were higher than those of the corresponding standard phospholipid suspensions (Tab. 4.6, Fig. 4.16C). Additionally and more importantly, the polydispersity of mixed PC/SC vesicle suspensions is usually increased due to the coexistence of vesicles with small mixed micelles and much larger aggregates with thread-like protrusions over a broad range of total cholate concentrations as observed by Elsayed and Cevc [181]. The reductions in vesicle size and polydispersity by roughly 40% measured after passage of the cholate-enriched VETs$_{800}$ through the PC200 membrane (Figs. 4.16A and C) can primarily be attributed to the breakdown of these large mixed aggregates.

The absolute values of external surface area results for SC-incorporating vesicles were clearly overestimated as mentioned previously for the S100/SC/POPE VETs$_{800}$ (Tab. 4.6) and indicated by $E > 50\%$ for the corresponding 200-nm sized dynamically extruded vesicles (Fig. 4.16B). This is a direct consequence of surfactant insertion into lipid vesicles which not only lowers bilayer bending rigidity [174, 181, 186, 187, 379] but simultaneously facilitates permeation of the mixed lipid bilayer [176, 182, 183, 188]. In the case of the TNBS assay, the increased bilayer permeability led to overestimated E values due to internal lipid labeling by permeation of the external reagent into the mixed lipid vesicles during time of analysis [10, 204]. An additional increase of the apparent relative external surface area of soft vesicles was probably caused by the presence of mixed micelles and thread-like mixed aggregates

in the S100/SC/POPE vesicle suspension [181]. Nevertheless, the relative initial vs. extruded external surface area results for the SC-containing vesicles (Fig. 4.16B) reflected the evolution of soft vesicle size at the different ROMER parameters studied (Fig. 4.16A). The collected data showed a small reduction of both mean vesicle size and lamellarity upon ROMER processing and negligible influence of the applied shear rate on the structure of soft vesicles using cylindrical pore membranes.

Homogenization of rigid MLVs by dynamically enhanced extrusion: As opposed to working with more elastic ROMER precursors, cholesterol was added to the initial VET_{800} suspension based on S100 to increase the bending rigidity [127, 128, 134, 137, 174] and lysis tension [11, 15, 380] of the vesicle bilayers.

Figure 4.16 includes the structural data for $VETs_{800}$ from S100/Chol/POPE 65:30:5 (mol/mol) collected after standard ROMER processing using the PC200 membrane at varying shear rates. It reveals a very similar behavior of S100-based $VETs_{800}$ with and without the addition of the membrane stiffening agent cholesterol under the evaluated processing conditions. Briefly, the average vesicle sizes and lamellarities were primarily reduced by the simple passage of $VETs_{800}$ through the cylindrical pore channels and showed a small decrease with increasing shear rates (Figs. 4.16A and B), whereas the suspension polydispersities were not affected by ROMER processing (Fig. 4.16C).

The breakup phenomena of cholesterol-containing $VETs_{800}$ along cylindrical pore channels in the ROMER device can, thus, be summarized in analogy to those described in the previous section for standard S100 $VETs_{800}$. In accordance to the scheme in Figure 4.15, large rigid vesicles break up mainly axisymmetrically at the opening of narrow cylindrical pores and travel through the channel in a smaller spherocylindrical shape. If the spherocylinder exiting the pore is large, i. e. deformed enough, its leading endcap is sheared off by the ROMER shear flow acting at the membrane outlet.

In spite of the increased bilayer rigidity of cholesterol-incorporating vesicles, the extent of shear-induced size reduction by ROMER processing was the same for VET_{800} precursors with and without the inclusion of cholesterol. For both standard and rigid vesicles, the diameter decreased by 6% with respect to the initial VET_{800} diameter at increasing shear rates between 0 and $60\,214\,s^{-1}$ (Fig. 4.16A). A possible explanation for this is the larger lysis tension of cholesterol-supplemented vesicle membranes allowing for larger area projections of the bilayer to be pulled into the pore before vesicle rupture [11, 122]. This results in larger spherocylinders traveling through the pore channel which requires a higher degree of vesicle deformation at constant pore diameter. The increased bilayer area dilation at the pore exit probably compensates for the higher cohesion of the cholesterol-incorporating bilayer and allows for the observed extent of shear-induced vesicle fragmentation at the membrane outlet.

Summary: Generally, the results presented in Figure 4.16 demonstrate again that the extent of vesicle homogenization in terms of size, lamellarity and polydispersity by ROMER processing was primarily influenced by the initial vesicle to pore size ratio. The larger the mean size, lamellarity, and polydispersity of the initial vesicle suspension was, the larger was the reduction of these structural parameters upon passage through the ROMER device at constant pore diameter, irrespective of the applied shear rate and the vesicle membrane elasticity.

4.3.6 Vesicle deformation and breakup criteria in dynamically enhanced pore extrusion

The importance of nanopore membrane effects at the channel outlet and the otherwise minor influence of the shear flow on vesicle deformation during ROMER processing can be demonstrated by evaluating a number of deformation parameters.
In analogy to droplet or bubble dynamics in viscous flow fields [381–383], a dimensionless capillary number Ca can be defined to describe the deformation and breakup behavior of vesicles in viscous fluids. Ca relates the disruptive forces of the flow stresses responsible for vesicle deformation to the opposing cohesive forces of the elastic bilayer that keep the vesicle in its equilibrium shape, generally a sphere [91]. At low Ca, the vesicle can constantly relax to its equilibrium shape of zero membrane tension and minimum curvature energy (Secs. 2.3.2 and 2.3.5), while at increasing Ca it is increasingly deformable until it breaks up when exceeding the so-called critical capillary number Ca_{crit}. It has to be noted that the deformation of fluid-phase lipid vesicles typically involves two types of independent local shape changes in the elastic bilayer, including isotropic area expansion and bending (Sec. 2.3.5) [122]. The two modes of deformation can be described separately by distinguishing between a **stretching capillary number Ca_K** [366, 384] and a **bending capillary number Ca_κ** [90, 92, 384, 385]. Ca_K and Ca_κ measure the ratio between the disruptive forces of the viscous flow and the vesicle's resistance to stretching (characterized by the elastic area expansion modulus K_A) and to bending (characterized by the elastic bending modulus κ_c), respectively:

$$Ca_K = \frac{\text{viscous flow stress}}{\text{bilayer area expansibility}} = \frac{\eta_{\text{ext}} G R_0}{K_A} \tag{4.4}$$

$$Ca_\kappa = \frac{\text{viscous flow stress}}{\text{bilayer bending rigidity}} = \frac{\eta_{\text{ext}} G R_0^3}{\kappa_c} \tag{4.5}$$

Here, η_{ext} is the viscosity of the external fluid, G the rate of deformation in laminar flow fields, and R_0 the radius of an equivalent sphere of the undeformed vesicle. G

is generally composed of the linear combination of shear and elongation rates acting in any type of mixed laminar flow according to $G = |\dot{\gamma}| + |\dot{\varepsilon}|$ [386].

Vesicle flow behavior in the linear shear flow of the ROMER shear gap

Considering the flow field in the shear gap of the ROMER apparatus as pure uniaxial shear flow in which the velocity changes only in y-direction (Fig. 4.15), the deformation rate G is represented by the induced shear rate only (Eq. 2.5). According to this, Ca_K and Ca_κ were calculated by replacing G in Equations 4.4 and 4.5 with the representative shear rate $\dot{\gamma}_{\mathrm{rep}}$ to evaluate the deformation behavior of S100 vesicles suspended in the ROMER shear flow. The radius R_0 of the undeformed vesicles in the shear gap was taken to be equal to $R_{h,\dot{\gamma}0} = D_{h,\dot{\gamma}0}/2 = 168\,\mathrm{nm}$ measured for the S100-based VETs$_{800}$ after passage through the PC200 membrane in the absence of a shear field (Fig. 4.14A). For the material parameters of S100 bilayers, the elastic moduli $K_A = 247\,\mathrm{mN/m}$ and $\kappa_c = 0.44 \times 10^{-19}\,\mathrm{J}$ for DLPC membranes were adopted from literature [14] since DLPC largely represents the phosphatidylcholine composition of the S100 mixture (Tabs. 4.1, 4.2, and 4.3).

The results for the different parameters describing the deformation of free-flowing S100 vesicles in the ROMER shear gap under standard process conditions are summarized in the upper part of Table 4.8. The lower part of the Table includes literature values of the corresponding critical deformation parameters for phosphatidylcholine vesicles in unconfined external shear flows, as well as the critical Ca_K and Ca_κ values for S100 vesicle breakup at the inlet and outlet of the PC200 membrane in the ROMER device.

Stretching capillary number *Ca_K*: The stretching capillary number Ca_K for S100 vesicles in the ROMER shear gap was around 10^{-5} for the entire range of investigated shear rates. This is three orders of magnitude below the critical stretching capillary number $Ca_{K,\mathrm{crit}} \approx 10^{-2}$ for lipid vesicle breakup observed in a three-dimensional shear flow near ultrasound-driven microbubbles in a glycerol/water mixture with $\eta_{\mathrm{ext}} = 20\eta_{\mathrm{water}}$ [366]. Performing the same acoustic streaming flow experiment in pure water resulted in $Ca_K \approx 10^{-4}$ to 10^{-3} and did not allow for vesicle rupture. In a numerical study on the flow behavior of lipid vesicles under linear shear flow in the small deformation regime, Biben and Misbah have chosen $Ca_K = 10^{-4}$ to preserve the local incompressibility of the vesicle membrane in the imposed shear flow [384]. These numbers strongly suggest that the shear-induced membrane tension of S100 vesicles moving through the ROMER shear gap at $Ca_K = 10^{-5}$ does not exceed the rupture tension of the bilayer. Exposure to the simple shear flow field does probably

Table 4.8: Deformation and breakup behavior of lipid vesicles in the fluid state in dynamically enhanced membrane extrusion using the ROMER device.

Upper part: Dynamical parameters describing the deformation and flow behavior of fluid-phase S100 vesicles freely suspended in the shear gap of the ROMER device assuming simple shear flow conditions ($\dot{\varepsilon} = 0$). Included are the stretching and bending capillary numbers Ca_K (Eq. 4.4) and Ca_κ (Eq. 4.5), the Taylor deformation parameter D (Eq. 4.6), the shear-induced membrane tension σ (Eq. 4.7), and the effective shear Reynolds number for vesicles Re_V (Eq. 4.9) as a function of the applied shear rate $\dot{\gamma}_{\mathrm{rep}}$. Shear gap height: $200\,\mu$m. Internal and external fluid: MilliQ water with $\eta = 0.89 \times 10^{-3}\,$Pa s and $\rho = 997\,$kg/m^3 at $T = 25\,°$C. Radius R_0 of undeformed vesicles in the shear gap = average radius of standard VETs$_{800}$ from S100/POPE 95:5 (mol/mol) after a single passage through the PC200 membrane in the absence of a shear field: $R_{h,\dot{\gamma}0} = 168\,$nm.

Lower part: Critical dynamical parameters describing the breakup behavior of fluid-phase phosphatidylcholine vesicles in unconfined external shear flows (literature data) [13, 90, 366], as well as at the outlet (confined simple shear flow) and at the inlet (confined uniaxial elongation flow) of the PC200 membrane pore channels incorporated in the ROMER device.

Rotor speed [rpm]	$\dot{\gamma}_{rep}$ [s^{-1}]	$Ca_K^{(a)}$ [-]	$Ca_\kappa^{(b)}$ [-]	$D^{(b,c)}$ [-]	σ [mN/m]	Re_V [-]
1000	6021	0.4×10^{-5}	0.6	0.12	0.9×10^{-2}	1.9×10^{-4}
5000	30107	1.8×10^{-5}	2.9	0.16	3.6×10^{-2}	9.5×10^{-4}
10000	60214	3.6×10^{-5}	5.7	0.17	6.6×10^{-2}	1.9×10^{-3}
Unconfined shear flow		1.0×10^{-2}	> 500	1.44	5.1	n. a.
ROMER membrane outlet		1.9×10^{-4}	8.0	0.01	5.1	n. a.
ROMER membrane inlet		7.3×10^{-6}	0.7	n. a.	5.1	n. a.

Literature values of material parameters for fluid phase PC vesicle membranes used in calculations:
[a] elastic area expansion modulus of DLPC bilayers $K_A = 247\,$mN/m [13]
[b] elastic bending modulus of DLPC bilayers $\kappa_c = 0.44 \times 10^{-19}\,$J [13]
[c] effective membrane tension of undeformed giant DMPC vesicles $\sigma_0 \approx 10^{-3}\,$mN m^{-1} [88]

hardly lead to a steady deformation of the vesicles if their shape is close to spherical, i.e. their excess area is small, as they are released from the nanopore membrane.

Bending capillary number Ca_κ: The same findings were revealed by the ROMER values for the bending capillary number Ca_κ of S100 vesicles which increased from 0.6 to 5.7 between the minimum and maximum shear rates tested (Tab. 4.8). According to the experimental results on lipid vesicle dynamics in the shear field of a Poiseuille flow by Mader *et al.* [90], the estimated Ca_κ values of the ROMER process were below the transition range of $10 < Ca_\kappa < 100$ for the onset of vesicle deformation. The experimental study by Mader *et al.* covered a very wide and high range of bending capillary numbers of $Ca_\kappa = 1.5$ to 527 compared to most other studies on vesicle dynamics in simple shear flow focusing on small deformation theories at $Ca_\kappa < 100$ [87, 92, 376, 385, 387, 388]. At high capillary numbers, Mader *et al.* showed that vesicles became increasingly sensitive to deformation due to the elongational component they experience in the Poiseulle flow, but they did not rupture under the investigated flow conditions. This confirms that the simple shear flow conditions in the ROMER device do not allow for the breakup of quasispherical S100 vesicles suspended in the shear gap, even when applying the maximum shear rate, i.e. $Ca_\kappa = 5.7$ (Tab. 4.8).

Small deformation theories: Based on the low capillary numbers found for S100 vesicles in the ROMER shear gap (Tab. 4.8), we can assume that the vesicle dynamics in the induced shear flow can be described by small deformation theories. In the small deformation limit, vesicles in linear shear flow reveal three types of motion, namely tank-treading, tumbling, and vacillating-breathing (also described as trembling or swinging). They are governed by three main control parameters: the excess area Δ, the viscosity ratio between the internal and external fluids $\lambda = \eta_{\text{int}}/\eta_{\text{ext}}$, and the bending capillary number Ca_κ that is also referred to as dimensionless shear rate χ [92, 376, 389–391].

In the absence of a viscosity contrast ($\lambda = 1$), which was the case for the investigated ROMER suspensions, the deformation of an initially spherical vesicle in linear shear flow resembles the deformation of an emulsion drop. It assumes a steady ellipsoidal shape and orients under a fixed inclination angle $\theta < \pi/4$ with respect to the shear flow direction, while the membrane undergoes a tank-treading motion [87, 89, 387, 392]. In this limit, the degree of vesicle deformation can be quantified by the Taylor deformation parameter $D = (L - B)/(L + B)$ originally introduced in a deformation model for liquid drops with static interfacial tension [393, 394]. Here, L and B are the major and minor axis of the ellipsoidal contour in the shear plane [88, 89, 91, 366, 376, 392, 395].

Since the instrument setup and the small dimensions of vesicles suspended in the ROMER shear gap did not allow to optically measure the vesicle shapes, D was estimated from a simple model by de Haas *et al.* describing the Taylor deformation

parameter D for giant vesicles in simple shear flow as a function of shear rate $\dot{\gamma}$ [88]:

$$\dot{\gamma} = \frac{4\sigma_0 D}{5R_0\eta_{\text{ext}}} \exp\left(\frac{64\pi\kappa_c}{15k_{\text{B}}T}D^2\right) \tag{4.6}$$

Here, σ_0 is the effective membrane tension of the undeformed vesicle (Sec. 2.3.5). In the study by de Haas *et al.* [88], σ_0 ranged from 10^{-4} to $10^{-2}\,\text{mN}\,\text{m}^{-1}$ for giant DMPC vesicles prepared by gentle hydration. Assuming an average σ_0 of $10^{-3}\,\text{mN}\,\text{m}^{-1}$ for the S100 vesicles subjected to the ROMER shear flow, we found a deformation parameter D of around 0.15 (Tab. 4.8). The small variation in D (0.12-0.17) as a function of the broad shear rate range evaluated can be explained by the tendency of the deformation parameter to saturation at sufficiently large strain rates in the small deformation regime, as shown experimentally [88, 392, 395], numerically [376], and theoretically [89]. In the regime of large deformations, Marmottant *et al.* predicted a critical deformation for lipid vesicles at burst of $D_{\text{crit}} = 1.44$ [366]. This exceeds the estimated D value for S100 vesicles in the ROMER shear gap by a factor of about 10.

Finally, the relation between the Taylor vesicle deformation D, the shear rate $\dot{\gamma}$, and the membrane tension σ during deformation by de Haas *et al.* [88]

$$D = \frac{4}{5}\frac{\eta_{\text{ext}}\dot{\gamma}R_0}{\sigma}, \tag{4.7}$$

indicates a shear-induced membrane tension σ of around $10^{-2}\,\text{mN}\,\text{m}^{-1}$ for the S100 vesicles suspended in the ROMER shear flow. Again, this is well below the lysis tension $\sigma_l = 5.1\,\text{mN}\,\text{m}^{-1}$ of DLPC membranes reported in literature [13].

Summary: Based on the dynamical parameters discussed above, including the stretching and bending capillary numbers Ca_K and Ca_κ, the Taylor deformation parameter D, and the shear-induced membrane tension σ, we conclude that free-flowing nanometer-sized S100 vesicles do not rupture by the sole action of ROMER shear forces in the evaluated shear rate range. Assuming unconfined simple shear flow conditions, i. e. neglecting any membrane and wall effects, they undergo a tank-treading motion at small stationary deformation instead. This was certainly the case for the S100-based vesicles emerging from the ROMER membrane in a quasi-spherical undeformed state, including the standard S100 vesicles exiting the conical pore openings of PET210 membranes (Figs. 4.14 and 4.15) as well as the soft SC-incorporating S100 vesicles with high initial bilayer curvatures that were unaffected by the passage through 200 nm pore channels (Fig. 4.16).

Requirements for theoretical vesicle breakup in the ROMER shear gap: According to the breakup criterion $Ca_{K,\text{crit}} \approx 10^{-2}$ by Marmottant *et al.* [366], the diameter

of unilamellar S100 vesicles freely moving through the ROMER shear gap at maximum shear rate ($\dot{\gamma}_{\mathrm{rep,max}} = 60\,214\,\mathrm{s}^{-1}$) would have to be $\geq 95\,\mu\mathrm{m}$ to allow for vesicle breakup under the simple shear flow conditions (Eq. 4.4). In this regard, it is surprising that Liu *et al.* observed a size reduction of tocopherol supplemented egg PC SUVs upon exposure to linear shear forces in a cone-plate geometry at $\dot{\gamma} \gtrsim 1000\,\mathrm{s}^{-1}$ [396]. In agreement with our observations, Natsume and Yoshimoto did not detect any significant size change in 100-200 nm sized POPC vesicles subjected to a cone-plate shear flow at $\dot{\gamma} \leqslant 1500\,\mathrm{s}^{-1}$ [397].

The breakdown of free-flowing MLVs with an initial mean diameter of around $1\,\mu\mathrm{m}$ into SUVs by viscous flow forces typically requires high energy inputs and mixed flow fields with an increased fraction of elongational flow components. Such flow conditions are for example generated by the popular ultrasound treatment [3, 195, 196, 398] and by well established homogenizing techniques [45], including microfluidization [3, 201, 347], French press [3, 194, 197], and high pressure valve homogenization [3, 199, 200]. The latter methods use high homogenizing pressures of roughly 200–2000 bar and, depending on the configuration of the mixing chamber, a combination of disruptive cavitational, shear, elongational, and inertial forces [346]. Vesicle rupture by sonication involves the action of three-dimensional shear fields generated by acoustic cavitation around oscillating microbubbles [195, 366, 399, 400].

Influence of lamellarity on vesicle deformation behavior: It has to be noted that the experimental studies on vesicle dynamics reported in literature and discussed here in relation to the ROMER deformation parameteres are based on unilamellar giant vesicles [74, 88, 90, 389, 392, 395]. Unilamellarity was also assumed for the calculation of the ROMER deformation parameters presented in Table 4.8, even though the samples collected from the ROMER device retained oligolamellar character (Figs. 4.14B and 4.16B). Since the effective elastic moduli of multilayered vesicles are larger than those of unilamellar vesicles [19, 88, 401–403], the actual deformation of extruded vesicles by the simple ROMER shear flow can be assumed to be even smaller than predicted by the estimated deformation parameters.

Fluid flow conditions in the ROMER shear gap: As to the flow conditions in the ROMER shear gap, it has to be mentioned that the flow regime was not purely laminar across the entire shear gap height under the experimental conditions used. This is indicated by the Reynolds number for the description of the fluid flow behavior between two parallel plates at the radial distance r [404]:

$$Re_{\mathrm{gap}} = \frac{\text{inertial flow forces}}{\text{viscous flow forces}} = \frac{\rho\omega r^2}{\eta} \tag{4.8}$$

where ω is the angular velocity of the rotating plate, i.e. the rotor in the ROMER setup. Inserting the viscosity $\eta = 0.89 \times 10^{-3}\,\mathrm{Pa\,s}$ and density $\rho = 997\,\mathrm{kg/m^3}$ of

water at 25 °C for the dilute vesicle suspension yielded high Re_{gap} numbers at the membrane outlet in a range of roughly 10^4 to 10^5 between the minimum and maximum shear rates applied. This could indicate that the flow field in the ROMER shear gap was also influenced by turbulent flow contributions and secondary flow effects outside of the laminar boundary layers [404]. To answer this consistently, the power characteristics of the ROMER device had to be known. Furthermore, above a rotational speed of 1000 rpm, the ROMER shear gap was periodically depleted due to fluid ejection by centrifugal forces.

Nevertheless, the influence of inertial forces on the deformation behavior of nanometer-sized vesicles in the ROMER shear flow can be excluded as predicted by the effective shear Reynolds number for a vesicle suspended in a shear flow [87, 384, 405]:

$$Re_{\text{V}} = \frac{\rho_{\text{ext}}\dot{\gamma}R_0^2}{\eta_{\text{ext}}} \qquad (4.9)$$

We find $Re_{\text{V}} \approx 10^{-4}$ to 10^{-3} for the ROMER shear gap in the evaluated shear rate range (Tab. 4.8) which is clearly in the range of negligible inertial forces at $Re_{\text{V}} \lesssim 10^{-2}$ [87, 384].

Shear-induced vesicle breakup at the membrane outlet of the ROMER device

In the previous section we demonstrated that an unconfined linear shear flow at the evaluted ROMER shear rates induces only small deformations in nanometer-sized lipid vesicles. However, if acting at the outlet of well-defined cylindrical pore membranes used for a preceding extrusion step, the same shear flow is able to break up S100-based vesicles to a small extent. This was shown by the slight decrease in vesicle size and lamellarity with increasing ROMER shear rates at the outlet of PC200 membranes when processing VET$_{800}$ precursors based on S100 PCs with and without the incorporation of cholesterol (Figs. 4.16A and B). These PC200 data and the otherwise low values of deformation parameters calculated for free-flowing S100 vesicles in the simple ROMER shear flow (upper part of Tab. 4.8) indicate that shear-induced vesicle breakup in the ROMER device can only happen directly at the membrane outlet. More specifically, the leading endcaps of vesicles emerging from and "held" at the cylindrical channel opening in a deformed state are sheared off as hypothesized previously (Fig. 4.15).

Determination of critical shear deformation parameters at membrane outlet:
According to the mechanism of shear-induced vesicle breakup directly at the membrane outlet of the ROMER device, the corresponding critical deformation parameters were estimated from the collected PC200 data assuming that the mean hydrodynamic vesicle diameter D_h measured after ROMER processing represented the
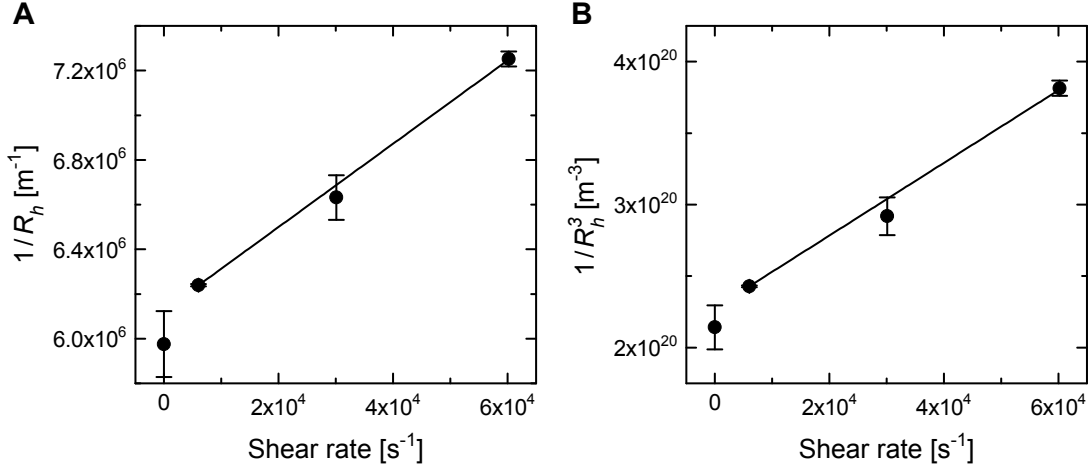
Figure 4.17: Determination of critical deformation parameters for shear-induced vesicle braekup at the membrane outlet of the ROMER device. Plotted are the reciprocal maximum vesicle sizes that persist during ROMER processing of VETs$_{800}$ from S100/POPE 95:5 (mol/mol) using PC200 membranes under the indicated shear flow conditions (data taken from Fig. 4.14A). Lines represent linear least-square fits between 6021 and 60 214 s^{-1}: (A) $\dot{\gamma} = 18.630 R_h^{-1} + 6.127 \times 10^6$; $R^2 = 0.9993$. (B) $\dot{\gamma} = 2.539 \times 10^{15} R_h^{-3} + 2.276 \times 10^{20}$; $R^2 = 0.9975$.

maximum diameter $D_{\max}$ of vesicles that were just stable to further disruption in their confined position at the pore outlet under the applied shear flow conditions. In the limit of shear-induced vesicle breakup, Equations 4.4 and 4.5 for the stretching and bending capillary numbers become

$$Ca_{K,\text{crit}} = \frac{\eta_{\text{ext}}\dot{\gamma}R_{\max}}{K_A} \tag{4.10}$$

$$Ca_{\kappa,\text{crit}} = \frac{\eta_{\text{ext}}\dot{\gamma}R_{\max}^3}{\kappa_c} \tag{4.11}$$

where R_0 has been replaced by $R_{\max} = R_h$.
The value of $Ca_{K,\text{crit}}$ was determined from the linear plot of $1/R_h$ vs. $\dot{\gamma}$ that has a slope of $\eta_{\text{ext}}/(Ca_{K,\text{crit}}K_A)$ (Fig. 4.17A). In analogy, $Ca_{\kappa,\text{crit}}$ was obtained from the slope of the linear plot of $1/R_h^3$ vs. $\dot{\gamma}$ which is described by $\eta_{\text{ext}}/(Ca_{\kappa,\text{crit}}\kappa_c)$ (Fig. 4.17B). The data of these plots were taken from the experimental ROMER series using standard VET$_{800}$ precursors from S100/POPE 95:5 (mol/mol) in water and PC200 membranes (Fig. 4.14A).

Results: The critical stretching capillary number $Ca_{K,\text{crit}}$ found for the S100/POPE vesicles exiting the PC200 membrane in the ROMER device at $\lambda = 1$ accounted for 1.9×10^{-4} and was two orders of magnitude below the corresponding critical value for lipid vesicle breakup in an unconfined shear flow (Tab. 4.8) [366]. In

fact, the obtained $Ca_{K,\mathrm{crit}}$ value was in a range of stretching capillary numbers ($Ca_K \approx 10^{-4}$ to 10^{-3}) that has previously been reported not to allow for the shear-induced rupture of free-flowing lipid vesicles in pure water, i.e. in non-viscosified external medium [366]. Likewise, the critical bending capillary number $Ca_{\kappa,\mathrm{crit}} = 8.0$ of the ROMER process was within a range of low Ca_κ numbers ($\leqslant 10$) in which lipid vesicles suspended in a Poiseuille flow would not even adopt a steady shape of deformation [90].

According to Equation 4.7, the plot of $1/R_h$ vs. $\dot{\gamma}$ in Figure 4.17A can also be used to estimate the critical Taylor deformation parameter for the S100-based vesicles emerging from PC200 pore channels during ROMER processing. In this case the slope of the linear fit is described by $4\eta_{\mathrm{ext}}/(5\sigma_l D_{\mathrm{crit}})$. We find $D_{\mathrm{crit}} = 0.01$ which is again two orders of magnitude below the corresponding critical value for free-flowing lipid vesicles in an external shear flow (Tab. 4.8) [366].

Relation of critical shear deformation parameters and mechanism of vesicle breakup at membrane outlet: The low values of $Ca_{K,\mathrm{crit}}$, $Ca_{\kappa,\mathrm{crit}}$ und D_{crit} of the ROMER process described above demonstrate that the membrane effects in dynamically enhanced vesicle extrusion significantly decrease the critical deformation parameters for the shear-induced breakup of lipid vesicles compared to those reported for unconfined shear flow conditions. In contrast to unconfined linear shear flows, the ROMER shear flow is able to create the critical breakup conditions for lipid vesicles in the case of pre-stretched vesicle bilayers draging along and slowly emerging from cylindrical pore channels in the form of deformed spherocylinders (Fig. 4.15). According to the simulations of vesicle extrusion by Bertrand and Joós [119], the maximum membrane tension induced in such spherocylindrical vesicles upon channel passage is just behind the frontal endcap which is, therefore, assumed to be preferentially sheared off by the ROMER cross flow (see also Eq. 2.9 and Fig. 2.11B in Background Sec. 2.6.4.)

Based on this possible mechanism of shear-induced vesicle breakup at the membrane outlet of the ROMER device, the corresponding values of $Ca_{K,\mathrm{crit}}$, $Ca_{\kappa,\mathrm{crit}}$ und D_{crit} most probably represent the additional area expansion, bending, and deformation required to shear off the frontal endcap of pre-deformed vesicles exiting the cylindrical PC200 pore channels. This explains the important decrease of the critical ROMER deformation parameters by about two orders of magnitude compared to those reported in literature for the breakup of quasispherical, i.e. relaxed, lipid vesicles in unconfined shear flows (Tab. 4.8). Furthermore, the confinement of spherocylindrical vesicles at the pore exit increases the efficiency of the ROMER shear flow as the confined vesicles are not able to rotate under the influence of the shear flow field which then fully acts on bilayer deformation.

After all, one has to bear in mind that the overall extent of vesicle breakup by the applied ROMER shear rates at the membrane outlet was small. This indicates

that the criteria for shear-induced vesicle breakup at the pore exit, including vesicle pre-deformation and confinement, were only met for a small fraction of the vesicle population to which the presented critical deformation parameters applied. The reason for this is the extensive pressure-induced breakdown of the large VET$_{800}$ precursors in the elongational flow fields at the pore inlets. The corresponding critical elongation capillary numbers for vesicle breakup at the inlet of the ROMER membrane are treated in the following and last section of this chapter.

Elongation-induced vesicle breakup at the membrane inlet of the ROMER device

The ROMER experiments presented in this study showed that vesicle breakup was much more pronounced upon simple inflow of large vesicles into narrow pore channels than in the subsequent pore outflow and superimposed shear flow. For comparison of the critical vesicle breakup conditions generated at the inlet and outlet of the ROMER membrane, we also estimated the critical elongation capillary numbers for the breakup of lipid vesicles in the pore entrance flow.

Determination of critical elongation deformation parameters at membrane intlet: Considering the sharp-edged entrance of a cylindrical PC200 pore channel as an abrupt contraction that induces an axisymmetric inflow field with a predominant fraction of elongational flow components, the critical capillary numbers for vesicle breakup at the pore inlet can be rewritten according to the general Equations 4.4 and 4.5 for the stretching and bending capillary numbers as:

$$Ca_{K,\text{crit}} = \frac{\eta_{\text{E}}\dot{\varepsilon}R_{h,\dot{\gamma}0}}{K_A} \tag{4.12}$$

$$Ca_{\kappa,\text{crit}} = \frac{\eta_{\text{E}}\dot{\varepsilon}R_{h,\dot{\gamma}0}^3}{\kappa_c} \tag{4.13}$$

Here, η_{E} is the elongational viscosity of the vesicle suspension flowing through the contraction, $\dot{\varepsilon}$ the elongation rate in the laminar entrance flow, and $R_{h,\dot{\gamma}0}$ the average hydrodynamic radius of vesicles collected after simple passage through the ROMER membrane in the absence of a shear flow, i.e. the mean size of vesicles that were stable to further disruption upon entering the pore channel under the applied extrusion conditions.

The elongation rate $\dot{\varepsilon}$ of the axisymmetric entrance flow was estimated using Cogswell's empirical analysis of contraction flows that considers both shear and elongational flow contributions in the contraction region [406, 407]:

$$\dot{\varepsilon} = \frac{4\eta\dot{\gamma}_{\text{app}}^2}{3(n+1)\Delta P} \tag{4.14}$$

η is the viscosity under simple shear flow described by the power-law model with the power-law index n ($\eta = C\dot{\gamma}^{n-1}$). ΔP is the pressure loss at the entrance of the contraction and $\dot{\gamma}_{\mathrm{app}}$ represents the apparent shear rate at the wall of the orifice:

$$\dot{\gamma}_{\mathrm{app}} = \frac{4Q}{\pi r^3} \tag{4.15}$$

with Q being the volumetric flow rate through the orifice of radius r.

For the dilute water-based vesicle suspensions used in our ROMER experiments we assumed Newtonian flow behavior, so that the shear viscosity η was taken to be constant and $n = 1$. The value of η of the vesicle suspension was, in a first approximation, set equal to the shear viscosity of water at $T = 25\,^{\circ}\mathrm{C}$ ($\eta = 0.89 \times 10^{-3}\,\mathrm{Pa\,s}$). Furthermore, we used $\eta_{\mathrm{E}} = 3\eta$ according to the Trouton ratio of elongational to shear viscosities of 3 for axisymmetric elongation flows of Newtonian fluids. Cogswell's analysis of the entrance flow into an abrupt contraction assumed locally fully developed flow kinematics in the converging region such that the resulting axial velocity profile was the same as that for a power law fluid undergoing Poiseuille flow through a channel of equal cross-sectional geometry [406, 407]. As a consequence, the results obtained from Cogswell's analysis have been shown to be in particularly good agreement with true elongational flow characteristics at high strain rates [408]. Based on this boundary condition, we used the process parameters and experimental results of the LIPEX device to estimate the elongation rate $\dot{\varepsilon}$ of the entrance flow into the PC200 pore channels (Eq. 4.14) and the resulting critical elongation capillary numbers for vesicle breakup at the membrane inlet (Eqs. 4.12 and 4.13). Extrusion experiments using the LIPEX device were carried out at much higher volumetric flow rates through its supported membrane disc compared to those applied through the free-standing, pressure-sensitive membrane configuration of the ROMER device. Indeed, flow rate-pressure dependencies recorded in preliminary extrusion experiments with the LIPEX device revealed a Poiseuille flow behavior of standard VET$_{800}$ pre-suspensions through the PC200 pore channels at extrusion pressures above 3 bar (data not shown).

Results: Adopting the experimental values of the extrusion of a standard VET$_{800}$ pre-suspension from S100/POPE 95:5 (mol/mol) through a PC200 membrane using the LIPEX device (Fig. 4.11A: extrusion pressure $\Delta P = 6$ bar, pore entrance radius $r = 100\,\mathrm{nm}$, single pore flow rate during first extrusion cycle $Q = 1.1 \times 10^{-7}\,\mathrm{ml\,min}^{-1}$, vesicle radius after 1 extrusion cycle $R_{h,1} = 127\,\mathrm{nm}$), we find $Ca_{K,\mathrm{crit}} = 7.3 \times 10^{-6}$ and $Ca_{\kappa,\mathrm{crit}} = 0.7$ for the elongation-induced breakup of lipid VET$_{800}$ precursors at the inlet of a PC200 membrane as used in the ROMER device.

Relation of critical elongation deformation parameters and mechanism of vesicle breakup at membrane inlet: The obtained values of $Ca_{K,\mathrm{crit}}$ and $Ca_{\kappa,\mathrm{crit}}$

describing the elongation-induced vesicle breakup at the membrane inlet of the ROMER device were about 1 to 1.5 orders of magnitude lower than the corresponding critical shear capillary numbers for the membrane outlet (Tab. 4.8). This confirms that large vesicles subjected to ROMER processing are more efficiently broken up at the constriction of the pore entrance than by the shear flow field at the pore exit. Furthermore, the presented set of critical elongation and shear capillary numbers gives another quantitative comparison for the two vesicle breakup mechanisms of the ROMER process which is in line with our experimental data. The vesicle size reduction resulting from simple inflow of the standard VET_{800} suspension into the PC200 pore channels was about 1 order of magnitude larger than that achieved by the subsequent shear flow at the membrane outlet at the maximum shear rate tested (Fig. 4.14A).

Summary: In conclusion, the experimental ROMER setup showed that uniaxial elongation flows as that developed at the constriction of a pore entrance are more efficient in breaking up lipid vesicles than simple shear flows as that induced at the membrane outlet. This is also well known from the intensively studied deformation and breakup behavior of drops in viscous flow fields [381–383]. Whereas uniaxial elongation forces fully act on the deformation of the relatively rigid vesicle membrane, linear shear forces are converted into the deformation as well as into the rotation of a tank-treading vesicle as described in this subchapter.
A final and important remark refers to the large difference between the stretching and bending capillary numbers Ca_K and Ca_κ reported in this study as well as in the literature (Tab. 4.8). The values for Ca_K are generally several orders of magnitude lower than the Ca_κ values. The same applies to the critical capillary numbers. This indicates that lipid bilayers are more sensitive and eventually rupture in response to area dilation rather than to bending as described previously [122, 409]. In other words, the bending energy is negligible in the problem of vesicle deformation and breakup in external flows and primarily sets the shape of vesicles at rest [73, 84, 409] (see Background Secs. 2.3.2 and 2.3.5).

4.4 Conclusions

This study aimed at designing and investigating a scalable and gentle process for the controlled production of well-defined, nanometer-sized vesicles for pharmaceutical, cosmetic, and food applications.

To this end, the ROMER device was constructed in collaboration with Bühler AG (Uzwil, Switzerland), built in house by Jan Corsano, and successfully put into operation in the frame of this study. It coupled the reliable but not optimally efficient conventional extrusion process with a defined shear flow directly at the outlet of a freestanding nanopore membrane allowing for continuous, dynamically enhanced vesicle extrusion. After selecting appropriate membrane systems (i: instrument setup), the ROMER process was investigated for its ability to efficiently and specifically homogenize lipid MLVs, more precisely $VETs_{800}$, by applying a single extrusion cycle and varying the shear rate, pore shape, and vesicle bilayer elasticity (ii: parameter study).

The extents of VET_{800} homogenization at varying process and material parameters were quickly and reliably analyzed in house, not only in terms of vesicle mean size and polydispersity using DLS, but also in terms of vesicle lamellarity using the TNBS assay for external vesicle surface area determination. This was only possible after optimizing earlier versions of the TNBS assay in terms of marker lipid consumption and time of analysis. The optimized protocol allowed to monitor vesicle integrity and provided comparative and representative average results for the degree of vesicle lamellarity generated during the ROMER parameter studies.

(i) Instrument setup: SEM studies revealed that the straight-through nanopore channels of the considered track-etched polymer membranes, PC200 and PET210, had uniform cylindrical or pronounced biconical shapes, respectively. The Cer200 membrane showed irregular pore shapes and tortuous paths as expected for sintered ceramic membranes.

Despite the biconical pore shape, the PET210 membrane performed equally well in conventional, static vesicle extrusion as the standard PC200 membrane. They yielded almost perfectly overlapping, narrow, and monomodal vesicle size distributions reflecting the 200-nm mean diameter of the cylindrical PC200 pores and the 210-nm mean constriction of the biconical PET210 pores. Insertion of the PC200 and PET210 membranes in the free-standing membrane configuration of the ROMER device allowed the extrusion of VET_{800} precursors at low transmembrane pressures (1-2 bar) without bursting of the membrane foils and under negligible loss of total lipids. Hence, the PC200 and PET210 membranes exhibiting well defined, straight-through pore channels and variable pore shapes were suitable for ROMER parameter studies, despite their limited pressure resistance.

Static vesicle extrusion through the Cer200 membrane was characterized by broad,

bimodal vesicle size distributions, irregular vesicle shapes, and very low lipid recovery rates. Consequently, the Cer200 membrane did not qualify for the application in dynamically enhanced vesicle extrusion in spite of the highly attractive properties of self-supporting, ceramic sinter membranes in terms of mechanical stability, durability, and back-flushing operations.

(ii) Parameter study: Generally, the shear flow induced at the outlet of a nanopore membrane had small or no influences on the homogenization of lipid $VETs_{800}$ in dynamically enhanced vesicle extrusion.

Increasing shear rates from 0 to $60\,214\,s^{-1}$ led to a small decrease of the mean size and lamellarity of S100 $VETs_{800}$ after dynamically enhanced extrusion through the cylindrical pores of the PC200 membrane. At these parameter settings, the vesicle size reduction resulting from the static extrusion component of the ROMER process accounted for 64% of the initial VET_{800} size, whereas the shear flow at the membrane outlet contributed to an additional down-sizing of only 6% at the maximum shear rate tested. Probing the PET210 membrane with biconical pore channels in the ROMER device under the same experimental conditions revealed no significant effect of the shear flow on the structure of dynamically extruded vesicles.

This demonstrated that the confinement of uniform, cylindrical pore exits and the pre-stretched state of vesicles emerging from these pores are prerequisites for the shearing-off of leading bilayer endcaps by the shear forces applied at the membrane outlet. Vesicles emerging from conical pore exits and entering the ROMER shear flow in an unconfined, quasispherical state are not broken up by the sole action of the viscous flow forces (Fig. 4.15). This was confirmed by the estimation of a set of dynamical parameters describing the deformation behavior of free-flowing, nanometer-sized S100 vesicles under linear ROMER shear flow conditions, including the stretching and bending capillary numbers Ca_K and Ca_κ, the Taylor deformation parameter D, and the shear-induced membrane tension σ. The obtained values were far below the corresponding critical deformation parameters reported in literature for the breakup of lipid vesicles in unconfined, external shear flow fields. In contrast, the confining effects of the cylindrical PC200 pores were found to shift the critical deformation parameters to considerably lower values allowing for the observed partial breakup of S100 vesicles at the outlet of the PC200 membrane by ROMER processing (Tab. 4.8).

Variation in bilayer elasticity of the VET_{800} precursors did not provide further insights into the effectivity of dynamically enhanced vesicle extrusion. More rigid, cholesterol containing S100 $VETs_{800}$ showed a very similar behavior in ROMER processing as that described above for plain S100 $VETs_{800}$. Incorporation of sodium cholate in the S100 host membrane did not only increase bilayer elasticity but led to a concomitant increase of spontaneous bilayer curvature and, hence, to significantly smaller VET_{800} precursors. Consequently, the more flexible, SC containing S100 $VETs_{800}$ were hardly affected by the passage through 200 nm pore membranes.

They exited the ROMER membrane in a predominantly undeformed state, even when using cylindrical PC200 pore membranes, and were insensitive to the subsequent shear flow in the evaluated shear rate range.

The latter experiment is a clear demonstration for the poor control of ROMER processing over the vesicle structure generated from self-assembled vesicle precursors. It is concluded that the ROMER process was not able to overcome the heterogeneity of spontaneously formed MLV pre-suspensions after a single dynamically enhanced extrusion cycle. As a result, varying shear rates applied at the outlet of a nanopore membrane did not allow to specifically and efficiently form homogeneous, unilamellar to n-multilamellar vesicles by dynamically enhanced MLV extrusion under the experimental conditions investigated. This was confirmed by morphological cryo-TEM and SANS studies of the vesicle suspensions collected after ROMER processing of plain S100 VETs$_{800}$ through PC200 membranes. They revealed the presence of heterogeneous, uni-, oligo- and mulitlamellar vesicles in the obtained suspensions, irrespective of the applied shear rate.

Nevertheless, the setup of the ROMER device gave valuable insight into the mechanism by which MLVs break up into smaller, more homogeneous vesicles upon conventional (static) extrusion through nanopore channels, which is still rather speculative. The minor influence of the strong shear flows induced at the outlet of nanopore membranes on MLV homogenization by ROMER processing supports the pressure-dependent mechanism of vesicle extrusion as described by Frisken and coworkers. According to this, vesicles are primarily broken up at the entrance of nanopore channels as they are forced into the constriction. Our results showed that the extent of vesicle breakup is practically the same whether the entering vesicles encounter this constriction at the entrance of cylindrical pores (PC200 membrane) or in the center of biconical pores (PET210 membrane). Again, this supports the pressure-induced breakup mechanism of vesicles upon entering the pore channel as opposed to a shear-induced fissioning of vesicles inside cylindrical pore channels. The effective breakup of vesicles at the pore entrance was further demonstrated by estimating the critical elongation capillary numbers for vesicle breakup in the uniaxial elongation flow into the PC200 pore inlets of the ROMER device. Indeed, the obtained values were considerably lower than the critical shear capillary numbers calculated for the breakup of vesicles at the pore outlets.

Dynamically enhanced membrane extrusion is still regarded as promising principle to tailor unilamellar vesicles of shear flow-controlled size if the ROMER setup could be adapted in such a way that it allows the direct shearing off of bilayer sheets bending into the shear flow. This would omit the discontinuous preparation step involving the uncontrolled formation of self-assembled, heterogeneous vesicle pre-suspensions. Furthermore, it would allow for the one-step loading of an aqueous solution into the
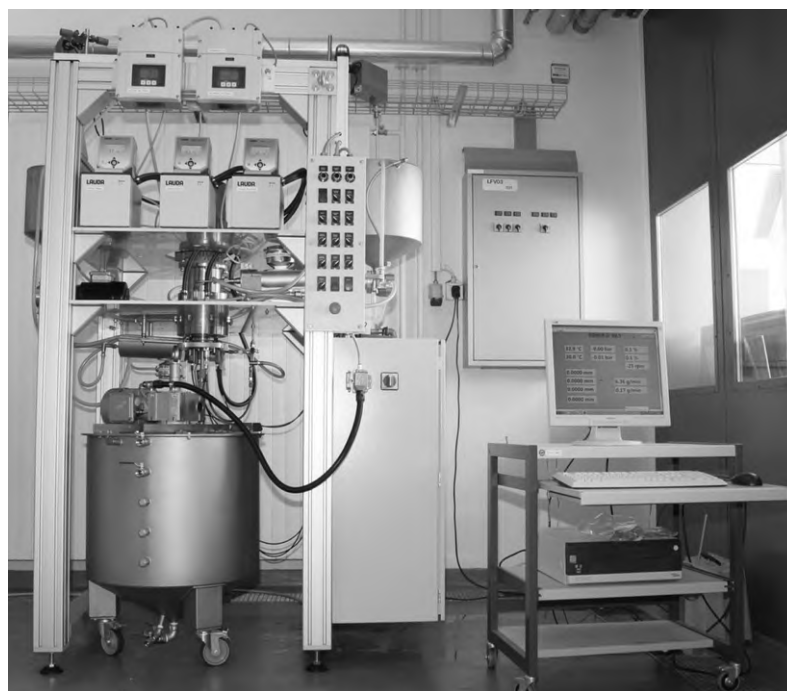
Figure 4.18: Photograph of the pilot scale ROMER II device developed for dynamically enhanced membrane emulsification and vesicle extrusion. For more details on the ROMER II setup and its technical data, please refer to the PhD thesis of Sebastian Holzapfel [221]. Reproduced from Holzapfel *et al.* [220] with kind permission from John Wiley & Sons Inc.

vesicles which will be suspended in the second, cross-flowing aqueous medium.

The latter option of separate internal and external fluid streams has been considered in the design of an optimized, pilot scale setup of the ROMER device. Based on the findings of this study and on our laboratory's expertise in dynamically enhanced membrane emulsification, the ROMER II device has been constructed and built in close collaboration with Bühler AG (Uzwil, Switzerland) for both dynamically enhanced membrane emulsification and vesicle extrusion. A photograph of the ROMER II setup is shown in Figure 4.18. The new device allows for the precise control of more defined flow conditions in the shear gap and disposes of additional elements to improve process control and monitoring. It has been described in detail and successfully applied in dynamically enhanced membrane emulsification using highly defined, micro engineered membranes in the PhD thesis of Sebastian Holzapfel carried out at the Laboratory of Food Process Engineering at ETH Zurich [220, 221].

The application of the ROMER II device in dynamically enhanced vesicle extrusion is currently hampered by the lack of mechanically stable nanopore membranes with well defined, straight-through pore channels [221].

5 Magnetic nanoparticle functionalized liposomes

5.1 Introduction

Vesicles can be functionalized with magnetic nanoparticles (MNPs) by assembling the MNPs into the aqueous core, in the hydrophobic membrane interior or at the outer membrane surface of the vesicles [24]. MNP functionalized vesicles in which the membranes are constituted from naturally occurring phospholipids are generally called *magnetoliposomes*. Included are also single MNPs or MNP clusters that are tightly coated with a lipid bilayer. This latter composite structure represents the pioneering type of magnetoliposomes described by De Cuyper and coworkers more than 20 years ago [31, 410, 411].
Magnetoliposomes have been widely studied and optimized as biocompatible contrast enhancing agents in magnetic resonance imaging (MRI) [31, 412, 413]. In addition to contrast enhancement, the versatile MNP-entrapping liposomes possess the ability to co-encapsulate hydrophilic molecules, such as fluorescent labels and drugs, allowing for multimodal imaging or a combination of therapy and diagnosis ('theragnostics') [30, 31]. The presence of superparamagnetic NPs in liposomes can further be exploited by applying an alternating magnetic field resulting in local heat generation [414]. This localized heating effect can be used for hyperthermia treatment of cancer after magnetically guiding the magnetoliposomes to the target tumor [37, 414]. For the design of smart drug delivery vehicles [24], the same heating effect has successfully been used for an alternating magnetic field-triggered content release from liposomes loaded with MNPs in their lumen [415–417] or in their membrane interior [273, 418, 419].

The ability of magnetoliposomes to move along an external magnetic field gradient is key to most of the applications listed above as it is used for example in separation steps during their synthesis [410, 420, 421], for specific tissue accumulation [37, 422], or for drug targeting [24]. Nevertheless, this basic feature has been considered to a very limited extent for the application of magnetoliposomes in magnetic separations of specific target molecules from biological fluids [423, 424], which are routinely carried out in life sciences and biotechnology using functionalized magnetic

particles [414, 425, 426]. With a few exceptions of new generation nanomagnets [427, 428], commercially available magnetic adsorbent particles are typically larger than 500 nm, most of them are ferromagnetic, and they have a limited capability for a chemically strong and reliable attachment of affinity ligands that bind the selected target molecules. In addition, the high price of the current commercial adsorbents limits their use in process-scale bioseparations despite the attractive quality and credibility of magnetic separations in a wide range of disciplines [429].

Aim: This study aims at combining the well-known properties of superparamagnetic NPs and liposomes in a reverse engineering approach to provide versatile and cost-effective magnetoliposome-based adsorbents for magnetic separation applications, e.g. for the extraction of high value pharmaceutical and nutraceutical products from crude bio-feedstocks (Fig. 1.1).

Approach: Water-based magnetic nanofluids (MNFs) containing unfunctionalized superparamagnetic iron oxide NPs are used to load MNPs into the lumen of liposomes during their formation in the aqueous MNF [412, 413, 430]. Provided that this synthesis protocol allows the quantitative encapsulation of MNPs into the liposome lumen under preservation of the structure-property functions of each component, the resulting functional composite bears the following potentials for bioseparation applications.

The entrapped MNPs impart magnetophoretic mobility to the liposome-based adsorbent [412]. The boundaries of the liposomes avoid extensive agglomeration of iron oxide NPs which is often an issue under the high salt concentrations of biological fluids [431]. Confinement of MNPs to the liposome lumen also prevents dilution of the MNPs in the feedstock and ensures high enough responsiveness of the adsorbent to an external magnetic field. At the same time, superparamagnetic NP-entrapping liposomes show no remanent magnetization, i.e. they become non-magnetic after removal of the magnetic field, allowing for fast sorption and desorption processes in magnetic separator devices [429]. Finally, the lipid bilayer shell of magnetoliposomes is highly biocompatible and its well-defined structure offers the possibility to undergo a wide variety of surface functionalization for biomolecule targeting [35]. Positively and negatively charged, as well as specifically functionalized (e.g. biotinylated or antibody-coupled) amphiphiles can readily be incorporated into the liposome membrane to design anion exchange, cation exchange, or affinity adsorbents based on magnetoliposomes [3, 35, 429].

To harness the full potential of functionalized vesicles, close control over the process-structure-property functions of each component and of the composite is required (Fig. 1.1). In the case of MNP-functionalized liposomes prepared by the passive encapsulation of a water-based MNF into the liposome lumen, this is reflected by the direct influence of the concentration and colloidal stability of MNPs in the water-based MNF, as well as of the size and lamellartiy of the vesicle carrier on the final magnetic loading. In this work, the superparamagnetic iron oxide NPs were ster-

ically and electrostatically stabilized in the aqueous medium by a dispersant shell consisting of a fatty acid bilayer, while vesicle size and lamellarity was controlled using the conventional extrusion technique.

Outline: This chapter reports on the ability of oleic acid (OA-OA) and lauric acid (LA-LA) bilayer stabilized, superparamagnetic iron oxide NPs to partition into the aqueous domains of pharmaceutical grade liposomes following the passive MNP encapsulation protocol. After the hydration step of a thin film in the aqueous MNF, this protocol includes homogenization of the obtained MLVs by sequential extrusion, followed by the removal of nonentrapped MNPs by size exclusion chromatography (SEC).

Since a high colloidal stability of MNPs is crucial throughout the different synthesis steps [24, 413], the aggregation behavior of the fatty acid bilayer coated MNPs in the hydration medium is first evaluated and minimized as a function of pH, buffer salt composition, and particle concentration using dynamic light scattering (DLS) and optical inspection. After the formation of MLVs in the water-based MNFs, the behavior of the composite suspensions during the extrusion and separation steps is described and discussed in the context of previous studies on magnetoliposome preparation. Total iron and phospholipid concentrations before and after each synthesis step are determined by atomic absorption spectroscopy (AAS) and chemical assays to report on the fate of MNPs and liposomes, respectively. Finally, the structure of MNPs and liposomes, as well as the amount of encapsulated MNPs in the obtained magnetoliposome suspensions is characterized by cryo transmission electron microscopy (cryo-TEM).

5.2 Materials and methods

5.2.1 Materials

Pharmaceutical grade phosphatidylcholines purified from soybean (LIPOID S100, abbreviated as S100; coarse agglomerates) were obtained from Lipoid (Ludwigshafen, Germany) and used as obtained. The chemical structure of DLPC, the predominant species of S100, is shown in Table 4.3. Tables 4.1 and 4.2 summarize the chemical composition and fatty acid distribution in the S100 PC isolate (see Chapter 4).

Chloroform (99.9%; stabilized with ethanol) was a product of ECSA Centonze (Balerna, Switzerland) and HCl fuming (37%) of Merck (Darmstadt, Germany). All other chemicals, namely sulfuric acid (98%), sodium hydroxide (98%), iron(II) sulfate heptahydrate ($\geq$ 99.5%), iron(III) chloride hexahydrate (98%), ammonium thiocyanate (99%), Triton X-100 (simply called Triton in this work), cross-linked Sepharose 2B, and buffer salts, including sodium phosphate monobasic dihydrate ($NaH_2PO_4 \cdot 2H_20$; $\geq$ 99.0%), sodium phosphate dibasic dihydrate ($Na_2HPO_4 \cdot 2H_20$; $\geq$ 99.0%), citric acid (99%), sodium acetate ($\geq$ 99.0%), tris(hydroxymethyl)aminomethane (Tris; $\geq$ 99.8%), and 4-(2-hydroxyethyl)piperazine-1-ethanesulfonic acid (HEPES; $\geq$ 99.5%), were of analytical grade and purchased from Sigma-Aldrich (Buchs, Switzerland). All experiments were carried out with ultrapure water from a Synergy water purification system (Merck Millipore, Billerica, MA, USA).

Water-based MNFs containing hydrophilic superparamagnetic NPs were provided by our collaborators from the Laboratory of Magnetic Fluids at the Romanian Academy – Timisoara Branch (RATB) headed by Prof. Ladislau Vékás.

The primary NPs consisted of a magnetite (Fe_3O_4) core with a diameter of 6-12 nm and were sterically and electrostatically stabilized by a bilayer of fatty acids, namely oleic acid (OA) or lauric acid (LA) (Figure 5.1A). Based on the common two-step procedure used to prepare the aqueous MNFs, including the synthesis of magnetic NPs by co-precipitation of Fe_3O_4 in the presence of the primary surfactant and the subsequent stabilization/dispersion of the NPs in water in the presence of the secondary surfactant, the inner monolayer of fatty acids was chemically adsorbed on the surface of the iron oxide particles, while the secondary fatty acids formed a physically adsorbed outer monolayer [432, 433]. During the dispersion step in water, fatty acid bilayer coated primary particles usually aggregate into small clusters of a few particles forming larger secondary particles as illustrated in Figure 5.1B [432, 434, 435]. The hydrodynamic diameter of secondary particles in the water-based MNFs obtained from RATB were in the range of 30 to 40 nm.

Table 5.1 summarizes the characteristics of the water-based MNFs used in this study, as provided by RATB. In the following, the short names OA-OA and LA-LA will

A

B
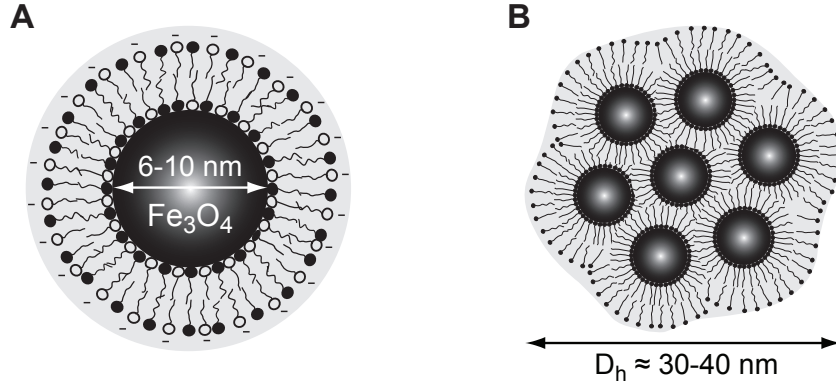
Figure 5.1: Schematic representation of hydrophilic iron oxide NPs stabilized with a bilayer of fatty acids. (A) Structure of the primary superparamagnetic NP consisting of a magnetite (Fe_3O_4) core and a stabilizing bilayer of fatty acids. Surfactants with filled head groups represent uncharged fatty acid molecules; surfactants with empty head groups represent negatively charged soap molecules (adapted from Shen *et al.* [434] and Walde *et al.* [436]). (B) In water-based magnetic nanofluids, bilayer stabilized primary particles are typically organized into condensed particle aggregates, i. e. secondary particles, of a small number of primary particles.

Table 5.1: Characteristics of the water-based magnetic nanofluids (MNFs) used in this work, as provided by the Laboratory of Magnetic Fluids at Romanian Academy – Timisoara Branch (RATB). Synthesis and characterization of the nanofluids were carried out at RATB.

Short name of MNF	OA-OA MNF	LA-LA MNF
Sample code from RATB	100105-62	110517-1
Matrix fluid	water	water
Particle core material	Fe_3O_4	Fe_3O_4
Particle coating structure	fatty acid bilayer	fatty acid bilayer
Particle coating composition	oleic acid (C18:1c9)	lauric acid (C12:0)[a]
Mean particle core diameter [nm]	< 10	< 10
Mean D_h of secondary particles [nm]	31	37
Density ρ of MNF [$g\,cm^{-3}$]	1.0365	1.0800
Particle volume fraction ϕ [v/v%][b]	0.947	1.989
Total iron concentration [$mg\,mL^{-1}$][c]	32.9	64.3
Total Fe_3O_4 concentration [$mg\,mL^{-1}$][c]	45.5	88.9
Magnetization [Gs]	70	100

[a] The abbreviation 18:1c9, for example, indicates that the linear fatty acid has 18 carbon atoms with one *cis* double bond between position 9 and 10, where the carboxy C atom is carbon n° 1.
[b] Calculated from $\phi = 100(\rho_{MNF} - \rho_{water})/(\rho_{magnetite} - \rho_{water})$ with $\rho_{water} = 0.9970\,g\,cm^{-3}$ and $\rho_{magnetite} = 5.17\,g\,cm^{-3}$ at $T = 25\,°C$.
[c] Obtained from AAS measurements carried out at ETH (see Sec. 5.2.4)

be used to refer to the double layer fatty acid coatings consisting of oleic acid and lauric acid bilayers, respectively.

Prior to every use of original or diluted MNFs for sample preparation, the water-based MNFs were treated by bath sonication for 15–30 min or by tip sonication for 10 s to minimize particle agglomeration.

5.2.2 Preparation of magnetoliposomes using hydrophilic MNPs

For the entrapment of hydrophilic magnetic NPs in the aqueous domains of vesicles, S100 vesicles were prepared following the most commonly used methods to form loaded vesicle suspensions. They include thin film hydration in an aqueous medium containing the to be encapsulated solute, followed by freeze–thaw cycles, sequential vesicle extrusion and, finally, a separation step to eliminate nonentrapped solutes [3, 36].

A thin lipid film was prepared by dissolving the S100 phospholipids in chloroform in a round-bottom flask and evaporating the solvent by rotary evaporation. To ensure complete solvent removal, the lipid film was further dried under high vacuum overnight. Particle-entrapping MLVs were formed by hydrating the lipid film directly in the appropriate amount of MNF to yield a total lipid concentration of 20 mM. If not stated otherwise, the particle concentration in the hydrating MNF had been adjusted to 0.1 v/v% using MilliQ water for the dilution of the original MNF. This corresponds to 3.5 mg mL^{-1} and 3.2 mg mL^{-1} of total iron, i.e. 4.8 mg mL^{-1} and 4.5 mg mL^{-1} of magnetite, in the case of OA-OA and LA-LA MNFs, respectively (see Table 5.1). The suspension was vortexed until complete film dispersion, before it was freeze-thawed six times to promote a homogeneous distribution of NPs inside and outside the vesicle boundaries and to enhance unilamellarity and, hence, encapsulation efficiencies of the generated vesicles [3, 9, 205].

The obtained MLVs were downsized to VETs$_{400}$ by sequentially extruding the dispersion at least 10 times through a polycarbonate membrane with 400-nm pore sizes (Whatman, Kent, UK) using a LIPEX extruder (Northern Lipids, BC, Canada) and compressed nitrogen gas (purity grade 4.5, 99.995%; PanGas, Dagmersellen, Switzerland). The resulting uni- and oligolamellar vesicles had a mean diameter of approximately 250 nm as obtained from DLS measurements.

Finally, nonentrapped MNPs were separated from the MNP containing vesicles by size-exclusion chromatography (SEC) using a lipid pre-saturated Sepharose CL-2B column (diameter: 1 cm; length: 20 cm, if not stated otherwise) and water as eluent. A sample volume of 0.4 mL was applied to the column and the flow rate was controlled at ≈ 0.3 mL min^{-1} using a peristaltic pump. Sample fractions of 0.8 mL were collected and analyzed for their total iron and phospholipid concentrations using

colorimetric assays to identify vesicle and particle fractions, to evaluate separation efficiencies, and to estimate the amount of encapsulated NPs. The vesicle fractions were combined for subsequent cryo-TEM investigations.

5.2.3 DLS

The mean hydrodynamic diameter D_h, polydispersity index *PDI*, and volume-weighted size distribution of the water-based OA-OA and LA-LA MNFs and of the magnetoliposome suspensions were characterized by dynamic light scattering (DLS). DLS experiments were performed on a Zetasizer Nano ZS (Malvern Instruments, UK) in the backscattering mode (scattering angle $\theta = 173°$). The use of these Non-Invasive Backscatter (NIBS) optics allowed the measurement of undiluted MNP-containing samples which were analyzed in duplicate or triplicate. The measuring temperature was set at 25 °C. Data were collected and analyzed as described in Section 3.2.4.

5.2.4 Iron quantification by AAS

The magnetite particle concentration in the MNFs and in the magnetoliposome suspensions were measured based on total iron using atomic absorption spectroscopy (AAS). The instrument used was a SpectrAA-240 K spectrometer equipped with a GTA-120 Graphite Tube Atomizer Varian Techtron (Varian Inc., now part of Agilent Technologies, CA, USA). Samples were diluted in 0.1 M HCl to reach a total iron concentration of approximately 5-10 µg L^{-1} and analyzed in duplicate. AAS measurements were carried out by Christophe Zeder at the Laboratory of Human Nutrition at ETH Zurich.

5.2.5 Iron quantification using 1,10-phenanthroline

The amount of total free and encapsulated magnetite particles in the magnetoliposome suspensions before and after SEC purification was determined based on total iron in the form of ferrous iron ions (Fe^{2+}) that form a strongly colored red-orange complex with 1,10-phenanthroline in the pH range between 3 and 9 [437].
Eluted sample fractions containing MNPs were diluted in ultrapure water to reach a total iron concentration of approximately 40 mg L^{-1}. For the complete dissolution of the magnetite particles by acid digestion, an aliquot of 5 mL of diluted sample and 0.5 mL of 40% sulfuric acid were added to a 100 mL volumetric flask and the mixture was kept at 50 °C for 2-3 hours. The pH of the obtained solution was readjusted to approximately 4.5 by adding 1 mL of 1 M NaOH and 4 mL of 3 M sodium acetate

buffer. Finally, 0.1 mL of 5 w/v% Triton was added to the flask to ensure complete liposome solubilization, i. e. avoid sample turbidity, and the sample was diluted to the mark using ultrapure water. The complexation reaction between Fe^{2+} and 1,10-phenanthroline was induced by adding 2.0 mL of the obtained analyte solution to a Dr. Lange iron test cuvette LCK321 with a measuring range of 0.2-6.0 mg L^{-1} Fe (HACH LANGE GmbH, Düsseldorf, Germany), following the test instructions. Fe^{3+} ions present in the analyte solution were, thereby, reduced to Fe^{2+} by the presence of ascorbic acid in the test cuvette. Total iron concentration was then obtained from the absorbance measurement of the test solution against a matrix blank using a Dr. Lange spectrophotometer.

Results obtained from the sample digestion protocol and the LANGE iron cuvette test described above were verified with standard iron solutions prepared from ferrous sulfate in a Fe^{2+} concentration range of 0.5-2.0 mg L^{-1}. They were also in good agreement with AAS results.

5.2.6 Phospholipid quantification using the Stewart assay

The phospholipid concentration in the S100 magnetoliposome fractions collected after SEC purification was determined according to the Steward assay protocol described in Section 4.2.7 [142, 298].

The liposome containing fractions were diluted in ultrapure water by a factor of 5-10 to reach a total S100 concentration of approximately 0.2 mg mL^{-1} in each of the collected magnetoliposome samples. The Stewart assay was initialized by mixing an aliquot of 200 μL of diluted magnetoliposome sample with 2.0 mL of chloroform and 2.0 mL of 0.1 M ammonium ferrothiocyanate. This ensured the concentration of the colored phospholipid-ammonium ferrothiocyanate complex in the chloroform phase (≈ 0.02 mg mL^{-1}) to be within the corresponding concentration range of the calibration curve (0.005-0.05 mg mL^{-1}; see Fig. 4.2).

5.2.7 cryo-TEM

Magnetoliposome suspensions were visualized before and after SEC purification by cryo-transmission electron microscopy (cryo-TEM) at the Electron Microscopy Center ETH Zurich (EMEZ). For cryo-TEM investigations, the total iron concentration in the samples was adjusted to approximately 1 mg mL^{-1}. Therefore, the initial MLV suspensions were prepared in OA-OA and LA-LA MNFs at a particle volume fraction of 0.03 v/v% and processed as described in Section 5.2.2. Specimens were prepared and analyzed by Takashi Ishikawa (Department of Biology, ETH Zurich and Biomolecular Research Laboratory, PSI Villigen) following the procedure described in Section 4.2.8 [353].

5.3 Results and discussion

5.3.1 Colloidal stability of fatty acid bilayer coated iron oxide NPs in aqueous solution

Since the MNP-entrapping liposomes were prepared by directly forming the vesicles in the water-based MNFs, medium conditions for optimum particle stability were first elucidated. These included the pH and buffer salt composition of the matrix fluid, as well as the particle concentration in the MNFs serving as lipid film hydration medium. The following sections summarize best particle suspension conditions identified to maximize colloidal stability and minimize the aggregation behavior of double layer fatty acid coated iron oxide NPs in the hydration medium. This is essential for a successful partitioning of hydrophilic nanometer-sized magnetic particles in the aqueous core and interlamellar space of uni- and oligolamellar vesicles.

Effect of solution pH on MNP stability

The pH of the MNF matrix fluid is expected to strongly influence the electrostatic stability of fatty acid bilayer coated particles as it controls the relative proportion of neutral and charged fatty acid species in the outer monolayer via the protonation of the carboxylic acid head groups (Fig. 5.1). The effect of matrix fluid pH on MNP stability was evaluated by dispersing LA-LA particles at a volume fraction of 0.2% in different buffer solutions covering a pH range of 4 to 8. The buffer solutions, each $100\,\mathrm{mM}$ in strength, were prepared from various mixtures of sodium phosphate monobasic/sodium phosphate dibasic and citric acid/sodium phosphate dibasic (see caption of Fig. 5.2).

Figure 5.2 shows the stability of the LA-LA particle dispersions as a function of pH in terms of macroscopic particle aggregation and sedimentation after an equilibration time of $18\,\mathrm{h}$ at room temperature. The MNPs were observed to be macroscopically stable in buffer solutions of pH > 6, including ultrapure water. Starting from a bulk pH $\lesssim 6$, particle aggregation was induced at increasing extents in buffer solutions with decreasing pH as revealed by the stronger degrees of particle sedimentation. At pH ≤ 4 the destabilized magnetite particles were even partially dissolved in the matrix fluid as indicated by the yellow supernatant.

These observations show that the carboxylic headgroups of the outer fatty acid monolayers are predominantly and increasingly protonated at bulk pH values decreasing from 6. As a consequence, the repulsive electrostatic forces acting between the fatty acid bilayer stabilized particles in the MNF are decreased to such an extent that the particles aggregate and precipitate. Considering the pKa of 4.6 characteristic of a carboxyl group in aqueous solution, the strong particle aggregation
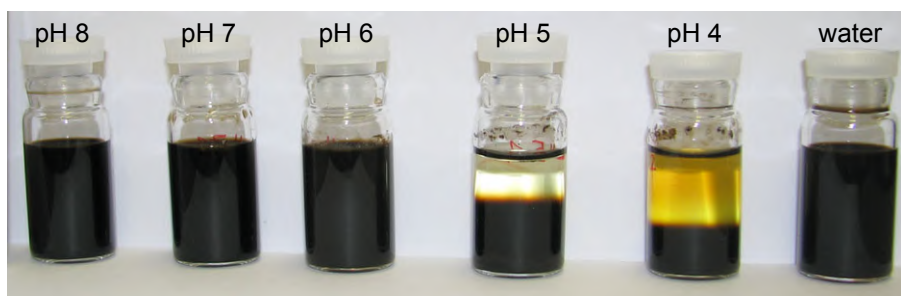
Figure 5.2: Stability of fatty acid bilayer coated MNPs in aqueous solution as a function of solution pH. Shown is the stability of 0.2 v/v% LA-LA iron oxide NPs in aqueous solutions of pH 4 to 8 as measured by macroscopic particle aggregation and sedimentation. Sample equilibration: 18 h at room temperature. pH 6–8: 0.1 M sodium phosphate monobasic/sodium phosphate dibasic. pH 4–5: 0.1 M citric acid/sodium phosphate dibasic.

behavior observed at relatively high pH was not expected in a first place. However, it is perfectly in line with the shift of the pKa of free carboxyl groups of fatty acid monomers in aqueous solution to an apparent pKa of 7 to 8.5 reported for carboxyl groups arranged at the interface of fatty acid bilayers [436].

From a more fundamental perspective, it is obvious that the colloidal stability of fatty acid bilayer coated MNPs is also dependent on the stability of the fatty acid bilayer itself. Fatty acid/soap vesicles, commonly called fatty acid vesicles, are known to be thermodynamically stable at a fatty acid to soap molar ratio close to 1 which is typically restricted to a rather narrow bulk pH range of around 7, 8, or 9, depending on the fatty acid. For fatty acid vesicles from OA and LA, the pH range of stable bilayers containing equimolar amounts of the acid and soap species is around 8.0-9.5 and 7.0-8.5, respectively. At the lower and upper boundary of the stable pH range, fatty acid vesicles coexist with soap micelles and fatty acid oil droplets, respectively. [436]. The half-ionization of stable fatty acid/soap bilayers is also indicated in the schematic representation of the fatty acid bilayer coating of a primary MNP in Figure 5.1A.

Optimum pH solution conditions: Based on the pH dependence observed for the aggregation behavior of fatty acid bilayer stabilized MNPs in aqueous solution (pH $\lesssim$ 6) and reported for the thermodynamic stability of bilayered fatty acid vesicles (pH $\approx$ 7-9), the pH of the hydration medium containing OA-OA or LA-LA particles should be controlled at neutral or slightly basic pH, ideally pH 8, for the preparation of magnetoliposomes by thin film hydration.
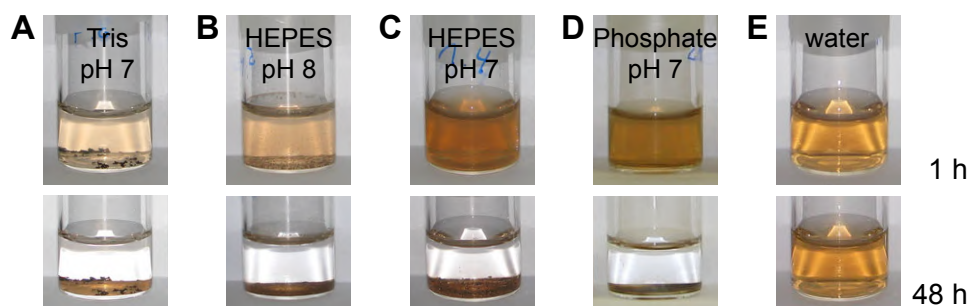
Figure 5.3: Stability of fatty acid bilayer coated MNPs in aqueous solution as a function of buffer salt composition. Shown is the macroscopic stability of 10^{-3} v/v% LA-LA iron oxide NPs in aqueous solutions of pH 7 and 8 in the presence of the buffer salts indicated on each flask. Sample equilibration: 1 h (*top*) and 48 h (*bottom*) at room temperature. Strength of buffer salts: 50 mM.

Effect of buffer salt composition on MNP stability

In order to control the pH of the MNF hydration medium in the identified range of optimum particle stability, MNP stability was now evaluated in the presence of different buffer salts added to the aqueous matrix fluid. The LA-LA MNF was diluted in different 50 mM buffer solutions, including Tris (pH 7), HEPES (pH 7 and 8), and sodium phosphate (pH 7). For each buffer composition tested, a 10-fold dilution series of the LA-LA MNF in the buffer solution was prepared at particle volume fractions ranging from 10^{-5} to 10^{-1} %. The same set of samples was prepared in ultrapure water as a control. Again, the colloidal particle stability was evaluated in terms of macroscopic aggregation and sedimentation behavior at room temperature over an observation time of 48 h.

Figure 5.3 shows the LA-LA particle dispersions in the different buffer solutions at a particle volume fraction of 10^{-3} % after a storage time of 1 h and 48 h, respectively. Both, the Tris buffer solution at pH 7 and the HEPES buffer solution at pH 8 induced immediate and strong LA-LA particle agglomeration at volume fractions of 10^{-3} % and smaller. This was indicated by the onset of particle sedimentation already 1 h after sample preparation (Figs. 5.3A and B). The corresponding LA-LA particle dispersions in HEPES buffer and sodium phosphate buffer, both at neutral pH, were initially more stable, but also ended in strong particle aggregation and complete sedimentation after an observation time of 48 h (Figs. 5.3C and D). In contrast, stable MNP dispersions were obtained over the entire range of volume fractions investigated when diluting the MNF in its matrix fluid itself, i. e. water. No particle sedimentation in the water-based LA-LA dispersions could be detected by eye after a storage time of 48 h (Fig. 5.3E).

Optimum buffer solution composition: Apparently, all evaluated buffer salts disturb the particle stabilizing bilayer of fatty acids in such a way that this type of

177

MNPs strongly precipitates in buffer solutions at $\phi \leq 10^{-3}\,\%$. Complete particle sedimentation in the presence of buffer salts was typically observed after an equilibration time of a few hours already. As a conclusion from the particle stability tests in the presence of buffer salts, the concentrated water-based MNFs obtained from RATB were dispersed in plain ultrapure water for further experiments, in spite of the lack of pH control in the resulting MNFs.

Effect of particle concentration on MNP stability

In a last step, the stability of OA-OA and LA-LA MNPs in water was studied as a function of particle concentration in order to identify a stable concentration range to follow throughout all steps of magnetoliposome preparation. Dilution series of the OA-OA and LA-LA MNFs in water were prepared in triplicate at particle volume fractions ranging from 10^0 to $10^{-7}\,\%$. The concentration-dependent particle aggregation was evaluated by measuring the size of secondary particles, i.e. particle aggregates, in the obtained dispersions using DLS after a sample equilibration time of 3 days at room temperature.

Figure 5.4 shows the mean hydrodynamic diameter D_h of OA-OA and LA-LA secondary particles formed in water as a function of particle volume fraction. It reveals a strong aggregation behavior of both particle systems at volume fractions smaller than $10^{-4}\,\%$. The formation of such particle clusters upon strong dilution of fatty acid bilayer coated NPs in aqueous solution can be attributed to the relatively high monomer solubility of fatty acids in water [436]. Above the critical particle concentration detected at $\phi \approx 10^{-4}\,\%$, the fatty acids of the physically adsorbed outer monolayer of the particle coating are in equilibrium with the monomers in the matrix fluid. Dilution of the particles below the critical concentration leads to the desorptive loss of part of the outer monolayer and, hence, to reversible particle aggregation [434].

Due to the different lengths of the hydrocarbon chains, the approximate free monomer concentration of the short-chain lauric acid in equilibrium with LA-LA bilayers ($\sim 23\,\mathrm{mM}$) is much higher than that of the long-chain oleic acid in equilibrium with OA-OA bilayers ($< 1\,\mathrm{mM}$) [436]. This explains the stronger extent of dilution-induced particle aggregation of the LA-LA NPs compared to the OA-OA NPs at $\phi < 10^{-4}\,\%$ (Fig. 5.4). At the same time, the differences in monomer solubilities would suggest the critical particle concentration for the onset of dilution-induced particle aggregation to be shifted to higher ϕ values in the case of the water-based LA-LA MNF. Indeed, strong particle aggregation in the LA-LA MNF was already observed at intermediate volume fractions between 5×10^{-3} and $2.5 \times 10^{-4}\,\%$, however, this aggregation behavior was completely transient within the mentioned ϕ range (Fig. 5.4). Strongest aggregation of the LA-LA particles within this range was found at $\phi \approx 7.5 \times 10^{-4}$–$10^{-3}\,\%$ as indicated by the intermediate D_h maximum
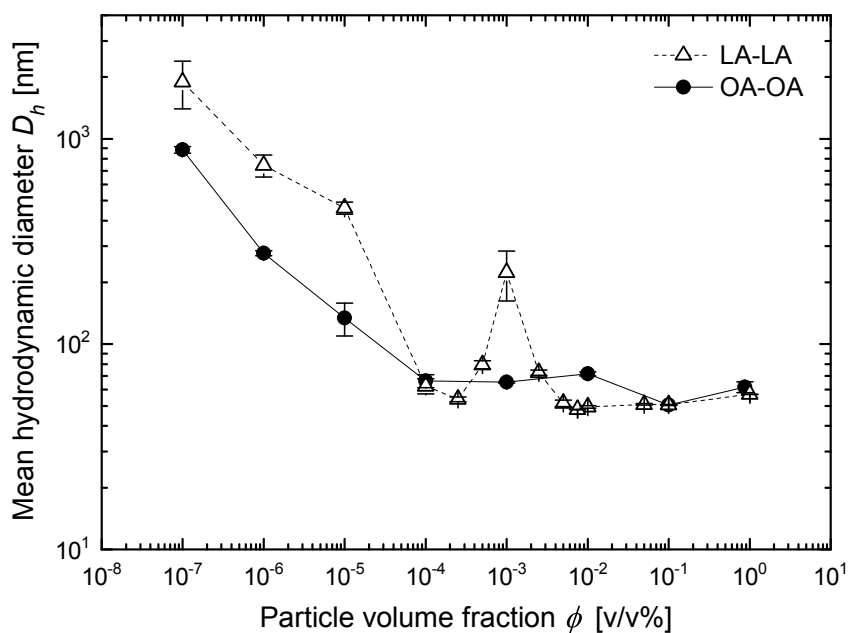
Figure 5.4: Aggregation behavior of fatty acid bilayer coated MNPs in aqueous solution as a function of particle concentration. The concentration-dependent aggregation behavior of OA-OA (●) and LA-LA (△) iron oxide NPs in water is shown through changes in the mean hydrodynamic diameter D_h of particle clusters as a function of particle volume fraction ϕ. Equilibration of particle dispersions prior to measurements: 3 days at room temperature. Results represent mean values of at least two independent dilutions of the original OA-OA and LA-LA MNFs (Tab. 5.1) in ultrapure water, respectively. The lines are drawn to guide the eye.
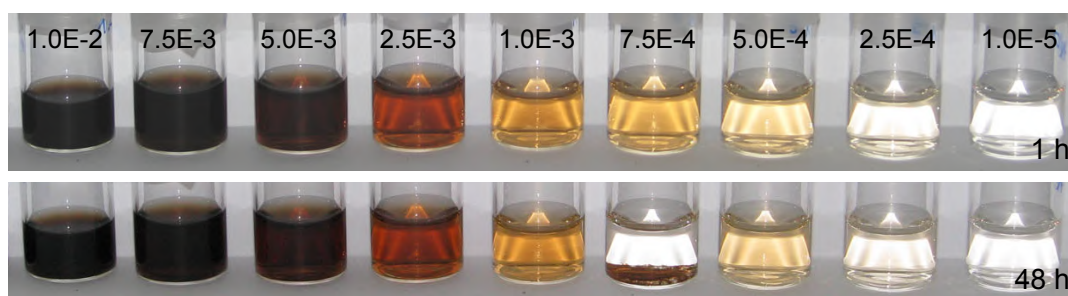

Figure 5.5: Stability of fatty acid bilayer coated MNPs in aqueous solution as a function of particle concentration. Shown is the macroscopic stability of LA-LA iron oxide NPs in water as a function of the particle volume fraction ϕ in v/v% indicated on each flask. Sample equilibration: 1 h (*top*) and 48 h (*bottom*) at room temperature.

in Figure 5.4 and by the complete particle sedimentation observed in some but not all of the replicate $7.5 \times 10^{-4}\,\%$ samples of the LA-LA dilution series as shown in Figure 5.5. Precipitated samples could not be analyzed by DLS measurements and were not considered in the data shown in Figure 5.4. The particle concentration dependent transient aggregation behavior of LA-LA MNPs in water was well reproducible, but it was specific to the LA-LA MNF sample used in this study and was not observed for other LA-LA MNF preparations obtained from RATB. We do not have an explanation for this peculiarity.

Optimum MNP concentration: To avoid the aggregation-inducing ranges of particle volume fractions reported in this section, the volume fractions of OA-OA and LA-LA MNPs were kept in the stable range of $\phi > 5 \times 10^{-3}\,\%$ during preparation of aqueous magnetoliposome suspensions (Fig. 5.4). Accounting for a dilution factor of the liposome fraction of 10 at the most during the separation step of magnetoliposomes from nonentrapped MNPs by column filtration [296], the initial volume fraction of OA-OA and LA-LA MNPs in the hydration medium was set at $10^{-1}\,\%$, 1.5 orders of magnitude above the upper critical particle concentration for LA-LA MNP agglomeration. At this particle volume fraction, the secondary particles from both OA-OA and LA-LA MNPs in water have a mean hydrodynamic diameter of around 50 nm as obtained from our DLS measurements (Fig. 5.4). This is larger than the mean D_h values of the concentrated OA-OA and LA-LA MNFs obtained from RATB (31 nm and 37 nm, respectively; Tab. 5.1), but it should still allow for the encapsulation of MNPs in uni- and oligolamellar vesicles prepared by thin film hydration and the sequential extrusion technique. Previous works reported on the successful entrapment of 30 nm and 60 nm-sized clusters of surfactant stabilized MNPs in the aqueous domains of LUVETs$_{100}$ and VETs$_{200}$, respectively [413, 438].

The initial particle concentration in the hydration medium is an important parameter when forming magnetoliposomes by passive encapsulation of a MNF as it directly influences the magnetic loading of the final magnetoliposomes. In the absence of interactions between the particles and the lipid membranes, the amount of encapsulated magnetic particles is linearly related to the initial MNP concentration [413, 438, 439].

The $0.1\,\mathrm{v/v\%}$ OA-OA and LA-LA particle dispersions used in the following as hydration medium contained $3.5\,\mathrm{mg\,mL^{-1}}$ and $3.2\,\mathrm{mg\,mL^{-1}}$ of total iron, i.e. $4.8\,\mathrm{mg\,mL^{-1}}$ and $4.5\,\mathrm{mg\,mL^{-1}}$ of magnetite, respectively, as determined by AAS. This is slightly above the range of total iron concentrations of approximately $0.05\text{-}2.5\,\mathrm{mg\,mL^{-1}}$ present in the MNP containing hydration media of previous studies describing the preparation of magnetoliposomes for magnetic drug targeting [273, 416, 438, 439]. Based on these figures, it can be assumed that the magnetoliposomes formed in $0.1\,\mathrm{v/v\%}$ OA-OA and LA-LA particle dispersions will be guidable along external magnetic field gradients in the case of quantitative MNP encapsulation in the aqueous vesicle interior. The apparent extent of OA-OA and LA-LA particle en-

capsulation in the aqueous domains of extruded liposomes will be elucidated and discussed in the following section.

For the envisioned application of magnetoliposomes in magnetic separation processes, higher magnetic loadings than those theoretically obtained from the initial $0.1\,v/v\%$ particle suspensions should be considered in further development steps. Magnetoliposomes that have been designed for a fast magnetic separation were, for example, prepared in a MNF containing $56\,mg\,mL^{-1}$ of total iron [421].

5.3.2 Preparation of magnetoliposomes using fatty acid bilayer coated iron oxide NPs

Multilamellar vesicles from S100 were now prepared by thin film hydration in the water-based OA-OA and LA-LA MNFs of optimum colloidal stability, that is in the absence of buffer salts and at a particle volume fraction of 0.1%. The concentration of total lipids was $20\,mM$ resulting in an initial iron-to-lipid molar ratio of around $310\,mol\%$ and $290\,mol\%$ in the OA-OA and LA-LA samples, respectively. These conditions allowed the formation of homogeneous and stable MLV suspensions in the two MNFs.

In the following, we describe the behavior of the composite systems throughout the remaining process steps towards uniform and purified magnetoliposomes, including sequential vesicle extrusion and size exclusion chromatography (SEC). The fate of MNPs and vesicles after each process step was evaluated by quantifying total iron and total phospholipid concentrations in the suspensions before and after the respective treatments. Finally, cryo-TEM was used to characterize the particle and vesicle structures, as well as the amount of encapsulated and contaminating external MNPs in the obtained magnetoliposome suspensions.

Extrusion of multilamellar vesicle/MNP composite suspensions

The MLVs formed in $0.1\,v/v\%$ OA-OA and LA-LA MNFs were homogenized in terms of size and lamellarity using the commonly applied extrusion technique [3, 9, 193, 206]. Membrane penetrability to the MNP containing vesicle suspensions was evaluated by sequentially extruding the suspensions 10 times through $400\,nm$, followed by 10 times through $200\,nm$ pores of track-etched polycarbonate filters (abbreviated in the following as PC400 and PC200 membranes). Sample aliquots were collected after 1, 5, and 10 extrusion cycles through each membrane type used and analyzed for total iron concentration by AAS to check for possible filter effects towards the MNPs (Fig. 5.6). As reported in Chapter 4.3.3 and known from literature, total lipids from initial MLV suspensions are typically recovered after repetitive extrusion through polycarbonate membranes [15, 212, 367]. Therefore,
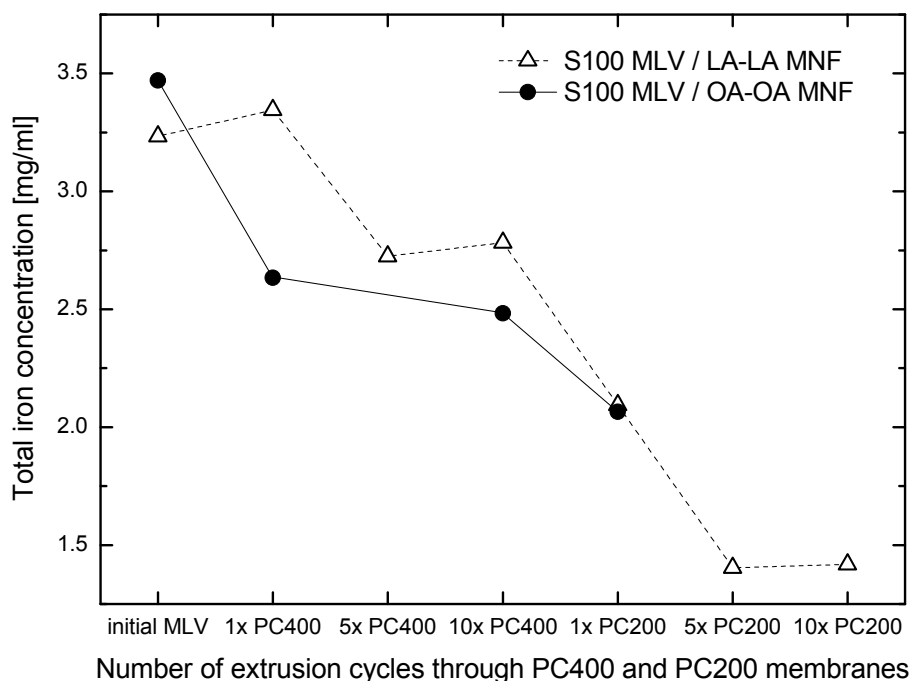
Figure 5.6: Filter effect towards iron oxide NPs upon repetitive extrusion of unpurified magnetoliposome suspensions. Total iron concentration of S100 MLV suspensions formed in 0.1 v/v% OA-OA (●) and LA-LA MNFs (△), respectively, after sequential extrusion the indicated number of times through 400 nm and 200 nm pores of track-etched polycarbonate membranes (PC400 and PC200). Initial composite suspension: 20 mM total lipids; 62 mM and 58 mM total iron in 0.1 v/v% OA-OA and LA-LA MNFs, respectively. Results represent mean values of two repeat AAS measurements of a single magnetoliposome sample. Lines are drawn to guide the eye.

the extrusion experiment was carried out without explicitly measuring the recovery of total lipids after extrusion.

Sequential extrusion of the initial MLV suspensions in 0.1 v/v% OA-OA and LA-LA MNFs through the PC400 membrane required increasing extrusion pressures of 5-15 bar and a small number of membrane replacements due to filter clogging during the first 5 extrusion cycles. The remaining 5 extrusion cycles were relatively straightforward and could be completed at a constant extrusion pressure of approximately 5 bar using a single filter membrane. Further extrusion of the obtained VET$_{400}$ suspensions in MNFs through the PC200 membrane progressed similarly but membrane penetrability was drastically decreased, so that the extrusion pressure had to be increased to 30-45 bar. Forcing the VET$_{400}$/LA-LA particle suspension through the PC200 membrane resulted in complete filter clogging after each of the first 5 extrusion cycles and became smoother during the remaining 5 passes. Extrusion of the corresponding OA-OA suspension through the PC200 membrane almost com-

pletely failed and the extrusion experiment was omitted after 2 cycles.

The clogging issues experienced during the first 1-5 extrusion cycles of the OA-OA and LA-LA magnetoliposome suspensions through both PC400 and PC200 membranes were reflected by an important drop in total iron concentration in the corresponding extruded samples (Fig. 5.6). Only after around 5 passes through membranes of a specific pore size, the iron concentration in the regularized magnetoliposome suspensions reached a value which then remained constant with increasing numbers of extrusion cycles. In the case of the final VET_{200}/LA-LA particle suspension, this value corresponded to only 44% of the total iron content initially present in the $0.1 \, v/v\%$ LA-LA MNF used for thin film hydration. The corresponding VET_{400} suspensions retained 72% and 86% of the initial iron content of the $0.1 \, v/v\%$ OA-OA and LA-LA MNFs, respectively.

The increasing loss of total iron detected in the magnetoliposome suspensions after extrusion through pore sizes decreasing from $400 \, nm$ to $200 \, nm$ (Fig. 5.6) clearly indicates the presence of a considerable amount of large particle aggregates with diameters $> 200 \, nm$, some of them even with diameters $> 400 \, nm$, in the initial MLV suspensions formed in $0.1 \, v/v\%$ OA-OA and LA-LA MNFs. The presented extrusion experiment showed that the particle aggregates exceeding the pore size of the filter membrane used are successfully removed during the extrusion procedure. At the same time, it has to be assumed that particle aggregates smaller than the pore size used for final extrusions will persist and coexist with the magnetically loaded vesicles and the free secondary MNP clusters in the extruded suspensions. Both the mean diameter of the magnetoliposomes and that of the largest particle aggregates that are just able to pass the membrane pores will represent the average pore diameter of the membrane used for final extrusions. This will most likely interfere with a clear separation of particle-entrapping vesicles from free MNPs by size exclusion chromatography.

For practical reasons outlined above, the S100 MLVs formed in $0.1 \, v/v\%$ OA-OA and LA-LA MNFs were, in the following, only taken through 10 extrusion cycles through PC400 membranes for homogenization. The obtained $VETs_{400}$ in the MNFs had a mean hydrodynamic diameter of approximately $250 \, nm$ as derived from DLS measurements (Fig. 5.7). This is in good agreement with the average diameter of aqueous VET_{400} suspensions prepared from pure phosphatidylcholines in the absence of MNPs [9, 10]. Figure 5.7 shows the volume-weighted particle size distribution of a VET_{400}/LA-LA particle suspension with the primary peak at $45 \, nm$ representing the free secondary LA-LA particles and the shoulder at $250 \, nm$ representing the liposomal fraction of the composite system.

Among the earlier studies on magnetoliposome formation by the passive encapsulation of hydrophilic MNPs in the vesicle core followed by sequential extrusion, most have reported the use of $200 \, nm$ pore membranes for final extrusions [412, 415, 416, 421, 438, 439], while only a few were able to prepare $LUVET_{100}$ in the presence of
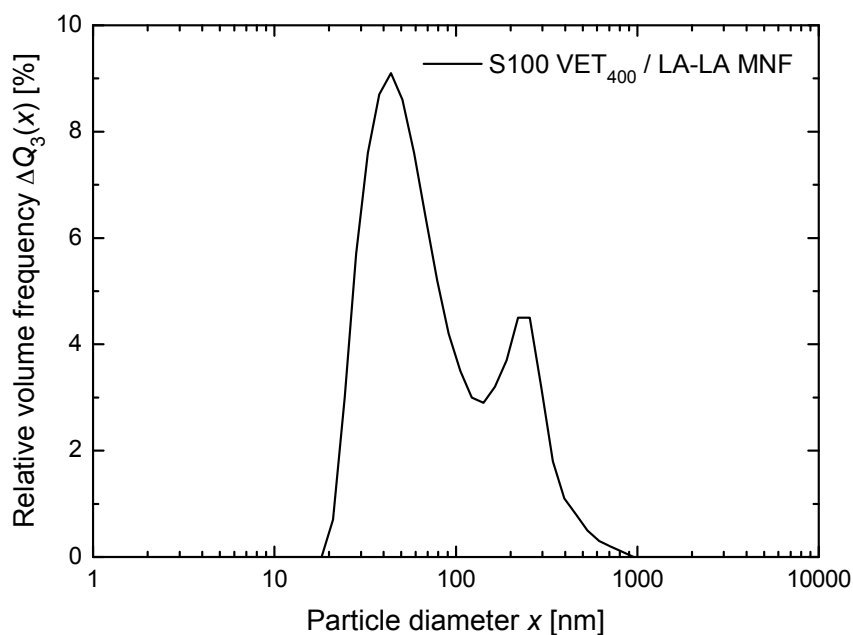
Figure 5.7: Particle size distribution of unpurified VET$_{400}$/MNP composite suspension. The composite suspension was formed by S100 thin film hydration in $0.1\,\mathrm{v/v\%}$ LA-LA MNF followed by sequential extrusion 10 times through $400\,\mathrm{nm}$ pores of track-etched polycarbonate membranes. Initial composite suspension: $20\,\mathrm{mM}$ total lipids; $58\,\mathrm{mM}$ total iron.

aqueous MNP dispersions [273, 413]. The authors of the latter works emphasized an optimal stabilization and dispersion of the MNPs in the hydration medium, a condition which was obviously not achieved in the course of our experiments using fatty acid bilayer coated MNPs. Garnier *et al.* also used a negatively charged layer of surface adsorbed dispersants, namely citric acid, for the stabilization of iron oxide NPs, but highlighted the cycles of excess citric acid elimination as critical steps for obtaining a well-dispersed aqueous MNF [413]. On the other hand, Amstad *et al.* worked with ultrastable colloidal suspensions of individually PEG-nitroDOPA stabilized iron oxide NPs which exhibited an irreversible binding of the dispersants to the iron oxide surface via a nitroDOPA anchor group [273].

Separation of magnetoliposomes from free MNPs by SEC

In a last step of magnetoliposome preparation, aliquots of the VET$_{400}$/MNP suspensions were passed down a SEC column with the aim of removing nonentrapped MNPs from the bulk solution. Under appropriate conditions, SEC is known to allow for excellent separation of liposomes from low molar mass compounds, proteins, and enzymes [36, 142, 440]. While the smaller nonentrapped molecules diffuse into and

through the porous beads packed in the column bed, liposomes percolate through the interbead spaces and elute first from the column (see Fig. 3.3 for an elution profile of calcein-entrapping liposomes and free dye molecules indicating a clear separation of the two fractions). SEC has also been shown to perform well in the purification of magnetoliposomes prepared by passive MNP encapsulation [412] and is widely used in this field [273, 413, 416, 421, 438, 439].

Figure 5.8A shows the elution profiles of the liposome and MNP fractions in terms of S100 phospholipids and iron concentrations, respectively, recorded after applying an aliquot of the VET_{400}/OA-OA particle suspension on the column. Sample elution was monitored throughout the time required for the entire bed volume to elute. The profiles of the liposome fraction and of the eluted OA-OA particle fraction completely overlapped in the entire elution time interval probed indicating basically no separation between liposomes and nonentrapped MNPs. However, it is noticeable that the upper column bed remained colored after running the composite sample through the column, even after extensive rinsing with elution buffer, i.e. water (Fig. 5.8C). Based on these observations, the fate of the secondary particle clusters and the larger particle aggregates both initially present in the unpurified VET_{400}/MNP suspension after column separation can be described as follows (see also schematic illustrations in Fig. 5.8C). Nonentrapped small particle clusters seem to be retained by the porous bead matrix in the column, while the external particle aggregates co-elute with similar-sized liposomes, which may or may not be loaded with small particle clusters.

Given the almost perfect overlay of the MNP and liposome elution profiles found for the VET_{400}/OA-OA particle suspension (Fig. 5.8A), it is very likely that the unsuccessful magnetoliposome purification by SEC was influenced by interactions between the fatty acid bilayer coated particles and the phospholipid vesicle membranes. At the same time, the overlay of the MNP and liposome elution profiles was just as good after separately loading the MNF used for magnetoliposome formation and a magnetically empty liposome suspension to the column, as carried out for the LA-LA composite sample. This is shown in Figure 5.8B by the overlapping elution profiles of iron and S100 phospholipids obtained after separate injection of a 0.1 v/v% LA-LA particle dispersion and a S100 VET_{400} suspension, respectively. The S100 VET_{400} suspension had been prepared in water containing calcein as low molecular weight marker molecule and the corresponding separation curve obtained from UV/Vis spectrophotometric measurements was included in Figure 5.8B for comparison. The first minor SEC peak representing the calcein-loaded VET_{400} fraction is in good agreement with that obtained from phospholipid analysis using the Stewart assay. The second SEC peak is the result of a delayed elution of nonentrapped small dye molecules after diffusion through the porous bead matrix.

The presented set of elution profiles confirms that the route through the porous beads was not accessible for both OA-OA and LA-LA MNPs under the evaluated
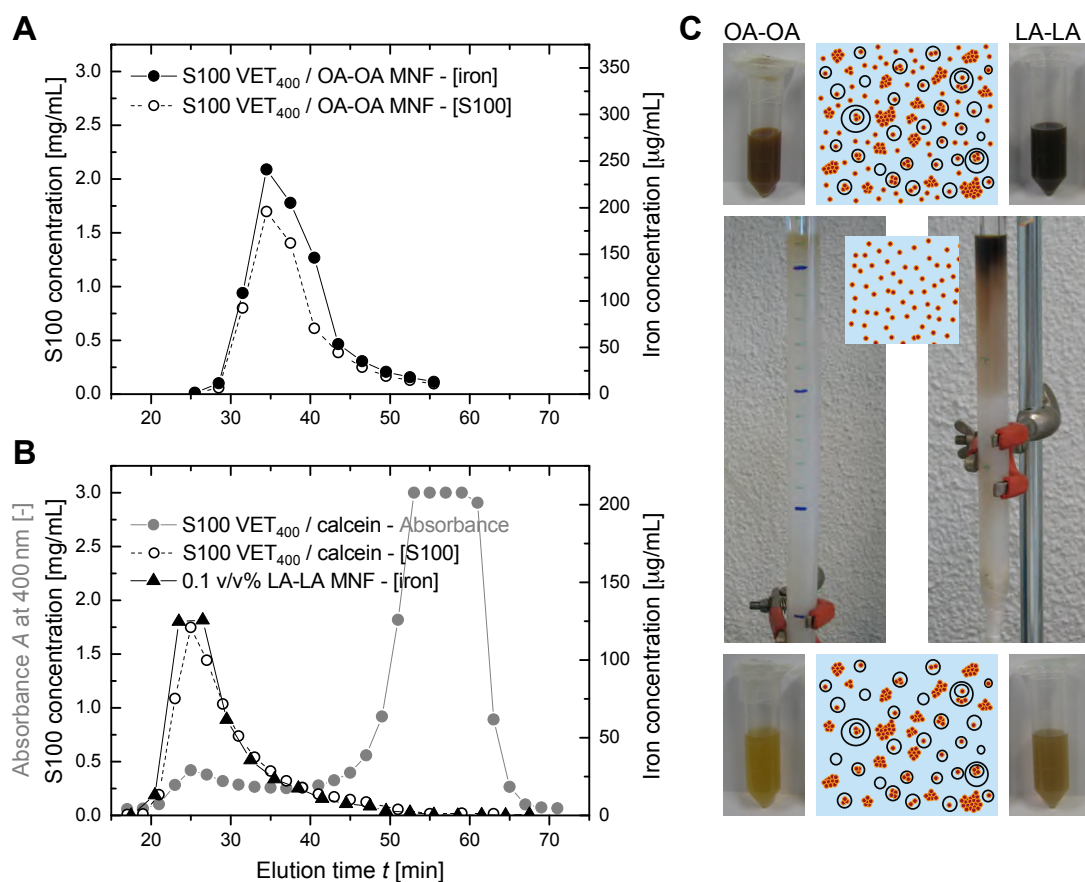
Figure 5.8: Separation of magnetic fluid-loaded VETs$_{400}$ from nonentrapped fatty acid bilayer coated MNPs by SEC. (A) Elution profiles of VETs$_{400}$ (○) and OA-OA MNPs (●) after loading a composite VET$_{400}$/OA-OA particle suspension. The composite suspension was prepared by 10 extrusion cycles of S100 MLVs formed in 0.1 v/v% OA-OA MNF through PC400 membranes. Composite suspension before SEC: $\approx$ 20 mM total lipids; $\approx$ 2.5 mg mL^{-1} total iron. Sepharose CL-2B column: 1×20 cm. Sample loading: 400 µL. Flow rate: 0.29 mL min^{-1}. (B) Elution profiles of VETs$_{400}$ (○) and LA-LA MNPs (▲) after separately loading a magnetically empty VET$_{400}$ suspension and a 0.1 v/v% LA-LA MNF (total iron: 3.2 mg mL^{-1}). The VET$_{400}$ suspension was prepared by 10 extrusion cycles of 20 mM S100 MLVs formed in 40 mM calcein through PC400 membranes. The corresponding separation curve of calcein-entrapped VETs$_{400}$ from free calcein (●) was recorded by UV/Vis spectrophotometry. Sepharose CL-2B column: 1×15 cm. Sample loading: 400 µL. Flow rate: 0.26 mL min^{-1}. The specific elution profiles of liposomes and MNPs were obtained from total phospholipid and iron concentration measurements, respectively. (C) Photographs of the SEC columns after the separation experiments presented in parts A and B, including schematic representations of the expected composite structures using OA-OA or LA-LA particles before and after SEC.

test conditions, whether the particles were solely contained in the water-based MNF or in a vesicular composite suspension. This shortcoming is primarily ascribed to the self-organization of the fatty acid bilayer coated MNPs into secondary particle clusters. Most of these secondary particles were too large, i.e. too similar in size to VETs$_{400}$, to allow for a successful separation of the liposome population from nonentrapped MNPs by SEC. The VET$_{400}$ fraction and large particle clusters co-eluted in the void volume of the column, while a considerable amount of free MNPs remained trapped in the column matrix in the case of both OA-OA and LA-LA particle suspensions (Fig. 5.8C).

The extent of particle trapping was much larger for the LA-LA MNF as evidenced by the dark residual color of the upper column bed and by the low LA-LA particle recovery after gel filtration. According to the ratios of the total amounts of iron loaded to and collected from the column during the separation experiments (Figs. 5.8A andB), the recovery of LA-LA particles was only around 26% compared to 75% of the initially loaded particles retrieved from the eluted OA-OA samples. The exact reason for particle retention in the column is not known. Fatty acid bilayer coated MNPs are unlikely to be adsorbed by the predominantly uncharged Sepharose bed since Sepharose contains only a small number of residual charged groups with like charges (negative) as the carboxylic fatty acid head groups. Instead, the increased sensitivity of LA-LA particles to aggregate in water (Fig. 5.4) suggests that particle aggregation and geometrical constraints also play a role in the high LA-LA particle loss observed during column filtration.

Due to a possible fouling of the bead matrix by particle retention, the separation experiments using OA-OA and LA-LA particle dispersions were carried out on separate freshly prepared SEC columns which were different in length. The one used for the VET$_{400}$/OA-OA particle sample was 20 cm long, while that involved in the LA-LA experiment measured 15 cm. This explains the longer elution times of the VETs$_{400}$ and particle aggregate fractions recorded after the OA-OA column (Fig. 5.8A) compared to those obtained from the LA-LA column (Fig. 5.8B).

Because of the unsuccessful SEC purification of the VET$_{400}$/MNP composite suspensions and the consequential presence of contaminating external MNPs in the eluted liposome fractions, the concentration data of S100 phospholipids and total iron collected before and after column separation could not be used for an estimation of encapsulation efficiencies. Instead, the extent of partitioning of the OA-OA and LA-LA stabilized MNPs into the aqueous domains of VETs$_{400}$ was evaluated by cryo-TEM as reported in the following and last section of this chapter.

Ensuring a clear separation of magnetoliposomes from nonentrapped MNPs by SEC is a delicate task that requires good MNP dispersion stabilities, as well as no interactions between the particles and the lipid membranes. Garnier *et al.* reported on very similar difficulties as described above during the separation step of magnetically loaded LUVETs$_{100}$ from nonentrapped citric acid coated iron oxid NPs by SEC

[413]. They also recorded overlapping elution profiles of magnetoliposomes and non-entrapped MNPs in preliminary experiments and attributed this failure to the large amount of particles applied to the SEC column. A good separation as demonstrated by the absence of nonentrapped MNPs in the final magnetoliposome suspensions using cryo-TEM was only possible after pre-clearing the composite suspensions from nonentrapped MNPs by a salt-induced aggregation and centrifugation step prior to SEC. In another study, VETs$_{200}$ were loaded with tetramethylammonium hydroxide stabilized iron oxide NPs and the magnetoliposome fraction recovered after SEC was described to be completely free of contaminating external MNPs [438]. However, the presented TEM micrographs revealed that most MNPs were in an aggregated form and localized outside the liposomes.

According to the intermediate separation step described by Garnier *et al.* [413], the separation efficiency of the composite suspension investigated in the present work could be improved by taking advantage of the pH or dilution dependent aggregation behavior of the fatty acid bilayer coated MNPs (Sec. 5.3.1). The resulting external MNP aggregates could then be removed by centrifugation. The same approach of separating nonentrapped MNPs from magnetoliposomes by density instead of size after inducing external MNP aggregation has been used in a number of other studies involving the preparation of magnetoliposomes by passive MNP encapsulation [417, 441, 442].

5.3.3 Characterization of magnetoliposome suspensions by cryo-TEM

The magnetoliposome suspensions prepared by the passive encapsulation of fatty acid bilayer coated MNPs as detailed above were visualized before and after SEC purification by cryo-TEM. This powerful technique allows to directly visualize and characterize the structures of liposomes and water-basted MNFs, as well as the localization of the MNPs in the composite suspensions.

Due to instrumental limitations, samples for cryo-TEM investigation were prepared at a total iron concentration of around $1\,\mathrm{mg\,mL^{-1}}$. To meet this criteria, the initial MLV suspensions were formed in OA-OA and LA-LA MNFs containing $0.03\,\mathrm{v/v\%}$ iron oxide particles instead of the standard particle volume fraction of $0.1\,\mathrm{v/v\%}$ used in the experiments described above. The initial lipid concentration was kept constant at $20\,\mathrm{mM}$. The behavior of the slightly lower concentrated composite suspensions during extrusion and gel filtration was comparable to that observed for the standard samples. The photographs of the magnetoliposome suspensions loaded to and collected from the SEC column included in Figure 5.8C actually represent those prepared for cryo-TEM imaging.

Figure 5.9 shows the cryo-TEM micrographs of the VET$_{400}$ suspensions prepared in
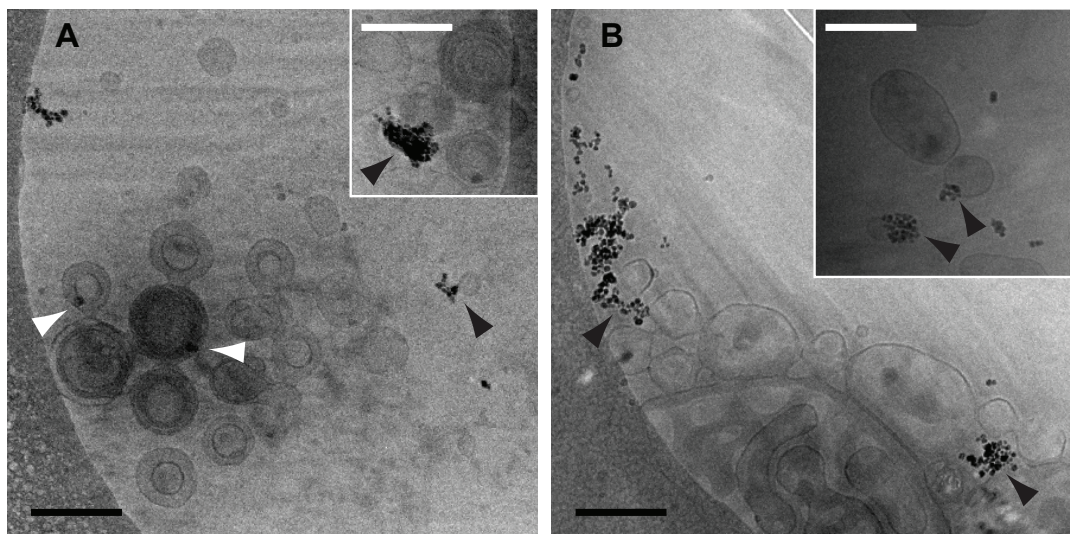
Figure 5.9: Cryo-TEM micrographs of unpurified and purified magnetoliposome suspensions containing fatty acid bilayer coated MNPs. Visualized are VET$_{400}$ suspensions prepared in OA-OA (A) and LA-LA MNFs (B) before and after (insets) SEC purification. The initial MLV suspensions were formed from 20 mM S100 in 0.03 v/v% OA-OA and LA-LA MNFs, respectively, and extruded 10 times through PC400 membranes. *White arrows*: Encapsulated MNPs. *Black arrows:* Interactions between MNP aggregates and liposome membranes. Scale bar = 200 nm.

OA-OA and LA-LA MNFs before and after (insets) SEC purification.

The liposomes dispersed in the water-based OA-OA MNF (Fig. 5.9 A) were predominantly spherical in shape and had uni- to oligolamellar character as expected for aqueous VET$_{400}$ preparations [9, 10, 219]. However, the MNPs were mainly localized outside the liposomes in the form of intermediate-sized aggregates, indicating poor encapsulation efficiency of OA-OA MNPs in VETs$_{400}$. It is striking that many of the OA-OA particle aggregates visualized were closely associated with vesicle surfaces (Fig. 5.9 A, black arrows). This confirms the assumption of particle-bilayer interactions that has been made earlier based on the overlapping MNP and liposome elution profiles recorded after gel filtration of the OA-OA composite suspension (Fig. 5.8 A). The white arrows in Figure 5.9 A highlight a few particle clusters that were small enough to partition into the liposomes. Their encapsulation was likely to be mediated by the same interactions between particles and, in this case, internal lamellae since the internal MNPs also seemed to be bound to lipid bilayers. No freely dispersed particles were observed in the lumen of the liposomes. It is also possible that these particle clusters represent external MNPs that were actually bound to the outer surface of the liposomes viewed from the top.

The micrograph in Figure 5.8 B confirms the susceptibility of the LA-LA MNPs used to form large particle aggregates in water as already predicted from their beha-

vior throughout the different steps of magnetoliposome preparation. Again, many particle aggregates were found to be associated with vesicle bilayers (Fig. 5.9 B, black arrows), but none of the LA-LA MNPs was integrated into the liposomes. In contrast to the spherical morphology of liposomes observed in the OA-OA nanocomposite (Fig. 5.8 A), the VETs$_{400}$ prepared in the LA-LA MNF were highly irregular in shape (Fig. 5.8 B). This can be explained by the presence of relatively large amounts of LA monomers in the matrix fluid of the LA-LA MNF. As mentioned earlier, based on the bilayer-monomer equilibrium existing between the fatty acid bilayer coating of the MNPs and the matrix fluid, the free monomer concentration of LA in the LA-LA MNF can be estimated to be around 23 mM compared to < 1 mM of OA monomers in the OA-OA MNF [436]. This results in a molar ratio of free LA monomers to S100 phospholipids (20 mM) during vesicle formation in the LA-LA MNF of more than 1. In the very probable case of the presence of excess LA in the LA-LA MNF, the concentration of free LA monomers is expected to be even higher. Therefore, the liposomes formed from S100 phospholipids in the LA-LA MNF most likely consisted of mixed S100/LA bilayers. Incorporation of short chain LA molecules into highly ordered diacyl phospholipid bilayers leads to increased flexibility and higher (local) curvature of the vesicle membranes resulting in the irregular equilibrium shapes observed in Figure 5.8 B.

5.3.4 Discussion on the stabilization and performance of iron oxide NPs for liposome functionalization

As revealed by the different experiments presented in this chapter, the coating of iron oxide NPs with a fatty acid bilayer provided rather poor steric MNP stabilization in water, as well as in liposome suspensions. The bilayer coating did not prevent the MNPs from agglomerating in aqueous solutions and from interacting with liposomal membranes, as seen in the cryo-TEM micrographs (Fig. 5.9). Ultimately, this did not allow for a successful assembly of MNPs in the liposome lumen, which was especially true for the LA-LA MNPs. The following discussion is amongst others based on a recent review on NP functionalized liposomes and capsules by Amstad and Reimult [24].
The colloidal stability of the OA-OA and LA-LA MNPs relies on two coating layers of fatty acids both of which are reversibly adsorbed to the iron oxide surface and to the inner fatty acid monolayer, respectively [443]. Together with the high monomer solubility of fatty acids in water [436], this results in a very dynamic coating layer that renders the MNPs prone to agglomeration. Agglomeration of the fatty acid bilayer coated particles was already apparent in the initial MNFs (Tab. 5.1 and Fig. 5.4). It then obstructed the different steps of magnetoliposome preparation (Sec. 5.3.2) and, finally, led to poor encapsulation efficiencies of MNPs in liposomes (Fig.

5.9). Similarly, a decrease in encapsulation efficiency upon MNP agglomeration prior to or during passive encapsulation was reported for starch-coated, agglomerated iron oxide NPs that were primarily located outside liposomes rather than in the liposome lumen [442]. Large amounts of nonentrapped particle agglomerates were also observed in the case of iron oxide NPs stabilized with anionic [444] and cationic surfactants [438].

To our knowledge, no previous study has reported the use of fatty acid bilayer stabilized MNPs for the preparation of magnetoliposomes by passive MNP encapsulation into the liposome lumen. However, hydrophobic MNPs coated with a monolayer of fatty acids, typically oleic acid, have been used in several studies for passive MNP incorporation into the hydrophobic core of the vesicle membrane [273, 418, 419, 445]. In accordance to the colloidal properties of hydrophilic fatty acid bilayer coated MNPs, the hydrophobic MNPs stabilized with a reversibly adsorbed oleic acid monolayer were shown to have a strong tendency to agglomerate into clusters. In most cases, these oleic acid monolayer stabilized MNP clusters were too large to be embedded in the membrane interior [24, 273, 418, 443]. Instead, they were surrounded by a phospholipid monolayer yielding stable, MNP functionalized micelles at the outer surface of the liposomes [273, 418, 446]. This very same behavior was also observed for hydrophobic OA MNPs obtained from RATB when trying to assemble them into liposome membranes by the hydration of a OA MNP functionalized lipid film following the method described by Amstad *et al.* [273]. Due to steric constraints, the OA MNPs did not insert into the bilayers but accumulated in the form of large particle aggregates at the liposome surface, as seen on cryo-TEM images (data not shown). Interestingly, these steric constraints could be overcome according to an alternative, recently developed synthesis procedure that is based on the transformation of MNP functionalized mixed micelles into vesicles rather than on passive MNP encapsulation. It allowed the inclusion of oleic acid monolayer stabilized MNP clusters of up to 60 nm in size into liposome bilayers [447].

The interactions observed between the hydrophilic OA-OA and LA-LA MNPs and the liposome membranes (Fig. 5.9) can be ascribed to a relatively low packing density of fatty acids on the iron oxide nanoparticles [273]. The phosphate head groups assembled at the membrane exterior have a high affinity to iron and, hence, strongly interact with partly exposed core surfaces of the iron oxide NPs [448]. Such particle-lipid bilayer interactions are common among iron oxide NPs that are sterically stabilized with reversibly adsorbing dispersants, such as starch, dextran or fatty acids [24]. The resulting accumulation of MNPs at the outer surface of liposomes as observed here was, for example, also reported for iron oxide NPs stabilized by carboxydextran [449] and could be visualized by confocal microscopy using rhodamine B surface modified $CoFe_2O_4$ and Fe_2O_3 NPs [430, 450]. It has to be noted that the binding of MNPs to the outer liposome surface does not allow for the complete removal of nonentrapped MNPs irrespective of the separation technique used, i.e. SEC, centrifugation, or magnetic sorting [412]. As mentioned before, the resulting

presence of externally associated MNPs obscures the quantitative determination of the encapsulation efficiency or of the number of MNPs encapsulated in the liposome lumen [449]. Furthermore, it disturbs the control of magnetoliposomes in external magnetic fields and often reduces their stability and efficiency [24, 412].

Based on the considerations discussed above, the steric stabilization of the magnetite NPs used in this study needs to be drastically improved in order to gain control over the assembly of MNPs into liposomes [24]. Only optimally stabilized MNPs will allow the preparation of magnetoliposome suspensions that encapsulate and retain a controlled amount of MNPs in the liposome lumen, while being free of contaminating external MNPs and maintaining the liposome membrane properties. Reducing the number of reversibly adsorbed dispersant layers from two to one would confine the dynamic nature of the dispersant shell and confer a higher MNP stability in aqueous solution and in the presence of liposomes. Physisorbed coating layers are found in many commercially available, superparamagnetic iron oxide based ferrofluids and typically consist of natural or synthetic polymers, inorganic molecules or surfactants [431, 451, 452]. Indeed, iron oxide NPs sterically stabilized with dextran [415], carboxydextran [449], siloxane [453], cationic surfactants [438], anionic surfactants [444], and citrate [412, 413, 416, 421] were successfully loaded into the lumen of nanometer-sized liposomes, even though the vast majority of these particles was in an agglomerated state. As described above, the stabilization of iron oxide NPs by reversible physisorption of sugars, polymers or surfactants still leads to substantial aggregation and particle-membrane interactions because of the poor affinity of these dispersants towards iron oxide [431, 452].

Alternatively, the colloidal stability and performance of iron oxide NPs in biological fluids can be drastically increased by the well-defined assembly of dispersants on the NP surface through covalently bound molecular anchors that have high affinity for the NP surface. Different strategies to sterically stabilize superparamagnetic iron oxid NPs by this modular and highly controlled buildup of core-shell structures have recently been described in a comprehensive review [431]. Dispersants that perform particularly well to individually stabilize iron oxide NPs are PEG-nitrocatechols. The high affinity nitrocatechol groups, including nitroDOPA and nitrodopamine, allow for an irreversible binding of dispersants to the iron oxide NP surface at extremely high packing density resulting in superior particle stabilization in terms of aggregation and membrane interaction [273, 443]. The use of individually stabilized iron oxide NPs would allow to closely control the magnetic loading of magnetoliposomes and their response to external magnetic fields, not only via the concentration of optimally dispersed MNPs in the liposome lumen, but also by the possibility of adjusting the core diameter and the dispersant shell thickness of the core-shell NPs [24]. However, the synthesis of such ultrastable core-shell MNPs is currently too expensive for the envisioned application in magnetoliposome-based absorbents for large-scale bioseparations. As mentioned in the introduction, this cost limita-

tion applies also to the direct use of core-shell MNPs functionalized with covalently attached affinity ligands [427, 428, 431] as magnetic absorbents in industrial applications, even though their superior colloidal and mechanical stability would allow for a high recyclability. Furthermore, it has to be noted that the use of free NPs of diameters $< 100\,\mathrm{nm}$ is currently not desired by the bioprocessing industries, especially the food and the feed industries.

5.4 Conclusions

Water-based magnetic nanofluids (MNFs) containing fatty acid bilayer stabilized, superparamagnetic iron oxide NPs were combined with liposomes with the aim of providing cost-effective and versatile MNP-functionalized liposomes for magnetic bioseparation applications.
The procedure used to encapsulate MNPs into the liposome lumen relied on passive encapsulation and involved four consecutive steps:

  (i) dispersion stabilization of the water-based MNFs,
 (ii) MLV formation by thin lipid film hydration in the water-based MNF,
(iii) MLV homogenization by the extrusion technique, and
(iv) separation of nonentrapped MNPs by size exclusion chromatography (SEC).

(i) Fatty acid bilayer stabilized iron oxide NPs in aqueous solution can be synthesized by chemical co-precipitation in large quantities and at low cost. However, the fatty acid bilayer coating is a very dynamic system that only reveals its full potential for electrostatic and steric NP stabilization under specific bulk solution conditions. The OA-OA and LA-LA bilayer coated MNPs used in this study were found to aggregate and precipitate in aqueous solution at bulk pH values $\lesssim 6$ and in the presence of buffer salts, including Tris, HEPES and sodium phosphate. Furthermore, dilution-induced desorption of fatty acids from the outer monolayer led to strong particle aggregation at particle volume fractions of $\phi < 10^{-4}\,\%$ and $\phi < 5 \times 10^{-3}\,\%$ in the OA-OA and LA-LA MNFs, respectively.
(ii) The use of water-based OA-OA and LA-LA MNFs under the established optimum dispersion conditions, that is in the absence of buffer salts and at $\phi > 10^{-2}\,\%$, allowed the formation of stable MLV suspensions by thin film hydration.

In spite of the optimized dispersion stability of fatty acid bilayer coated MNPs, the presence of MNP agglomerates in the obtained MLV composite suspensions was still apparent and obstructed the remaining process steps towards uniform and purified magnetoliposomes.

(iii) 15-30% of the initial MNP concentration was filtered out during sequential extrusion of the MLV composite suspensions 10 times through 400 nm pore membranes. Further extrusion of the obtained VET$_{400}$ composite suspensions through 200 nm pore membranes was not practicable. It resulted in extensive filter clogging and in an overall MNP loss of more than 50% after 10 extrusion cycles.

(iv) MNP loss was also observed after running the VET$_{400}$ composite suspensions through the SEC column. Furthermore, the elution profiles of the VET$_{400}$ fraction and of nonentrapped MNPs completely overlapped as a result of unsuccessful separation between magnetoliposomes and free particle agglomerates by SEC.

cryo-TEM investigations of the final magnetoliposome suspensions confirmed the presence of OA-OA and LA-LA MNPs in a predominantly aggregated form. Due to steric constraints, the MNP aggregates were mainly localized outside the liposomes resulting in poor encapsulation efficiency of fatty acid bilayer stabilized MNPs in nanometer-sized liposomes. The micrographs also revealed accumulation of OA-OA and LA-LA MNP aggregates at the outer surface of liposomes indicating interactions between fatty acid bilayer coated iron oxide NPs and phospholipid bilayers. While the VETs$_{400}$ formed in the OA-OA MNF were spherical in shape, the liposomes observed in the LA-LA composite had highly irregular equilibrium shapes following the integration of excess LA molecules in the vesicle membrane.

The assembly of fatty acid bilayer stabilized iron oxide NPs into pharmaceutical grade phospholipid vesicles was obviously not successful. Nevertheless, the results presented in this chapter demonstrate the importance of controlling the process-structure-property functions of both functional nanomaterials and vesicle carriers if they are to be combined in a functional composite, in which the structure and properties of each component are preserved (Fig. 1.1).

The stabilization of fatty acid monolayer coated iron oxide NPs in water by physisorption of an outer fatty acid monolayer typically results in the entrapment of multiple primary particles. Thereby, the control over the size of fatty acid bilayer coated MNP clusters, i.e. secondary particles, is already poor during MNP synthesis. As evidenced throughout the preparation steps of magnetoliposomes and in the final composite structure, fatty acid bilayer coated MNPs were prone to further agglomeration and to interactions with phospholipid bilayers. Ultimately, the poor steric stabilization of iron oxide NPs provided by the reversibly adsorbed fatty acid bilayer did not allow for the passive encapsulation of the MNPs into the liposome lumen. In the case of the MNF containing LA-LA bilayer stabilized MNPs, the combination of the MNF with liposomes did not preserve the structure and properties of liposomes in the composite suspension. Liposome deformation was induced by alterations in the composition and fluidity of the liposome membrane upon LA integration in the phospholipid bilayer.

To gain control over the assembly of MNPs into the aqueous domains of nanometer-

sized liposomes, the process-structure-property functions of fatty acid bilayer stabilized MNPs need to be better controlled in a first place. Different strategies for the steric stabilization of superparamagnetic iron oxide NPs have been discussed in this chapter to further exploit the potential of magnetoliposomes in magnetic bioseparation applications.

6 General conclusions and outlook

The aim of this work was to evaluate new design and process strategies to structure functionalized vesicles for applications in the food sector, in particular. In this regard, special emphasis was placed on food grade, scalable, and cost-effective vesicle and production systems. The main conclusions drawn from the experimental results of this study, their impact on possible applications, and some ideas for future research and developments in the field are summarized in the following paragraphs sorted by Chapters 3–5.

Edible polymersomes: Aiming at health promoting vesicle applications in functional foods, we have successfully formed food grade polymersomes using a new type of biocompatible and biodegradable PEO-*b*-PMCL diblock copolymer (Chapter 3). Despite the high molecular weight of the amphiphilic copolymer and the increased thickness of its bilayer membrane, the passive permeability barrier of PEO-*b*-PMCL vesicles towards encapsulated hydrophilic molecules has been found to be only slightly larger than that of their standard lipid analogues from POPC. At the same time, the presence of external bile salts at duodenal concentration induces a defined first-order release kinetic from loaded PEO-*b*-PMCL vesicles, whereas POPC vesicles are immediately disintegrated under concomitant loss of cargo. These release characteristics owe to the structural and physicochemical properties of the polymer and lipid vesicle bilayers. Compared to the highly ordered, densely packed, and fluid-like POPC bilayer with an aliphatic hydrocarbon core, the PEO-*b*-PMCL bilayer exhibits a lower packing density and an increased membrane rigidity due to polymer chain entanglement as well as a lower hydrophobicity of the polyether membrane core. Experimental evidence of the increased rigidity of thick-walled PEO-*b*-PMCL bilayers has also been obtained from electroformation experiments as PEO-*b*-PMCL vesicle membranes require higher ac electric field voltages to grow into GUVs and are more resistant to lateral fusion than POPC bilayers.

The edible and tough PEO-*b*-PMCL vesicles offer a very interesting carrier system for delivery-release applications of functional food components. Their controlled destabilization under duodenal stress conditions allows for a triggered cargo release close to the site of absorption, thereby increasing the bioavailability of the encapsulated agent. Furthermore, the rigid polymersome membrane is likely to resist high

mechanical stresses during optional integration of loaded PEO-*b*-PMCL vesicles into a food matrix and/or preparation of the functional food by the consumer.

To investigate this more specifically, PEO-*b*-PMCL vesicles should be loaded with a nutritionally relevant, active component and incorporated in a selected food matrix, e. g. a beverage. The osmotic, mechanical, and physicochemical vesicle stability in terms of load retention should then be studied through all steps of functional food production, storage, and preparation as well as during the passage through the GI tract to the target destination, i. e. the site of nutrient absorption in the small intestine. The delivery-release behavior of the PEO-*b*-PMCL carriers to the small intestine could be further optimized by taking advantage of the versatility of block copolymer chemistry and of the adjustability of vesicle membrane properties. Additional functions could be introduced, e. g. for specific targeting of the vesicle carrier to the small intestinal mucosa, triggered cargo release, and enhanced intestinal permeability, to maximize the absorption rate and bioavailability of the encapsulated agent. These concepts are also being explored in vesicle-based (oral) drug delivery applications [22, 23, 40, 157, 289]. The mechanical and rheological properties of the considered PEO-*b*-PMCL-based membranes could be measured on GUV model systems following our adjusted electroformation protocol and the experimental techniques referred to in Section 3.3.3.

With a view to industrial implementations, the PEO-*b*-PMCL molecules and their loaded polymersomes need to be produced in a highly controlled manner and at large scale, which is still a challenge. At the same time, both synthesis protocols should be optimized towards reduced formation of coexisting mixed morphologies and increased vesicle yield as well as encapsulation efficiency.

Dynamically enhanced vesicle extrusion: Based on the need of the pharmaceutical, cosmetic, and food industries for the controlled and gentle large-scale production of defined vesicle structures, the scalable process of dynamically enhanced vesicle extrusion has been introduced by designing and successfully putting the ROMER device into operation (Chapter 4).

Experimental ROMER results using 200-nm pore membranes gave valuable insight into the efficiency and mechanism for the breakup, i. e. homogenization, of lipid MLVs by static and dynamically enhanced vesicle extrusion. Large vesicles that are forced through narrow pore channels extensively break up by a pressure-induced rupture mechanism at the constriction of the pore entrance where the flow pattern is dominated by uniaxial elongation flows. Thereby, the extent of vesicle breakup is the same whether the entering vesicles encounter this constriction at the very entrance of cylindrical pore channels or in the center of biconical pore channels. Further vesicle breakup in the subsequent pore outflow and simple ROMER shear flow induced at the pore exit is only possible if the vesicles emerge from the pore

channel in a confined and deformed, i. e. pre-streched, state as supported by cylindrical pore channels. However, following the extensive vesicle breakup at the pore entrance, these shear-induced breakup criteria are only met for a small fraction of the extruded vesicle population. The structure of free-flowing vesicles exiting from biconical pore channels in a quasipherical, i. e. relaxed, state is not influenced by the ROMER shear flow.

As a consequence, dynamically enhanced MLV extrusion allows only a small additional decrease in mean vesicle size and lamellarity as a function of the applied shear rate if the linear shear forces act at the outlet of a cylindrical nanopore membrane. Because of the low efficiency of the ROMER shear flow for vesicle breakup at the pore exit, ROMER processing of MLV precursors does not overcome the heterogeneity of the initial self-assembly system after a single dynamically enhanced extrusion cycle. The obtained vesicle suspension is characterized by the presence of uni-, oligo-, and multilamellar vesicles, irrespective of the applied shear rate. We conclude that, in contrast to dynamically enhanced membrane emulsification, dynamically enhanced vesicle extrusion does not allow the controlled generation of homogeneous, unilamellar to n-multilamellar vesicles by adjusting the shear rate at the membrane outlet when working with spontaneously formed MLV pre-suspensions.

Further considerations of shear enhanced vesicle extrusion would certainly require the availability of more robust nanopore membranes with defined, straight-through pore channels. Micro engineering techniques are increasingly being used to design self-supporting membranes with highly defined pores in terms of size, position, and shape. However, the fabrication of mechanically stable nanopore membranes with pore diameters down to $\approx 400\,\text{nm}$ is highly sophisticated and still delicate [221]. Once $\approx 200\,\text{nm}$ pore membranes with a pronounced conical pore geometry are available, it would be interesting to test their performance in shear enhanced vesicle extrusion using the current ROMER device. Having the narrowest constriction of the pore channel at the pore exit would localize both the elongation- and shear-induced vesicle breakup towards the channel outlet. This could increase the efficiency of the ROMER shear flow in shearing off bilayer fragments which would then self-close to possibly form smaller, unilamellar vesicles. However, one has to bear in mind that this approach would still include the discontinuous and uncontrolled process step for the formation of self-assembled MLV pre-suspensions.

For the dynamically enhanced production of defined vesicle structures, it would be most advantageous to eliminate the preparation and use of heterogeneous MLV precursors altogether. One possibility to do so is to modify the ROMER device such that it allows the direct shearing off of bilayer sheets bending into the shear flow. Vesicle formation could then be combined with the simultaneous loading of an aqueous solution into the vesicle lumen with the internal solution forming the outward flow onto the bending bilayer and the external, cross-flowing medium detaching the vesicle. The feasibility of this principle has already been demonstrated

for the controlled formation of loaded GUVs in a microfluidic model setup [350].

Magnetoliposomes: With the aim of creating cost-effective and versatile magnetic absorbents for bioseparation applications, we considered fatty acid bilayer stabilized, superparamagnetic iron oxide NPs for encapsulation into the lumen of pharmaceutical grade phospholipid vesicles (Chapter 5).

Under optimum dispersion conditions of the fatty acid bilayer stabilized MNPs in water (pH $\approx$ 7-9, particle volume fraction $\phi > 10^{-2}\,\%$, absence of buffer salts), stable magnetic MLV suspensions can be obtained by thin film hydration in the MNP dispersion. However, the strong tendency of fatty acid bilayer stabilized MNPs to agglomerate and to interact with phospholipid bilayers hampers the subsequent homogenization of the MLV composite suspensions by extrusion through pore sizes $< 400\,$nm as well as the removal of nonentrapped particle agglomerates by SEC. For the same reason, fatty acid bilayer stabilized MNPs do not partition into the lumen of nanometer-sized liposomes following this method of passive MNP encapsulation. The experimental results suggest that the dynamic nature of the fatty acid bilayer coating and its reversible adsorption to the iron oxide particle surface do not provide the high steric stabilization of MNPs required for their controlled assembly into vesicles. It is concluded that the combination of fatty acid bilayer stabilized, superparamagnetic iron oxide NPs with phospholipid vesicles does not allow the successful preparation of MNP-functionalized liposomes in which the structure and property of each component is preserved. The latter is pivotal for further developments and applications of MNP-functionalized liposomes as versatile magnetic absorbents in bioseparation processes.

There is a number of alternative, reversibly adsorbed coating materials that have previously been used to sterically stabilize iron oxide NPs in aqueous medium, followed by encapsulation into the lumen of liposomes (see Sec. 5.3.4). Whereas substantial particle aggregation and particle-bilayer interactions is still an issue in many of these composite systems, citrate stabilized iron oxide NPs are currently the most established and reliable low cost, hydrophilic MNPs for the formation of magnetoliposomes by the passive encapsulation and extrusion methods [412, 413, 416, 421]. The protocol by Garnier *et al.* is especially advisable as it pays close attention to an optimal MNP dispersion during the synthesis of the water-based nanofluid. This allows the preparation of well defined magnetoliposomes with diameters down to 100 nm, high magnetic loading, and no contaminating external MNPs [413].

Since there is no need of an actual aqueous compartment within vesicle-based magnetic absorbents, magnetoliposomes for magnetic separations could also be prepared by tightly assembling a phospholipid bilayer around MNP clusters [410, 454, 455]. These simple synthesis protocols allow the use of hydrophobically coated MNPs dispersed in aqueous or organic medium and do not rely on high colloidal MNP sta-

bilization as opposed to the methods based on passive MNP encapsulation. They ensure a high magnetic loading, but probably at the expense of magnetoliposome unifomity.

Polymersomes would also be an interesting template for the design of vesicle-based magnetic absorbents. Due to their increased membrane thickness they could also accommodate hydrophobic superparamagnetic NPs within the vesicle membrane core, probably even in a clustered form [273, 447, 456]. As for the methods mentioned above, this would involve the generally easier synthesis and better stabilization of hydrophobic MNPs in organic solvents as opposed to water-based magnetic nano-fluids. Furthermore, the higher robustness of polymersomes would probably allow for an improved recyclability of polymersome-based magnetic absorbents compared to their lipid analogues. On the other hand, the surface of polymersome membranes is less ordered and defined than the outer hydrophilic head group layer of liposome membranes so that the former could primarily serve as ion-exchanger rather than for the presentation of affinity ligands on highly selective absorbents.

Summarizing, this thesis highlights the structural and functional versatility of vesicles as it studied new design and processing strategies in a nutritional (Chapter 3), large-scale processing (Chapter 4), and technological context (Chapter 5) for food, pharmaceutical, and cosmetic applications. The effectiveness of the considered vesicle formulations and processing technologies was evaluated according to their process-structure-property functions using a comprehensive set of characterization methods. Most of them involve simple measuring techniques that provide fast and reliable average results. They constitute a valuable toolbox for the further development and quality control of vesicle formulations and their production processes.

Bibliography

[1] Discher, D. E. and A. Eisenberg: *Polymer vesicles.* Science, 297:967–973, 2002.

[2] Israelachvili, J. N.: *Intermolecular and Surface Forces.* Academic Press, San Diego, CA, 3rd edition, 2011.

[3] Walde, P.: *Preparation of vesicles (liposomes).* In Nalwa, H. S. (editor), *Encyclopedia of Nanoscience and Nanotechnology*, volume 9, pp. 43–79. American Scientific Publishers, California, 2004.

[4] Kita-Tokarczyk, K., J. Grumelard, T. Haefele, and W. Meier: *Block copolymer vesicles – using concepts from polymer chemistry to mimic biomembranes.* Polymer, 46: 3540–3563, 2005.

[5] Walde, P., K. Cosentino, H. Engel, and P. Stano: *Giant vesicles: preparations and applications.* ChemBioChem, 11:848–865, 2010.

[6] Maherani, B., E. Arab-Tehrany, M. R. Mozafari, C. Gaiani, and M. Linder: *Liposomes: a review of manufacturing techniques and targeting strategies.* Current Nanoscience, 7:436–452, 2011.

[7] Lee, J. S. and J. Feijen: *Polymersomes for drug delivery: design, formation and characterization.* Journal of Controlled Release, 161:473–483, 2012.

[8] Abdelkader, H., A. W. G. Alani, and R. G. Alany: *Recent advances in non-ionic surfactant vesicles (niosomes): self-assembly, fabrication, characterization, drug delivery applications and limitations.* Drug Delivery, 21:87–100, 2014.

[9] Mayer, L. D., M. J. Hope, and P. R. Cullis: *Vesicles of variable sizes produced by a rapid extrusion procedure.* Biochimica et Biophysica Acta, 858:161–168, 1986.

[10] Engel, H., E. Rondeau, E. Windhab, and P. Walde: *External surface area determination of lipid vesicles using trinitrobenzene sulfonate and ultraviolet/visible spectrophotometry.* Analytical Biochemistry, 442:262–271, 2013.

[11] Needham, D. and R. S. Nunn: *Elastic deformation and failure of lipid bilayer membranes containing cholesterol.* Biophysical Journal, 58:997–1009, 1990.

[12] Discher, B. M., Y.-Y. Won, D. S. Ege, J. C.-M. Lee, F. S. Bates, D. E. Discher, and D. A. Hammer: *Polymersomes: tough vesicles made from diblock copolymers.* Science, 284:1143–1146, 1999.

[13] Olbrich, K., W. Rawicz, D. Needham, and E. Evans: *Water permeability and mechanical strength of polyunsaturated lipid bilayers.* Biophysical Journal, 79:321–327, 2000.

[14] Rawicz, W., K. C. Olbrich, T. McIntosh, D. Needham, and E. Evans: *Effect of chain length and unsaturation on elasticity of lipid bilayers.* Biophysical Journal, 79:328–339, 2000.

[15] Patty, P. J. and B. J. Frisken: *The pressure-dependence of the size of extruded vesicles.* Biophysical Journal, 85:996–1004, 2003.

[16] Discher, D. E. and F. Ahmed: *Polymersomes.* Annual Review of Biomedical Engineering, 8:323–341, 2006.

[17] Battaglia, G., A. J. Ryan, and S. Tomas: *Polymeric vesicle permeability: a facile chemical assay.* Langmuir, 22:4910–4913, 2006.

[18] Dimova, R., S. Aranda, N. Bezlyepkina, V. Nikolov, K. A. Riske, and R. Lipowsky: *A practical guide to giant vesicles. Probing the membrane nanoregime via optical microscopy.* Journal of Physics: Condensed Matter, 18:S1151–S1176, 2006.

[19] Shimanouchi, T., H. Ishii, N. Yoshimoto, H. Umakoshi, and R. Kuboi: *Calcein permeation across phosphatidylcholine bilayer membrane: effects of membrane fluidity, liposome size, and immobilization.* Colloids and Surfaces B - Biointerfaces, 73:156–160, 2009.

[20] Bangham, A. D. and R. W. Horne: *Negative staining of phospholipids and their structural modification by surface-active agents as observed in the electron microscope.* Journal of Molecular Biology, 8:660–668, 1964.

[21] Peer, D., J. M. Karp, S. Hong, O. C. Farokhzad, R. Margalit, and R. Langer: *Nanocarriers as an emerging platform for cancer therapy.* Nature Nanotechnology, 2:751–760, 2007.

[22] Meng, F., Z. Zhong, and J. Feijen: *Stimuli-responsive polymersomes for programmed drug delivery.* Biomacromolecules, 10:197–209, 2009.

[23] Sawant, R. R. and V. P. Torchilin: *Liposomes as 'smart' pharmaceutical nanocarriers.* Soft Matter, 6:4026–4044, 2010.

[24] Amstad, E. and E. Reimhult: *Nanoparticle actuated hollow drug delivery vehicles.* Nanomedicine, 7:145–164, 2012.

[25] Karlsson, M., M. Davidson, R. Karlsson, A. Karlsson, J. Bergenholtz, Z. Konkoli, A. Jesorka, T. Lobovkina, J. Hurtig, M. Voinova, and O. Orwar: *Biomimetic nanoscale reactors and networks.* Annual Review of Physical Chemistry, 55:613–649, 2004.

[26] Kim, K. T., S. A. Meeuwissen, R. J. M. Nolte, and J. C. M. van Hest: *Smart nanocontainers and nanoreactors.* Nanoscale, 2:844–858, 2010.

[27] Tanner, P., S. Egli, V. Balasubramanian, O. Onaca, C. G. Palivan, and W. Meier: *Can polymeric vesicles that confine enzymatic reactions act as simplified organelles?* FEBS Letters, 585:1699–1706, 2011.

[28] Bally, M., K. Bailey, K. Sugihara, D. Grieshaber, J. Vörös, and B. Städler: *Liposome and lipid bilayer arrays towards biosensing applications.* Small, 6:2481–2497, 2010.

[29] Connelly, J. T., S. Kondapalli, M. Skoupi, J. S. L. Parker, B. J. Kirby, and A. J. Baeumner: *Micro-total analysis system for virus detection: microfluidic pre-concentration coupled to liposome-based detection.* Analytical and Bioanalytical Chemistry, 402:315–323, 2012.

[30] Fattahi, H., S. Laurent, F. Liu, N. Arsalani, L. V. Elst, and R. N. Muller: *Magnetoliposomes as multimodal contrast agents for molecular imaging and cancer nanotheragnostics.* Nanomedicine, 6:529–544, 2011.

[31] Soenen, S. J., G. Vande Velde, A. Ketkar-Atre, U. Himmelreich, and M. De Cuyper: *Magnetoliposomes as magnetic resonance imaging contrast agents.* Wiley Interdisciplinary Reviews - Nanomedicine and Nanobiotechnology, 3:197–211, 2011.

[32] Walde, P.: *Building artificial cells and protocell models: experimental approaches with lipid vesicles.* Bioessays, 32:296–303, 2010.

[33] Kamat, N. P., J. S. Katz, and D. A. Hammer: *Engineering polymersome protocells.* Journal of Physical Chemistry Letters, 2:1612–1623, 2011.

[34] Kurihara, K., M. Tamura, K. Shohda, T. Toyota, K. Suzuki, and T. Sugawara: *Self-reproduction of supramolecular giant vesicles combined with the amplification of encapsulated DNA.* Nature Chemistry, 3:775–781, 2011.

[35] Torchilin, V. P.: *Recent advances with liposomes as pharmaceutical carriers.* Nature Reviews Drug Discovery, 4:145–160, 2005.

[36] Walde, P. and S. Ichikawa: *Enzymes inside lipid vesicles: preparation, reactivity and applications.* Biomolecular Engineering, 18:143–177, 2001.

[37] Soenen, S. J. H., M. Hodenius, and M. De Cuyper: *Magnetoliposomes: versatile innovative nanocolloids for use in biotechnology and biomedicine.* Nanomedicine, 4: 177–191, 2009.

[38] Igarashi, E.: *Factors affecting toxicity and efficacy of polymeric nanomedicines.* Toxicology and Applied Pharmacology, 229:121–134, 2008.

[39] Malam, Y., M. Loizidou, and A. M. Seifalian: *Liposomes and nanoparticles: nano-sized vehicles for drug delivery in cancer.* Trends in Pharmacological Sciences, 30: 592–599, 2009.

[40] Allen, T. M. and P. R. Cullis: *Liposomal drug delivery systems: from concept to clinical applications.* Advanced Drug Delivery Reviews, 65:36–48, 2013.

[41] Taylor, T. M., P. M. Davidson, B. D. Bruce, and J. Weiss: *Liposomal nanocapsules in food science and agriculture.* Critical Reviews in Food Science and Nutrition, 45: 587–605, 2005.

[42] Mozafari, M. R., C. Johnson, S. Hatziantoniou, and C. Demetzos: *Nanoliposomes and their applications in food nanotechnology.* Journal of Liposome Research, 18: 309–327, 2008.

[43] Keller, B. C.: *Liposomes in nutrition.* Trends in Food Science & Technology, 12: 25–31, 2001.

[44] McClements, D. J., E. A. Decker, Y. Park, and J. Weiss: *Structural design principles for delivery of bioactive components in nutraceuticals and functional foods.* Critical Reviews in Food Science and Nutrition, 49:577–606, 2009.

[45] Wagner, A. and K. Vorauer-Uhl: *Lipsosome technology for industrial purposes.* Journal of Drug Delivery, 2011:1–9, 2011.

[46] Tanford, C.: *The Hydrophobic Effect: Formation of Micelles and Biological Membranes.* Wiley, New York, 2nd edition, 1980.

[47] Holmberg, K., B. Jönsson, B. Kronberg, and B. Lindmann: *Surfactants and Polymers in Aqueous Solution.* John Wiley & Sons, Chichester, UK, 2nd edition, 2003.

[48] Evans, D. F. and H. Wennerström: *The Colloidal Domain: Where Physics, Chemistry, Biology, and Technology Meet.* Wiley-VCH, New York, 2nd edition, 1999.

[49] Garti, N., P. Somasundaran, and R. Mezzenga (editors): *Self-Assembled Supramolecular Architectures: Lyotropic Liquid Crystals.* Wiley, Hoboken, NJ, 2012.

[50] Mezzenga, R., P. Schurtenberger, A. Burbidge, and M. Michel: *Understanding foods as soft materials.* Nature Materials, 4:729–740, 2005.

[51] Battaglia, G. and A. J. Ryan: *Effect of amphiphile size on the transformation from a lyotropic gel to a vesicular dispersion.* Macromolecules, 39:798–805, 2006.

[52] Braun, J., N. Bruns, T. Pfohl, and W. Meier: *Phase behavior of vesicle-forming block copolymers in aqueous solutions.* Macromolecular Chemistry and Physics, 212: 1245–1254, 2011.

[53] Koynova, R. and B. Tenchov: *Transitions between lamellar and non-lamellar phases in membrane lipids and their physiological roles.* OA Biochemistry, 1:1–9, 2013.

[54] Koynova, R. and M. Caffrey: *Phases and phase transitions of the phosphatidylcholines.* Biochimica et Biophysica Acta - Reviews on Biomembranes, 1376:91–145, 1998.

[55] Helfrich, W.: *Lyotropic lamellar phases.* Journal of Physics: Condensed Matter, 6: A79–A92, 1994.

206

[56] Battaglia, G and AJ Ryan: *The evolution of vesicles from bulk lamellar gels*. Nature Materials, 4:869–876, 2005.

[57] Battaglia, G. and A. J. Ryan: *Pathways of polymeric vesicle formation*. Journal of Physical Chemistry B, 110:10272–10279, 2006.

[58] Hishida, M., H. Seto, N. L. Yamada, and K. Yoshikawa: *Hydration process of multi-stacked phospholipid bilayers to form giant vesicles*. Chemical Physics Letters, 455: 297–302, 2008.

[59] Jesorka, A. and O. Orwar: *Liposomes: technologies and analytical applications*. Annual Review of Analytical Chemistry, 1:801–832, 2008.

[60] Battaglia, G and AJ Ryan: *Bilayers and interdigitation in block copolymer vesicles*. Journal of the American Chemical Society, 127(24):8757–8764, JUN 22 2005.

[61] Lasic, D. D.: *Liposomes: From Physics to Applications*. Elsevier, Amsterdam, 1993.

[62] Lasic, D D: *Handbook of Nonmedical Applications of Liposomes*, volume 1–4. CRC Press, Boca Raton, 1996.

[63] Uchegbu, I. F. (editor): *Synthetic Surfactant Vesicles: Niosomes and Other Non-Phospholipid Vesicular Systems*. Harwood Academic Publishers, Australia, 2000.

[64] Blanazs, A., S. P. Armes, and A. J. Ryan: *Self-assembled block copolymer aggregates: from micelles to vesicles and their biological applications*. Macromolecular Rapid Communications, 30:267–277, 2009.

[65] LoPresti, C., H. Lomas, M. Massignani, T. Smart, and G. Battaglia: *Polymersomes: nature inspired nanometer sized compartments*. Journal of Materials Chemistry, 19: 3576–3590, 2009.

[66] Aranda-Espinoza, H., H. Bermudez, F. S. Bates, and D. E. Discher: *Electromechanical limits of polymersomes*. Physical Review Letters, 87:208301, 2001.

[67] Bermudez, H., A. K. Brannan, D. A. Hammer, F. S. Bates, and D. E. Discher: *Molecular weight dependence of polymersome membrane structure, elasticity, and stability*. Macromolecules, 35:8203–8208, 2002.

[68] Lee, J. C.-M., M. Santore, F. S. Bates, and D. E. Discher: *From membranes to melts, rouse to reptation: diffusion in polymersome versus lipid bilayers*. Macromolecules, 35:323–326, 2002.

[69] Döbereiner, H.-G.: *Properties of giant vesicles*. Current Opinion in Colloid & Interface Science, 5:256–263, 2000.

[70] Lasic, D. D.: *Giant vesicles: a historical introduction*. In Luisi, P. L. and P. Walde (editors), *Perspectives in Supramolecular Chemistry: Giant Vesicles*, volume 6, chapter 2, pp. 11–24. John Wiley & Sons, Chichester, 2000.

[71] Antonietti, M. and S. Förster: *Vesicles and liposomes: a self-assembly principle beyond lipids.* Advanced Materials, 15:1323–1333, 2003.

[72] Förster, S. and K. Borchert: *Polymer Vesicles*, pp. 1–52. Encyclopedia of Polymer Science and Technology. John Wiley & Sons, Inc., 2005.

[73] Seifert, U. and R. Lipowsky: *Morphology of vesicles.* In Lipowsky, R. and E Sackmann (editors), *Structure and Dynamics of Membranes*, volume 1 of *Handbook of Biological Physics*, chapter 8, pp. 403–463. North-Holland, 1995.

[74] Deschamps, J., V. Kantsler, and V. Steinberg: *Phase diagram of single vesicle dynamical states in shear flow.* Physical Review Letters, 102:118105, 2009.

[75] Mabrouk, E., D. Cuvelier, L.-L. Pontani, B. Xu, P. Lévy, D.and Keller, F. Brochard-Wyart, P. Nassoy, and M.-H. Li: *Formation and material properties of giant liquid crystal polymersomes.* Soft Matter, 5:1870–1878, 2009.

[76] Zupancich, J. A., F. S. Bates, and M. A. Hillmyer: *Aqueous dispersions of poly(ethylene oxide)-b-poly(γ-methyl-ϵ-caprolactone) block copolymers.* Macromolecules, 39:4286–4288, 2006.

[77] Malinova, V., S. Belegrinou, D. de Bruyn Ouboter, and W. P. Meier: *Biomimetic block copolymer membranes.* In Meier, W. P. and W. Knoll (editors), *Polymer membranes/Biomembranes*, volume 224 of *Advances in Polymer Science*, pp. 113–165. Springer-Verlag, Berlin Heidelberg, 2010.

[78] Kumar, M., M. Grzelakowski, J. Zilles, M. Clark, and W. Meier: *Highly permeable polymeric membranes based on the incorporation of the functional water channel protein Aquaporin Z.* Proceedings of the National Academy of Sciences of the United States of America, 104:20719–20724, 2007.

[79] Qi, W., P. P. Ghoroghchian, G. Li, D. A. Hammer, and M. J. Therien: *Aqueous self-assembly of poly(ethylene oxide)-block-poly(ε-caprolactone) (PEO-b-PCL) copolymers: disparate diblock copolymer compositions give rise to nano- and meso-scale bilayered vesicles.* Nanoscale, 5:10908–10915, 2013.

[80] Döbereiner, H.-G.: *Fluctuating vesicle shapes.* In Luisi, P. L. and P. Walde (editors), *Perspectives in Supramolecular Chemistry: Giant Vesicles*, volume 6, chapter 10, pp. 149–167. John Wiley & Sons, Chichester, 2000.

[81] Cevc, G.: *Material transport across permeability barriers by means of lipid vesicles.* In Lipowsky, R. and E. Sackmann (editors), *Structure and Dynamics of Membranes*, volume 1 of *Handbook of Biological Physics*, chapter 9, pp. 465–490. North-Holland, 1995.

[82] Heerklotz, H.: *Interactions of surfactants with lipid membranes.* Quarterly Reviews of Biophysics, 41:205–264, 2008.

[83] Deuling, H. J. and W. Helfrich: *The curvature elasticity of fluid membranes: a catalogue of vesicle shapes.* Journal de Physique, 37:1335–1345, 1976.

[84] Seifert, U., K. Berndl, and R. Lipowsky: *Shape transformations of vesicles: phase diagram for spontaneous-curvature and bilayer-coupling models.* Physical Review A, 44:1182–1202, 1991.

[85] Miao, L., U. Seifert, M. Wortis, and H.-G. D͗obereiner: *Budding transitions of fluid-bilayer vesicles: the effect of area-difference elasticity.* Physical Review E, 49:5389–5407, 1994.

[86] Svetina, S. and B. Žekš: *Membrane bending energy and shape determination of phospholipid vesicles and red blood cells.* European Biophysics Journal, 17:101–111, 1989.

[87] Kraus, M., W. Wintz, U. Seifert, and R. Lipowsky: *Fluid vesicles in shear flow.* Physical Review Letters, 77:3685–3688, 1996.

[88] Haas, K. H. de, C. Blom, D. van den Ende, M. H. G. Duits, and J. Mellema: *Deformation of giant lipid bilayer vesicles in shear flow.* Physical Review E, 56: 7132–7137, 1997.

[89] Seifert, U.: *Fluid membranes in hydrodynamic flow fields: formalism and an application to fluctuating quasispherical vesicles in shear flow.* European Physical Journal B, 8:405–415, 1999.

[90] Mader, M.-A., V. Vitkova, M. Abkarian, A. Viallat, and T. Podgorski: *Dynamics of viscous vesicles in shear flow.* European Physical Journal E, 19:389–397, 2006.

[91] Danker, G., C. Verdier, and C. Misbah: *Rheology and dynamics of vesicle suspension in comparison with droplet emulsion.* Journal of Non-Newtonian Fluid Mechanics, 152:156–167, 2008.

[92] Kaoui, B., A. Farutin, and C. Misbah: *Vesicles under simple shear flow: elucidating the role of relevant control parameters.* Physical Review E, 80:061905, 2009.

[93] Vlahovska, P. M., T. Podgorski, and C. Misbah: *Vesicles and red blood cells in flow: from individual dynamics to rheology.* Comptes Rendus Physique, 10:775–789, 2009.

[94] Lasic, D. D., R. Joannic, B. C. Keller, P. M. Frederik, and L. Auvray: *Spontaneous vesiculation.* Advances in Colloid and Interface Science, 89:337–349, 2001.

[95] Nakano, M., M. Fukuda, T. Kudo, N. Matsuzaki, T. Azuma, K. Sekine, H. Endo, and T. Handa: *Flip-flop of phospholipids in vesicles: kinetic analysis with time-resolved small-angle neutron scattering.* Journal of Physical Chemistry B, 113:6745–6748, 2009.

[96] Nichols, J. W.: *Thermodynamics and kinetics of phospholipid monomer-vesicle interaction.* Biochemistry, 24:6390–6398, 1985.

[97] Homan, R. and H. J. Pownall: *Transbilayer diffusion of phospholipids: dependence on headgroup structure and acyl chain length.* Biochimica Et Biophysica Acta, 938: 155–166, 1988.

[98] Kamp, J. A. F. Op den: *Lipid asymmetry in membranes.* Annual Review of Biochemistry, 48:47–71, 1979.

[99] Carlsen, A., N. Glaser, J.-F. Le Meins, and S. Lecommandoux: *Block copolymer vesicle permeability measured by osmotic swelling and shrinking.* Langmuir, 27: 4884–4890, 2011.

[100] Deamer, D. W. and J. Bramhall: *Permeability of lipid bilayers to water and ionic solutes.* Chemistry and Physics of Lipids, 40:167–188, 1986.

[101] Walter, A. and J. Gutknecht: *Permeability of small nonelectrolytes through lipid bilayer membranes.* Journal of Membrane Biology, 90:207–217, 1986.

[102] Thomae, A. V.: *Experimental and theoretical investigations on lipid bialyer permeation.* PhD thesis, ETH Zürich, 2007.

[103] Rodríguez-García, R., M. Mell, I. López-Montero, J. Netzel, T. Hellweg, and F. Monroy: *Polymersomes: smart vesicles of tunable rigidity and permeability.* Soft Matter, 7:1532–1542, 2011.

[104] Papahadjopoulos, D., K. Jacobson, S. Nir, and T. Isac: *Phase transitions in phospholipid vesicles. fluorescence polarization and permeability measurements concerning effect of temperature and cholesterol.* Biochimica et Biophysica Acta, 311:330–348, 1973.

[105] Bittman, R. and L. Blau: *The phospholipid-cholesterol interaction. kinetics of water permeability in liposomes.* Biochemistry, 11:4831–4839, 1972.

[106] Armstrong, V. T., M. R. Brzustowicz, S. R. Wassall, L. J. Jenski, and W. Stillwell: *Rapid flip-flop in polyunsaturated (docosahexaenoate) phospholipid membranes.* Archives of Biochemistry and Biophysics, 414:74–82, 2003.

[107] Mouritsen, O. G. and M. J. Zuckermann: *What's so special about cholesterol?* Lipids, 39:1101–1113, 2004.

[108] Bloom, M., E. Evans, and O. G. Mouritsen: *Physical properties of the fluid lipid-bilayer component of cell membranes: a perspective.* Quarterly Reviews of Biophysics, 24:293–397, 1991.

[109] Komatsu, H. and P. L.-G. Chong: *Low permeability of liposomal membranes composed of bipolar tetraether lipids from thermoacidophilic archaebacterium Sulfolobus acidocaldarius.* Biochemistry, 37:107–115, 1998.

[110] Mathai, J. C., S. Tristram-Nagle, J. F. Nagle, and M. L. Zeidel: *Structural determinants of water permeability through the lipid membrane.* The Journal of General Physiology, 131:69–76, 2008.

[111] Cevc, G.: *Membrane electrostatics.* Biochimica et Biophysica Acta - Reviews on Biomembranes, 1031:311–382, 1990.

[112] Barbet, J., P. Machy, A. Truneh, and L. D. Leserman: *Weak acid-induced release of liposome-encapsulated carboxyfluorescein.* Biochimica et Biophysica Acta, 772: 347–356, 1984.

[113] Gennis, R. B.: *Biomembranes: Molecular Structure and Function.* Springer Verlag, New York, 1989.

[114] Hauser, H., D. Oldani, and M. C. Phillips: *Mechanism of ion escape from phosphatidylcholine and phosphatidylserine single bilayer vesicles.* Biochemistry, 12: 4507–4517, 1973.

[115] Bai, Z., B. Zhao, and T. P. Lodge: *Bilayer membrane permeability of ionic liquid-filled block copolymer vesicles in aqueous solution.* Journal of Physical Chemistry B, 116:8282–8289, 2012.

[116] Clary, L., G. Verderone, C. Santaella, and P. Vierling: *Membrane permeability and stability of liposomes made from highly fluorinated double-chain phosphocholines derived from diaminopropanol, serine or ethanolamine.* Biochimica et Biophysica Acta - Biomembranes, 1328:55–64, 1997.

[117] Spulber, M., A. Najer, K. Winkelbach, O. Glaied, M. Waser, U. Pieles, W. Meier, and N. Bruns: *Photoreaction of a hydroxyalkyphenone with the membrane of polymersomes: a versatile method to generate semipermeable nanoreactors.* Journal of the American Chemical Society, 135:9204–9212, 2013.

[118] Garcia, A. M.: *Determination of ion permeability by fluorescence quenching.* Methods in Enzymology, 207:501–510, 1992.

[119] Bertrand, M. and B. Joós: *Extrusion of small vesicles through nanochannels: a model for experiments and molecular dynamics simulations.* Physical Review E, 85:051910, 2012.

[120] Dimova, R., K. A. Riske, S. Aranda, N. Bezlyepkina, R. L. Knorr, and R. Lipowsky: *Giant vesicles in electric fields.* Soft Matter, 3:817–827, 2007.

[121] Aranda, S., K. A. Riske, R. Lipowsky, and R. Dimova: *Morphological transitions of vesicles induced by alternating electric fields.* Biophysical Journal, 95:L19–L21, 2008.

[122] Evans, E. and D. Needham: *Physical properties of surfactant bilayer membranes: thermal transitions, elasticity, rigidity, cohesion, and colloidal interactions.* Journal of Physical Chemistry, 91:4219–4228, 1987.

[123] Dimova, R., U. Seifert, B. Pouligny, S. Förster, and H.-G. Döbereiner: *Hyperviscous diblock copolymer vesicles.* European Physical Journal E, 7:241–250, 2002.

[124] Merkel, R., E. Sackmann, and E. Evans: *Molecular friction and epitactic coupling between monolayers in supported bilayers.* Journal de Physique, 50:1535–1555, 1989.

[125] Seifert, U.: *The concept of effective tension for fluctuating vesicles.* Zeitschrift für Physik B, 97:299–309, 1995.

[126] Gradzielski, M.: *Vesicles and vesicle gels – structure and dynamics of formation.* Journal of Physics: Condensed Matter, 15:R655–R697, 2003.

[127] Méléard, P., C. Gerbeaud, T. Pott, L. Fernandez-Puente, I. Bivas, M. D. Mitov, J. Dufourcq, and P. Bothorel: *Bending elasticities of model membranes: influences of temperature and sterol content.* Biophysical Journal, 72:2616–2629, 1997.

[128] Arriaga, L. R., I. López-Montero, F. Monroy, G. Orts-Gil, B. Farago, and T. Hellweg: *Stiffening effect of cholesterol on disordered lipid phases: a combined neutron spin echo + dynamic light scattering analysis of the bending elasticity of large unilamellar vesicles.* Biophysical Journal, 96:3629–3637, 2009.

[129] Kučerka, N., Y. Liu, N. Chu, H. I. Petrache, S. Tristram-Nagle, and J. F. Nagle: *Structure of fully hydrated fluid phase DMPC and DLPC lipid bilayers using X-ray scattering from oriented multilamellar arrays and from unilamellar vesicles.* Biophysical Journal, 88:2626–2637, 2005.

[130] Dimova, R.: *Recent developments in the field of bending rigidity measurements on membranes.* Advances in Colloid and Interface Science, 208:225–234, 2014.

[131] Marsh, D.: *Elastic curvature constants of lipid monolayers and bilayers.* Chemistry and Physics of Lipids, 144:146–159, 2006.

[132] Henriksen, J., A. C. Rowat, E. Brief, Y. W. Hsueh, J. L. Thewalt, M. J. Zuckermann, and J. H. Ipsen: *Universal behavior of membranes with sterols.* Biophysical Journal, 90:1639–1649, 2006.

[133] Keough, K. M. W. and N. Kariel: *Differential scanning calorimetric studies of aqueous dispersions of phosphatidylcholines containing two polyenoic chains.* Biochimica et Biophysica Acta, 902:11–18, 1987.

[134] Henriksen, J., A. C. Rowat, and J. H. Ipsen: *Vesicle fluctuation analysis of the effects of sterols on membrane bending rigidity.* European Biophysics Journal with Biophysics Letters, 33:732–741, 2004.

[135] Lee, J. C.-M., H. Bermudez, B. M. Discher, Y.-Y. Sheehan, M. A .and Won, F. S. Bates, and D. E. Discher: *Preparation, stability, and in vitro performance of vesicles made with diblock copolymers.* Biotechnology and Bioengineering, 73:135–145, 2001.

[136] Trollsås, M., M. A. Kelly, H. Claesson, R. Siemens, and J. L. Hedrick: *Highly branched block copolymers: design, synthesis, and morphology.* Macromolecules, 32:4917–4924, 1999.

[137] Liang, X. M., G. Z. Mao, and K. Y. S. Ng: *Mechanical properties and stability measurement of cholesterol-containing liposome on mica by atomic force microscopy.* Journal of Colloid and Interface Science, 278:53–62, 2004.

[138] Anglin, T. C. and J. C. Conboy: *Kinetics and thermodynamics of flip-flop in binary phospholipid membranes measured by sum-frequency vibrational spectroscopy.* Biochemistry, 48:10220–10234, 2009.

[139] Seu, K. J., L. R. Cambrea, R. M. Everly, and J. S. Hovis: *Influence of lipid chemistry on membrane fluidity: tail and headgroup interactions.* Biophysical Journal, 91: 3727–3735, 2006.

[140] New, R. R. C. In New, R. R. C. (editor), *Liposomes: A Practical Approach*, pp. 105–160. Oxford University Press, New York, 1990.

[141] Manojlovic, V., K. Winkler, V. Bunjes, A. Neub, R. Schubert, B. Bugarski, and G. Leneweit: *Membrane interactions of ternary phospholipid/cholesterol bilayers and encapsulation efficiencies of a RIP II protein.* Colloids and Surfaces B - Biointerfaces, 64:284–296, 2008.

[142] Torchilin, V. P. and V. Weissig: *Liposomes: A Practical Approach.* Oxford University Press, New York, 2nd edition, 2003.

[143] Larsson, K.: *Lipids: Molecular Organization, Physical Functions and Technical Applications.* The Oily Press, Dundee, Scotland, UK, 1994.

[144] Bergenståhl, B. and K. Fontell: *Phase equilibria in the system soybean lecithin/water.* Progress in Colloid and Polymer Science, 68:48–52, 1983.

[145] Thompson, A. K., J. P. Hindmarsh, D. Haisman, T. Rades, and H. Singh: *Comparison of the structure and properties of liposomes prepared from milk fat globule membrane and soy phospholipids.* Journal of Agricultural and Food Chemistry, 54: 3704–3711, 2006.

[146] Zhou, Y., C. K. Berry, P. A. Storer, and R. M. Raphael: *Peroxidation of polyunsaturated phosphatidyl-choline lipids during electroformation.* Biomaterials, 28:1298–1306, 2007.

[147] Kunimoto, M., K. Inoue, and S. Nojima: *Effect of ferrous ion and ascorbate-induced lipid peroxidation on liposomal membranes.* Biochimica et Biophysica Acta - Biomembranes, 646:169–178, 1981.

[148] Chatterjee, S. N. and S. Agarwal: *Liposomes as membrane model for study of lipid peroxidation.* Free Radical Biology and Medicine, 4:51–72, 1988.

[149] Litman, B. J.: *Lipid model membranes. Characterization of mixed phospholipid vesicles.* Biochemistry, 12:2545–2554, 1973.

[150] Olson, F., C. A Hunt, F. C. Szoka, W. J. Vail, and D. Papahadjopoulos: *Preparation of liposomes of defined size distribution by extrusion through polycarbonate membranes.* Biochimica et Biophysica Acta, 557:9–23, 1979.

[151] Zhang, L. and A. Eisenberg: *Multiple morphologies of "crew-cut" aggregates of polystyrene-b-poly(acrylic acid) block copolymers.* Science, 268:1728–1731, 1995.

[152] Holder, S. J., R. C. Hiorns, N. A. J. M. Sommerdijk, S. J. Williams, R. G. Jones, and R. J. M. Nolte: *The first example of a poly(ethylene oxide)-poly(methylphenylsilane) amphiphilic block copolymer: vesicle formation in water.* Chemical Communications, (14):1445–1446, 1998.

[153] Broz, P., S. Driamov, J. Ziegler, N. Ben-Haim, S. Marsch, W. Meier, and P. Hunziker: *Toward intelligent nanosize bioreactors: a pH-switchable, channel-equipped, functional polymer nanocontainer.* Nano Letters, 6:2349–2353, 2006.

[154] Onaca, O., R. Enea, D. W. Hughes, and W. Meier: *Stimuli-responsive polymersomes as nanocarriers for drug and gene delivery.* Macromolecular Bioscience, 9:129–139, 2009.

[155] Pata, V., F. Ahmed, D. E. Discher, and N. Dan: *Membrane solubilization by detergent: resistance conferred by thickness.* Langmuir, 20:3888–3893, 2004.

[156] Lodge, T. P. and M. C. Dalvi: *Mechanisms of chain diffusion in lamellar block copolymers.* Physical Review Letters, 75:657–660, 1995.

[157] Li, M.-H. and P. Keller: *Stimuli-responsive polymer vesicles.* Soft Matter, 5:927–937, 2009.

[158] Pawar, P. V., S. V. Gohil, J. P. Jain, and N. Kumar: *Functionalized polymersomes for biomedical applications.* Polymer Chemistry, 4:3160–3176, 2013.

[159] Róg, T., M. Pasenkiewicz-Gierula, I. Vattulainen, and M. Karttunen: *Ordering effects of cholesterol and its analogues.* Biochimica et Biophysica Acta - Biomembranes, 1788:97–121, 2009.

[160] Mannock, D. A., R. N. A. H. Lewis, T. P. W. McMullen, and R. N. McElhaney: *The effect of variations in phospholipid and sterol structure on the nature of lipid-sterol interactions in lipid bilayer model membranes.* Chemistry and Physics of Lipids, 163:403–448, 2010.

[161] Harroun, T. A., J. Katsaras, and S. R. Wassall: *Cholesterol hydroxyl group is found to reside in the center of a polyunsaturated lipid membrane.* Biochemistry, 45:1227–1233, 2006.

[162] Huang, J.: *Exploration of molecular interactions in cholesterol superlattices: effect of multibody interactions.* Biophysical Journal, 83:1014–1025, 2002.

[163] Urbina, J. A., S. Pekerar, H.-B. Le, J. Patterson, B. Montez, and E Oldfield: *Molecular order and dynamics of phosphatidylcholine bilayer membranes in the presence of cholesterol, ergosterol and lanosterol: a comparative study using ^{2}H-, ^{13}C- and ^{31}P-NMR spectroscopy.* Biochimica et Biophysica Acta - Biomembranes, 1238:163–176, 1995.

[164] Kučerka, N., J. Pencer, M.-P. Nieh, and J. Katsaras: *Influence of cholesterol on the bilayer properties of monounsaturated phosphatidylcholine unilamellar vesicles.* European Physical Journal E, 23:247–254, 2007.

[165] Miao, L., M. Nielsen, J. Thewalt, J. H. Ipsen, M. Bloom, M. J. Zuckermann, and O. G. Mouritsen: *From lanosterol to cholesterol: structural evolution and differential effects on lipid bilayers.* Biophysical Journal, 82:1429–1444, 2002.

[166] Schreier-Muccillo, S., D. Marsh, H. Dugas, H. Schneider, and I. C.P. Smith: *A spin probe study of the influence of cholesterol on motion and orientation of phospholipids in oriented multibilayers and vesicles.* Chemistry and Physics of Lipids, 10:11–27, 1973.

[167] Marsh, D. and I. C.P. Smith: *An interacting spin label study of the fluidizing and condensing effects of cholesterol on lecithin bilayers.* Biochimica et Biophysica Acta - Biomembranes, 298:133–144, 1973.

[168] Marsh, D.: *Liquid-ordered phases induced by cholesterol: a compendium of binary phase diagrams.* Biochimica et Biophysica Acta - Biomembranes, 1798:688–699, 2010.

[169] Feigenson, G. W.: *Phase diagrams and lipid domains in multicomponent lipid bilayer mixtures.* Biochimica et Biophysica Acta - Biomembranes, 1788:47–52, 2009.

[170] Carruthers, A. and D. L. Melchior: *Studies of the relationship between bilayer water permeability and bilayer physical state.* Biochemistry, 22:5797–5807, 1983.

[171] Zocher, F., D. van der Spoel, P. Pohl, and J. S. Hub: *Local partition coefficients govern solute permeability of cholesterol-containing membranes.* Biophysical Journal, 105:2760–2770, 2013.

[172] Moreno, M. J., L. M. B. B. Estronca, and W. L. C. Vaz: *Translocation of phospholipids and dithionite permeability in liquid-ordered and liquid-disordered membranes.* Biophysical Journal, 91:873–881, 2006.

[173] Endress, E.and Bayerl, S., K. Prechtel, C. Maier, and T. M. Merkel, R.and Bayerl: *The effect of cholesterol, lanosterol, and ergosterol on lecithin bilayer mechanical properties at molecular and microscopic dimensions: a solid-state NMR and micropipet study.* Langmuir, 18:3293–3299, 2002.

[174] Brown, M. F., R. L. Thurmond, S. W. Dodd, D. Otten, and K. Beyer: *Elastic deformation of membrane bilayers probed by deuterium NMR relaxation.* Journal of the American Chemical Society, 124:8471–8484, 2002.

[175] Smaby, J. M., M. M. Momsen, H. L. Brockman, and R. E. Brown: *Phosphatidylcholine acyl unsaturation modulates the decrease in interfacial elasticity induced by cholesterol.* Biophysical Journal, 73:1492–1505, 1997.

[176] Treyer, M., P. Walde, and T. Oberholzer: *Permeability enhancement of lipid vesicles to nucleotides by use of sodium cholate: basic studies and application to an enzyme-catalyzed reaction occurring inside the vesicles.* Langmuir, 18:1043–1050, 2002.

[177] Cevc, G.: *Transfersomes.* In Rathbone, M. J., J. Hadgraft, and M. S. Roberts (editors), *Modified-Release Drug Delivery Technology*, volume 1, chapter 44, pp. 533–546. Informa Healthcare, New York: Marcel Dekker, 2nd edition, 2003.

[178] Paternostre, M.-T., M. Roux, and J.-L. Rigaud: *Mechanisms of membrane protein insertion into liposomes during reconstitution procedures involving the use of detergents. 1. Solubilization of large unilamellar liposomes (prepared by reverse-phase evaporation) by Triton X-100, octyl glucoside, and sodium cholate.* Biochemistry, 27:2668–2677, 1988.

[179] Lichtenberg, D., H. Ahyayauch, and F. M. Goñi: *The mechanism of detergent solubilization of lipid bilayers.* Biophysical Journal, 105:289–299, 2013.

[180] Almgren, M.: *Mixed micelles and other structures in the solubilization of bilayer lipid membranes by surfactants.* Biochimica et Biophysica Acta - Biomembranes, 1508:146–163, 2000.

[181] Elsayed, M. M. A. and G. Cevc: *The vesicle-to-micelle transformation of phospholipid-cholate mixed aggregates: a state of the art analysis including membrane curvature effects.* Biochimica et Biophysica Acta - Biomembranes, 1808:140–153, 2011.

[182] Maza, A. de la and J. L. Parra: *Vesicle to micelle phase transitions involved in the interaction of sodium cholate with phosphatidylcholine liposomes.* Colloids and Surfaces A - Physicochemical and Engineering Aspects, 127:125–134, 1997.

[183] Simões, S. I., C. M. Marques, M. E. M. Cruz, G. Cevc, and M. B. F. Martins: *The effect of cholate on solubilisation and permeability of simple and protein-loaded phosphatidylcholine/sodium cholate mixed aggregates designed to mediate transdermal delivery of macromolecules.* European Journal of Pharmaceutics and Biopharmaceutics, 58:509–519, 2004.

[184] Stuart, M. C. A. and E. J. Boekema: *Two distinct mechanisms of vesicle-to-micelle and micelle-to-vesicle transition are mediated by the packing parameter of phospholipid–detergent systems.* Biochimica et Biophysica Acta - Biomembranes, 1768:2681–2689, 2007.

[185] Pantaler, E., D. Kamp, and C. W.M Haest: *Acceleration of phospholipid flip-flop in the erythrocyte membrane by detergents differing in polar head group and alkyl chain length.* Biochimica et Biophysica Acta - Biomembranes, 1509:397–408, 2000.

[186] Wachter, C., U. Vierl, and G. Cevc: *Adaptability and elasticity of the mixed lipid bilayer vesicles containing non-ionic surfactant designed for targeted drug delivery across the skin.* Journal of Drug Targeting, 16:611–625, 2008.

[187] Evans, E., W. Rawicz, and A. F. Hofmann: *Lipid bilayer expansion and mechanical disruption in solutions of water-soluble bile acid.* In Hofmann, A. F., G. Paumgartner, and A. Stiehl (editors), *Bile Acids in Gastroenterology: Basic and Clinical*

Advances, volume 80 of *Falk Symposium*, pp. 59–68, Dordrecht, Netherlands, 1995. Kluwer Academic Publisher.

[188] Cevc, G., A. G. Schätzlein, H. Richardsen, and U. Vierl: *Overcoming semipermeable barriers, such as the skin, with ultradeformable mixed lipid vesicles, transfersomes, liposomes, or mixed lipid micelles.* Langmuir, 19:10753–10763, 2003.

[189] Cevc, G.: *Lipid vesicles and other colloids as drug carriers on the skin.* Advanced Drug Delivery Reviews, 56:675–711, 2004.

[190] Pabst, G., M. Rappolt, H. Amenitsch, and P. Laggner: *Structural information from multilamellar liposomes at full hydration: full q-range fitting with high quality X-ray data.* Physical Review E, 62:4000–4009, 2000.

[191] Shimanouchi, T., H. Umakoshi, and R. Kuboi: *Kinetic study on giant vesicle formation with electroformation method.* Langmuir, 25:4835–4840, 2009.

[192] Lasic, D. D.: *The mechanism of vesicle formation.* Biochemical Journal, 256:1–11, 1988.

[193] Mui, B. and M. J. Hope: *Formation of large unilamellar vesicles by extrusion.* In Gregoriadis, G. (editor), *Liposome Technology*, volume 1, chapter 4, pp. 55–65. Informa Healthcare, New York, 3rd edition, 2006.

[194] Lichtenberg, D. and Y. Barenholz: *Liposomes: preparation, characterization, and preservation.* Methods of Biochemical Analysis, 33:337–462, 1988.

[195] Woodbury, D. J., E. S. Richardson, A. W. Grigg, R. D. Welling, and B. H. Knudson: *Reducing liposome size with ultrasound: bimodal size distributions.* Journal of Liposome Research, 16:57–80, 2006.

[196] Yamaguchi, T., M. Nomura, T. Matsuoka, and S. Koda: *Effects of frequency and power of ultrasound on the size reduction of liposome.* Chemistry and Physics of Lipids, 160:58–62, 2009.

[197] Hamilton, R. L., J. Goerke, L. S. S. Guo, M. C. Williams, and R. J. Havel: *Unilamellar liposomes made with the french pressure cell: a simple preparative and semiquantitative technique.* Journal of Lipid Research, 21:981–992, 1980.

[198] Brandl, M., M. Drechsler, D. Bachmann, C. Tardi, M. Schmidtgen, and K.-H. Bauer: *Preparation and characterization of semi-solid phospholipid dispersions and dilutions thereof.* International Journal of Pharmaceutics, 170:187–199, 1998.

[199] Brandl, M., D. Bachmann, M. Drechsler, and K. H. Bauer: *Liposome preparation by a new high pressure homogenizer Gaulin Micron Lab 40.* Drug Development and Industrial Pharmacy, 16:2167–2191, 1990.

[200] Bachmann, D., M. Brandl, and G. Gregoriadis: *Preparation of liposomes using a Mini-Lab 8.30 H high-pressure homogenizer.* International Journal of Pharmaceutics, 91:69–74, 1993.

[201] Barnadas-Rodríguez, R. and M. Sabés: *Factors involved in the production of liposomes with a high-pressure homogenizer.* International Journal of Pharmaceutics, 213:175–186, 2001.

[202] Sorgi, F. L. and L. Huang: *Large scale production of DC-Chol cationic liposomes by microfluidization.* International Journal of Pharmaceutics, 144:131–139, 1996.

[203] Nongonierma, A. B., M. Abrlova, M. A. Fenelon, and K. N. Kilcawley: *Evaluation of two food grade proliposomes to encapsulate an extract of a commercial enzyme preparation by microfluidization.* Journal of Agricultural and Food Chemistry, 57: 3291–3297, 2009.

[204] Gruber, H. J. and H. Schindler: *External surface and lamellarity of lipid vesicles: a practice-oriented set of assay methods.* Biochimica et Biophysica Acta - Biomembranes, 1189:212–224, 1994.

[205] Mayer, L. D., M. J. Hope, P. R. Cullis, and A. S. Janoff: *Solute distributions and trapping efficiencies observed in freeze-thawed multilamellar vesicles.* Biochimica et Biophysica Acta, 817:193–196, 1985.

[206] Hope, M. J., M. B. Bally, G. Webb, and P. R. Cullis: *Production of large unilamellar vesicles by a rapid extrusion procedure. Characterization of size distribution, trapped volume and ability to maintain a membrane potential.* Biochimica Et Biophysica Acta, 812:55–65, 1985.

[207] Northern Lipids Inc. (Burnaby, BC, Canada). http://www.northernlipids.com.

[208] Hunter, D. G. and B. J. Frisken: *Effect of extrusion pressure and lipid properties on the size and polydispersity of lipid vesicles.* Biophysical Journal, 74:2996–3002, 1998.

[209] Frisken, B. J., C. Asman, and P. J. Patty: *Studies of vesicle extrusion.* Langmuir, 16:928–933, 2000.

[210] CPL SACHSE (Berlin, Germany). www.cpl-sachse.de.

[211] Schneider, T., A. Sachse, G. Rössling, and M. Brandl: *Large-scale production of liposomes of defined size by a new continuous high pressure extrusion device.* Drug Development and Industrial Pharmacy, 20:2787–2807, 1994.

[212] Berger, N., A. Sachse, J. Bender, R. Schubert, and M. Brandl: *Filter extrusion of liposomes using different devices: comparison of liposome size, encapsulation efficiency, and process characteristics.* International Journal of Pharmaceutics, 223: 55–68, 2001.

[213] Avestin Inc. (Ottawa, ON, Canada). www.avestin.com.

[214] Avanti Polar Lipids Inc. (Alabaster, AL, USA). www.avantilipids.com.

[215] MacDonald, R. C., R. I. MacDonald, B. Ph.M. Menco, K. Takeshita, N. K. Subbarao, and L.-R. Hu: *Small-volume extrusion apparatus for preparation of large, unilamellar vesicles.* Biochimica et Biophysica Acta - Biomembranes, 1061:297–303, 1991.

[216] Mui, B., L. Chow, and M. J. Hope: *Extrusion technique to generate liposomes of defined size.* Methods in Enzymology, 367:3–14, 2003.

[217] Kölchens, S., V. Ramaswami, J. Birgenheier, L. Nett, and D. F. O'Brien: *Quasi-elastic light-scattering determination of the size distribution of extruded vesicles.* Chemistry and Physics of Lipids, 65:1–10, 1993.

[218] Fröhlich, M., V. Brecht, and R. Peschka-Süss: *Parameters influencing the determination of liposome lamellarity by ^{31}P-NMR.* Chemistry and Physics of Lipids, 109: 103–112, 2001.

[219] Schmiedel, H., L. Almásy, and G. Klose: *Multilamellarity, structure and hydration of extruded POPC vesicles by SANS.* European Biophysics Journal with Biophysics Letters, 35:181–189, 2006.

[220] Holzapfel, S., E. Rondeau, P. Mühlich, and E. J. Windhab: *Drop detachment from a micro-engineered membrane surface in a dynamic membrane emulsification process.* Chemical Engineering & Technology, 36:1785–1794, 2013.

[221] Holzapfel, S.: *Dynamically enhanced membrane emulsification using micro engineered membranes with controlled surface properties.* PhD thesis, ETH Zürich, 2013.

[222] Angelova, M. I. and D. S. Dimitrov: *Liposome electroformation.* Faraday Discussions, 81:303–311, 1986.

[223] Angelova, M. and D. S. Dimitrov: *A mechanism of liposome electroformation.* In Degiorgio, V. (editor), *Trends in Colloid and Interface Science II*, volume 76 of *Progress in Colloid & Polymer Science*, pp. 59–67. Steinkopff, 1988.

[224] Dimitrov, D. S. and M. I. Angelova: *Lipid swelling and liposome formation mediated by electric fields.* Bioelectrochemistry and Bioenergetics, 19:323–336, 1988.

[225] Bagatolli, L. A.: *To see or not to see: lateral organization of biological membranes and fluorescence microscopy.* Biochimica et Biophysica Acta - Biomembranes, 1758: 1541–1556, 2006.

[226] Bucher, P., A. Fischer, P. L. Luisi, T. Oberholzer, and P. Walde: *Giant vesicles as biochemical compartments: the use of microinjection techniques.* Langmuir, 14: 2712–2721, 1998.

[227] Angelova, M. I.: *Liposome electroformation.* In Luisi, P. L. and P. Walde (editors), *Perspectives in Supramolecular Chemistry: Giant Vesicles*, volume 6, chapter 3, pp. 26–36. John Wiley & Sons, Chichester, 2000.

[228] Angelova, M. I., S. Soléau, P. Méléard, J. F. Faucon, and P. Bothorel: *Preparation of giant vesicles by external AC electric fields. kinetics and applications.* In Helm, C., M. Losche, and H. Mohwald (editors), *Trends in Colloid and Interface Science VI*, volume 89 of *Progress in Colloid and Polymer Science*, pp. 127–131, Berlin, 1992. Dr Dietrich Steinkopff Verlag.

[229] Estes, D. J. and M. Mayer: *Electroformation of giant liposomes from spin-coated films of lipids.* Colloids and Surfaces B - Biointerfaces, 42:115–123, 2005.

[230] Mathivet, L., S. Cribier, and P. F. Devaux: *Shape change and physical properties of giant phospholipid vesicles prepared in the presence of an ac electric field.* Biophysical Journal, 70:1112–1121, 1996.

[231] Salipante, P. F., R. L. Knorr, R. Dimova, and P. M. Vlahovska: *Electrodeformation method for measuring the capacitance of bilayer membranes.* Soft Matter, 8:3810–3816, 2012.

[232] Lomas, H., M. Massignani, K. A. Abdullah, I. Canton, C. Lo Presti, S. MacNeil, J. Du, A. Blanazs, J. Madsen, S. P. Armes, A. L. Lewis, and G. Battaglia: *Non-cytotoxic polymer vesicles for rapid and efficient intracellular delivery.* Faraday Discussions, 139:143–159, 2008.

[233] Reiner, J. E., J. M. Wells, R. B. Kishore, C. Pfefferkorn, and K. Helmerson: *Stable and robust polymer nanotubes stretched from polymersomes.* Proceedings of the National Academy of Sciences of the United States of America, 103:1173–1177, 2006.

[234] Vriezema, D. M., A. Kros, R. de Gelder, J. J. L. M. Cornelissen, A. E. Rowan, and R. J. M. Nolte: *Electroformed giant vesicles from thiophene-containing rod–coil diblock copolymers.* Macromolecules, 37:4736–4739, 2004.

[235] Khalifat, N., N. Puff, S. Bonneau, J.-B. Fournier, and M. I. Angelova: *Membrane deformation under local pH gradient: mimicking mitochondrial cristae dynamics.* Biophysical Journal, 95:4924–4933, 2008.

[236] Menger, F. M. and M. I. Angelova: *Giant vesicles: imitating the cytological processes of cell membranes.* Accounts of Chemical Research, 31:789–797, 1998.

[237] Bagatolli, L. A., T. Parasassi, and E. Gratton: *Giant phospholipid vesicles: comparison among the whole lipid sample characteristics using different preparation methods – a two photon fluorescence microscopy study.* Chemistry and Physics of Lipids, 105: 135–147, 2000.

[238] Wick, R., M. I. Angelova, P. Walde, and P. L. Luisi: *Microinjection into giant vesicles and light microscopy investigation of enzyme-mediated vesicle transformations.* Chemistry & Biology, 3:105–111, 1996.

[239] Holopainen, J. M., M. Angelova, and P. K. J. Kinnunen: *Giant liposomes in studies on membrane domain formation.* Methods in Enzymology, 367:15–23, 2003.

[240] García-Sáez, A. J. and P. Schwille: *Fluorescence correlation spectroscopy for the study of membrane dynamics and protein/lipid interactions.* Methods, 46:116–122, 2008.

[241] Peterlin, P., Arrigler. V., H. Diamant, and E Haleva: *Permeability of phospholipid membrane for small polar molecules determined from osmotic swelling of giant phospholipid vesicles.* Advances in Planar Lipid Bilayers and Liposomes, 16:301–335, 2012.

[242] Clerc, S. G. and T.E. Thompson: *A possible mechanism for vesicle formation by extrusion.* Biophysical Journal, 67:475–476, 1994.

[243] Apel, P.: *Track etching technique in membrane technology.* Radiation Measurements, 34:559–566, 2001.

[244] Apel, P. Yu., I. V. Blonskaya, S. N. Dmitriev, O. L. Orelovitch, and B. Sartowska: *Structure of polycarbonate track-etch membranes: origin of the "paradoxical" pore shape.* Journal of Membrane Science, 282:393–400, 2006.

[245] Bruinsma, R.: *Rheology and shape transitions of vesicles under capillary flow.* Physica A, 234:249–270, 1996.

[246] Richardson, R.: *Scattering and Reflection Techniques*, chapter 12, pp. 228–254. Blackwell Publishing, 2009.

[247] Hallett, F. R., J. Watton, and P. Krygsman: *Vesicle sizing: number distributions by dynamic light scattering.* Biophysical Journal, 59:357–362, 1991.

[248] Egelhaaf, S. U, E. Wehrli, M. Müller, M. Adrian, and P. Schurtenberger: *Determination of the size distribution of lecithin liposomes: a comparative study using freeze fracture, cryoelectron microscopy and dynamic light scattering.* Journal of Microscopy, 184:214–228, 1996.

[249] Jin, A. J., D. Huster, K. Gawrisch, and R. Nossal: *Light scattering characterization of extruded lipid vesicles.* European Biophysics Journal with Biophysics Letters, 28: 187–199, 1999.

[250] Frisken, B. J.: *Revisiting the method of cumulants for the analysis of dynamic light-scattering data.* Applied Optics, 40:4087–4091, 2001.

[251] Maulucci, G., M. De Spirito, G. Arcovito, F. Boffi, A. C. Castellano, and G. Briganti: *Particle size distribution in DMPC vesicles solutions undergoing different sonication times.* Biophysical Journal, 88:3545–3550, 2005.

[252] Patty, P. J .and Frisken, B. J.: *Direct determination of the number-weighted mean radius and polydispersity from dynamic light-scattering data.* Applied Optics, 45: 2209–2216, 2006.

[253] Pecora, R. (editor): *Dynamic Light Scattering: Applications of Photon Correlation Spectroscopy.* Plenum Press, New York, 1985.

[254] Chu, B.: *Laser Light Scattering: Basic Principles and Practice.* Academic Press, Boston, 2nd edition, 1991.

[255] Berne, J. B. and R. Pecora: *Dynamic Light Scattering: With Applications to Chemistry, Biology and Physics.* Dover Publications, Mineola, N. Y. 2nd edition, 2000.

[256] Schätzel, K.: *Single-photon correlation techniques.* In Brown, W. (editor), *Dynamic Light Scattering: The Method and Some Applications*, pp. 76–148. Oxford University, Oxford, UK, 1993.

[257] De Jaeger, N., H. Demeyere, R. Finsy, R. Sneyers, J. Vanderdeelen, P. van der Meeren, and M. van Laethem: *Particle sizing by photon correlation spectroscopy. Part I: Monodisperse lattices: influence of scattering angle and concentration of dispersed material.* Particle & Particle Systems Characterization, 8:179–186, 1991.

[258] Stepanek, P.: *Data analysis in dynamic light scattering.* In Brown, W. (editor), *Dynamic Light Scattering: The Method and Some Applications*, pp. 177–240. Oxford University, Oxford, UK, 1993.

[259] Koppel, D. E.: *Analysis of macromolecular polydispersity in intensity correlation spectroscopy: The method of cumulants.* Journal of Chemical Physics, 57:4814–4820, 1972.

[260] Morrison, I. D., E. F. Grabowski, and C. A. Herb: *Improved techniques for particle size determination by quasi-elastic light scattering.* Langmuir, 1:496–501, 1985.

[261] Pike, E.R., D. Watson, and F. M. Watson: *Analysis of polydisperse scattering data II.* In Dahneke, B. E. (editor), *Measurement of Suspended Particles by Quasi-Elasitc Light Scattering*, pp. 107–128. Wiley, New York, 1983.

[262] Provencher, S. W.: *CONTIN: A general purpose constrained regularization program for inverting noisy linear algebraic and integral equations.* Computer Physics Communications, 27:229–242, 1982.

[263] Finsy, R. and N. De Jaeger: *Particle sizing by photon correlation spectroscopy. Part II: Average values.* Particle & Particle Systems Characterization, 8:187–193, 1991.

[264] Mie, G.: *Articles on the optical characteristics of turbid tubes, especially colloidal metal solutions.* Annalen der Physik, 25:377–445, 1908.

[265] Wiscombe, W. J.: *Improved mie scattering algorithms.* Applied Optics, 19:1505–1509, 1980.

[266] Strawbridge, K. B. and F. R. Hallett: *Polydisperse Mie theory applied to hollow latex spheres: an integrated light-scattering study.* Canadian Journal of Physics, 70: 401–406, 1992.

[267] Heberle, F. A., J. Pan, R. F. Standaert, P. Drazba, N. Kučerka, and J. Katsaras: *Model-based approaches for the determination of lipid bilayer structure from small-angle neutron and X-ray scattering data.* European Biophysics Journal with Biophysics Letters, 41:875–890, 2012.

[268] Lemmich, J., K. Mortensen, J. H. Ipsen, T. Hønger, R. Bauer, and O. G. Mouritsen: *Small-angle neutron scattering from multilamellar lipid bilayers: theory, model, and experiment.* Physical Review E, 53:5169–5180, 1996.

[269] Balgavý, P., M. Dubničková, N. Kučerka, M. A. Kiselev, S. P. Yaradaikin, and D. Uhríková: *Bilayer thickness and lipid interface area in unilamellar extruded 1,2-diacylphosphatidylcholine liposomes: a small-angle neutron scattering study.* Biochimica et Biophysica Acta - Biomembranes, 1512:40–52, 2001.

[270] Pencer, J., M.-P. Nieh, T. A. Harroun, S. Krueger, C. Adams, and J. Katsaras: *Bilayer thickness and thermal response of dimyristoylphosphatidylcholine unilamellar vesicles containing cholesterol, ergosterol and lanosterol: a small-angle neutron scattering study.* Biochimica et Biophysica Acta - Biomembranes, 1720:84–91, 2005.

[271] Kučerka, N., M. A. Kiselev, and P. Balgavý: *Determination of bilayer thickness and lipid surface area in unilamellar dimyristoylphosphatidylcholine vesicles from small-angle neutron scattering curves: a comparison of evaluation methods.* European Biophysics Journal with Biophysics Letters, 33:328–334, 2004.

[272] Kiselev, M. A., E. V. Zemlyanaya, V. K. Aswal, and R. H. H. Neubert: *What can we learn about the lipid vesicle structure from the small-angle neutron scattering experiment?* European Biophysics Journal with Biophysics Letters, 35:477–493, 2006.

[273] Amstad, E., J. Kohlbrecher, E. Müller, T. Schweizer, M. Textor, and E. Reimhult: *Triggered release from liposomes through magnetic actuation of iron oxide nanoparticle containing membranes.* Nano Letters, 11:1664–1670, 2011.

[274] Kučerka, N., D. Uhríková, J. Teixeira, and P. Balgavý: *Bilayer thickness in unilamellar phosphatidylcholine vesicles: small-angle neutron scattering using contrast variation.* Physica B - Condensed Matter, 350:E639–E642, 2004.

[275] Kučerka, N., J. Gallová, D. Uhríková, P. Balgavý, M. Bulacu, S.-J. Marrink, and J. Katsaras: *Areas of monounsaturated diacylphosphatidylcholines.* Biophysical Journal, 97:1926–1932, 2009.

[276] Pencer, J., T. Mills, V. Anghel, S. Krueger, R. M. Epand, and J. Katsaras: *Detection of submicron-sized raft-like domains in membranes by small-angle neutron scattering.* European Physical Journal E, 18:447–458, 2005.

[277] Pan, J., F. A. Heberle, R. S. Petruzielo, and J. Katsaras: *Using small-angle neutron scattering to detect nanoscopic lipid domains.* Chemistry and Physics of Lipids, 170: 19–32, 2013.

[278] Devaux, P. F., P. Fellmann, and P. Hervé: *Investigation on lipid asymmetry using lipid probes: comparison between spin-labeled lipids and fluorescent lipids.* Chemistry and Physics of Lipids, 116:115–134, 2002.

[279] Hope, M. J., T. E. Redelmeier, K. F. Wong, W. Rodrigueza, and P. R. Cullis: *Phospholipid asymmetry in large unilamellar vesicles induced by transmembrane pH gradients.* Biochemistry, 28:4181–4187, 1989.

[280] McIntyre, J. C. and R. G. Sleight: *Fluorescence assay for phospholipid membrane asymmetry.* Biochemistry, 30:11819–11827, 1991.

[281] Cayot, P. and G. Tainturier: *The quantification of protein amino groups by the trinitrobenzenesulfonic acid method: a reexamination.* Analytical Biochemistry, 249: 184–200, 1997.

[282] Grotzky, A., Y. Manaka, S. Fornera, M. Willeke, and P. Walde: *Quantification of α-polylysine: a comparison of four UV/Vis spectrophotometric methods.* Analytical Methods, 2:1448–1455, 2010.

[283] Barenholz, Y., D. Gibbes, B. J. Litman, J. Goll, T. E. Thompson, and F. D. Carlson: *Simple method for the preparation of homogeneous phospholipid vesicles.* Biochemistry, 16:2806–2810, 1977.

[284] Nordlund, J. R., C. F. Schmidt, S. N. Dicken, and T. E. Thompson: *Transbilayer distribution of phosphatidylethanolamine in large and small unilamellar vesicles.* Biochemistry, 20:3237–3241, 1981.

[285] Williams, E. E., J. A. Cooper, W. Stillwell, and L. J. Jenski: *The curvature and cholesterol content of phospholipid bilayers alter the transbilayer distribution of specific molecular species of phosphatidylethanolamine.* Molecular Membrane Biology, 17:157–164, 2000.

[286] Cevc, G and G Blume: *New, highly efficient formulation of diclofenac for the topical, transdermal administration in ultradeformable drug carriers, transfersomes.* Biochimica et Biophysica Acta - Biomembranes, 1514:191–205, 2001.

[287] Cevc, G. and U. Vierl: *Nanotechnology and the transdermal route. A state of the art review and critical appraisal.* Journal of Controlled Release, 141:277–299, 2010.

[288] Surnar, B. and M. Jayakannan: *Stimuli-responsive poly(caprolactone) vesicles for dual drug delivery under the gastrointestinal tract.* Biomacromolecules, 14:4377–4387, 2013.

[289] Al-Hilal, T. A., F. Alam, and Y. Byun: *Oral drug delivery systems using chemical conjugates or physical complexes.* Advanced Drug Delivery Reviews, 65:845–864, 2013.

[290] German, J. B., A. M. Zivkovic, D. C. Dallas, and J. T. Smilowitz: *Nutrigenomics and personalized diets: what will they mean for food?* Annual Review of Food Science and Technology, 2:97–123, 2011.

[291] Ghoroghchian, P. P., G. Li, D. H. Levine, K. P. Davis, F. S. Bates, D. A. Hammer, and M. J. Therien: *Bioresorbable vesicles formed through spontaneous self-assembly of amphiphilic poly(ethylene oxide)-block-polycaprolactone.* Macromolecules, 39: 1673–1675, 2006.

[292] Rajagopal, K., A. Mahmud, D. A. Christian, J. D. Pajerowski, A. E. X. Brown, S. M. Loverde, and D. E. Discher: *Curvature-coupled hydration of semicrystalline polymer amphiphiles yields flexible worm micelles but favors rigid vesicles: polycaprolactone-based block copolymers.* Macromolecules, 43:9736–9746, 2010.

[293] Vangeyte, P., B. Leyh, M. Heinrich, J. Grandjean, C. Bourgaux, and R. Jérôme: *Self-assembly of poly(ethylene oxide)-b-poly(ε-caprolactone) copolymers in aqueous solution.* Langmuir, 20:8442–8451, 2004.

[294] Vangeyte, P., S. Gautier, and R. Jérôme: *About the methods of preparation of poly(ethylene oxide)-b-poly(ε-caprolactone) nanoparticles in water. analysis by dynamic light scattering.* Colloids and Surfaces A - Physicochemical and Engineering Aspects, 242:203–211, 2004.

[295] Petersen, M. A., L. Yin, E. Kokkoli, and M. A. Hillmyer: *Synthesis and characterization of reactive PEO-PMCL polymersomes.* Polymer Chemistry, 1:1281–1290, 2010.

[296] Benachir, T. and M. Lafleur: *Study of vesicle leakage induced by melittin.* Biochimica et Biophysica Acta - Biomembranes, 1235:452–460, 1995.

[297] Ueno, K., T. Imamura, and K. L. Cheng: *Handbook of organic anlytical reagents.* CRC Press, 2nd edition, 1992.

[298] Stewart, J. C. M.: *Colorimetric determination of phospholipids with ammonium ferrothiocyanate.* Analytical Biochemistry, 104:10–14, 1980.

[299] Marcotte, L., J. Barbeau, and M. Lafleur: *Permeability and thermodynamics study of quaternary ammonium surfactants—phosphocholine vesicle system.* Journal of Colloid and Interface Science, 292:219–227, 2005.

[300] Kučerka, N., S. Tristram-Nagle, and J. F. Nagle: *Structure of fully hydrated fluid phase lipid bilayers with monounsaturated chains.* Journal of Membrane Biology, 208:193–202, 2005.

[301] Allen, T. M. and L. G. Cleland: *Serum-induced leakage of liposome contents.* Biochimica et Biophysica Acta, 597(2):418–426, 1980.

[302] Allen, T. M.: *Calcein as a tool in liposome methodology.* In Gregoriadis, G. (editor), *Liposome Technology*, volume 3, pp. 177–182. CRC Press, Boca Raton, FL, 1984.

[303] Benachir, T. and M. Lafleur: *Osmotic and pH transmembrane gradients control the lytic power of melittin.* Biophysical Journal, 70:831–840, 1996.

[304] Kaszuba, M., D. McKnight, M. T. Connah, F. K. McNeil-Watson, and U. Nobb-mann: *Measuring sub nanometre sizes using dynamic light scattering.* Journal of Nanoparticle Research, 10:823–829, 2008.

[305] Sommer, K.: *40 years of presentation particle size distributions – Yet still incorrect?* Particle & Particle Systems Characterization, 18:22–25, 2001.

[306] Beck, P.: *Magnetic field assisted biomaterials processing.* PhD thesis, ETH Zürich, 2009.

[307] Jain, S. and F. S. Bates: *Consequences of nonergodicity in aqueous binary PEO-PB micellar dispersions.* Macromolecules, 37:1511–1523, 2004.

[308] Schmitt, A. L., M. H. Repollet-Pedrosa, and M. K. Mahanthappa: *Polydispersity-driven block copolymer amphiphile self-assembly into prolate-spheroid micelles.* ACS Macro Letters, 1:300–304, 2012.

[309] Yu, K. and A. Eisenberg: *Multiple morphologies in aqueous solutions of aggregates of polystyrene-block-poly(ethylene oxide) diblock copolymers.* Macromolecules, 29: 6359–6361, 1996.

[310] Won, Y.-Y., A. K. Brannan, H. T. Davis, and F. S. Bates: *Cryogenic transmission electron microscopy (cryo-TEM) of micelles and vesicles formed in water by poly(ethylene oxide)-based block copolymers.* Journal of Physical Chemistry B, 106: 3354–3364, 2002.

[311] Jain, S. and F. S. Bates: *On the origins of morphological complexity in block copolymer surfactants.* Science, 300:460–464, 2003.

[312] Won, Y.-Y., H. T. Davis, and F. S. Bates: *Molecular exchange in PEO-PB micelles in water.* Macromolecules, 36:953–955, 2003.

[313] Hayward, R. C. and D. J. Pochan: *Tailored assemblies of block copolymers in solution: it is all about the process.* Macromolecules, 43:3577–3584, 2010.

[314] Napoli, A., M. Valentini, N. Tirelli, M. Müller, and J. A. Hubbell: *Oxidation-responsive polymeric vesicles.* Nature Materials, 3:183–189, 2004.

[315] Cerritelli, S., D. Velluto, and J. A. Hubbell: *PEG-SS-PPS: reduction-sensitive disulfide block copolymer vesicles for intracellular drug delivery.* Biomacromolecules, 8: 1966–1972, 2007.

[316] Sato, T., M. Kijima, Y. Shiga, and Y. Yonezawa: *Photochemically controlled ion permeability of liposomal membranes containing amphiphilic azobenzene.* Langmuir, 7:2330–2335, 1991.

[317] Straubinger, R. M., K. Hong, D. S. Friend, and D. Papahadjopoulos: *Endocytosis of liposomes and intracellular fate of encapsulated molecules: encounter with a low pH compartment after internalization in coated vesicles.* Cell, 32:1069–1079, 1983.

[318] Silvander, M., M. Johnsson, and K. Edwards: *Effects of PEG-lipids on permeability of phosphatidylcholine/cholesterol liposomes in buffer and in human serum.* Chemistry and Physics of Lipids, 97:15–26, 1998.

[319] Chen, P.-Y., D. Pearce, and A. S. Verkman: *Membrane water and solute permeability determined quantitatively by self-quenching of an entrapped fluorophore.* Biochemistry, 27:5713–5718, 1988.

[320] Gier, J. de: *Osmotic behavior and permeability properties of liposomes.* Chemistry and Physics of Lipids, 64:187–196, 1993.

[321] Bramhall, J.: *Electrostatic forces control the penetration of membranes by charged solutes.* Biochimica et Biophysica Acta, 778:393–399, 1984.

[322] Nardin, C., S. Thoeni, J. Widmer, M. Winterhalter, and W. Meier: *Nanoreactors based on (polymerized) ABA-triblock copolymer vesicles.* Chemical Communications, 15:1433–1434, 2000.

[323] Choucair, A., P. L. Soo, and A. Eisenberg: *Active loading and tunable release of doxorubicin from block copolymer vesicles.* Langmuir, 21:9308–9313, 2005.

[324] Mayer, L. D., M. B. Bally, M. J. Hope, and P. R. Cullis: *Uptake of antineoplastic agents into large unilamellar vesicles in response to a membrane potential.* Biochimica et Biophysica Acta, 816:294–302, 1985.

[325] Wu, J. and A. Eisenberg: *Proton diffusion across membranes of vesicles of poly(styrene-b-acrylic acid) diblock copolymers.* Journal of the American Chemical Society, 128:2880–2884, 2006.

[326] Diamond, J. M. and Y. Katz: *Interpretation of nonelectrolyte partition coefficients between dimyristoyl lecithin and water.* Journal of Membrane Biology, 17:121–154, 1974.

[327] Stein, W. D.: *Kinetics of the multidrug transporter (P-glycoprotein) and its reversal.* Physiological Reviews, 77:545–590, 1997.

[328] Frézard, F., C. Santaella, P. Vierling, and J. G. Riess: *Permeability and stability in buffer and in human serum of fluorinated phospholipid-based liposomes.* Biochimica et Biophysica Acta - Biomembranes, 1192:61–70, 1994.

[329] Fischer, A., T. Oberholzer, and P. L. Luisi: *Giant vesicles as models to study the interactions between membranes and proteins.* Biochimica et Biophysica Acta - Biomembranes, 1467:177–188, 2000.

[330] Zangenberg, N. H., A. Müllertz, H. G. Kristensen, and L. Hovgaard: *A dynamic in vitro lipolysis model. I. Controlling the rate of lipolysis by continuous addition of calcium.* European Journal of Pharmaceutical Sciences, 14:115–122, 2001.

[331] Hur, S. J., B. O. Lim, E. A. Decker, and D. J. McClements: *In vitro human digestion models for food applications.* Food Chemistry, 125:1–12, 2011.

[332] Holm, R., A. Müllertz, and H. Mu: *Bile salts and their importance for drug absorption.* International Journal of Pharmaceutics, 453:44–55, 2013.

[333] Kragh-Hansen, U., M. le Maire, and J. V. Møller: *The mechanism of detergent solubilization of liposomes and protein-containing membranes.* Biophysical Journal, 75:2932–2946, 1998.

[334] Holopainen, J. M., M. I. Angelova, T. Söderlund, and P. K. J. Kinnunen: *Macroscopic consequences of the action of phospholipase C on giant unilamellar liposomes.* Biophysical Journal, 83:932–943, 2002.

[335] Eissa, A. M., M. J. P. Smith, A. Kubilis, J. A. Mosely, and N. R. Cameron: *Polymersome-forming amphiphilic glycosylated polymers: synthesis and characterization.* Journal of Polymer Science Part A - Polymer Chemistry, 51:5184–5193, 2013.

[336] Howse, J. R., R. A. L. Jones, G. Battaglia, R. E. Ducker, G. J. Leggett, and A. J. Ryan: *Templated formation of giant polymer vesicles with controlled size distributions.* Nature Materials, 8:507–511, 2009.

[337] Foster, T., K. D. Dorfman, and H. T. Davis: *Giant biocompatible and biodegradable PEG-PMCL vesicles and microcapsules by solvent evaporation from double emulsion droplets.* Journal of Colloid and Interface Science, 351:140–150, 2010.

[338] Lorenceau, E., A. S. Utada, D. R. Link, G. Cristobal, M. Joanicot, and D. A. Weitz: *Generation of polymerosomes from double-emulsions.* Langmuir, 21:9183–9186, 2005.

[339] Shum, H. C., J.-W. Kim, and D. A. Weitz: *Microfluidic fabrication of monodisperse biocompatible and biodegradable polymersomes with controlled permeability.* Journal of the American Chemical Society, 130:9543–9549, 2008.

[340] Shum, H. C., D. Lee, I. Yoon, T. Kodger, and D. A. Weitz: *Double emulsion templated monodisperse phospholipid vesicles.* Langmuir, 24:7651–7653, 2008.

[341] Monnard, P.-A., N. Berclaz, K. Conde-Frieboes, and T. Oberholzer: *Decreased solute entrapment in 1-palmitoyl-2-oleoyl-sn-glycero-3-phosphocholine liposomes prepared by freeze/thaw in the presence of physiological amounts of monovalent salts.* Langmuir, 15:7504–7509, 1999.

[342] Juliano, R. L. and D. Stamp: *The effect of particle size and charge on the clearance rates of liposomes and liposome encapsulated drugs.* Biochemical and Biophysical Research Communications, 63:651–658, 1975.

[343] Litzinger, D. C., A. M. J. Buiting, N. van Rooijen, and L. Huang: *Effect of liposome size on the circulation time and intraorgan distribution of amphipathic poly(ethylene glycol)-containing liposomes.* Biochimica et Biophysica Acta - Biomembranes, 1190:99–107, 1994.

[344] Allen, T. M. and P. R. Cullis: *Drug delivery systems: entering the mainstream.* Science, 303:1818–1822, 2004.

[345] Martin, F. J.: *Pharmaceutical manufacturing of liposomes.* In Tyle, P. (editor), *Specialized Drug Delivery Systems: Manufacturing and Production Technology*, pp. 267–316. Marcel Dekker, New York, 1990.

[346] McClements, D. J.: *Food Emulsions: Principles, Practices, and Techniques*, chapter 6. CRC Press, 2nd edition, 2004.

[347] Barnadas-Rodríguez, R. and M. X. Sabés: *Liposomes prepared by high-pressure homogenizers.* Methods in Enzymology, 367:28–46, 2003.

[348] Schadler, V. and E. J. Windhab: *Continuous membrane emulsification by using a membrane system with controlled pore distance.* Desalination, 189:130–135, 2006.

[349] Feigl, K., F. X. Tanner, and E. J. Windhab: *Numerical investigation of the formation and detachment of droplets from pores in a shear flow field.* AIP Conference Proceedings, 1281:1684–1687, 2010.

[350] Ota, S., S. Yoshizawa, and S. Takeuchi: *Microfluidic formation of monodisperse, cell-sized, and unilamellar vesicles.* Angewandte Chemie - International Edition, 48: 6533–6537, 2009.

[351] Cevc, G.: *Phospholipids Handbook*, pp. 939–956. Marcel Dekker, 1993.

[352] Bartlett, G. R.: *Phosphorus assay in column chromatography.* Journal of Biological Chemistry, 234:466–468, 1959.

[353] Ishikawa, T., H. Sakakibara, and K. Oiwa: *The architecture of outer dynein arms in situ.* Journal of Molecular Biology, 368:1249–1258, 2007.

[354] Frühwirth, T., G. Fritz, N. Freiberger, and O. Glatter: *Structure and order in lamellar phases determined by small-angle scattering.* Journal of Applied Crystallography, 37:703–710, 2004.

[355] Kohlbrecher, J.: *Software package sasfit for fitting small-angle scattering curves.* https://kur.web.psi.ch/sans1/SANSSoft/sasfit.html, 2014.

[356] Wimley, W. C. and T. E. Thompson: *Transbilayer and interbilayer phospholipid exchange in dimyristoylphosphatidylcholine/dimyristoylphosphatidylethanolamine large unilamellar vesicles.* Biochemistry, 30:1702–1709, 1991.

[357] Vries, A. H. de, A. E. Mark, and S. J. Marrink: *The binary mixing behavior of phospholipids in a bilayer: a molecular dynamics study.* Journal of Physical Chemistry B, 108:2454–2463, 2004.

[358] Edwards, K., M. Johnsson, G. Karlsson, and M. Silvander: *Effect of polyethyleneglycol-phospholipids on aggregate structure in preparations of small unilamellar liposomes.* Biophysical Journal, 73:258–266, 1997.

[359] Subczynski, W. K. and A. Wisniewska: *Physical properties of lipid bilayer membranes: relevance to membrane biological functions.* Acta Biochimica Polonica, 47: 613–625, 2000.

[360] Fleischer, R. L., R. B. Price, and R. M. Walker: *Nuclear Tracks in Solids: Principles and Applications.* University of California Press, Berkeley, CA, 1975.

[361] Zhu, Z., Y. Maekawa, H. Koshikawa, Y. Suzuki, N. Yonezawa, and M. Yoshida: *Role of UV light illumination and DMF soaking in production of PET ion track membranes.* Nuclear Instruments & Methods in Physics Research Section B - Beam Interactions with Materials and Atoms, 217:449–456, 2004.

[362] Mukaibo, H., L. P. Horne, D. Park, and C. R. Martin: *Controlling the length of conical pores etched in ion-tracked poly(ethylene terephthalate) membranes.* Small, 5:2474–2479, 2009.

[363] Sartowska, B., W. Starosta, P. Apel, O. Orelovitch, and I. Blonskaya: *Polymeric track etched membranes – application for advanced porous structures formation.* Acta Physica Polonica A, 123:819–821, 2013.

[364] Apel, P. Y., Y. E. Korchev, Z. Siwy, R. Spohr, and M. Yoshida: *Diode-like single-ion track membrane prepared by electro-stopping.* Nuclear Instruments & Methods in Physics Research Section B - Beam Interactions with Materials and Atoms, 184: 337–346, 2001.

[365] Patil, Y. P., A. K. Ahluwalia, and S. Jadhav: *Isolation of giant unilamellar vesicles from electroformed vesicle suspensions and their extrusion through nano-pores.* Chemistry and Physics of Lipids, 167:1–8, 2013.

[366] Marmottant, P., T. Biben, and S. Hilgenfeldt: *Deformation and rupture of lipid vesicles in the strong shear flow generated by ultrasound-driven microbubbles.* Proceedings of the Royal Society A - Mathematical Physical and Engineering Sciences, 464:1781–1800, 2008.

[367] Hatfield, R. M. and L. W.-M. Fung: *Molecular properties of a stratum corneum model lipid system: large unilamellar vesicles.* Biophysical Journal, 68:196–207, 1995.

[368] Kučerka, N., J. Pencer, J. N. Sachs, J. F. Nagle, and J. Katsaras: *Curvature effect on the structure of phospholipid bilayers.* Langmuir, 23:1292–1299, 2007.

[369] Risselada, H. J. and S. J. Marrink: *Curvature effects on lipid packing and dynamics in liposomes revealed by coarse grained molecular dynamics simulations.* Physical Chemistry Chemical Physics, 11:2056–2067, 2009.

[370] Guinier, A. J.: *X-ray diffraction at small angles.* Annales de Physique, 12:161–237, 1939.

[371] Porod, G.: *Die Abhängigkeit der Röntgenkleinwinkelstreuung von Form und Grösse der kolloiden Teilchen in verdünnten Systemen, IV.* Acta Physica Austriaca, 2: 255–292, 1948.

[372] Pabst, G., R. Koschuch, B. Pozo-Navas, M. Rappolt, K. Lohner, and P. Laggner: *Structural analysis of weakly ordered membrane stacks.* Journal of Applied Crystallography, 36:1378–1388, 2003.

[373] Hosemann, R. and S. N. Bagchi: *Direct Analysis of Diffraction by Matter.* North-Holland Publishing Company, Amsterdam, 1962.

[374] Guinier, A. J.: *X-Ray Diffraction: In Crystals, Imperfect crystals, and Amorphous Bodies.* Freeman, San Francisco, 1963.

[375] Nagle, J. F. and S. Tristram-Nagle: *Structure of lipid bilayers.* Biochimica et Biophysica Acta - Reviews on Biomembranes, 1469:159–195, 2000.

[376] Yazdani, A. and P. Bagchi: *Three-dimensional numerical simulation of vesicle dynamics using a front-tracking method.* Physical Review E, 85:056308, 2012.

[377] Benson, H. A. E.: *Elastic liposomes for topical and transdermal drug delivery.* In Weissig, V. (editor), *Liposomes*, volume 605 of *Methods in Molecular Biology*, chapter 4, pp. 77–86. Humana Press, 2010.

[378] Cevc, G., A. Schätzlein, and H. Richardsen: *Ultradeformable lipid vesicles can penetrate the skin and other semi-permeable barriers unfragmented. Evidence from double label CLSM experiments and direct size measurements.* Biochimica et Biophysica Acta - Biomembranes, 1564:21–30, 2002.

[379] Cevc, G.: *Transfersomes, liposomes and other lipid suspensions on the skin: permeation enhancement, vesicle penetration, and transdermal drug delivery.* Critical Reviews in Therapeutic Drug Carrier Systems, 13:257–388, 1996.

[380] Kim, D. H. and J. A. Frangos: *Effects of amyloid β-peptides on the lysis tension of lipid bilayer vesicles containing oxysterols.* Biophysical Journal, 95:620–628, 2008.

[381] Grace, H. P.: *Dispersion phenomena in high viscosity immiscible fluid systems and application of static mixers as dispersion devices in such systems.* Chemical Engineering Communications, 14:225–277, 1982.

[382] Rallison, J. M.: *The deformation of small viscous drops and bubbles in shear flows.* Annual Review of Fluid Mechanics, 16:45–66, 1984.

[383] Stone, H. A.: *Dynamics of drop deformation and breakup in viscous fluids.* Annual Review of Fluid Mechanics, 26:65–102, 1994.

[384] Biben, T. and C. Misbah: *Tumbling of vesicles under shear flow within an advected-field approach.* Physical Review E, 67:031908, 2003.

[385] Beaucourt, J., F. Rioual, T. Séon, T. Biben, and C. Misbah: *Steady to unsteady dynamics of a vesicle in a flow.* Physical Review E, 69:011906, 2004.

[386] Windhab, E. J., M. Dressler, K. Feigl, P. Fischer, and D. Megias-Alguacil: *Emulsion processing – from single-drop deformation to design of complex processes and products.* Chemical Engineering Science, 60:2101–2113, 2005.

[387] Keller, S. R. and R. Skalak: *Motion of a tank-treading ellipsoidal particle in a shear flow.* Journal of Fluid Mechanics, 120:27–47, 1982.

[388] Misbah, C.: *Vacillating breathing and tumbling of vesicles under shear flow.* Physical Review Letters, 96:028104, 2006.

[389] Kantsler, V. and V. Steinberg: *Transition to tumbling and two regimes of tumbling motion of a vesicle in shear flow.* Physical Review Letters, 96:036001, 2006.

[390] Noguchi, H. and G. Gompper: *Swinging and tumbling of fluid vesicles in shear flow.* Physical Review Letters, 98:128103, 2007.

[391] Danker, G., T. Biben, T. Podgorski, C. Verdier, and C. Misbah: *Dynamics and rheology of a dilute suspension of vesicles: higher-order theory.* Physical Review E, 76:041905, 2007.

[392] Kantsler, V. and V. Steinberg: *Orientation and dynamics of a vesicle in tank-treading motion in shear flow.* Physical Review Letters, 95:258101, 2005.

[393] Taylor, G. I.: *The formation of emulsions in definable fields of flow.* Proceedings of the Royal Society of London Series A - Containing Papers of a Mathematical and Physical Character, 146:0501–0523, 1934.

[394] Cox, R. G.: *The deformation of a drop in a general time-dependent fluid flow.* Journal of Fluid Mechanics, 37:601–623, 1969.

[395] Kantsler, V., E. Segre, and V. Steinberg: *Vesicle dynamics in time-dependent elongation flow: wrinkling instability.* Physical Review Letters, 99:178102, 2007.

[396] Liu, D.-Z., W.-Y. Chen, L.-M. Tasi, and S.-P. Yang: *Microcalorimetric and shear studies on the effects of cholesterol on the physical stability of lipid vesicles.* Colloids and Surfaces A - Physicochemical and Engineering Aspects, 172:57–67, 2000.

[397] Natsume, Tomotaka and Makoto Yoshimoto: *Membrane permeability and stability of liposomes suspended in shear flow.* Journal of Dispersion Science and Technology, 34:1557–1562, 2013.

[398] Huang, C.-H.: *Studies on phosphatidylcholine vesicles. Formation and physical characteristics.* Biochemistry, 8:344–352, 1969.

[399] Marmottant, P. and S. Hilgenfeldt: *Controlled vesicle deformation and lysis by single oscillating bubbles.* Nature, 423:153–156, 2003.

[400] Richardson, E. S., W. G. Pitt, and D. J. Woodbury: *The role of cavitation in liposome formation.* Biophysical Journal, 93:4100–4107, 2007.

[401] Servuss, R. M., W. Harbich, and W. Helfrich: *Measurement of curvature-elastic modulus of egg lecithin bilayers.* Biochimica et Biophysica Acta, 436:900–903, 1976.

[402] Kwok, R. and E. Evans: *Thermoelasticity of large lecithin bilayer vesicles.* Biophysical Journal, 35:637–652, 1981.

[403] Akashi, K., H. Miyata, H. Itoh, and K. Jr. Kinosita: *Preparation of giant liposomes in physiological conditions and their characterization under an optical microscope.* Biophysical Journal, 71:3242–3250, 1996.

[404] Ellenberger, J. and J. M. H. Fortuin: *A criterion for purely tangential laminar flow in the cone-and-plate rheometer and the parallel-plate rheometer.* Chemical Engineering Science, 40:111–116, 1985.

[405] Salac, D. and M. J. Miksis: *Reynolds number effects on lipid vesicles.* Journal of Fluid Mechanics, 711:122–146, 2012.

[406] Cogswell, F. N.: *Converging flow of polymer melts in extrusion dies.* Polymer Engineering and Science, 12:64–73, 1972.

[407] Padmanabhan, M. and C. W. Macosko: *Extensional viscosity from entrance pressure drop measurements.* Rheologica Acta, 36:144–151, 1997.

[408] Laun, H. M. and H. Schuch: *Transient elongational viscosities and drawability of polymer melts.* Journal of Rheology, 33:119–175, 1989.

[409] Vitkova, V., M. Mader, and T. Podgorski: *Deformation of vesicles flowing through capillaries.* Europhysics Letters, 68:398–404, 2004.

[410] De Cuyper, M. and M. Joniau: *Magnetoliposomes: formation and structural characterization.* European Biophysics Journal, 15:311–319, 1988.

[411] De Cuyper, M. and M. Joniau: *Mechanistic aspects of the adsorption of phospholipids onto lauric acid stabilized Fe_3O_4 nanocolloids.* Langmuir, 7:647–652, 1991.

[412] Martina, M.-S., J.-P. Fortin, C. Ménager, O. Clément, G. Barratt, C. Grabielle-Madelmont, F. Gazeau, V. Cabuil, and S. Lesieur: *Generation of superparamagnetic liposomes revealed as highly efficient MRI contrast agents for in vivo imaging.* Journal of the American Chemical Society, 127:10676–10685, 2005.

[413] Garnier, B., S. Tan, S. Miraux, E. Bled, and A. R. Brisson: *Optimized synthesis of 100 nm diameter magnetoliposomes with high content of maghemite particles and high MRI effect.* Contrast Media & Molecular Imaging, 7:231–239, 2012.

[414] Krishnan, K. M.: *Biomedical nanomagnetics: a spin through possibilities in imaging, diagnostics, and therapy.* IEEE Transactions on Magnetics, 46:2523–2558, 2010.

[415] Tai, L.-A., P.-J. Tsai, Y.-C. Wang, Y.-J. Wang, L.-W. Lo, and C.-S. Yang: *Thermosensitive liposomes entrapping iron oxide nanoparticles for controllable drug release.* Nanotechnology, 20:135101, 2009.

[416] Nappini, S., M. Bonini, F. Baldelli Bombelli, F. Pineider, C. Sangregorio, P. Baglioni, and B. Nordèn: *Controlled drug release under a low frequency magnetic field: effect of the citrate coating on magnetoliposomes stability.* Soft Matter, 7:1025–1037, 2011.

[417] Bothun, G. D., A. Lelis, Y. Chen, K. Scully, L. E. Anderson, and M. A. Stoner: *Multicomponent folate-targeted magnetoliposomes: design, characterization, and cellular uptake.* Nanomedicine: Nanotechnology, Biology, and Medicine, 7:797–805, 2011.

[418] Chen, Y., A. Bose, and G. D. Bothun: *Controlled release from bilayer-decorated magnetoliposomes via electromagnetic heating.* ACS Nano, 4:3215–3221, 2010.

[419] Katagiri, K., Y. Imai, K. Koumoto, T. Kaiden, K. Kono, and S. Aoshima: *Magnetoresponsive on-demand release of hybrid liposomes formed from Fe_3O_4 nanoparticles and thermosensitive block copolymers.* Small, 7:1683–1689, 2011.

[420] Nakao, R., Y. Matuo, F. Mishima, T. Taguchi, S. Maenosono, and S. Nishijima: *Development of magnetic separation system of magnetoliposomes.* Physica C - Superconductivity and its Applications, 469:1840–1844, 2009.

[421] Gomes, J., A. Rank, A. Kronenberger, J. Fritz, M. Winterhalter, and Y. Ramaye: *Polyelectrolyte-coated unilamellar nanometer-sized magnetic liposomes.* Langmuir, 25:6793–6799, 2009.

[422] Weber, W., C. Lienhart, M. Daoud-El Baba, R. N. Grass, T. Kohler, R. Müller, W. J. Stark, and M. Fussenegger: *Magnet-guided transduction of mammalian cells and mice using engineered magnetic lentiviral particles.* Journal of Biotechnology, 141:118–122, 2009.

[423] Domingo, J. C., M. Mercadal, J. Petriz, and M. A. De Madariaga: *Preparation of PEG-grafted immunomagnetoliposomes entrapping citrate stabilized magnetite particles and their application in CD34+ cell sorting.* Journal of Microencapsulation, 18:41–54, 2001.

[424] Bucak, S., D. A. Jones, P. E. Laibinis, and T. A. Hatton: *Protein separations using colloidal magnetic nanoparticles.* Biotechnology Progress, 19:477–484, 2003.

[425] Pankhurst, Q. A., J. Connolly, S. K. Jones, and J. Dobson: *Applications of magnetic nanoparticles in biomedicine.* Journal of Physics D - Applied Physics, 36:R167–R181, 2003.

[426] Ito, A., M. Shinkai, H. Honda, and T. Kobayashi: *Medical application of functionalized magnetic nanoparticles.* Journal of Bioscience and Bioengineering, 100:1–11, 2005.

[427] Grass, R. N., E. K. Athanassiou, and W. J. Stark: *Covalently functionalized cobalt nanoparticles as a platform for magnetic separations in organic synthesis.* Angewandte Chemie - International Edition, 46:4909–4912, 2007.

[428] Turbobeads GmbH (Zurich, Switzerland). http://www.turbobeads.com.

[429] Franzreb, M., M. Siemann-Herzberg, T. J. Hobley, and O. R. T. Thomas: *Protein purification using magnetic adsorbent particles.* Applied Microbiology and Biotechnology, 70:505–516, 2006.

[430] Beaune, G., C. Ménager, and V. Cabuil: *Location of magnetic and fluorescent nanoparticles encapsulated inside giant liposomes.* Journal of Physical Chemistry B, 112:7424–7429, 2008.

[431] Amstad, E., M. Textor, and E. Reimhult: *Stabilization and functionalization of iron oxide nanoparticles for biomedical applications.* Nanoscale, 3:2819–2843, 2011.

[432] Vékás, L., M. V. Avdeev, and D. Bica: *Magnetic nanofluids: synthesis and structure.* In Shi, D. (editor), *Nanoscience in Biomedicine*, chapter 25, pp. 650–728. Springer, Berlin Heidelberg, 2009.

[433] Bica, D., L. Vékás, M. V. Avdeev, O. Marinică, V. Socoliuc, M. Bălăsoiu, and V. M. Garamus: *Sterically stabilized water based magnetic fluids: Synthesis, structure and properties.* Journal of Magnetism and Magnetic Materials, 311:17–21, 2007.

[434] Shen, L., A. Stachowiak, S.-E. K. Fateen, P. E. Laibinis, and T. A. Hatton: *Structure of alkanoic acid stabilized magnetic fluids. A small-angle neutron and light scattering analysis.* Langmuir, 17:288–299, 2001.

[435] Avdeev, M. V., V. L. Aksenov, M. Balasoiu, V. M. Garamus, A. Schreyer, G. Török, L. Rosta, D. Bica, and L. Vékás: *Comparative analysis of the structure of sterically stabilized ferrofluids on polar carriers by small-angle neutron scattering.* Journal of Colloid and Interface Science, 295:100–107, 2006.

[436] Walde, P., T. Namani, K. Morigaki, and H. Hauser: *Formation and properties of fatty acid vesicles (liposomes).* In Gregoriadis, G. (editor), *Liposome Technology*, volume 1, chapter 1, pp. 1–19. Informa Healthcare, New York, 3rd edition, 2006.

[437] Skoog, D. A., D. M. West, F. J. Holler, and S. R. Crouch: *Analytical Chemistry - An Introduction.* Saunders College Publishing, Fort Worth, TX, 7th edition, 2000.

[438] Sabaté, R., R. Barnadas-Rodríguez, J. Callejas-Fernández, R. Hidalgo-Álvarez, and J. Estelrich: *Preparation and characterization of extruded magnetoliposomes.* International Journal of Pharmaceutics, 347:156–162, 2008.

[439] Nappini, S., F. Baldelli Bombelli, M. Bonini, B. Nordèn, and P. Baglioni: *Magnetoliposomes for controlled drug release in the presence of low-frequency magnetic field.* Soft Matter, 6(1):154–162, 2010.

[440] *Gel Filtration: Principles and Methods.* GE Healthcare, Uppsala, Sweden, 2010.

[441] Pradhan, P., J. Giri, R. Banerjee, J. Bellare, and D. Bahadur: *Preparation and characterization of manganese ferrite-based magnetic liposomes for hyperthermia treatment of cancer.* Journal of Magnetism and Magnetic Materials, 311:208–215, 2007.

[442] Pradhan, P., J. Giri, F. Rieken, C. Koch, O. Mykhaylyk, M. Döblinger, R. Banerjee, D. Bahadur, and C. Plank: *Targeted temperature sensitive magnetic liposomes for thermo-chemotherapy.* Journal of Controlled Release, 142:108–121, 2010.

[443] Amstad, E., T. Gillich, I. Bilecka, M. Textor, and E. Reimhult: *Ultrastable iron oxide nanoparticle colloidal suspensions using dispersants with catechol-derived anchor groups.* Nano Letters, 9:4042–4048, 2009.

[444] Bothun, G. D. and M. R. Preiss: *Bilayer heating in magnetite nanoparticle-liposome dispersions via fluorescence anisotropy.* Journal of Colloid and Interface Science, 357:70–74, 2011.

[445] Nappini, S., M. Bonini, F. Ridi, and P. Baglioni: *Structure and permeability of magnetoliposomes loaded with hydrophobic magnetic nanoparticles in the presence of a low frequency magnetic field.* Soft Matter, 7:4801–4811, 2011.

[446] Ginzburg, V. V. and S. Balijepailli: *Modeling the thermodynamics of the interaction of nanoparticles with cell membranes.* Nano Letters, 7:3716–3722, 2007.

[447] Bonnaud, C., C. A. Monnier, D. Demurtas, C. Jud, D. Vanhecke, X. Montet, R. Hovius, M. Lattuada, B. Rothen-Rutishauser, and A. Petri-Fink: *Insertion of nanoparticle clusters into vesicle bilayers.* ACS Nano, 8:3451–3460, 2014.

[448] Aliouane, N., S. Chafaa, T. Douadi, J.-J. Hélesbeux, M. A. Khan, O. Duval, and G. Bouet: *Novel polydentate phosphonic acids: protonation and stability constants of complexes with Fe(III) and Cu(II) in aqueous medium.* Heteroatom Chemistry, 21:51–62, 2010.

[449] Cintra, E. R., F. S. Ferreira, J. L. Santos Jr., J. C. Campello, L. M. Socolovsky, E. M. Lima, and A. F. Bakuzis: *Nanoparticle agglomerates in magnetoliposomes.* Nanotechnology, 20:045103, 2009.

[450] Nappini, S., T. Al Kayal, D. Berti, B. Nordèn, and P. Baglioni: *Magnetically triggered release from giant unilamellar vesicles: visualization by means of confocal microscopy.* Journal of Physical Chemistry Letters, 2:713–718, 2011.

[451] Jung, C. W. and P. Jacobs: *Physical and chemical properties of superparamagnetic iron oxide MR contrast agents: ferumoxides, ferumoxtran, ferumoxsil.* Magnetic Resonance Imaging, 13:661–674, 1995.

[452] Lin, M. M., D. K. Kim, A. J. El Haj, and J. Dobson: *Development of superparamagnetic iron oxide nanoparticles (SPIONS) for translation to clinical applications.* IEEE Transactions on Nanobioscience, 7:298–305, 2008.

[453] Skouras, A., S. Mourtas, E. Markoutsa, M.-C. De Goltstein, C. Wallon, S. Catoen, and S. G. Antimisiaris: *Magnetoliposomes with high USPIO entrapping efficiency, stability and magnetic properties.* Nanomedicine - Nanotechnology Biology and Medicine, 7:572–579, 2011.

[454] Hodenius, M., M. De Cuyper, L. Desender, D. Müller-Schulte, A. Steigel, and H. Lueken: *Biotinylated stealth® magnetoliposomes.* Chemistry and Physics of Lipids, 120:75–85, 2002.

[455] Namiki, Y., T. Namiki, H. Yoshida, Y. Ishii, A. Tsubota, S. Koido, K. Nariai, M. Mitsunaga, S. Yanagisawa, H. Kashiwagi, Y. Mabashi, Y. Yumoto, S. Hoshina, K. Fujise, and N. Tada: *A novel magnetic crystal-lipid nanostructure for magnetically-guided in vivo gene delivery.* Nature Nanotechnology, 4:598–606, 2009.

[456] Lecommandoux, S., O. Sandre, F. Chécot, J. Rodriguez-Hernandez, and R. Perzynski: *Magnetic nanocomposite micelles and vesicles.* Advanced Materials, 17:712–718, 2005.

Curriculum Vitae

Helen Alicia ENGEL

Personal Data

Date of birth	16 May 1981
Place of birth	Zurich
Nationality	Swiss

Education

03/2008 - 06/2014	**Ph. D. studies at the Laboratory of Food Process Engineering**, Swiss Federal Institute of Technology (ETH), Zurich, Switzerland Candidate for degree: Dr. sc. ETH Zurich
08/2001 - 06/2007	**Graduate studies in Food Science** at ETH Zurich Diploma thesis in Food Process Engineering: Dispersing of oil coated microgels in aqueous media Degree: Dipl. Lm.-Ing. ETH Zurich
09/2005 - 04/2006	Erasmus student at Ecole Nationale d'Ingénieurs des Technique des Industries Agricoles et Alimentaires (ENITIAA), Nantes, France Term paper in Microencapsulation
08/1994 - 01/2001	**High school** at Kantonsschule Zürcher Oberland (KZO), Switzerland Degree: Swiss Matura Typus B (Latin)
02/1998 - 01/1999	High school at Colegio Misericordia, Rosario, Argentina Graduation 5∘ liceo as an exchange student (AFS)

Work experience

08/2004 - 05/2005	**Industrial placement with Cereal Partners Worldwide (CPW)**, Welwyn Garden City, UK 50:50 joint venture between Nestlé and General Mills Department for Research and Development
06/2007 - 09/2007 08/2005 - 09/2005 07/2004 - 08/2004	**Summer jobs on Swiss alp Uina Dadaint**, Sent, Switzerland Tending cows, making cheese, serving tourists
08/2001 - 09/2001	**Internship at Dairy Bühl**, Gibswil, Switzerland Cheese manufacturing, quality control, cleaning
2000 - 2014	**Support in the Medical Translation and Life Science Department at Five Office Ltd**, Wetzikon, Switzerland Clinical Research, Regulatory, Health Marketing and Communication

Publications

- Walde, P., K. Cosentino, H. Engel, P. Stano. *Giant vesicles: preparations and applications.* ChemBioChem, 11:848–865, 2010.

- Engel, H., E. Rondeau, E. J. Windhab, P. Walde. *External surface area determination of lipid vesicles using trinitrobenzene sulfonate and ultraviolet/visible spectrophotometry.* Analytical Biochemistry , 442:262–271, 2013.

- Rondeau, E., S. Holzapfel, H. Engel, E. J. Windhab. *Vesicles and composite particles by rotating membrane pore extrusion.* In *Upscaling of Bio-Nano-Processes*, H. Nirschl, K. Keller (Eds.), as part of the series *Lecture Notes in Bioengineering*, pp. 77–96. ISBN 978-3-662-43898-5. Springer-Verlag, Berlin Heidelberg, 2014.

Patent

- Bohm, A., J. Lisner, J. Braun, H. Engel, E. J. Windhab, W. Meier. *Verfahren und Vorrichtungen zur Vesikelbildung, insbesondere unter Verwendung von Block-Copolymeren.* Patent number: WO 2011124589 A2. 2011.